TRANSACTIONS
OF THE ASME
Series C

Journal of HEAT TRANSFER

August 1959

RADIATION • CONDUCTION • CONVECTION • COMPLEX SYSTEMS • PHASE CHANGES AND MIXTURES • TRANSIENT PHENOMENA • THERMOPHYSICAL PROPERTIES • EXPERIMENTAL TECHNIQUES • THERMOMETRY • ANALOG METHODS • ANALYTICAL AND NUMERICAL METHODS • APPLICATIONS • DESIGN TECHNIQUES • HEAT EXCHANGERS • INSULATION • ECONOMIC FACTORS BIOTECHNOLOGY • ASTRONAUTICS

Published Quarterly by
THE AMERICAN SOCIETY OF MECHANICAL ENGINEERS

TRANSACTIONS OF THE ASME
Series C

Journal of
HEAT TRANSFER
VOL. 81 • SERIES C • NO. 3
August 1959

CONTENTS

175 **Heat Transfer Between Concentric Rotating Clyinders**
I. S. Bjorklund and W. M. Kays

187 **Full-Scale Human-Body-Model Thermal Exchange Compared With Equational Condensation of Human Calorimetric Data**
L. P. Herrington

195 **The Emissivity and Absorptivity of Parachute Fabrics**
J. P. Hartnett, E. R. G. Eckert, and R. Birkebak

202 **An Experimental and Analytical Study of Vortex-Flow Temperature Separation by Superposition of Spiral and Axial Flows—Part 1**
J. E. Lay

213 **An Experimental and Analytical Study of Vortex-Flow Temperature Separation by Superposition of Spiral and Axial Flows—Part 2**
J. E. Lay

223 **Analysis of the Aerodynamic Heating for a Re-Entrant Space Vehicle**
M. J. Brunner

230 **A Photographic Study of Boiling in the Absence of Gravity**
R. Siegel and C. Usiskin

237 **Some Radiator Design Criteria for Space Vehicles**
J. P. Callinan and W. P. Berggren

245 **Optimization of a Conventional-Fuel-Fired Thermoelectric Generator**
B. W. Swanson and E. V. Somers

TECHNICAL BRIEFS

249 **Heat Transfer From a Rotating Disk to Fluids of Any Prandtl Number**
E. M. Sparrow and J. L. Gregg

251 **An Approximate Treatment of Unsteady Heat Conduction in Semi-Infinite Solids With Variable Thermal Properties**
K.-T. Yang and Albin Szewczyk

EDITORIAL DEPARTMENT

Editor, J. J. JAKLITSCH, JR.
Editor Emeritus, GEORGE A. STETSON
Consulting Editor, LEO BLODGETT
Production, JEAN NORTH
Art Editor, HENRY BALFOUR

HEAT TRANSFER DIVISION

Chairman, W. E. HAMMOND
Secretary, J. P. WACHUNAS
Consulting Editor, S. P. KEZIOS

OFFICERS OF THE ASME

President, G. B. WARREN
Secretary, O. B. SCHIER, II
Treasurer, E. J. KATES
Assistant Treasurer, H. J. BAUER

PUBLICATIONS COMMITTEE

Chairman, JOHN de S. COUTINHO
R. G. A. SKROTZKI
HENDLEY N. BLACKMON
R. D. MINDLIN
MARTIN GOLAND
Junior Representatives
A. T. WUSKA
A. S. GOLDSTEIN

REGIONAL ADVISORY BOARD

Region I, ROY L. PARSELL
Region II, GLENN R. FRYLING
Region III, F. J. HEINZE
Region IV, FRANCIS C. SMITH
Region V, H. M. CATHER
Region VI, C. R. EARLE
Region VII, M. POPOVICH
Region VIII, LINN HELANDER

Published quarterly by The American Society of Mechanical Engineers. Publication office at 20th and Northampton Streets, Easton, Pa. The editorial department is located at the headquarters of the Society, 29 West Thirty-Ninth Street, New York 18, N. Y. Cable address, "Mechaneer," New York. Price $3.00 a copy, $10.00 annually; to members, $1.50 a copy, $5.00 annually. Add 50 cents for postage to all countries outside the United States and Canada. Changes of address must be received at Society headquarters seven weeks before they are to be effective on the mailing list. Please send old as well as new address. . . . By-Law: The Society shall not be responsible for statements or opinions advanced in papers or . . . printed in its publications (B13, Par. 4). . . . Second-class mail privileges authorized at Easton, Penna. . . . This publication is authorized to be mailed at the special rates of postage prescribed by Section 132.122 . . . © Copyrighted, 1959, by The American Society of Mechanical Engineers. Reprints from this publication may be made on condition that full credit be given the TRANSACTIONS OF THE ASME, Series C—Journal of Heat Transfer, and the author, and that date of publication be stated.

TRANSACTIONS OF THE ASME
is indexed by the Engineering Index, Inc.

TRANSACTIONS OF THE ASME Series B

Journal of
ENGINEERING FOR INDUSTRY
Volume 81 • Series B • Number 3

CONTENTS FOR AUGUST, 1959

187 Factors Influencing the Performance of Grinding Wheels, by E. J. Krabacher. (58—SA-40)
201 Vibrations of Flexible Precision Grinding Spindles, by R. S. Hahn. (58—A-97)
207 The Effect of Process Variables on Extrusion Pressures of Lead, by J. Frisch and E. G. Thomsen. (58—A-109)
217 Approximate Solutions to a Problem of Press Forging, by S. Kobayashi and E. G. Thomsen. (58—A-140)
228 Theory and Experiment of Press Forging Axisymmetric Parts of Aluminum and Lead, by S. Kobayashi, R. Herzog, J. T. Lapsley, Jr., and E. G. Thomsen. (58—A-154)
239 A Three-Dimensional, Tool-Life Equation—Machining Economics, by B. N. Colding. (58—A-123)
251 Some Observations on the Shearing Process in Metal Cutting, by S. Kobayashi and E. G. Thomsen. (58—A-139)
263 Observations on the Angle Relationships in Metal Cutting, by D. M. Eggleston, R. Herzog, and E. G. Thomsen. (58—A-138)

TRANSACTIONS OF THE ASME Series A

Journal of
ENGINEERING FOR POWER
Volume 81 • Series A • Number 3

CONTENTS FOR JULY, 1959

1958 Gas Turbine Progress Report

215 Introduction, by R. T. Sawyer. (58—A-46 A)
219 Materials, by A. W. Herbenar and G. R. Heckman. (58—A-46 B)
226 Turbine Cooling, by J. B. Esgar. (58—A-46 C)
234 Fuels, by A. D. Foster. (58—A-46 D)
244 Cycle Components, by P. F. Martinuzzi. (58—A-46 E)
259 Compound Piston-and-Turbine Engines, by A. L. London. (58—A-46 F)
265 Aviation, by O. E. Lancaster. (58—A-46 G)
280 Rocket Turbines, by O. E. Lancaster and C. J. Bates. (58—A-46 H)
290 Automotive, by F. L. Schwartz. (58—A-46 I)
298 Railroad, by P. R. Broadley, W. M. Meyer, D. S. Neuhart, E. L. Barlow, R. C. Bond, D. S. D. Williams, and B. W. C. Cooke. (58—A-46 J)
311 Marine, by J. W. Sawyer and H. M. Simpson. (58—A-46 K)
344 Industrial and Central Station, by B. G. A. Skrotzki. (58—A-46 L)
352 Nuclear, by R. P. Godwin and E. S. Dennison. (58—A-46 M)

TRANSACTIONS OF THE ASME Series D

Journal of
BASIC ENGINEERING
Vol. 81 • Series D • No. 2

CONTENTS FOR JUNE, 1959

101 Elastic and Damping Properties of Cylindrical Journal Bearings, by B. Sternlicht. (58—Lub-3)
109 Axial, Relative Motion of a Circular Step Bearing, by L. Licht. (58—Lub-1)
118 Friction and Wear of Metals to 1000 C, by E. P. Kingsbury and E. Rabinowicz. (58—Lub-6)
123 Friction Factors for Turbulent Flow in Curved Pipes, by H. Itō. (58—SA-14)
135 Characteristics of a Self-Lubricated Stepped Thrust Pad of Infinite Width With Compressible Lubricant, by K. C. Kochi. (58—A-194)
147 Direct Measurement of Net Positive Suction Head, by R. B. Jacobs, K. B. Martin, and R. J. Hardy. (58—A-38)
153 Transitional Phenomena in Ultrasonic Shock Waves Emitted by Cavitation on Hydrofoils, by F. Numachi. (58—A-117)
167 Cavitation and NPSH Requirements of Various Liquids, by Victor Salemann. (58—A-82)
181 The Unsteady Wake Interaction in Turbomachinery and Its Effect on Cavitation, by Hsuan Yeh and J. J. Eisenhuth. (58—A-114)
190 Thermal-Stress Ratchet Mechanism in Pressure Vessels, by D. R. Miller. (58—A-129)
197 Refractory Metal Facings for Protection of Metal Surfaces Subjected to Repeated High-Temperature Pulses, by Aaron Cohen and Edward Homer. (58—A-188)
203 The Failure of Structural Metals Subjected to Strain-Cycling Conditions, by R. W. Swindeman and D. A. Douglas. (58—A-198)
213 Evaluation of Material Wear and Self-Welding in Sodium-Cooled Reactor Systems, by R. B. Jerman, R. C. Williams, and D. O. Leeser.
226 Irradiation of Haynes-25 and Inconel-X Compression Springs in High-Temperature High-Pressure Water, by R. L. Mehan. (58—A-94)
233 Energy Losses of Balls Rolling on Plates, by R. C. Drutowski. (58—A-190)
239 On the Effect of Lubricant Inertia in the Theory of Hydrodynamic Lubrication, by A. A. Milne (58—A-195)
245 Surface Finish and Clearance Effects on Journal-Bearing Load Capacity and Friction, by F. W. Ocvirk and G. B. DuBois. (58—A-134)
254 Statistical Optimization of Regulators Employing a Binary Error Criterion, by J. H. Milsum. (58—A-71)
263 An Introduction to the Time-Modulated Acceleration Switching Electrohydraulic Servomechanism, by S. A. Murtaugh, Jr. (58—A-159)
272 Discussion on previously published paper by B. Sternlicht and R. C. Elwell.

TRANSACTIONS OF THE ASME Series E

Journal of
APPLIED MECHANICS
Volume 81 • Series E • Number 2

CONTENTS FOR JUNE, 1959

TECHNICAL PAPERS

161 Effect of a Nonisothermal Free Stream on Boundary-Layer Heat Transfer, E. M. Sparrow and J. L. Gregg. (58—A-42)

166 Visual Studies of the Wall Layers of the Turbulent Boundary Layer, S. J. Kline and P. W. Runstadler. (58—A-64)

171 Unsteady Laminar Boundary Layers Over an Arbitrary Cylinder, Kwang-Tzu Yang. (58—A-49)

179 On Journal Bearings of Finite Length With Variable Viscosity, L. N. Tao. (58—A-75)

184 Analysis of Complex Kinematic Chains With Influence Coefficients, J. Modrey. (58—A-74)

189 A Theory of Oil Whip, Yukio Hori. (59—APM-2)

199 On Critical Speeds of a Shaft Supported by a Ball Bearing, Toshio Yamamoto. (59—APM-12)

205 Root-Locus Analysis of Structural Coupling in Control Systems, R. H. Cannon, Jr. (58—A-65)

210 Normal Vibrations of Uniform Plate Carrying Any Number of Finite Masses, W. F. Stokey and C. F. Zorowski. (58—A-28)

217 Transients in Simple Undamped Oscillators Under Inertial Disturbances, Antongiulio Dornig. (58—A-58)

224 On Laterally Loaded Semicircular Plate With Clamped Edges, W. H. Jurney. (59—APM-3)

227 Direct Determination of Stresses in Plane Elasticity Problems, P. S. Theocaris. (58—A-43)

235 Stresses in a Stretched Slab Having a Spherical Cavity, Chih-Bing Ling. (58—A-45)

241 Influence Coefficients for Edge-Loaded Short, Thin, Conical Frustums, J. H. Baltrukonis.

246 Upper and Lower Bounds for Special Eigenvalues, F. C. Appl and C. F. Zorowski. (59—APM-18)

251 Analysis of a Compression Test of a Model of a Granular Medium, C. W. Thurston and H. Deresiewicz. (58—A-48)

259 A Reassessment of Deformation Theories of Plasticity, Bernard Budiansky. (58—A-54)

265 Collapse Loads of Rings and Flanges Under Uniform Twisting Moment, Burton Paul. (58—A-55)

271 Creep of Thick-Walled Tubes Under Internal Pressure, F. P. J. Rimrott. (59—APM-6)

276 Strain-Hardening Solutions to Plate Problems, Nicholas Perrone and P. G. Hodge, Jr.

285 Determination of Creep Deflection of a Rivet in Double Shear, Joseph Marin. (58—A-47)

DESIGN DATA AND METHODS

290 The Frequency of Vibration of Rectangular Isotropic Plates, H. J. Fletcher.

BRIEF NOTES

291 Large Deflections of a Clamped Elliptical Plate, W. A. Nash and I. D. Cooley. 293 Thermal Stresses at Spherical Cavities, A. L. Florence and J. N. Goodier. 294 Deflection of a Thick Ring in Diametral Compression, Alexander Blake. 296 The Biot-Willis Coefficients for a Sandstone, I. Fatt. 297 Circular Plates on Elastic Foundation, G. D. Galletly. 298 Frequencies of Vibration of Stiffened Plates, R. L. Thorkildsen and W. H. Hoppmann, II. 300 Design of a π Network for Heat-Flow Analog, D. G. Stephenson and G. O. Starke. 301 Stress Distribution in a Square Tube, M. A. Sadowsky and E. E. Zwicky, Jr.

DISCUSSION

303 Discussion of previously published papers by R. H. Cannon, Jr.; C. G. Van Niekerk; M. Hetényi and P. H. McDonald, Jr.; K. A. Foss; N. J. Huffington, Jr., and W. H. Hoppmann, II; T. J. Harvey; H. Tramposch and G. Gerard; C. E. Crede; C. J. Ancker, Jr., and J. N. Goodier; H. Poritsky and F. A. Fend; K. L. Johnson; J. H. Haywood and L. B. Wilson.

317 **BOOK REVIEWS**

Heat Transfer Between Concentric Rotating Cylinders

I. S. BJORKLUND

Shell Development Company, Emeryville, Calif.

W. M. KAYS

Professor, Mechanical Engineering, Stanford University, Stanford, Calif. Mem. ASME

In this paper the problem of convective heat transfer between concentric rotating cylinders is studied. Experimental heat-transfer data are presented for four different values of clearance between the cylinders and for several combinations of outer to inner cylinder speed. The heat-transfer performance indicates three regimes of flow; the first at low peripheral velocities, in which laminar flow and heat transfer by conduction prevail, the second at cylinder speeds above a theoretically predictable value, in which vortex flow occurs and is the controlling mechanism, and a third at still higher speeds, in which a distorted type of vortex motion may be present. The data for the case of the inner cylinder only rotating can be correlated by the equation

$$N_{Nu}/N_{Nu_{cond}} = 0.175\ N_{Ta}^{1/2}$$

for the Taylor number range 90 to 2000. A heat-and-momentum-transfer-analogy solution for this case follows the trend of the data, but gives results which are somewhat high. The combined effects of rotation of both cylinders may be correlated by the empirical equation

$$\frac{N_{Nu}}{N_{Nu_{cond}}} = 1.1\left[\frac{N_{Ta} - (N_{Ta_{cr_q}} - N_{Ta_{cr_0}})(1 - 3.5\ d/R_1)}{41.1 + (N_{Ta_{cr_q}} - N_{Ta_{cr_0}})(3.5\ d/R_1)}\right]^{1/2}$$

for values of the abscissa from about 2 to 50.

Objectives and Introduction

In a previous paper [1][1] the heat transfer from a single rotating cylinder to still air and to a cross-stream of air was investigated. Analysis of the thermal behavior of machinery often involves not only heat transfer from rotating elements to a surrounding fluid of large expanse, but also heat transfer from confined rotating parts. Such a problem might arise in connection with consideration of the thermal behavior of enclosed shafting, multiple concentric drives, turbine rotors, and similar machine parts. Heat transfer from a long rotating cylinder to a concentric cylindrical shell is geometrically the simplest of the possible configurations, and perhaps one of the most widely encountered; it has thus been chosen as the subject for investigation.

The objectives of the present work have been to study the heat-transfer characteristics of such a system and to determine the influences of the ratio of outer to inner cylinder angular velocity, η, and of the relative radial clearance between the cylinders, d/R_1, on the heat-transfer rate. Consideration is restricted to the case of no axial flow of fluid in the annulus between the cylinders.

A number of authors have dealt with the flow between concentric cylinders with the inner one rotating. Taylor [2], in a very early paper, showed that above a critical speed of rotation the laminar Couette flow breaks down into a flow consisting of pairs of three-dimensional ring-shaped vortexes. Hagerty [3] and Kaye and Elgar [4] have also photographed such vortex patterns. A sketch of this flow pattern is shown in Fig. 1(*a*).

Taylor [5] also measured the velocity and temperature profiles

[1] Numbers in brackets designate References at end of paper.

Contributed by the Heat Transfer Division and presented at the Annual Meeting, New York, N. Y., November 30–December 5, 1958, of The American Society of Mechanical Engineers.

Note: Statements and opinions advanced in papers are to be understood as individual expressions of their authors and not those of the Society. Manuscript received at ASME Headquarters, August 7, 1958. Paper No. 58—A-99.

Nomenclature

English Letter Symbols

- A = surface heat-transfer area of heated cylinder, ft²
- c_p = specific heat at constant pressure, Btu/(lb deg F)
- d = radial clearance between concentric cylinders, ft
- f = friction factor for concentric cylinders, dimensionless
- g_c = proportionality factor in Newton's Second Law, 32.2 $(lb_M)/(lb_F) \times$ ft/sec²
- h = unit convection conductance on surface of heated cylinder, Btu/-(hr ft² deg F)
- k = unit thermal conductivity, Btu/-(hr ft² deg F/ft)
- q = heat-transfer rate, Btu/hr
- R_1 = radius of heated cylinder, ft
- r = radial co-ordinate in boundary layer, ft
- t = temperature, deg F
- u = velocity relative to heated cylinder, ft/sec
- V = velocity, ft/sec
- y = distance from surface of heated cylinder to a point in the boundary layer, ft

Greek Letter Symbols

- α = thermal diffusivity, $k/\rho c_p$, ft²/hr
- ϵ_H = eddy diffusivity for heat, ft²/hr
- ϵ_M = eddy diffusivity for momentum, ft²/hr

(Continued on next page)

occurring at very high rotational speeds and found that both the circumferential velocity and the moment of momentum apparently increased in moving toward the outer cylinder. He supposed that this was due to the effect of the total-pressure tube used in the measurements, and by extrapolating to zero tube diameter he concluded that the true velocity distribution was one of constant moment of momentum, or uR = constant, through about 80 per cent of the gap. From a comparison with the measured temperature profile it was proposed that vorticity rather than momentum is transferred by turbulent diffusion in the annular space between the two cylinders.

Much later work by Pai [6] indicates that this may not be the case, but that the phenomenon which Taylor observed was quite likely due to the persistence of the vortex flow, even at speeds several hundred times the critical speed at which it begins. Pai's measurements with a hot wire indicate that a distorted vortex pattern, as shown in Fig. 1(b), exists and that the mean-velocity profile obtained depends upon where the velocity traverses are made relative to the positions of the vortexes. If mean-velocity profiles for several positions along the length of the cylinder are averaged, the averaged curve is found to be one of constant mean velocity over a large part of the gap. The secondary motion is found to play an essential part in the transport of moment of momentum, and in regions where secondary flow is negligible, the momentum follows the laws for homologous turbulence.

Velocity measurements by Hromas and Thompson [7] agree with those of Pai, although their measurements with the inner cylinder rotating are very limited, the bulk of their data being taken in the laminar flow region with the outer cylinder rotating.

A great deal of attention has been given to the determination of the point at which vortex flow begins. Taylor [2] has derived an equation for the speed at which laminar flow becomes unstable for small disturbances when the two cylinders are rotated in the same direction with a relative velocity. This may be expressed in the notation of the present work as,

$$N_{\mathrm{Ta}_{cr}} = \left\{ \frac{48.70(2 + d/R_1)}{(1 - \eta)[1 - \eta(1 + d/R_1)^2]\left[0.0571\left(\frac{1 + \eta}{1 - \eta} - 0.652d/R_1\right) + \frac{0.00056}{\frac{1 + \eta}{1 - \eta} - 0.652d/R_1}\right]} \right\}^{1/2} \quad (1)$$

where N_{Ta} is a dimensional group shown by Kaye and Elgar [4] to be a significant parameter in concentric rotating cylinder work.

Taylor's experiments and those of Lewis [8] confirm this expression quite well. Lewis' experiments indicate that it is valid for values of d/R_1 at least as high as 0.71, and is also valid for small negative values of η (cylinders rotating in opposite directions). The limiting value of critical Taylor number given by this expression, for the outer cylinder stationary ($\eta = 0$) and very small clearance ratio ($d/R_1 \to 0$), is 41.1.

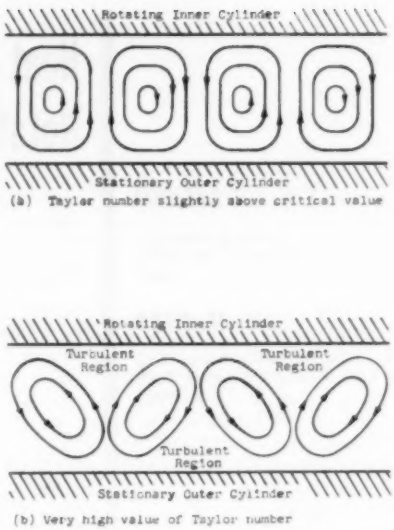

Fig. 1 Probable vortex patterns between concentric rotating cylinders

Meksyn [9, 10, 11], in a series of papers, has presented a number of stability criteria. His expression for the critical speed with the cylinders rotating in the same direction is somewhat more complex than that given by Taylor, but reduces to the same value for limiting cases. For the cylinders rotating in opposite directions his results may be expressed as:

$$N_{\mathrm{Ta}_{cr}} = \left\{ \frac{141.6(d/R_1)^3(1 + d/R_1)[(1 + d/R_1)^2 - 1]^2(1 - \eta)^{1/2}}{[(1 + d/R_1)(1 - \eta)^{1/2} - [1 - \eta(1 + d/R_1)^2]^{1/2}]^3} \right\}^{1/2} \quad (2)$$

This equation is valid provided that $(-\eta)$ is not much smaller than one half.

Critical values calculated from these expressions are shown with the present experimental results in Figs. 6 through 9, where it may be seen that they predict quite accurately the transition from laminar flow performance.

Friction data for concentric cylinders with either the inner cylinder or the outer cylinder rotating have also been obtained by Taylor [12]. Some of his data for the inner cylinder rotating,

Nomenclature

η = ratio of outer cylinder rpm to inner cylinder rpm; η is (+) for corotation and (−) for counterrotation
ν = kinematic viscosity, μ/ρ, ft²/hr
ρ = fluid density, lb/ft³
τ_0 = fluid shear stress, lb$_F$/ft²
ω_1 = angular velocity of inner cylinder, rad/sec
ω_2 = angular velocity of outer cylinder, rad/sec

Nondimensional Groupings

u^+ = nondimensional relative velocity in boundary layer, $u/\sqrt{g_c\tau_0/\rho}$
y^+ = nondimensional distance from heated cylinder surface, $y\sqrt{g_c\tau_0/\rho}/\nu$
N_{Nu} = Nusselt number, hd/k
N_{Pr} = Prandtl number, $\mu c_p/k$
N_{Ta} = Taylor number, $\sqrt{d/R_1}\,(R_1\omega_1 d/\nu)$
$N_{\mathrm{Ta}_{cr_\eta}}$ = Taylor number for transition from laminar to vortex flow, when cylinder speed ratio has the value η

NOTE: All fluid properties in the experimental correlations have been evaluated at a temperature halfway between the surface temperatures of the two cylinders.

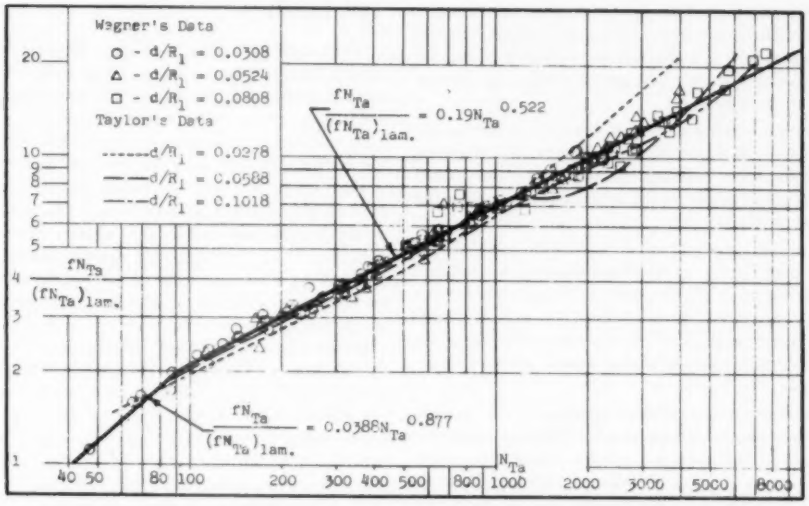

Fig. 2 Concentric cylinder friction data of Taylor and of Wagner, inner cylinder only rotating

along with a large number of data taken by Wagner [13] for cylinders with small clearance ratios, are shown on Fig. 2. These data have been replotted in terms of a grouping of variables which correlates the data for various clearance ratios with a single curve. The laminar flow friction factor used in the ordinate may be expressed as:

$$(f N_{Ta})_{lam} = \frac{4(d/R_1)^{3/2}}{1 - \left(\frac{1}{1 + d/R_1}\right)^2} \qquad (3)$$

Fig. 2 indicates, in addition to the transition at a Taylor number of about 41, what appears to be a second transition at a Taylor number of about 90.

Becker[15], in a very recent work, gives some experimental heat-transfer data for concentric cylinders with the inner cylinder only rotating.[2] The only previously available data for this case are those which have resulted from experiments related to the cooling of electric motors. Most of these latter data have been for slotted surfaces or for axial air flow in the annulus, but some of the data by Gazley [14] are for smooth cylindrical surfaces and no axial air flow. These data are included on Fig. 10 for comparison with the results of the present investigation and, along with an analogy solution proposed by Gazley, will be discussed in a later section of this paper.

Description of Test Apparatus

The details of construction of the test system are shown on Fig. 3. The inner cylinder has been discussed in a previous paper [1] and will be described only briefly here. It consists of an electrically heated test section 18¼ in. long and 2.26 in. in diameter. Plastic spacers insulate the copper section from the steel stub shafts at the ends, and the entire inner cylinder assembly is supported by double sets of ball bearings to minimize bending moment at the joints. Heater power is supplied through a Variac control to slip rings on the cylinder, and measured by means of a high-current watt-meter. Rotation is provided by vee-belt drive from a d-c motor on a variable voltage source.

The temperature of the heated cylinder is sensed by a stationary thermocouple which projects into a cavity in the solid end of the rotating copper test section. This system eliminated the

[2] Becker's data were discovered too late to include for comparison in Fig. 10. They cover one clearance ratio, $d/R_1 = 0.233$, a Taylor number range to about 500, and correspond very well with the data of this paper.

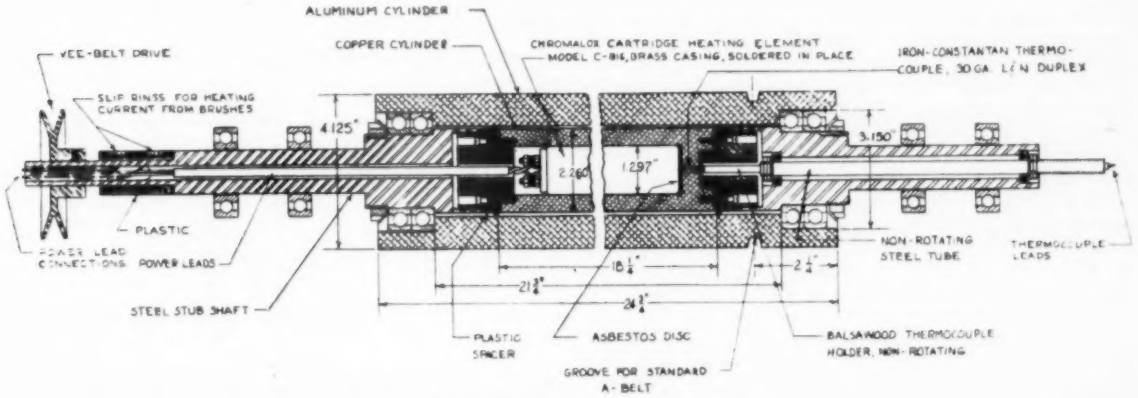

Fig. 3 Construction details of assembled cylinders

need for slip-rings in the thermocouple circuit and was found to indicate adequately the local temperature of the copper cylinder. The measured temperature is corrected for variation along the length of the cylinder due to end leakage to obtain the average temperature of the heated cylinder.

The outer aluminum cylinder is mounted concentrically on the inner cylinder by means of duplexed ball bearings, and the axial flow of air through the space between the cylinders is obstructed by soft leather rings glued to the plastic spacers at the ends of the heated-cylinder test section.

By means of suitable gears and/or pulleys the outer cylinder is driven from the same motor as used to rotate the heated cylinder. By altering the train of gears and/or pulleys, either cylinder can be rotated separately, or both may be rotated simultaneously at fixed speed ratios either in the same or in opposite directions. The speed of rotation of each cylinder is measured by means of a Strobotac.

The temperature of the outer cylinder is measured by means of a thermocouple imbedded at the point where the local temperature is closely equal to the average temperature of the active length of the aluminum cylinder, and thus no correction for temperature variation is necessary. The thermocouple leads are brought out to iron and constantan contacts on the surface of the cylinder, and iron and constantan pickups are used to complete the circuit to the potentiometer.

It was found necessary to take the reading of this temperature with the outer cylinder stationary, since the use of slip-rings with the cylinder rotating gave erroneous readings. This was apparently due to the large diameter, and consequently high surface speed, that was necessary for the slip-rings. This measurement is made by quickly stopping the cylinder at the end of a run, completing the thermocouple circuit by pivoting the pickups into place against the contacts on the cylinder, and reading the potentiometer; the entire procedure takes about half a minute. Because of the large time constant of the rather thick-walled aluminum cylinder, this method of measurement does not introduce significant error into the results. An analysis making rather severe assumptions indicates that the temperature difference between the cylinder and the surroundings can not drop as much as 1 per cent in the time required for the measurement.

The various gap widths used in the tests were all accomplished using the same cylinders. Between each series of runs the aluminum outer cylinder was simply dismounted and its inner surface rebored to the larger diameter required for the next clearance ratio to be examined.

A crossflow of air to cool the outer cylinder is provided through a duct which discharges vertically downward a few inches above the test cylinders.

From an analysis of experimental uncertainty it may be concluded that the test system is capable of yielding Nusselt number determinations within an uncertainty interval of $\pm 4^1/_2$ per cent. The Taylor number determination is within an uncertainty interval of about $\pm 3^1/_2$ per cent. A possible source of error which does not lend itself to analysis arises in connection with the large time constant of the cylinder, especially at low rotational speeds and large clearance ratio. The system does not respond quickly to variations in line voltage and variations in surface conductance accompanying speed variation. To minimize this source of error, a regulated voltage supply was used in the heater circuit, and the d-c drive motor was supplied with power from a portable ac-dc motor generator set which helped to isolate the system from variations in the supply. Great care was taken to see that a steady state had been achieved before readings were taken. Errors arising from unsteady-state conditions would be random in nature, and the best check is the self-consistency of the test data.

Test Results

Tests were performed with four different ratios of radial clearance to inner cylinder radius. For each of these configurations several series of runs were made with different ratios of outer cylinder to inner cylinder angular velocity, and the speed varied over the entire possible test range. The temperature difference between the cylinders was between 40 and 60 F.

Fig. 4 and 5 illustrate graphically the flow regimes covered for two of the four clearance ratios. On these figures the angular velocity of the inner cylinder is plotted against that of the outer cylinder. The conditions for each series of runs at a constant value of η are shown by the dashed straight lines. Superimposed on these graphs are the conditions for solid body rotation, $\omega_1 = \omega_2$; potential vortex flow, $\omega_1 = (1 + d/R_1)^2\omega_2$; and the critical conditions for the transition from laminar to vortex flow, as given by equations (1) and (2). All regions below the latter curve are in the laminar flow regime, while above this curve are conditions for which Taylor vortexes will exist. Also shown is a curve representing a tentatively proposed second transition which the present data indicate may exist, and which may separate the different vortex regions indicated in Fig. 1.

The data for the four clearances are shown on Figs. 6, 7, 8, and 9, where the ratio of Nusselt number to the Nusselt number for pure conduction[3] is plotted versus Taylor number, with cylinder velocity ratio as a parameter. For each case, the Nusselt number approaches the conduction value, $(d/R_1)/\ln(1 + d/R_1)$, for low values of Taylor number, and for Taylor number above a criti-

[3] The Nusselt number for pure conduction, $(d/R_1)/\ln(1 + d/R_1)$ is a function of clearance ratio only. Its introduction reduces the results for different clearances to a common basis for easy comparison. The same result could have been obtained by defining the convection conductance h in terms of a log-mean heat-transfer area rather than the surface area of the heated cylinder.

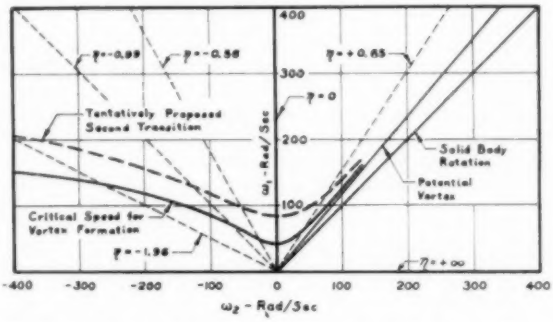

Fig. 4 Flow regime diagram showing areas covered by tests, $d/R_1 = 0.084$

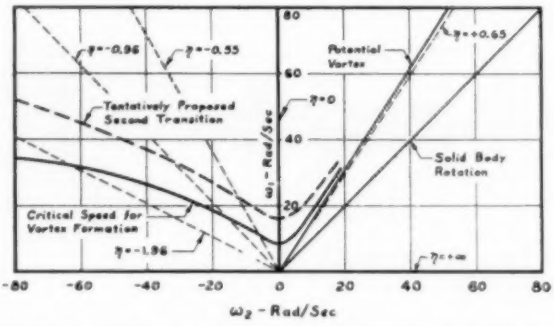

Fig. 5 Flow regime diagram showing areas covered by tests, $d/R_1 = 0.246$

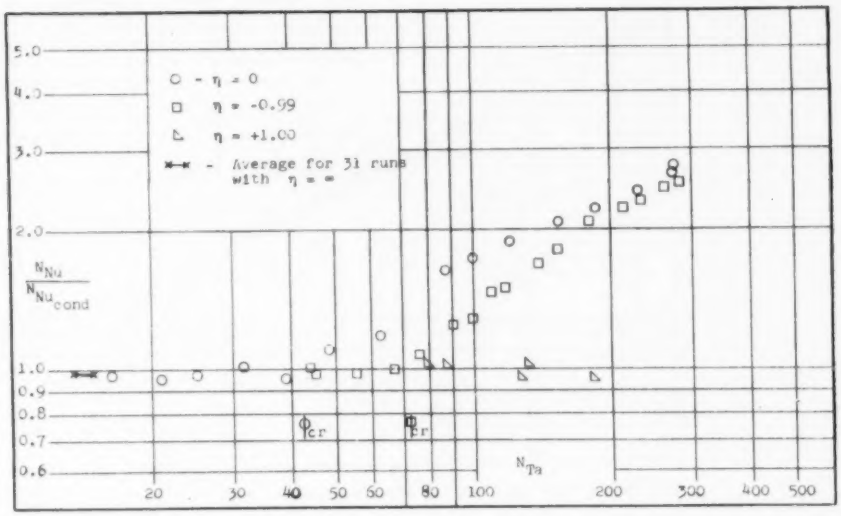

Fig. 6 Test results for $d/R_i = 0.054$

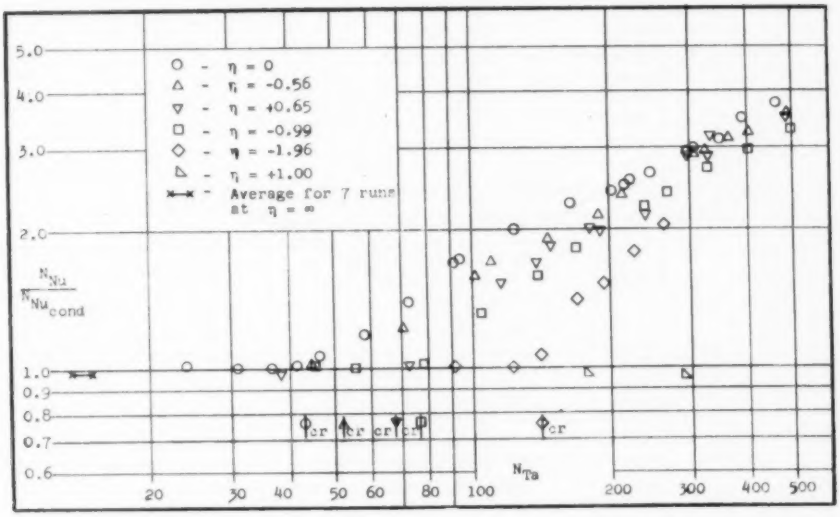

Fig. 7 Test results for $d/R_i = 0.084$

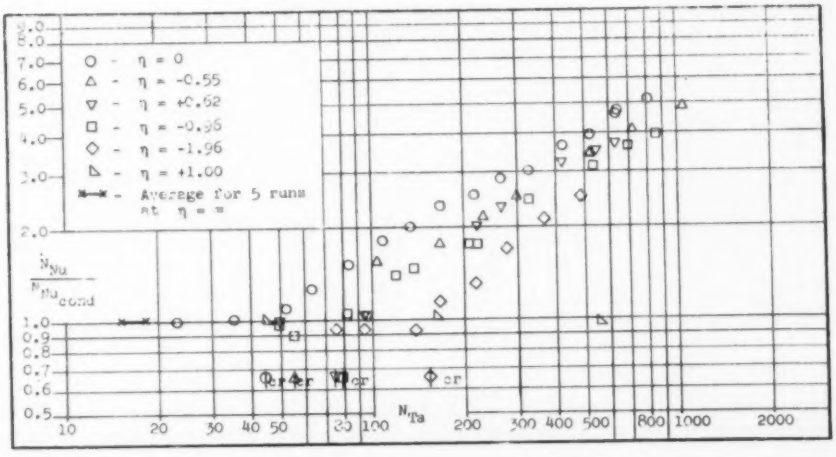

Fig. 8 Test results for $d/R_i = 0.128$

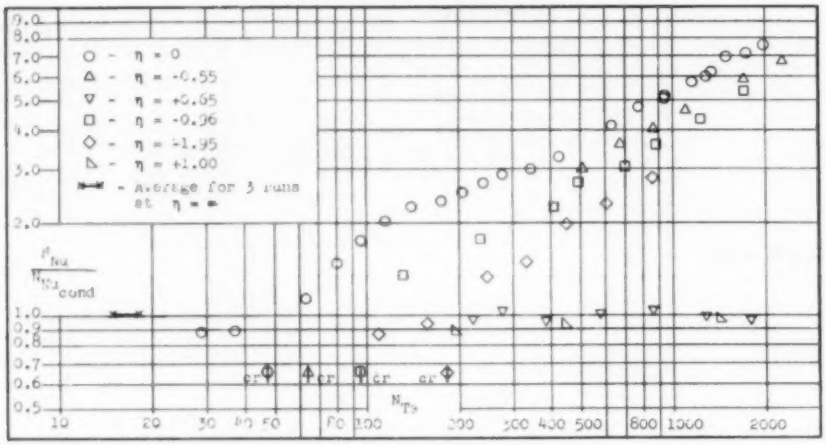

Fig. 9 Test results for $d/R_1 = 0.246$

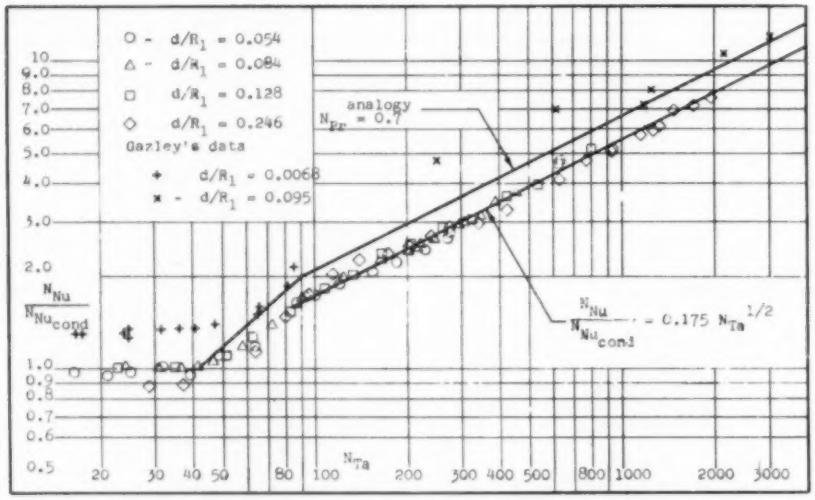

Fig. 10 Correlated test results for inner cylinder only rotating

cal value the Nusselt number increases. Also shown on these figures are the average values of Nusselt number obtained for several runs with only the outer cylinder rotating. These data were taken principally as a check on the accuracy of the test results, since it was not possible, in the speed range attainable, to achieve anything beyond laminar flow, or pure conduction behavior, with the inner cylinder stationary.

Fig. 10 shows the data for the inner cylinder only rotating ($\eta = 0$) for all four clearance ratios tested. Plotted on the basis of Taylor number rather than a Reynolds number, all of these data fall quite accurately on a single line. Thus it is seen that the Taylor number, as suggested by Kaye and Elgar [4], provides a good correlating parameter. Above a Taylor number of about 90, the data for this case can be well represented by the equation

$$\frac{N_{Nu}}{N_{Nu_{cond}}} = 0.175\, N_{Ta}^{1/2} \tag{4}$$

Data of Gazley [14] for clearance ratios of 0.0068 and 0.095 are also shown on this figure. Probable reasons for the large discrepancy between Gazley's data and that of the present investigation are presented in a later section of this paper. The results of a heat-and-momentum-transfer-analogy solution developed later are also included on Fig. 10.

It would be most desirable to find some combination of variables which would bring together the results obtained for the different cylinder velocity ratios in the same way that Taylor number has done this for the different clearance ratios with only the inner cylinder rotating. The most obvious requirement of such a grouping is that it should bring the transition points, or critical Taylor numbers, for all of the cases to one value, or at least to a very much reduced range of values. Thus the difference between the critical Taylor number at a particular speed ratio, and the critical Taylor number for the inner cylinder only rotating might be expected to play some part in this grouping.

Examination of Fig. 6 shows that for this small clearance ratio, the horizontal distance between the curves for different speed ratios, on the logarithmic scale, decreases greatly with increasing Taylor number. The two curves on that figure are, in fact, separated by an almost constant difference in Taylor number, in-

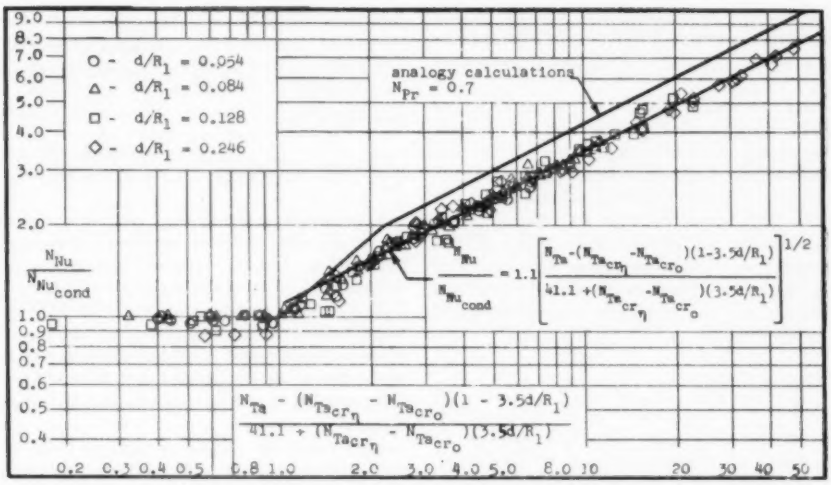

Fig. 11 Final correlation including effects of clearance ratio and rotation of both cylinders in the same or opposite directions

dicating that for this case it might be possible to reduce the two curves to one by using Taylor number minus the difference in critical Taylor numbers as the abscissa.

The data for the larger clearance ratios do not, however, confirm this proposal. Examination of Fig. 9, for the largest clearance ratio, shows that in this case the horizontal spacing of pairs of curves on the logarithmic plot is nearly constant, indicating that for this case a promising group to be used as the abscissa might be the ratio of Taylor number to the critical Taylor number for each of the speed ratios.

From the foregoing it is apparent that any combination of variables which will correlate all of the data for different speed ratios as well as different clearance ratios must include the clearance ratio explicitly, as well as implicitly in the critical Taylor number. An empirical combination of variables which reduces approximately to the forms proposed for the smallest and largest clearance ratios is

$$\frac{N_{Ta} - (N_{Ta_{cr_\eta}} - N_{Ta_{cr_0}})(1 - 3.5d/R_1)}{41.1 + (N_{Ta_{cr_\eta}} - N_{Ta_{cr_0}})(3.5d/R_1)}$$

where $N_{Ta_{cr_\eta}}$ is the critical Taylor number at cylinder speed ratio η, and $N_{Ta_{cr_0}}$ is the critical Taylor number for the inner cylinder only rotating, or η equal to zero. 41.1 is the value of critical Taylor number for η equal to zero, and clearance ratio, d/R_1, approaching zero; this is used rather than $N_{Ta_{cr_0}}$, which is a function of d/R_1, so that the rather good results obtained by plotting against Taylor number alone will not be altered for the case where η equals zero. In this grouping, the coefficient of d/R_1 could have any value from about 3 to 4 without making a significant change in the agreement obtained in the results.

Fig. 11 shows all of the data for concentric cylinders plotted on the basis of this group of variables, and falling very close to a single curve. In fact, the scatter of the data is little greater than that occurring in some of the individual series of runs. For values of the abscissa greater than about 2, all of the data may be represented to a good approximation by the expression

$$\frac{N_{Nu}}{N_{Nu_{cond}}} = 1.1\left[\frac{N_{Ta} - (N_{Ta_{cr_\eta}} - N_{Ta_{cr_0}})(1 - 3.5d/R_1)}{41.1 + (N_{Ta_{cr_\eta}} - N_{Ta_{cr_0}})(3.5d/R_1)}\right]^{1/2} \quad (5)$$

The data lie well within a ±15 per cent band from this straight line.

The analogy solution is also shown on this graph, since, if the proposed combination of variables does actually compensate for the rotation of the outer cylinder, the analogy solution should be as applicable here as for the case of only the inner cylinder rotating.

Heat-and-Momentum-Transfer-Analogy Solution for Concentric Cylinders With the Inner One Rotating

A heat-and-momentum-transfer-analogy solution for heat transfer between concentric cylinders with the inner one rotating may be of value both in giving a semitheoretical basis for extending the experimental data into other regions, and also in examining the flow regimes and transfer mechanisms occurring in this case.

Gazley [14] has made an analogy solution for very small clearance ratios, based only on the assumption of a Karman-Nikuradse velocity profile (laminar sublayer and turbulent core only) throughout the fluid space, but this assumption actually reduces the problem to that of flow between parallel planes in motion relative to each other, since it ignores the effects of Taylor vortexes in the core, and curvature in general. Gazley's analysis leads to Nusselt number as a function of Reynolds number based on inner cylinder velocity and gap width, rather than a function of Taylor number, which the experimental results of the present work, available friction data, and theories on stability indicate to be more pertinent.

The basic difference between the flow between rotating cylinders and that between planes in relative motion is the existence, even for vanishingly small clearance ratios, of large scale stable vortexes in the central part of the annular space between the cylinders. In this region the usual concept of small scale turbulent mixing is not appropriate because of the gross mixing caused by the vortexes. Measurements by Pai [6] indicate that the mean velocity profile, when averaged with respect to cylinder length, has a region of essentially constant velocity in the center of the gap, due to the vortex motion. There are also regions near the walls in which the velocity distribution is of the logarithmic type in agreement with the theory of homologous turbulence.

In the present analysis, friction data of Wagner [13] and of Taylor [12], along with information on transition from laminar to vortex flow, were used in conjunction with reasonable assump-

tions concerning the transfer mechanisms and velocity profiles in the boundary layers in an attempt to predict the heat-transfer rate from a heated rotating cylinder to a stationary concentric cylindrical shell.

In essence, the analysis was similar to the usual heat and momentum analogies applied to other systems, and the usual dimensionless variables were used, but the form of the velocity profiles dealt with in the boundary layers was somewhat modified to fit observed phenomena. The sublayers were considered sufficiently thin that the shear stress and heat flux through them could be treated as constants, and the clearance ratio d/R_1 was considered small enough so that shear stress and heat flux through the sublayers on the inner and outer cylindrical surfaces could be the same constants. Also, small d/R_1 allowed the use of a simplified shear stress equation,

$$\tau_0 = \frac{\rho}{g_c}(\epsilon_M + \nu)\frac{du}{dy}$$

For larger values, du/dy might more properly have been replaced by $(du/dy - V/r)$ for transport of moment of momentum, or by $(du/dy + V/r)$ for transport of the forced vortex parameter suggested by Kreith [16], the latter form being reasonable since this combination appears in the expression for laminar flow viscous stress. However, V/r becomes small relative to du/dy with decreasing clearance ratio, and either of the other possible equations reduces to the simplified one just given.

The equation for heat flux was

$$(q/A)_0 = \rho c_p(\epsilon_H + \alpha)\frac{dt}{dy}$$

As a basic part of the analogy ϵ_H and ϵ_M were assumed equal.

The assumed velocity profile used in the analogy solution consisted of a laminar sublayer, a buffer layer, and vortex core. The laminar sublayer velocity profile was assumed to be $u^+ = y^+$, and it was taken to extend so far that, at a Taylor number of 41, the approximate value of critical Taylor number for small clearance ratio, the entire fluid space consisted of two laminar sublayers meeting at the center of the space. This, along with the laminar flow friction factor, $f_{\text{lam}} = \left(2\sqrt{d/R_1}\right)/N_{\text{Ta}}$ established the limit of the laminar sublayer as $y^+_l = 3.2/(d/R_1)^{1/4}$.

A velocity profile of the form used in the Karman-Nikuradse profile, but with the constants adjusted to give continuity of slope at the junction with the laminar sublayer was chosen for the buffer layer.

$$u^+ = \frac{3.2}{(d/R_1)^{1/4}}\left[1 + \ln\frac{y^+}{3.2/(d/R_1)^{1/4}}\right]$$

Since the measured velocity profiles of Pai [6], and the whole idea of a large scale vortex region with intense mixing, indicate that the velocity is constant in the vortex core, the buffer layer was assumed to extend far enough so that at its limit, y_b^+, the velocity was equal to half that of the moving inner surface. This resulted in the expression

$$y_b^+ = \frac{3.2}{(d/R_1)^{1/4}}\exp\left[\frac{(d/R_1)^{1/4}}{6.4\sqrt{f/2}} - 1\right]$$

The temperature drops in the sublayers were calculated in the usual manner and, since the vortex core has been assumed to be a region of uniform velocity and intense mixing, it is thus a region of constant temperature. The total temperature drop is then only the sum of the drops in the sublayers at the two cylinder surfaces.

Using the friction data on Fig. 2, and setting Prandtl number equal to 0.7, leads to the following expressions for Nusselt number:

For $41 < N_{\text{Ta}} < 90$

$$N_{\text{Nu}} = \frac{0.0308\, N_{\text{Ta}}^{0.9285}}{1 + 1.43 \ln\left[0.7 \exp\left(0.794\, N_{\text{Ta}}^{0.0615} - 1\right) + 0.3\right]} \quad (6)$$

For $N_{\text{Ta}} > 90$

$$N_{\text{Nu}} = \frac{0.0682\, N_{\text{Ta}}^{0.781}}{1 + 1.43 \ln\left[0.7 \exp\left(0.358\, N_{\text{Ta}}^{0.238} - 1\right) + 0.3\right]} \quad (7)$$

These results of the analogy solution have been plotted on Figs. 10 and 11, along with the experimental results for various clearance ratios. The curve representing the analogy solution is seen to follow the trend of the experimental results quite well, but for values of Taylor number above 90 the analogy results are uniformly about 20 per cent above the data points. While closer numerical agreement might be desired, the fact that the two curves are essentially parallel, and differ as little as they do, lends some support to the mechanisms and flow regions postulated in the analogy solution.

A critical review of the assumptions made in the analysis may give some clue as to the reason for the discrepancy between the predicted and the experimentally observed behavior.

A fundamental assumption of the analysis was that of the equality of the eddy diffusivities for heat and for momentum. Although this assumption may not be accurate, it cannot be responsible for the disagreement, for in the range of Taylor numbers up to at least 200, the thermal resistance in the laminar sublayer is so predominant that no reasonable adjustment in eddy diffusivity could affect the results.

It is realized that the assumed sublayers imperfectly represent the true flow situation especially in the Taylor number range just above the transition from laminar Couette flow. In this region the laminar sublayer is too thick, since the flow visualization photographs of other investigators indicate that only slightly above the predicted transition point vortexes develop and occupy a large part of the space between the cylinders. At higher Taylor numbers the assumed sublayers have a more realistic thickness, especially if the vortex pattern proposed by Pai is taken to be the one prevailing, and it is realized that the profiles assumed in the analysis must attempt to represent an average behavior along the length of the cylinders, where vortex motion and small scale turbulence seem to alternate in predominance. Thinner sublayers in the low Taylor number range, while perhaps in better agreement with observed behavior, would lead only to worse disagreement in the predicted heat-transfer performance.

The final assumption which must be subjected to examination is that of a uniform temperature in the vortex region, and it appears that in this assumption lies the reason for the discrepancy in the results of the analysis. Although the measurements of Pai indicate that this is a region of uniform average mean velocity, it seems that the vortexes must be an imperfect coupling mechanism between the inner and outer sublayers as far as heat transfer is concerned. The fluid in the vortex region might be thought of as acting very much like the intermediate fluid in a coupled heat exchanger system. If, acting in this capacity, it is not capable of transmitting all of the thermal energy which the inner cylinder sublayers are capable of delivering to it, then some transfer through the vortex region would occur by ordinary conduction and eddy diffusion, with an accompanying temperature drop. Because of the relative thickness of the vortex region, the temperature gradient through it would not have to be great to account for enough additional temperature drop to bring the results of the analysis and the experimental work into correspondence. The existence of a small temperature gradient in the vortex region is in agreement with a measured temperature profile of Taylor [5], which shows a small but continuous temperature drop through the central part of the gap between the cylinders. It

was thought at first that this observed behavior might be local at the particular section of the vortex pattern through which the temperature profile was measured, and that it might be compensated for, on the average, by the temperature distribution at another section along the length of the cylinders, as seemed to be the case in measured velocity profiles, but perhaps it does represent a true average temperature profile. This temperature profile was measured at a Taylor number of about 13,000, and with a clearance ratio d/R_1 of about 1.04, both of which are beyond the range of the present work, but it does tend to support the reasoning that some temperature gradient may exist in the vortex core.

Summary and Conclusions

In this paper test results have been presented for convection heat transfer between two concentric rotating cylinders with no axial flow of the annulus fluid. The test variables cover clearance ratios from 0.054 to 0.246 and six variations of angular velocity ratios including counterrotation, corotation, the inner cylinder stationary, and the outer cylinder stationary. The flow regimes covered are illustrated graphically on Figs. 4 and 5.

The test results substantiate very well the stability criteria of Taylor and Meksyn for transition from laminar to vortex flow. It is found that the Taylor number, as suggested by Kaye and Elgar, serves very adequately as a correlating parameter for the effects of variations in clearance ratio, Fig. 10. It is further demonstrated, Fig. 11, that the effects of both clearance ratio and angular velocity ratio, including both corotation and counterrotation, can be correlated by use of a complex parameter based on the Taylor number and the critical Taylor number at which transition to vortex flow takes place.

An analogy heat-transfer solution, based on friction measurements for concentric rotating cylinders, is included to provide some insight into the heat-transfer mechanisms involved. It is concluded that, at least in the Prandtl number range of air, the heat-transfer resistance is predominantly in sublayers close to the two cylinder surfaces. However, there is evidence that about 20 per cent of the temperature change takes place in the vortex region, probably due to an imperfect coupling between the Taylor vortexes and the sublayers.

Acknowledgments

This work was accomplished as part of a program at Stanford University sponsored by the USN Office of Naval Research, the Bureau of Ships, and the Bureau of Aeronautics.

References

1 W. M. Kays and I. S. Bjorklund, "Heat Transfer From a Rotating Cylinder With and Without Crossflow," TRANS. ASME, vol. 80, 1958, p. 70.

2 G. I. Taylor, "Stability of a Viscous Liquid Contained Between Two Rotating Cylinders," *Philosophical Transactions, Royal Society (London)*, series A, vol. 223, 1923, p. 289.

3 W. W. Hagerty, "Use of an Optical Property of Glycerine-Water Solution to Study Viscous Fluid-Flow Problems," *Journal of Applied Mechanics*, vol. 17, TRANS. ASME, vol. 72, 1950, p. 54.

4 Joseph Kaye and Everett C. Elgar, "Modes of Adiabatic Fluid Flow in an Annulus With an Inner Rotating Cylinder," Research Laboratory of Heat Transfer in Electronics, Report No. RLHTE-13, Massachusetts Institute of Technology, February 15, 1957.

5 G. I. Taylor, "Distribution of Velocity and Temperature Between Concentric Rotating Cylinders," *Proceedings, Royal Society (London)*, series A, vol. 151, 1935, p. 494.

6 Shih-I Pai, "Turbulent Flow Between Rotating Cylinders," NACA TN 892, 1943.

7 Leslie A. Hromas and Thomas R. Thompson, "Experimental Investigation of Flow With Heat Transfer Between Concentric Rotating Cylinders," Technical Report for Army Ordnance Contract DA 33-088 ORD 888, Report No. A-56-3, Purdue University, October, 1956.

8 J. W. Lewis, "An Experimental Study of the Motion of a Viscous Liquid Contained Between Two Coaxial Cylinders," *Proceedings, Royal Society (London)*, series A, vol. 117, 1928, p. 388.

9 D. Meksyn, "Stability of Viscous Flow Between Rotating Cylinders, I," *Proceedings, Royal Society (London)*, series A, vol. 187, 1946, p. 115.

10 D. Meksyn, "Stability of Viscous Flow Between Rotating Cylinders, II," *Proceedings, Royal Society (London)*, series A, vol. 187, 1946, p. 480.

11 D. Meksyn, "Stability of Viscous Flow Between Rotating Cylinders, III," *Proceedings, Royal Society (London)*, series A, vol. 187, 1946, p. 492.

12 G. I. Taylor, "Fluid Friction Between Rotating Cylinders, I—Torque Measurement," *Proceedings, Royal Society (London)*, series A, vol. 157, 1936, p. 546.

13 Edmond M. Wagner, "Frictional Resistance of a Cylinder Rotating in a Viscous Fluid Within a Coaxial Cylinder," thesis for the degree of engineer, Stanford University, June, 1932.

14 Carl Gazley, Jr., "Heat-Transfer Characteristics of the Rotational and Axial Flow Between Concentric Cylinders," TRANS. ASME, vol. 80, 1958, p. 79.

15 Kurt M. Becker, "An Experimental and Theoretical Study of Heat Transfer in an Annulus With an Inner Rotating Cylinder," ScD thesis, Massachusetts Institute of Technology, August 28, 1957.

16 Frank Kreith, "The Influence of Curvature on Heat Transfer to Incompressible Fluids," ASME Paper No. 54—A-55, 1954.

DISCUSSION

F. Kreith[4]

The careful experimental measurements and the original theoretical treatment of heat transfer through air contained between two horizontal concentric rotating cylinders represents a valuable contribution to the understanding of heat transfer in rotating systems. The flow and transfer phenomena in rotating systems are exceedingly complex and it appears therefore pertinent to point out some possible limitations of the phenomenological viewpoint of the authors. Although the following comments bear no direct relation to the particular system treated in this paper, they may shed some light on transfer phenomena in geometrically similar, but fluid-mechanically dissimilar systems.

Since the flow and transfer medium in this study was gaseous, it filled the entire gap between the cylinders and was not appreciably affected by gravity. In the analytical treatment of the problem the physical properties of the medium were taken into account by specifying the appropriate Prandtl number in the evaluation of the Nusselt number in Equations (6) and (7) of the paper. As seen in Fig. 10, the theoretical analogy calculations confirm the trend of the experimental data and above the critical Taylor number the Nusselt number increases continuously with increasing Taylor number.

In an experimental study carried out at Lehigh University in a geometrically similar system, but with water as the transfer medium, some additional phenomena were observed. The water system differed from the system used by the authors because the fluid passed through the annulus at low velocity. The phenomena observed in the water system were, however, independent of the axial velocity and are therefore likely to occur also in an enclosed system such as the one used by the authors.

With both cylinders rotating at the same speed, the Nusselt number was found to remain unaffected by rotation until the rotational speed reached a critical value. This critical value corresponded to a value of the Taylor number given by Equation (2) of the paper if the clearance d was taken as one half of the distance between the cylinders. Taylor's stability criterion would not predict instabilities to occur when η is unity, but vortexes were visually observed even without any axial flow; i.e., in a closed system analogous to that used by the authors. At Taylor numbers above this critical value an increase in rotational speed produced a corresponding increase in the Nusselt number. This trend continued, however, only until the rotational speed reached

[4] Aeronautical Professor of Engineering, University of Colorado, Boulder, Colo. Mem. ASME.

a value at which the centrifugal force was equal to the gravitational force. At this point a second break in the curve of Nusselt number versus Taylor number occurred.

Although the reasons for the foregoing phenomena are as yet not completely clear, the observations made in the water system suggest that in a liquid further complication may be expected and the analogy theory may have to be modified. It would therefore be of interest to repeat the tests reported in this paper using water instead of air as the transfer medium.

In passing an apparent misprint should be noted. If the forced vortex parameter is taken as a transferable property the shearing stress will be proportional to $(du/dy - V/r)$, but not to $(du/dy + V/r)$ as stated in the paper.

A. H. Nissan[5] and F. C. Haas[5]

In Figs. 6 to 9 the authors present a number of data which indicate that the critical Taylor number is dependent upon η. It is noted that the data represent families of parallel curves of which η is the parameter, and the authors proceed to combine the data into a single curve as shown in Fig. 11.

We wonder whether work done by Brewster and Nissan[6] and by Brewster, Grosberg, and Nissan[7] on instability of flow in curved annuli may be of use here. These papers consider the onset of instability for a variety of conditions arising from rotation of cylinders as well as pumping of fluids circumferentially. Thus different velocity distributions arise in the gap. In certain of these, e.g., when the two cylinders are rotating in opposite directions, there will be two distinct regions within the gap separated by a surface of zero velocity. In one of these regions circulation will increase outward; in the second, circulation will decrease outward. Following Rayleigh's principle, only the second region will be potentially unstable; the first is stable. Thus instability does not extend over the full gap distance but rather occupies only a portion of the gap, designated as δ; δ, the width of the region of instability, is easily calculated by an approximation for small gaps,

$$\delta = \frac{1}{1 - \eta}$$

or more precisely from the Couette flow equation,

$$\omega = \frac{A}{R^2} + B$$

by calculating the radius of zero velocity. Nissan and this co-

[5] Department of Chemical Engineering, Rensselaer Polytechnic Institute, Troy, N. Y.

[6] D. B. Brewster and A. H. Nissan, "The Hydrodynamics of Flow Between Horizontal Concentric Cylinders—I, Flow Due to Rotation of Cylinder," *Chemical Engineering Science*, vol. 7, 1958, p. 215.

[7] D. B. Brewster, P. Grosberg, and A. H. Nissan, "The Stability of Viscous Flow Between Horizontal Concentric Cylinders," *Proceedings, Royal Society (London)*, in press.

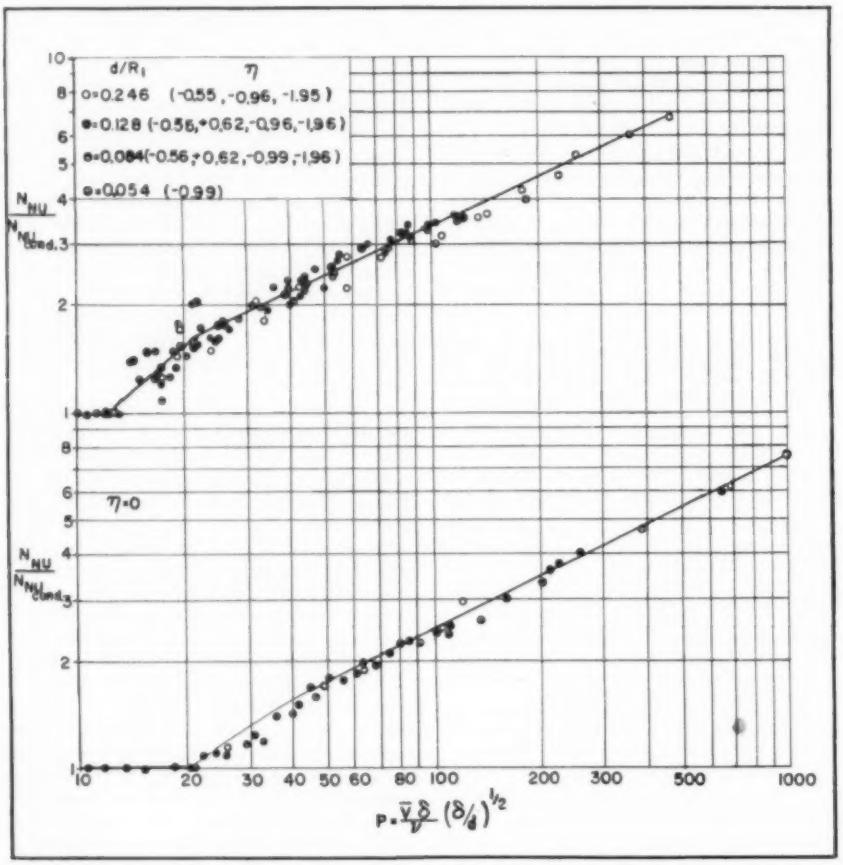

Fig. 12 Correlation of $N_{Nu}/N_{Nu\,cond}$ with P for all cases given

workers define a parameter P which is a modified Taylor number based on the instability region, δ, rather than the gap distance, and it is defined in a manner which makes it suitable for all combinations of rotation and pumping.

$$P = \frac{\bar{V}\delta}{r}\sqrt{\frac{\delta}{R_1}}$$

$\bar{V}$ is the average velocity in the gap due to rotation, pumping, or both. For the case considered here a simplified expression applies.

$$P = \frac{1}{2}\left(\frac{\delta}{d}\right)^{3/2} N_{Ta}$$

The factor of one half is introduced to account for the average velocity which is required in systems which include pumping.

On the basis of data taken from the literature for vertical concentric cylinders and their experimental work with horizontal concentric cylinders, these workers define the following critical values for P:

$$0 < \delta/d \leq 2/3 \qquad P_c = 12.0$$

$$2/3 < \delta/d \leq 1 \qquad P_c = 20.7\left(\frac{\delta}{d}\right)^{3/2}\left[\frac{2\delta/d - 1}{(2\delta/d - 1)^2 + 0.01}\right]^{1/2}$$

Applying the parameter, P, to data given in Figs. 6 to 9, it is found (Table 1) that P_c is indeed fairly constant, having an average value of 12.8, for all cases of counter and corotation. The difference between the calculated and theoretical values may be attributed to experimental error and error in reading the graphs, but the constancy of P_c is noteworthy. For the two cases of corotation in which instability was encountered, the Taylor number was adjusted by basing it on the difference in cylinder angular velocities, rather than the angular velocity of the inner cylinder. The correlation of the given data using P shows itself to be quite satisfactory, Fig. 12, herewith. The data lie within the ±15 per cent band expressed by the authors for the correlation in their Fig. 11. The data for $\eta = 0$ similarly fall on one line with

$$P = \frac{1}{2} N_{Ta}$$

Table 1 Calculated critical values of P

d/R_1	η	P_c
0.054	−0.99	12.10
0.084	−0.56	12.70
0.084	−0.99	12.55
0.084	−1.96	12.20
0.128	−0.55	13.30
0.128	−0.96	12.80
0.128	−1.96	13.10
0.246	−0.55	13.25
0.246	−0.96	13.80
0.246	−1.95	13.10
0.084	+0.65	11.60
0.128	+0.62	13.70
d/R_1	η	P_c
0.054	0	21.00
0.084	0	21.00
0.128	0	22.00
0.246	0	23.00

The one drawback of this approach is the fact of having the data fall naturally on two parallel lines. One line correlates the data for conditions when both cylinders rotate and the other line correlates the data for a stationary outer cylinder; however, the correlation is simpler to handle and has theoretical justification.

H. J. Sneck[8] and G. R. Fox[9]

We wish to commend the authors for their excellent piece of work and add some additional experimental information which may be of interest.

Fig. 13 shows the results of recent experimental work performed at the Bearing and Lubricant Center of the writers' company. These tests were performed on a 4-in-diam bearing having various clearance-to-diameter and length-to-radius ratios, lubricated with 70 SUS (at 100 F) oil. The shaft was maintained concentric with the bearing and only the shaft was allowed to rotate, Fig. 14. The oil was fed into the bearing through four feeding holes while seals prevented excessive leakage from the ends of the

[8] General Engineering Laboratory, General Electric Company, Schenectady, N. Y.

[9] General Engineering Laboratory, General Electric Company, Schenectady, N. Y. Assoc. Mem. ASME.

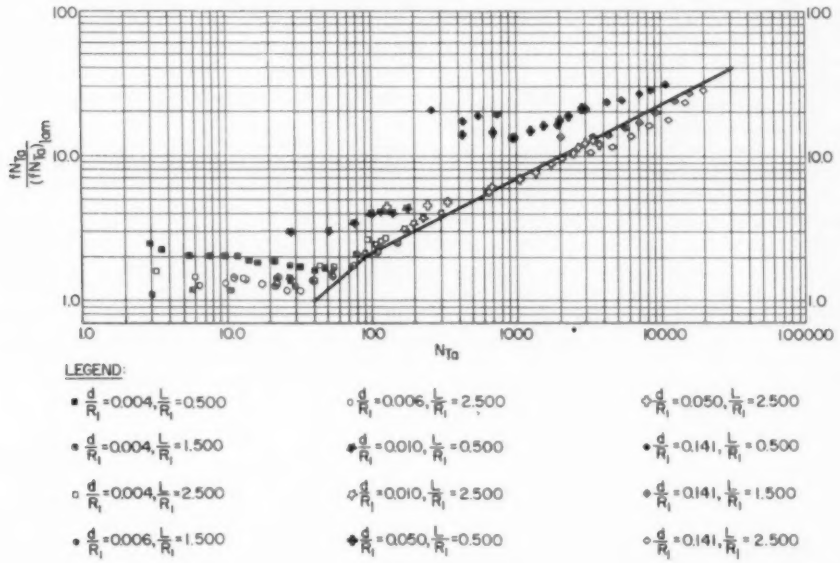

Fig. 13

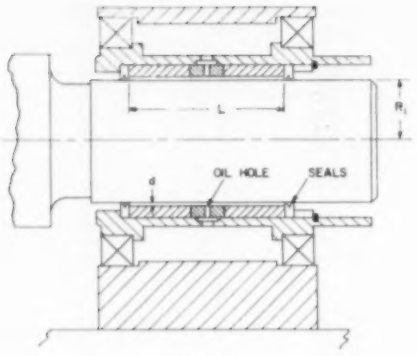

Fig. 14

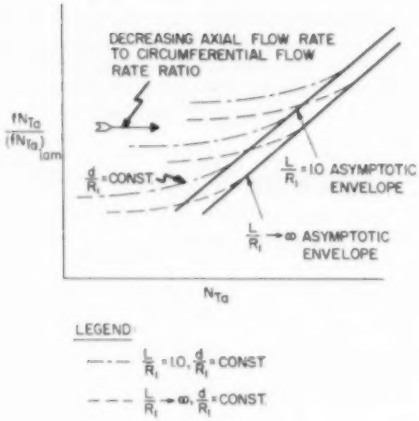
DECREASING AXIAL FLOW RATE TO CIRCUMFERENTIAL FLOW RATE RATIO
$\frac{fN_{Ta}}{(fN_{Ta})_{lam}}$
$\frac{d}{R_1}$ = CONST
$\frac{L}{R_1}$ = 10 ASYMPTOTIC ENVELOPE
$\frac{L}{R_1} \to \infty$ ASYMPTOTIC ENVELOPE
N_{Ta}
LEGEND:
$\frac{L}{R_1}$ = 10, $\frac{d}{R_1}$ = CONST
$\frac{L}{R_1} \to \infty$, $\frac{d}{R_1}$ = CONST

Fig. 15

bearing. Thermocouples were placed in the inlet and exit of the bearing and the flow through the bearing was regulated to maintain the temperature rise through the bearing less than 80 deg F at the highest rotational speeds. The kinematic viscosity was evaluated at the arithmetic average temperature. Total flow rates for the oil supplied to the bearing range from approximately 0.6 gpm for $d/R_1 = 0.004$ to about 1.0 gpm for all the other cases. The bearing-inlet pressure under these circumstances was in the order of 10 psig. In all cases the ratio of the mean axial velocity to the maximum tangential velocity was less than 1/4 and in most cases much less than this value, decreasing with increasing N_{Ta} in our experiment. No heat-transfer data were taken.

The test conditions here differ from those of Wagner and Taylor in three important respects.

(*a*) The medium is a liquid.

(*b*) Various degrees of axial-flow velocity are purposely introduced.

(*c*) The length-to-radius ratios are much smaller, corresponding to the range of values commonly encountered in bearing practice.

The solid line of Fig. 13 is the same as shown in Fig. 12. For a wide range of d/R_1, $L/R_1 > 1$, and $N_{Ta} > 40$, agreement is very good. For $N_{Ta} < 40$, $\left[\frac{fN_{Ta}}{(fN_{Ta})_{lam}}\right]$ is independent of N_{Ta} as predicted by laminar theory. However, when $L/R_1 < 1$, the data show a definite shift upward to higher values of $\left[\frac{fN_{Ta}}{(fN_{Ta})_{lam}}\right]$. For $N_{Ta} > 90$ these data exhibit a transition. A closer inspection of Wagner's and Taylor's data as well as the $L/R_1 > 1.0$ data of our experiment shows the same tendency.

Our data suggest that the solid line in Fig. 14 is the asymptotic envelope of a family of curves for large L/R_1 and vanishingly small axial to circumferential flow-rate ratio that at higher flow-rate ratios these curves extend horizontally to the left (independent of N_{Ta}), and that similar families exist for other L/R_1 ratios with the envelope shifting to the left for smaller L/R_1, Fig. 15.

We believe that further visual and quantitative investigation of these deviations would prove very fruitful.

Authors' Closure

The authors wish to thank the discussers for their interesting and valuable comments.

Although the system described by Mr. Krieth is somewhat different from that investigated by the authors, his remarks on the phenomena are quite interesting. While the details of his tests are not known, it is suggested that because of different apparatus size, Mr. Krieth's tests covered an additional flow regime which was beyond those which could be obtained with the authors' apparatus. It should be pointed out that the relative importance of centrifugal and gravitational forces is independent of the fluid medium, since both these forces vary in the same manner with density.

With regard to the "apparent misprint" which Mr. Krieth points out, it was, unfortunately, not specifically mentioned in the paper that the relative velocity u was taken as positive in the direction opposite to that of the cylinder rotation. This definition of u was chosen in order to make the velocity profile equations more similar to the usual pipe flow equations, and with this definition the shear stress equations are correct as given.

The work described by Messrs. Nissan and Haas may indeed be of use in providing a correlating parameter for concentric cylinder heat-transfer data. It is not obvious to the authors that the simplified expression given by Messrs. Nissan and Haas,

$$P = \frac{1}{2}\left(\frac{\delta}{d}\right)^{3/2} N_{Ta}$$

is applicable for any case other than that in which the outer cylinder is stationary, since this expression implies that $\bar{V}$, the "average velocity in the gap due to rotation, pumping, or both," is equal to $\frac{1}{2} V_1$. The authors will be most interested in seeing the paper by Brewster, Grosberg, and Nissan when it is available, since it will no doubt clarify this matter and also present the theoretical basis for their correlation.

The additional experimental friction data presented by Messrs. Sneck and Fox, and their interpretation of these data, are a valuable contribution.

L. P. HERRINGTON
The John B. Pierce Foundation, New Haven, Conn.

Full-Scale Human-Body-Model Thermal Exchange Compared With Equational Condensations of Human Calorimetric Data

RELIABLE INSTRUMENTS which have advanced knowledge of biothermal heat exchange are the human calorimeter [4, 10, 12][1] and heated models of the human body [2, 5]. Both instruments provide excellent data on a heat exchanger characterized by thermal feedback alteration of conductance, evaporative process, and heat production. These bio-engineering properties combined with complex shape, variable compound insulation, and a wide range variation of possible ambient exposures, vastly complicate the strict application of the rational heat-exchange equations established in thermal engineering practice.

In an earlier paper [6] prepared for the Committee on Biotechnology of the Heat Transfer Division, the author suggested that the empirical human heat-exchange data provided by human calorimeters (and models) are most useful to engineers when they are condensed into multivariate equations. Work was reported to the committee in which, by algebraic and least-squares concepts, a five-element linear differential equation was derived to describe 540 hours of calorimetric data on the seated clothed human subject in the range of 40 to 80 deg F. The coefficients of this equation establish, for this large data collection, the partial rates of change of the skin boundary temperature with respect to metabolic heat input, evaporative cooling, ambient air, and ambient radiation temperature.

The current report will extend this analysis with respect to four principal topics:

1 The comparison of data obtained with electrically heated body models as instruments of measurement with the heat exchange indicated by a linear differential equation for human subjects in the calorimeter.

2 The comparison of the original observed calorimeter data on human subjects with the heat exchange indicated by the equational derivation.

3 The presentation of four new equations representing the response of different segments of the human body to internal and ambient factors affecting heat exchange, and an indication of their use in man-machine problems of heat tolerance prediction.

4 A report of the extension of this study to instrumentally recorded data of the human calorimeter in the region above 80 deg F, in which thermally provoked evaporative regulation results in an empirically derived linear differential expression of distinctly different coefficients.

[1] Numbers in brackets designate References at end of paper.

Contributed by the Heat Transfer Division and presented at the Annual Meeting, New York, N. Y., November 30–December 5, 1958, of THE AMERICAN SOCIETY OF MECHANICAL ENGINEERS.

NOTE: Statements and opinions advanced in papers are to be understood as individual expressions of their authors and not those of the Society. Manuscript received at ASME Headquarters, August 29, 1958. Paper No. 58—A-181.

The Equilibrium Skin-Boundary Temperature of an Electrically Heated Model of the Human Body and a Vertical Cylinder Compared With Equational Predictions Based on Condensed Human Calorimeter Data

In military supply planning a persistent problem is the rapid estimation of the total effective thermal protection of complex assemblies of clothing items of changing design and multiple combination possibilities. Shape and air-layer factors have made the solution of this problem by summation of flat-plate heat-transmission resistances unsatisfactory. During World War II, the use of electrically heated models [2, 12] to determine a resistance value for each item as worn led to the definition of *col* units of insulation [3], and the construction of maps showing the approximate *clo* value required at a given season. Thus a map location showing a January average minimum of 20 F might be indexed as 4 *clo*. This index value would indicate that a thermally adequate clothing assembly when placed on an electrically heated model would produce a gradient of approximately 64 deg F between ambient air and skin boundary as a result of the action of a thermal head of about 400 Btu per hr.

Fig. 1 shows such a model. Constructed of $^1/_{16}$-in. copper to human dimensions with a total surface of 19.40 sq ft (1.8 M^2), it is provided with segmentally distributed heating units permitting inputs of 1 to 4× normal heat production of 400 Btu per hr, so distributed as to give segmental skin-boundary temperatures typical of subjects nude in a comfortable environment at 85 F, air and wall, relative humidity 50 per cent, and air movement of 15 ft per min.

The wide use of such models for tests under a specific condition makes it desirable to contrast the values from any generalized calculation equation deduced from calorimetric data on human subjects with the experimentally observed model values. In the earlier paper [6] equation (1) was presented as the best linear differential expression for the relations obtaining between mean skin temperature, metabolism, evaporative loss, air temperature, and radiant temperature in 180 three-hour calorimeter experiments on seated male subjects wearing standard civilian dress (2-piece cotton underwear, cotton shirt, socks, low leather shoes, dark single-ply suit, $^3/_4$ lined coat, and lined vest). The equation is descriptive of the range of ambient temperatures from 40 to 80 F, which in physiological parlance is often referred to as the zone of body cooling and vasomotor regulation (tissue conductance alteration by blood flow) [9].

$$\underset{T_S}{X_1} = \underset{(T_A)}{0.286X_2} + \underset{(T_W)}{0.142X_3} + \underset{(M)}{0.105X_4} + \underset{(E)}{0.092X_5} + 53.39 \quad (1)$$

where T_S, T_A, T_W, refer, respectively, to mean skin temperature, air and wall temperatures, in deg F; and M and E refer, respec-

Fig. 1 Heated model of the human body

Constructed of $^1/_{16}$-in. copper and provided with segmentally distributed internal electrical heating units which may be adjusted to 1 to 4 times the normal resting metabolism. Copper surface of 19.4 sq ft (1.80 sq m) covered with black rubber-base paint and provided with segmental thermocouple system registering the mean surface temperature of the head, the upper extremities, the trunk, lower extremities, and the total skin temperature.

tively, to metabolism and to evaporation in kg cal per hr per man, average height 180 cm (5 ft, 11 in.), average weight 70.8 kg/(156 lb), average DuBois surface area 1.76 sq meters (18.9 sq ft). (In the discussion of the original paper [6], it was shown that, in the practical calculation form just given, expression of the physiological units in the British system would require unnecessary conversion, on each reference to authoritative sources from which entry values for M and E must be taken. When such tables are common in British units, equation (1) may be altered readily to accommodate editorial uniformity. In a later section, the coefficients of the equation are given in beta form which permits the comparison of the partial rates of change in variational form independent of unit systems.)

We now wish to compare the prediction of the human calorimeter equation (1), with the observations made on the heated model, clothed with similar dress, and brought to equilibrium at ambient operative temperatures of 60, 65, 70, and 75 F (air and radiant temperatures equal at these temperatures and air movement of 15 ft/min).

In Table 1 the observed equilibrium mean skin temperature of the clothed copper model has been compared with the mean skin temperature of human subjects after 3 hours exposure, as computed from equation (1), based on human data from the calorimeter. Interpolation in the table shows that at an equal air-wall environmental temperature of 68.7 F (15 ft/min) the observations on the model and human subjects agree. The copper model of low thermal inertia is in complete equilibrium. The data on which equation (1) is based involve a mean degree of equilibrium for the human subjects after a 3-hr exposure. A reasonable inference from Table 1 is that clothed adult males with resting heat production about equal to males of average American age (circa 40 years) may be expected to be in approximate thermal equilibrium with an operative temperature of 68.7 F after a 3-hr exposure. Although heated models are quite convenient for the measurement of insulation values, many bio-engineering problems of protective clothing require human subjects. The foregoing data have value in suggesting an environmental condition and subject status in which human and model evaluation of normal clothing may be expected to show agreement in so far as the important factor of skin boundary temperature is concerned.

The thermal theory of static models of such unique shape as the human body has not been analyzed thoroughly. However, satisfactory experimental results have been attained in studies of radiation area and radiation and air conduction-convection factors [7, 8] for the nude human body.

The experiments reported have afforded an opportunity to compare in the same laboratory some of the thermal-exchange properties of the unclothed model of the human body with the properties of a simpler shape. Of the heated shapes that have been studied in this laboratory, the one most similar to the approximate vertical cylinders which the human extremities and trunk resemble is a blackened vertical cylinder with hemispherical ends, 24 in. in total height and 8 in. in diameter. The surface emissivity of this cylinder is 0.93 per cent. In the calorimeter environment in which the model and human data of Table 1 were obtained, the heat exchange of this cylinder at surface temperatures 5 to 40 F above the environment is accurately given in Btu per sq ft per hr by

$$H_c + H_r = 0.51(\Delta t)^{0.86} + 16 \times 10^{-10}\,(T_{sur}^4 - T_r^4) \qquad (2)$$

(H_c, H_r, convection and radiation exchange in Btu per sq ft per hour; temperature, deg F, absolute scale, second term)

Table 1 Skin boundary temperatures of blackened copper body model[1] compared with values from linear differential equation derived from calorimeter data on human subjects of comparable size and clothing insulation

(1) Calorimeter temperature, deg F	(2) Observed mean equilibrium skin temp, model, deg F	(3) Δt (2 − 1)	(4) Predicted T_{skin} human subjects 3-hr exposure, deg F	(5) Difference subject-model, deg F
60.1	80.5	+20.4	85.18	+4.68
65.0	85.3	+20.3	87.28	+1.98
70.2	90.2	+20.0	89.51	−0.69
75.2	95.4	+20.2	91.65	−3.75
(68.7)[2]	(88.9)	(+20.2)	(88.9)	(0.0)

[1] Surface area of the human body model 1.8 square meters (19.4 sq ft), heat input 72.24 kg cal per hour (287 Btu per hour); mean surface of the calorimeter subjects 1.76 square meters (18.9 sq ft); predicted human subjects skin temperature for the model's heat input computed from equation (1), [similar heat input, and insensible evaporative loss of 16.46 kg cal per hour per man (65.3 Btu per hour per man) a value proportional to the mean relation between metabolism and evaporation in the human calorimeter data]. Skin temperature on both subjects and model measured at 15 standard points [12].

[2] The environmental temperature at which boundary temperatures of the model and human subjects are equal, as indicated by interpolation in Table 1.

It is desirable to establish a connection between the heat loss of the blackened anatomical model of Table 1 and this more common cylinder shape. We report in Table 2 the equilibrium surface temperature of the unclothed body model with the same heat input (per unit area) as used in the clothed comparison of Table 1, and compare the heat input necessary to bring the cylinder to the same mean surface temperature.

The data of Table 2 indicate that, under still air conditions, uncomplicated by differences in air and radiant temperature, the heat loss of a blackened copper cylinder, of dimensions roughly comparable to large cylinder-like segments of the human body, has combined radiation-convection loss per unit area similar to that of our blackened copper model of a human subject. Under conditions of forced air movement, different air and radiation temperatures, variable clothing insulation, and different postures, the comparison is less useful, and many complications have to be considered. However, the values of Table 2 do relate the thermal behavior of the model used in these studies to a heat exchanger of standard shape, under conditions of heat input and gradient similar to those which obtain in studies with human subjects.

It is the thesis of this paper and a preceding one [6] that, although rational calculation methods may be usefully applied to analogies existing between cylinder, anatomical model, and the nude body in still air, complexities of environment and clothing recommend a careful study of equations which condense calorimetric data on human exchange with a minimum of assumptions.

Observational Calorimeter Data on Clothed Human Subjects in the Range From 40 to 80 F Compared With a Linear Differential Equation Giving the Partial Rates of Change of Skin Boundary Temperature as Functions of Metabolism, Evaporation, Air, and Radiant Temperature

Discussion of the data presented by the author at the June, 1957, meeting of the Society and inquiries relative to the shorter form of the paper published in *Mechanical Engineering* [6] indicate an interest in the comparison of the predictions of equation (1) over the total temperature range of the calorimeter studies. This should be presented so that degree of fit of the equation for conditions of widely different air and radiant temperature is apparent. In the earlier publication [6] the validation of the equation as a data fit of 5 variables was indicated by the computation of a multiple coefficient of correlation ($R_{1.2345} = 0.908 \pm 0.030$), and a comparison of values for the observed and equationally predicted means of the five variables studied.

The intra-range comparisons desired can be obtained from Table 3. In this table, 11 sets of calorimeter conditions covering 180 three-hour exposures on subjects of different build are reported from the original data. The mean values recorded are the clothed averages of subject VII and subject IX for the calorimeter conditions indicated, and these data were obtained from Tables 1 and 2 of the original publication [11].

The significant features of Table 3 are column 4, giving the mean skin temperature of each group of 3-hr experiments at a given calorimeter air and radiant condition; column 5, the predicted mean skin temperature from equation (1); and column 6, the differences between the observed and predicted skin temperatures. As may be seen, the validity of the equation as a linear differential expression for the partial rates of change of skin-boundary temperature with metabolism, evaporation, and ambient air and radiant effects, is very satisfactory. For the 11 groups, the differences are positive in 6 instances and negative in 5 instances. The sum of the positive differences for the 11 groups is +3.26 F, that of the negative differences −3.23 deg F, yielding a mean difference between calorimeter observation and equational values of +0.003 deg F. A linear differential expression for these data is clearly justified.

Inspection of the air and radiant temperatures shows that the calorimeter data incorporated in the equation cover a wide range of air and radiant temperatures, the range of air temperatures being from 41 to 72 F, and that of the radiant temperatures from 41 to 100 F. It is the opinion of the author that all calorimetric data on human subjects under various conditions of activity and insulation should be condensed in this manner for bio-engineering use. It is the intention of the author to accomplish this for all data in the Pierce Foundation calorimeter series with which he has had an experimental identification.

A criticism commonly made of such equations is that, in substituting a generalized linear differential expression based on physical analysis for specific-case design values and calculation from explicit heat-exchange functions, we shorten the process at the expense of information on the operation of the separate factors. This overlooks the fact that, in animate heat exchangers in which properties change on a feedback principle, no efficient method of numerical description can easily afford to discard the advantages of calculation constants which include the effect of the style of response. In short, methods highly reliable for inanimate exchangers of relatively fixed properties are short of efficient description if they do not conveniently describe the process of adjustment. It is obvious that equation (1) does include a mathematical description of the basic physical process and, what is equally basic biologically, the process of adjustment as observed.

In addition to this feature, the process of derivation for such equations does permit one to contrast the effective coefficients for heat transfer by the various physical processes. This may be made clear by the following brief analysis. The coefficients of the terms $X_2 - X_5$ in equation (1), its computation form, cannot be

Table 2 Heat exchange of a blackened copper model of the human body and a vertical hemispherically capped cylinder at a common air[1] and surface temperature

	Area, sq ft	Heat input, Btu per hr	Mean surface, deg F	Δt, $T_A - T_S$ deg F	Air temp, deg F	H_r, Btu/ft² per hr	H_c, Btu/ft² per hr	$H_r + H_c$, Btu/ft² per hr
Vertical cylinder[2]	4.19	61.1	89.7[4]	9.7	80.0	10.06	4.53	14.59
Human body model[3]	19.4	287.0	89.7	9.7	80.0	...	...	14.79[5]

[1] Air and wall temperatures equal at 80 F, air velocity 15 ft per min.

[2] Black rubber base paint on 1/16-in. copper; 24 in. in height, 8 in. in diameter; evacuated and heated by an axial Nichrome resistance wire; 8 thermocouples in parallel on outer surface, spaced along the vertical height.

[3] As described in the text and shown in Fig. 1.

[4] Heat input regulated to give surface temperature equivalent to that resulting in the model from heat input of 287 Btu per hour (72.24 kg cal per hour) per total surface of 1.8 M².

[5] The partition of the total heat input might be made from radiation area and radiation/convection ratios for the human body [7], but direct analysis of these factors for static body models in the standing posture have not been reported.

Table 3 Experimental and equational values for the mean skin boundary temperature of th e clothed human body, male subjects seated at calorimeter operative temperatures[1] in the 40 to 80 F range

Calorimeter condition group no.	(1) T_O, deg F	(2) T_A, deg F	(3) T_W, deg F	(4) T_S Exptl, deg F	(5) T_S Equat. (1), deg F	(6) col. 4–col. 5	(7) T_{CL}, deg F	(8) T_B, deg F	(9) Metabolism, kg cal/hr	(10) Evaporation, kg cal/hr
25	41.72	41.72	41.72	81.23	80.57	+0.66	70.88	98.15	103.52	−16.80
17	50.45	50.45	50.45	83.93	82.93	+1.00	75.38	98.33	89.60	−15.84
19	54.32	32.81	71.24	81.95	81.50	+0.45	71.33	98.15	100.96	−21.60
18	54.60	40.19	66.02	81.41	83.69	−2.28	71.15	98.15	102.72	−14.72
5	60.26	59.36	61.07	86.45	86.56	−0.11	80.78	98.60	88.00	−18.72
6	61.61	49.46	71.15	84.47	84.78	−0.31	77.18	98.51	87.52	−22.24
7	63.50	41.63	80.60	84.47	84.65	−0.18	76.55	98.42	92.48	−19.52
1	71.87	71.87	71.87	91.22	91.16	+0.06	87.08	98.64	85.12	−20.96
3	72.41	49.91	90.14	86.99	86.89	+0.10	81.14	98.69	82.40	−24.16
2	72.41	60.35	81.95	87.98	88.33	−0.35	83.12	98.15	84.80	−31.04
4	74.57	41.63	100.49	87.71	86.72	+0.99	83.03	98.51	90.40	−25.44
Mean	61.61	49.03	71.52	85.25	85.25		77.97	98.39	91.60	−21.00
Std. dev'n.	10.17	10.70	16.15	3.26	...		...	...	7.72	5.70

[1] T_O, T_A, T_W, operative, air, and radiant temperatures, respectively; T_{CL}, clothing surface temperature; T_B, body temperature (rectal).

directly compared as estimates of the relative weights of the basic processes of convection, radiation, and evaporation. This is because application convenience demands that the variables refer both to physical and biological units of measurement. Despite the reasonable requirements of editorial order, it is more efficient to link the data of fields as separate as engineering and biology, retaining the equational entry units which are authoritative in the references of the separate fields. Since the engineer applying equation (1) will define the environment in deg F, and will use tables of heat production and evaporation standardized in kilogram calories, the equation preserves these units of entry.

However, we may evaluate the relative importance of the variables by reporting here a step in the derivation of the equation.

Equation (1), written in the general form,

$$X_1 = B_2X_2 + B_3X_3 + \dots . \quad (3)$$

has coefficients B_2, etc., in which both the intrinsic variation of X_1 with the independent variables and the effect of units of measurement are combined. However, in developing this equation by multiple regression methods, deviation units are used, and if we set z = (X − mean)/standard deviation, our equation may be written

$$z_1 = \beta_2 z_2 + \beta_3 z_3 \dots \quad (4)$$

By the usual methods these beta coefficients are determined by operations such that the average of the squared deviations is a minimum. The beta coefficients for equation (1) are reported in Table 4 for those who are interested in comparing the relative importance of the various independent variables in determining the skin boundary temperature.

Table 4 Beta coefficients of equation (1)

	Deviation units	Relative	Process
$\beta_{12.345}$ =	0.9395	1.000	Convection
$\beta_{13.245}$ =	0.7025	0.748	Radiation
$\beta_{14.235}$ =	0.2492	0.265	Heat production
$\beta_{15.234}$ =	0.1517	0.172	Evaporation

The beta coefficients of Table 4 apply to calorimeter heat exchange of the clothed resting subject with mean air temperature of 49.03 F ± 10.70, mean radiant temperature of 71.52 F ± 16.15, associated with a metabolic heat production of 91.55 kg cal per hr ± 7.72 (363.3 Btu per hr ± 30.6); per man of 1.76 sq m (18.9 sq ft); with an evaporative loss of −20.86 kg cal per hr ± 5.70 (−82.78 Btu per hr ± 22.6). The mean operative temperature is 61.61 F ± 10.17. In general, B_2 of equation (1) is related to β_2 (indexed in Table 4 as $\beta_{12.345}$, the partial rate of change of X_1 with X_2, with variables 3, 4, and 5 constant) by the relation $B_2 = \beta_2(\sigma_1/\sigma_2)$ where sigma is a standard deviation accompanying such mean values as those given previously, the subscripts being identified by equation (1). The ratios of the heat processes in the experimental data are thus identified. The heat input, the temperature gradients, the convection-conduction surface, and the radiation area for the seated posture are known (0.75 × anatomical surface) [7]. These are the elements required for a study of the individual processes of heat exchange in a physical and analytic sense. It therefore appears to the author that this method of condensing calorimetric data for bio-engineering use is not limited to the convenience of empirical-data summation in a linear differential form but qualifies fully as a technical method of advancing the physical description of such complex heat-exchange problems by rational methods familiar to the engineer.

Extension of the Analysis to the Heat Exchange of the Body Segments

In a previous report [6] to the Committee on Biotechnology of the Heat Transfer Division, an equation was given which resembles equation (1) except that its purpose is the prediction of the local segmental temperature of the legs, as a function of air and radiant temperature, metabolism, and evaporation. It was thought that such an equation would be useful for those who may wish to use an easily measured body-surface temperature as a partial index of the state of adjustment of the total surface, or in circumstances in which there is a special interest in the effect of the environment on a local body area. We now wish to report the full set of such equations for the principal body segments head, upper extremities, trunk, and lower extremities.

The various body segments have different properties as heat exchangers, and an important element in this is the ratio of surface to volume in different body areas. Table 5 gives a good approximation of these surface/volume ratios, based upon anatomical model measurements. As may be seen, the extremities have a large relative surface and are excellent heat exchangers. As such, their surface temperature varies much more than the trunk, and the environmental condition at which lower extremity surface temperatures approach 94 to 95 F is often taken as a topographical temperature mark of the inflection of human heat adjustment from a phase of adjustment through conductance change to one of primary adjustment through sweat secretion [1, 9]. This is evident since, as the temperature topography of different body segments converges on the 95 F value, additional environmental heat load is compensated pari passu by evaporation, with-

Table 5 Surface/volume ratios[1] of the principal heat-exchanger segments of the human body

Body segment	Surface, per cent of total	Volume, per cent of total	Ratio, surface/volume
Head	7.0	7.0	1.0
Upper extremities	18.4	10.7	1.72
Arm	7.0	6.4	1.09
Forearm	6.3	3.0	2.10
Hands	5.1	1.3	3.92
Trunk	31.2	52.3	0.60
Lower extremities	43.4	30.0	1.45
Thigh	18.7	17.5	1.07
Leg	16.9	9.5	1.78
Feet	7.8	3.0	2.60

[1] The values are considered approximate. Biological variability is considerable, and for estimation of surface alone, the DuBois surface is generally used, this being based upon a large data collection. In the DuBois series the relative surface is head 7 per cent, upper extremities 21 per cent, trunk 31 per cent, lower extremities 41 per cent. However, associated volume figures were not available. For this reason we have used the above comparison based on a body model.

out marked increases in skin temperature, to the physical and physiological limits of the process.

The surface-temperature response of these various body segments for seated, clothed subjects in the range from 40 to 80 F operative temperature is known since segmental measurements, as well as mean surface temperature, were made in the 180 three-hour experiments which were referred to earlier in this paper. In Table 6, the observed segmental temperatures for various combinations of observed air and radiant temperature, metabolism, and evaporation are given. In adjoining columns the values obtained from five element linear differential equations derived to condense the data are given.

A systematic relation exists between the segmental temperatures and the mean skin temperatures in the calorimeter data reported in Tables 3 and 6, in that studies of human surface area have indicated the segmental distribution of surface area is as follows: Head 7 per cent, upper extremities 21 per cent, trunk 31 per cent, and lower extremities 41 per cent [4], and these values are established in physiological studies of human heat loss as weighing factors for the derivation of mean skin [7]. Measurements are generally made at 15 points of definite anatomical location as in the data presently being analyzed.

The following linear differential equations have been determined, by methods described earlier in this paper, for each of the 4 primary body segments. In conjunction with equation (1), these 5 equations constitute a complete condensation of the Pierce Foundation calorimeter studies on seated clothed subjects referred to in Table 3.

The equations comparable to equation (1) for the four principal body segments have been analyzed in terms of T_o, the operative temperature, defined hereafter, and the difference between radiant temperature and air temperature, in order to study the beta coefficients of air-wall differences, and the relative convenience of such expression as compared with separate equational entries for air and radiant temperature. The four equations are:

$$X_{10} = 0.315X_8 - 0.045X_9 - 0.001X_4 - 0.138X_5 + 67.00 \quad (5)$$

$$X_{11} = 0.550X_8 - 0.144X_9 + 0.085X_4 + 0.051X_5 + 44.96 \quad (6)$$

$$X_{12} = 0.138X_8 - 0.022X_9 - 0.005X_4 - 0.006X_5 + 84.55 \quad (7)$$

$$X_{13} = 0.595X_8 - 0.133X_9 + 0.206X_4 + 0.245X_5 + 33.61 \quad (8)$$

where X_{10}, X_{11}, X_{12}, and X_{13} are, respectively, the temperatures in deg F for the head, upper extremities, trunk, and lower extremities. $X_8 = T_o$, operative temperature [11] technically given by

$$T_o = \frac{k_R T_W + k_C T_A}{k_O} \quad (9)$$

where T_W = radiant wall temperature, T_A = air temperature, k_R and k_C = subject radiation and convection heat-exchange constants as determined by calorimeter experiments, and $k_O = k_R + k_C$. $X_9 = (T_W - T_A)$, X_4 and X_5 are, respectively, the metabolism and evaporation in kg cal per hr per man (subjects dimensionally described in Table 1). The values of variables 8, 9, 4 are positive, and variable 5 negative, prior to equational entry.

The coefficients of multiple correlation for the foregoing segmental skin temperatures are: T_h, head temperature (X_{10}), 0.925; T_u, upper extremities (X_{11}), 0.934; T_t, trunk (X_{12}), 0.880; T_L, lower extremities (X_{13}), 0.822. These values indicate that such linear differential equations fit the original data very well. However, a record of the original data and the intra-range fit similar to that computed for equation (1) in Table 3 is desirable.

In Table 6, the mean values of the observed segmental temperatures for each of the 11 environmental conditions are compared with the predicted segmental temperatures from the corresponding segmental equations. Inspection of the values of Table 6 shows that the intra-range correspondence is good, and the mean error small.

Extension of the Program of Human Calorimeter Data Condensation for Bio-Engineering Use to the Environmental Region Above 80 F

In the seated clothed subject at rest or engaged in light activity, the physiological response to increasing environmental temperature through the range of comfortable temperatures is primarily one of rising skin temperature and increasing peripheral tissue conductance, modulated by peripheral blood flow. An initial skin-temperature topography under comfortable conditions with segmental values ranging from approximately 80 to 93 or 94 F gradually converges in all segments on a level of 94 to 95 F. At this point there is a gradient of 3 to 4 deg F between deep body temperature and the skin boundary. Major increase in cardiac action would be required to hold deep body temperature constant if the process of peripheral evaporation were not stimulated to lower radically the rate of rise in skin temperature with increasing environmental heat load.

This temperature control feature of the human body is the factor which prevents the extension of equation (1) to air temperatures of approximately 80 F or higher.

However, the adjustment in this new range of thermal effect is again systematic over a wide range of increasing heat load. Inspection of the log of Pierce Foundation human calorimetric studies showed that a group of 150 three-hour experiments were available ranging in operative temperature from 79 to 105 F with evaporative heat losses ranging from the mean of the value observed in the sub 80 F series, equation (1), to 125 kg cal per hr per man. This value is some 6 times that of the cooler series. While other data are available, these seemed particularly worth analysis since they were based on the same subjects and same clothing used in the cool-region analysis [11].

In the period since the last Biotechnology Committee program in San Francisco, these data in the zone of human evaporative regulation have been partially processed for the derivation of 5 variable linear differential equations for mean and segmental skin-boundary temperatures. Detailed checking procedures are still in progress, and final operations on the correlation matrix for the segmental data are to be completed. However, the means check of the observed and equationally predicted mean skin temperature is quite satisfactory. Since it is a reference convenience to have comparable equations for the 40 to 80 F and the 80 to 105 F regions in the same source, the new equation is reported here

Table 6 Experimental and equational values for skin boundary temperatures of the 4 principal body segments. Group means for seated, clothed, male subjects, at calorimeter operative temperatures[1] in the 40 to 80 F range.

Calorimeter condition group no.	(1) T_O, deg F	(2) T_A, deg F	(3) T_W, deg F	(4) $T_W - T_A$, deg F	(5) Exptl. T_H, deg F	(6) Equat. (5) T_H, deg F	(7) Col. 5–6	(8) Exptl. T_U, deg F
25	41.72	41.72	41.72	0.00	81.59	84.16	−2.57	77.27
17	50.45	50.45	50.45	0.00	86.09	85.08	+1.01	80.87
19	54.32	32.81	71.24	38.43	85.01	85.36	−0.35	77.09
18	54.60	40.19	66.02	25.83	84.29	85.07	−0.78	76.64
5	60.26	59.36	61.07	1.71	89.24	88.48	+0.76	83.57
6	61.61	49.46	71.15	21.69	88.79	88.50	+0.29	80.51
7	63.50	41.63	80.60	38.97	88.70	87.94	+0.76	80.60
1	71.87	71.87	71.87	0.00	92.05	92.52	−0.47	91.05
3	72.41	49.91	90.14	40.23	92.03	91.34	+0.69	85.10
2	72.41	60.35	81.95	21.60	91.67	93.12	−1.45	87.17
4	74.57	41.63	100.49	58.86	91.22	91.35	−0.13	85.55
Mean	61.61	49.03	71.52	22.48	88.24	88.45		82.31
Std. deviation	10.17	10.70	16.15	19.39	3.67	...		4.54
Difference, Experimental-equational value							−0.21	

Calorimeter condition group no.	(9) Equat. (6) T_U, deg F	(10) Col. 8–9	(11) Exptl. T_T, deg F	(12) Equat. (7) T_T, deg F	(13) Col. 11–12	(14) Exptl. T_L, deg F	(15) Equat. (8) T_L, deg F	(16) Col. 14–15
25	75.84	+1.43	90.32	89.89	+0.43	76.28	75.64	+0.64
17	79.52	+1.35	91.31	91.16	+0.15	79.61	78.21	+1.40
19	76.78	+0.31	89.87	90.83	−0.96	77.90	76.63	+1.27
18	79.25	−2.61	90.50	91.10	−0.60	76.55	80.21	−3.66
5	84.38	−0.81	92.84	92.50	+0.34	82.85	82.77	+0.08
6	82.04	−1.53	92.30	92.26	+0.04	79.88	79.97	−0.09
7	81.04	−0.44	92.66	92.11	+0.55	79.61	80.48	−0.87
1	90.56	+0.49	94.01	94.17	−0.16	88.97	88.83	+0.14
3	84.77	+0.33	93.38	93.39	−0.01	82.31	82.39	−0.08
2	87.31	−0.14	93.11	93.83	−0.72	84.11	83.68	+0.43
4	83.87	+1.68	93.83	93.25	+0.58	83.66	82.53	+1.13
Mean	82.31		92.19	92.23		81.07	81.03	
Std. deviation	...		1.49	...		4.35	...	
Difference, Experimental-equational value		−0.00			−0.04			+0.04

1 T_O, T_A, T_W, operative, air, and radiant temperatures, respectively; T_H, T_U, T_T, T_L, head, upper extremities, trunk, and lower extremities, respectively. Additional metabolism and evaporation values needed in conjunction with columns 2 and 3, for calculation of columns 6, 9, and 12, are given in Table 3.

Table 7 Mean values of hot-region calorimetric data, mature male subjects,[1] normal clothing, seated posture

	Skin temp, deg F	Air temp, deg F	Radiant temp, deg F	Operative temp, deg F	Metabolism, kg cal/hr	Evaporation, kg cal/hr
Mean	94.23	75.60	105.73	92.43	83.88	−67.02
Std. deviation	2.00	12.67	12.75	7.56	7.10	34.63
No. of experiments	150	150	150	150	150	150

[1] Subject characteristics, units, and variables identical with those reported in [6] and other tables of this report.

The associated regional analysis and detailed data comparison, comparable to Tables 3 and 6, are deferred until this study is extended to the analysis of the humidity and vapor-pressure features of similar data.

In Table 7 are the general descriptive features of equation (10) now available as a condensation of human calorimetric data on the seated clothed subject for the range from 80 to 105 F.

The linear differential description of the data of Table 7 is given in equation (10).

$$X_{14} = 0.171X_{15} + 0.137X_{16} + 0.082X_{17} + 0.02X_{18} + 61.34 \quad (10)$$
$$T_S \qquad T_A \qquad T_W \qquad M \qquad E$$

Equation (10) gives a value for mean skin temperature of 94.29 F when the means of the independent variables are used to enter the equation. The experimental mean of the series is 94.23 F. This is satisfactory as a means check, and will be supplemented in later work with an intra-range comparison. Since the multiple correlation coefficient of equation (10) is +0.93 it is probable that the intra-range fit will be of the same order as that reported in Tables 3 and 6 for the region below 80 F.

Summary

It has been the purpose of this paper, considered jointly with

a preceding one [6], to serve several reasonable interests of the Committee on Biotechnology of the Heat Transfer Division.

(*a*) One of these aims has been achieved by condensing calorimetric data on seated, clothed human subjects into linear differential equations which permit the bio-engineer to quickly approximate the effect of complex air and radiant temperatures on the human element of a man-machine design problem.

(*b*) These aims have been accomplished for a range of thermal loads typical of the region from 40 to 80 F, and separately by reason of different human temperature regulation characteristics, for the range from 80 to 105 F.

(*c*) Static heat exchangers—an electrically heated model of the human body and a hemispherically capped cylinder—have been used to establish an experimental connection between the heat-exchange properties of these inanimate bodies and linear differential equations which generalize the thermal interchanges of the human body as observed in a calorimeter environment.

References

1 E. F. Adolph, et al., "Physiology of Man in the Desert," Interscience Press, New York, N. Y., 1947.

2 H. S. Belding, "Protection Against Dry Cold, in Physiology of Heat Regulation, and the Science of Clothing," L. H. Newburgh, editor, W. B. Saunders, Philadelphia, Pa., 1949.

3 A. P. Gagge, A. C. Burton, and H. C. Bazett, "A Practical System of Units for the Description of the Heat Exchange of Man With His Environment," *Science*, vol. 94, 1941, pp. 428–430.

4 J. D. Hardy and E. F. DuBois, "The Technic of Measuring Radiation and Convection," *Journal of Nutrition*, vol. 15, 1938, pp. 624–631.

5 L. P. Herrington, "Basic Procedures in the Calculation of the Heat Exchange of the Clothed Human Body," *Yale Journal of Biology and Medicine*, vol. 19, 1947, pp. 735–755.

6 L. P. Herrington, "The Biotechnical Problem of the Human Body as a Heat Exchanger," Paper No. 57—SA-5, ASME Semi-Annual Meeting, San Francisco, Calif., June 10, 1957; also, *Mechanical Engineering*, vol. 79, 1957, pp. 1029–1031.

7 L. P. Herrington and J. D. Hardy, "Temperature and Humidity in Relation to the Thermal Interchange Between the Human Body and the Environment," chapter 13, "Human Factors in Undersea Warfare," National Research Council, Washington, D. C., 1949.

8 F. W. Hutchinson, "Industrial Heat Transfer," Industrial Press, New York, N. Y., 1952, p. 40.

9 Lovatt Evans, "Starling's Principles of Human Physiology," twelfth edition, Lea and Febiger, Philadelphia, Pa., 1956, pp. 1061–1066.

10 C. L. Taylor and K. Buettner, "Influence of Evaporative Forces Upon Skin Temperature Dependency of Human Perspiration," *Journal of Applied Physiology*, vol. 6, 1953, pp. 113–123.

11 C. E.-A. Winslow, L. P. Herrington, and A. P. Gagge, "The Relative Influence of Radiation and Convection Upon the Temperature of the Clothed Body," *American Journal of Physiology*, vol. 124, no. 1, 1938, pp. 51–61.

12 C. E.-A. Winslow and L. P. Herrington, "Temperature and Human Life," Princeton University Press, Princeton, N. J., 1949, 266 pp.

DISCUSSION

E. F. Adolph[2]

The author reduces the results of certain measurements of heat exchanges by clothed men to linear equations. These equations are based on the concept that the physical components of exchange—radiation, conduction, convection, and evaporation—as well as metabolic heat production, combine to influence the mean surface temperature of the human body. Radiative or wall temperatures were varied independently of the convective or air temperatures, to provide a wide range of atmospheric conditions for men from whom the necessary data were obtained. A previous paper of the author covered the range of "operative" environmental temperatures from 40 to 80 F; the range 80 to 105 F is now included by a similar linear equation which, however, has different coefficients for each of the five terms. In this range the physiological regulation of body surface temperature differs greatly, since evaporative cooling now predominates.

It is very satisfying to have an empirical equation that condenses into it the varieties of information needed for assessing the steady state of heat regulation achieved by resting clothed individuals. The author's contribution consists chiefly in the use of surface temperature as the parameter most readily related to the physical conditions of environment. By this means, his two equations, of similar dimensions, become available to describe the net physiological state in any environment within the wide range indicated.

I agree with the author that this method of presenting calorimetric data advances the physical description of heat exchanges of the human body. It would be interesting to compare the accuracies of prediction of physiological effects, first from these two equations, and then from charts for effective temperatures and for other empirical relations that have been in use.

I also like the author's partial evaluation of the differences in heat exchange between the "copper man" as a model system and the average human subject. Differences between model and subject will allow us to identify special characteristics of heat regulation in man.

[2] Department of Physiology, The University of Rochester, Rochester, N. Y.

Alan H. Woodcock[3]

This paper, extending an earlier one by the same author, will be welcomed both by engineers and others who must consider the thermal relationships between man and his environment. The author and his co-workers have accumulated great quantities of pertinent information. However, to those not thoroughly familiar with this field, such masses of data are often baffling. His reduction or condensation of it into the form of simple linear equations, which can be easily used, is indeed a real service and, needless to say, must be performed by one thoroughly familiar with it.

The results with the life-sized model of man in this paper are reassuring as they indicate that man obeys the physical laws of heat transfer in a manner similar to an inanimate object. Table 1 indicates that the equation derived from human data gives good agreement with the model at an air temperature of 68.7 F. However, over the relatively small range (15 deg) of calorimeter temperature, the difference in skin temperature between equation and model shows a rather poor correlation. For the model with fixed heat input, the term in equation (1) representing metabolic heat input is constant and that for evaporation is also considered as a constant. Reference to Table 3 shows that neither metabolism nor evaporation remain constant for man as ambient temperature varies. If it did, these terms would have been omitted. Had the author used a variable heat to his model to correspond with man's variable metabolic heat production at varying temperatures and also corrected his evaporative term to correspond with temperature, I am sure he would have obtained a closer agreement between model and equation at all temperatures. Such corrections are, however, complications which are not necessary if, as the author recommends, the correct ambient temperature is used.

His introduction of a much simplified model in the form of a cylinder with hemispherical ends has both advantages and disadvantages. Its advantages are the reduced size and simplification of shape which, of course, reduces cost and at the same time makes an instrument much easier to store and use. Its disadvantage is that the effects of different types of clothing cannot be compared on the cylinder since it is impossible to duplicate the fit and drape of clothing. However, such complications are really beyond the scope of the author's objective which is to rid

[3] Quartermaster Research & Engineering Command, Natick, Mass.

the problem of its complications and present the data in its original form. An instrument somewhat similar to this cylinder, which is used in a slightly different manner, is the globe thermometer of Vernon. This globe thermometer, which is a six-inch diameter hollow-blackened copper sphere with a thermometer inserted in it, has been used with considerable success to integrate the effects of air and radiant temperature and is rapidly gaining popularity in this country.

In a later section of his paper, the author proposes a new equation [his equation (10)] to extend the range up to 105 F. A comparison of equations (1) and (10) shows that all the numerical coefficients in equation (10) except the constant term have been reduced. This indicates that at higher temperatures variation of skin temperature decreases. Indeed, skin temperatures become a relatively poor index of heat stress on man since they are so insensitive.

The effect of humidity is also not included in equation (10) although it is well known that it is an important factor. However, he indicates that his work will be extended to include these factors. Such an extension is definitely required and it is hoped that he will complete it in the near future.

Author's Closure

Dr. Woodcock comments on an interesting feature of equation (1) for the 40 to 80-deg F range as compared with equation (10) for the 80 to 105-deg F range. He notes that the coefficients of equation (10) for the hot region are reduced with respect to equation (1) for the cool region. This fact is interpreted as an indication of a smaller skin temperature variability at higher ambient temperatures, and possibly as a restriction on the use of skin temperature as an index of heat stress in the hot region. It is true that the rate of change of skin temperature is slower as ambient stress increases. However, where the measurement panel contains the evaporative value whose systematic increment (of opposed sign) maintains this slower skin rise, there is no change in the total amount of information incorporated by empirical multiple variable equations of equally good fit in the two regions. In general, one cannot compare the absolute coefficient values of such equations as (1) and (10) without expressing them in beta form, see equation (3).

Likewise, the equations do not contain a thesis as to which variable is the best index of heat stress. From the value of the multiple correlation coefficient for equation (10) the total information extracted from the hot-series data is of the same order as that incorporated in the cool-region analysis equation.

These equations are numerical devices for expressing condensed interrelations as measured. Since they have simple algebraic properties, the total evaporation (E) could be made the dependent variable, if we regard this as the best thermal stress measure. In bio-engineering application within the range of the equation and its individual variables, the data interrelations will remain constant for this body of calorimetric data, analyzed by the methods described, without regard to which variable is regarded as the predicted variable.

An analysis in process will include a vapor pressure term. For documentation of equation (10) which is briefly mentioned in the text, and equation (1) it may be added that relative humidities were held between 40 and 50 per cent for every experimental air temperature.

J. P. HARTNETT

Professor of Mechanical Engineering, University of Minnesota, Minneapolis, Minn. Mem. ASME

E. R. G. ECKERT

Professor of Mechanical Engineering, University of Minnesota, Minneapolis, Minn. Mem. ASME

R. BIRKEBAK

Instructor, Mechanical Engineering Department, University of Minnesota, Minneapolis, Minn.

The Emissivity and Absorptivity of Parachute Fabrics[1]

The use of parachutes for recovery of information and equipment from high-speed vehicles has directed attention to the heating problem which in some instances may be so severe as to cause destruction of the parachute. Consequently, the parachute engineer requires sufficient information on the heat-transfer characteristics of geometries resembling those of parachutes and on the heat-transfer properties of the materials used to allow a calculation of the temperature history of a descending parachute. In particular, the radiation properties of the parachute materials must be known since the parachute is receiving radiant energy from the sun and loses energy by radiation to the surroundings. The measurement of radiation properties for such parachute materials is more complicated than for solid surfaces since an appreciable amount of energy is transmitted by such fabrics. It is the purpose of this paper to describe the equipment which was used to measure the absorptivity for solar radiation and the long-wave-length emissivity for such parachute materials and to report these data for a number of important parachute materials.

Consider a material in the form of a thin sheet as shown in Fig. 1 and radiant energy consisting of parallel or nearly parallel rays impinging on surface 1 of this material under an angle β. Part of this radiation is reflected from the surface. Two limiting cases for the space distribution of the reflected radiation are specular and diffuse reflectivity. Usually, the actual reflection of surfaces used in engineering is in its space distribution between these extremes with larger amounts of energy reflected in a range near the specularly reflected rays, but some reflection occurring diffusely also [1].[2] In its details, the space distribution depends on the surface condition and on the material of the sheet. In this paper, the space distribution of reflected radiation will not be investigated. The ratio of the total amount of reflected energy—regardless of direction—to the amount of impinging energy will be called reflectivity and will be denoted by ρ.

The radiant energy which penetrates through the surface 1 is partially absorbed in the sheet. The rest leaves it through its surface 2. The directional distribution of this radiation depends again on the surface condition and on the material of the sheet. The ratio of the total energy integrated over all directions in space—which leaves surface 2 to the impinging energy will be called transmissivity and will be denoted by τ.

The rest of the radiant energy is absorbed in the material so that with an absorptivity α defined in an analogous manner, the following equation holds

$$\rho + \alpha + \tau = 1 \tag{1}$$

The radiation properties α, ρ, and τ depend generally on the temperature of the sheet and on the wave length of the impinging radiation. In engineering applications, the impinging radiation comprises usually a large range of wave lengths and the radiation properties consider the respective energies integrated over all wave lengths. It has to be kept in mind that these total radiation properties depend then on the wave-length distribution of the incident radiation. In particular, energy considerations on parachutes have to deal with solar radiation and with radiation from sources of moderate temperature. The radiation properties in this paper consider, therefore, these radiation sources.

According to Kirchhoff's law, the monochromatic emissivity is equal to the monochromatic absorptivity. For the values which are integrated over all wave lengths, however, the relation

$$\alpha = \epsilon$$

holds only when the source for the incident radiation is a black body with a temperature equal to the temperature of the absorb-

[1] Publication from the Heat Transfer Laboratory, University of Minnesota, Minneapolis, Minn.

[2] Numbers in brackets designate References at end of paper.

Contributed by the Heat Transfer Division and presented at the Annual Meeting, New York, N. Y., November 30–December 5, 1958, of The American Society of Mechanical Engineers.

Note: Statements and opinions advanced in papers are to be understood as individual expressions of their authors and not those of the Society. Manuscript received at ASME Headquarters, July 31, 1958. Paper No. 58—A-125.

Nomenclature

C = amount of energy reaching thermopile from test surface divided by actual amount leaving test surface

e = amount of energy emitted by surface, Btu/hr sq ft

G = radiation impinging on thermopile receiving surface, Btu/hr sq ft

J_i = incident energy, solar energy or black-body radiation, Btu/hr sq ft

k_1, k_2, k_3 = proportionality constants

T = absolute temperature, deg R

α = total absorptivity

ϵ = total emissivity

ρ = total hemispherical reflectivity

ρ' = reflectivity for radiation emitted by thermopile surface

τ = total hemispherical transmissivity

σ = Stefan-Boltzmann constant, 0.1714×10^{-8} Btu/hr ft^2 R^4

Δ = galvanometer reading

Subscripts

m = hemispherical mirrored surface

r = refers to readings when reference surface is in position

s = refers to readings when test surface is in position

t = thermopile

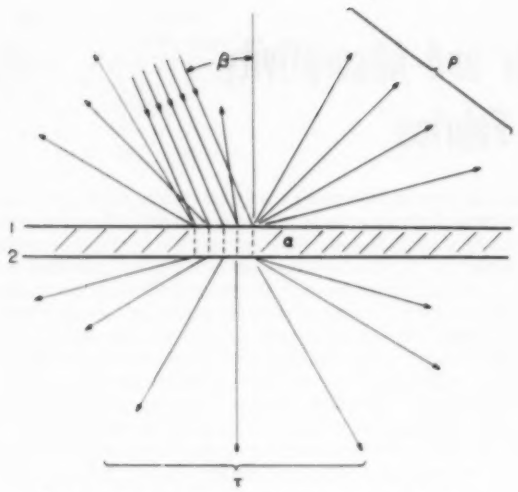

Fig. 1 Radiation reflected and transmitted on a thin sheet

ing sheet, and as good approximation, where the two temperatures do not differ much.[3] In this paper, the absorptivities presented in Table 1 can be interpreted as emissivities.

It can be expected that the radiation properties as just defined change with the angle of the incident radiation. This has been observed for solid materials of a thickness sufficient to make the transmitted radiation practically zero [2]. For thin sheets like the materials investigated in this paper, an even stronger dependence on angle may be expected. The measurements reported here are all for normal incidence of the radiation.

The radiation properties depend also on the medium which surrounds the sheet. In the present experiments this medium was always air.

Description of Apparatus

The hemispherical integrating radiometer, shown in Fig. 2 and previously described in [3], was used to measure the reflectivity and transmissivity of the various parachute fabrics for normal incident solar radiation. These radiation properties were determined also for infrared radiation using the same basic instrument, but with the source of radiant energy being a low-temperature black body as shown in Fig. 3. For convenience in the program, a separate radiometer with the minor modifications shown in this figure was constructed for the infrared measurements. For both instruments, the hemispherical shells are made out of glass with 9.625 in. ID and with apertures 9/16 in. diam. The inner surface of the hemisphere is coated with aluminum selected because of its resistance to tarnishing and also for its relatively constant and high spectral reflectivity. The hemisphere is surrounded by a cooling jacket to maintain defined conditions around the thermopile and test surfaces at all times.

A Kipp and Zonen Solarimeter, type G-19, thermopile without base and screen is used in the instrument with the receiving surface of the thermopile being approximately 1/4 sq in. The thermopile and the test surfaces are mounted on a stand which can be rotated so that radiant energy is directed either on the thermopile or on the test surfaces. The test-surface holder for the solar measurements is provided with positions for six test surfaces. When the measurements on one surface are completed, another surface can be rotated into the measuring position.

[3] An estimate of the deviation of both values can be made from Fig. 108 of reference [2].

Table 1 Radiation properties of parachute cloth for normally incident black-body radiation at 350 F

Material	Reflectivity	Transmissivity	Absorptivity[a]
Dacron, 100 lb	0.08	0.17	0.75
Dacron, 300 lb	0.07	0.14	0.79
Dacron, 600 lb	0.07	0.07	0.86
Dacron, 800 lb	0.07	0.03	0.90
Nylon rip-stop (orange) 1.1 oz per sq yd, MIL—C—7020	0.05	0.19	0.76
Nylon rip-stop 1.1 oz per sq yd (white) MIL—C—7020	0.06	0.21	0.73
Nylon rip-stop 1.6 oz per sq yd (white) MIL—C—7020B Type III	0.07	0.21	0.72
Nylon cloth 2.25 oz per sq yd, MIL—C—7350B Type I	0.07	0.05	0.88
Nylon cloth 4.30 oz per sq yd, MIL—C—8021 Type I	0.07	0.06	0.87
Nylon cloth 7.0 oz per sq yd, MIL—C—8021 Type II	0.10	0.05	0.85
Nylon cloth 14.0 oz per sq yd, MIL—C—8021 Type III	0.10	0.04	0.86

[a] This value is equal to the emissivity of the material at 350 F when the monochromatic absorptivity is considered independent of temperature.

Since the fabric test surfaces transmit energy, the background behind the test surfaces for the reflectivity measurements was designed to absorb any transmitted energy. For the solar-energy measurements the background surface was the blackened top of the test-surface holder, while for the infrared measurements, the background surface was a water-cooled black body as shown in Fig. 3. The energy reaching the thermopile when a test surface was in test position over that coming from the background was then due to the reflected energy.

When making the solar measurements, a fused-quartz window 2 mm thick was installed over the aperture to eliminate effects of convection currents on the thermopile readings. Throughout the important part of the solar spectrum, 0.3 to 3.0 μ, the fused quartz filters evenly and has a transmissivity of 92 per cent [4].

Experimental Procedure

A comparison technique is used for the measurement of the reflectivity. The thermopile and the test surface are located on conjugate foci of the hemisphere. If radiant energy is reflected from the test surface, then the necessary integration of energy reflected at all angles is accomplished by the hemispherical surface since, for the small distance (0.75 in.) between the foci, the hemisphere is practically identical in shape with an ellipsoid. The reading of the galvanometer connected to the thermopile is then an indication of the amount of energy reflected at all angles since it is integrated by the hemispherical surface and focused onto the thermopile. By taking the ratio of the energy reflected from the test surface onto the thermopile to that reflected by the reference surface on the thermopile and using the value of the reflectivity of the reference surface, the reflectivity of the test surface is calculated. The details of the data analysis may be found in the Appendix.

To obtain a high accuracy with the described technique, the reference surface should have reflection characteristics similar to the test surfaces; i.e., similar directional distribution of the reflectivity. In the visible region of the spectrum one can determine readily whether the reference surface and test surface reflect similarly, while in the infrared one should use a reference surface made from the same type of material. A reference surface which satisfies these requirements in the solar region of the spectrum is

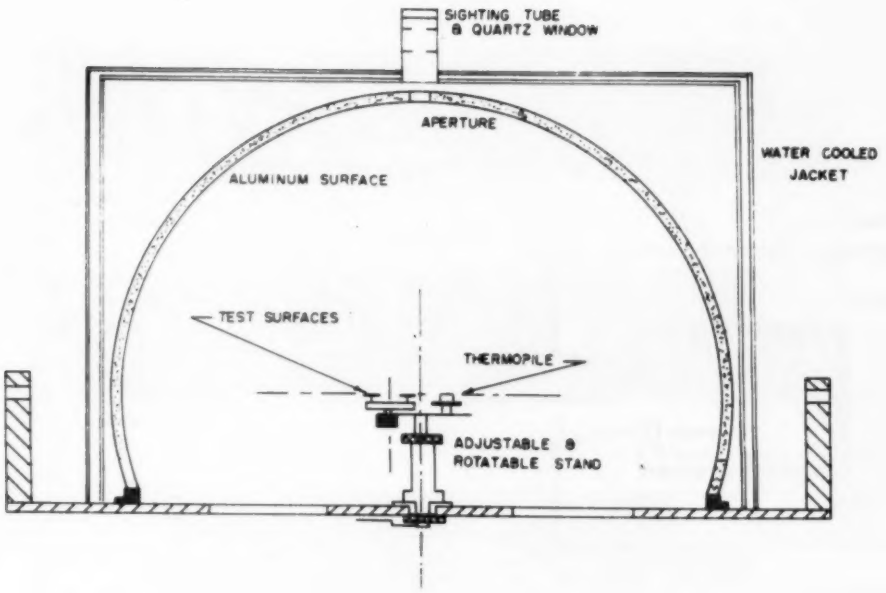

INTEGRATING RADIOMETER

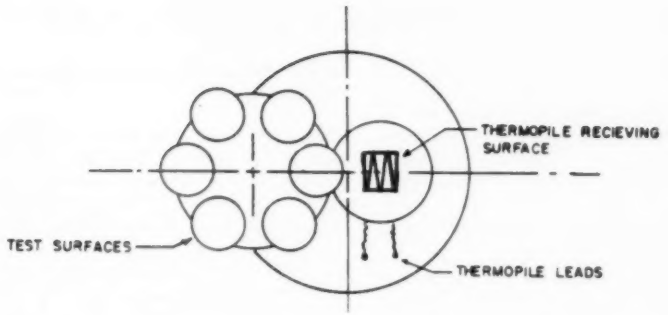

TOP VIEW

Fig. 2 Hemispherical integrating radiometer for solar-energy measurements

magnesium oxide (MgO). The MgO surface was prepared by methods for which the reflectivity was well established [5–10]. The reference surface consisted of an MgO layer, 1 to 2 mm thick, smoked on a block of compressed MgO. This surface has a reflectivity in the solar spectrum of 0.94 ± 0.02. The reference surface used in the infrared region of the spectrum was a cloth material designated QM7 (Quarter Master Corps standard cloth) for which monochromatic reflectivity information was available in the literature [11]. A check on the reliability of the infrared reflectivity measurements was made by measuring the reflectivity for normally impinging solar radiation and by comparing it to the value calculated from the information in this reference. The value determined in this investigation was 0.29, while the value obtained from [11] was 0.25. The reflectivity of the reference surface for black-body radiation from a source at 350 F was then calculated from the information in [11] and found to be 0.12.

For the transmissivity measurements, the test surface holders were modified so that the test surface, when in the measuring position, completely covered the receiving surface of the thermopile. With no test surface in position, the radiant energy passing through the aperture was made incident on the thermopile. The thermopile indication is then a measure of the incident radiant energy. Next, the test surface was rotated into the test position. Since the test surface is directly over the thermopile, all the transmitted energy was reaching the thermopile. By taking the ratio of the transmitted energy to that directly incident on the thermopile, the transmissivity is determined.

From these measured values of the reflectivity and transmissivity, the absorptivity of the test surface is calculated with Equation (1).

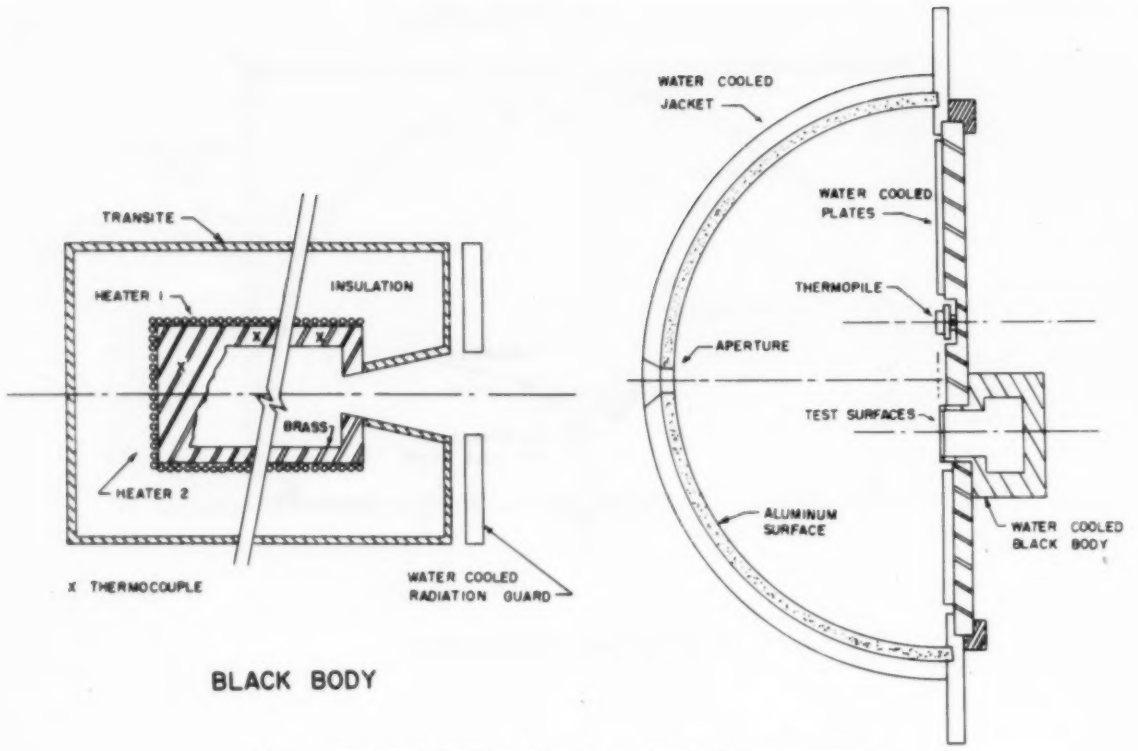

Fig. 3 Hemispherical integrating radiometer for infrared radiation measurements

Test Results and Discussion

Radiation Properties for Incident Solar Radiation. To establish the reliability of the present measuring technique, data were first obtained using cloth samples supplied by Profs. R. V. Dunkle and J. T. Gier of the University of California. For these materials, the radiation properties are reported in [11]. Table 2 compares the results of our measurements with those in this reference. It may be seen that they are in substantial agreement.

Having established confidence in the measuring technique, the measurements were then extended to the parachute fabrics. The resulting values of the reflectivity and the transmissivity for solar radiation are given in Table 3. The absorptivity is calculated from Equation (1).

Representative photomicrographs of the parachute fabrics are shown in Fig. 4. To allow for possible variations in the materials, several different samples were used for each material and the results were averaged. It is apparent from Table 3 that the major portion of the impinging solar radiation is either reflected or transmitted, and that the resulting absorptivity values vary from 0.05 for the lightweight weaves to 0.19 for the heavier fabrics.

Table 2 Comparison of present reflectivity values with previous investigations

Material	Measured by reference [11]	Present measurements
QM1, cotton sheeting bleached, 4 oz per yd	0.62-0.66	0.63
QM2, cotton sateen prepared for dyeing, 9 oz per yd	0.68-0.72	0.70
QM4, cotton sateen, undyed, 9 oz per yd	0.69-0.72	0.69
QM6, cotton sateen, medium gray, 9 oz per yd	0.53	0.54
QM7, cotton sateen, dark gray, 9 oz per yd	0.24	0.29
50% wool, 50% cotton, knit, undyed, 10.5 oz per yd	0.62	0.60
Cotton knit, undyed, 3 oz/yd	0.60	0.58

Table 3 Radiation properties of parachute cloth for normally incident solar radiation

Material	Reflectivity	Transmissivity	Absorptivity
Dacron, 100 lb	0.35	0.60	0.05
Dacron, 300 lb	0.54	0.35	0.11
Dacron, 600 lb	0.61	0.27	0.12
Dacron, 800 lb	0.62	0.19	0.19
Nylon rip stop (orange) 1.1 oz per sq yd, MIL—C—7020B Type I	0.23	0.64	0.13
Nylon rip-stop 1.1 oz per sq yd (white) MIL—C—7020	0.27	0.65	0.08
Nylon rip-stop 1.6 oz per sq yd (white) MIL—C—7020B Type III	0.22	0.72	0.06
Nylon cloth 2.25 oz per sq yd, MIL—C—7350B Type I	0.36	0.59	0.05
Nylon cloth 4.30 oz per sq yd, MIL—C—8021 Type I	0.44	0.48	0.08
Nylon cloth 7.0 oz per sq yd, MIL—C—8021 Type II	0.46	0.41	0.13
Nylon cloth 14.0 oz per sq yd, MIL—C—8021 Type III	0.62	0.27	0.11

Radiation Properties in Infrared Region of Spectrum. The measuring technique used in this study was analogous to the one for the solar-radiation measurements. The hemispherical radiometer with the black-body source is shown in Fig. 3. Using the reference surface QM7 and the test surface, the reflectivity and

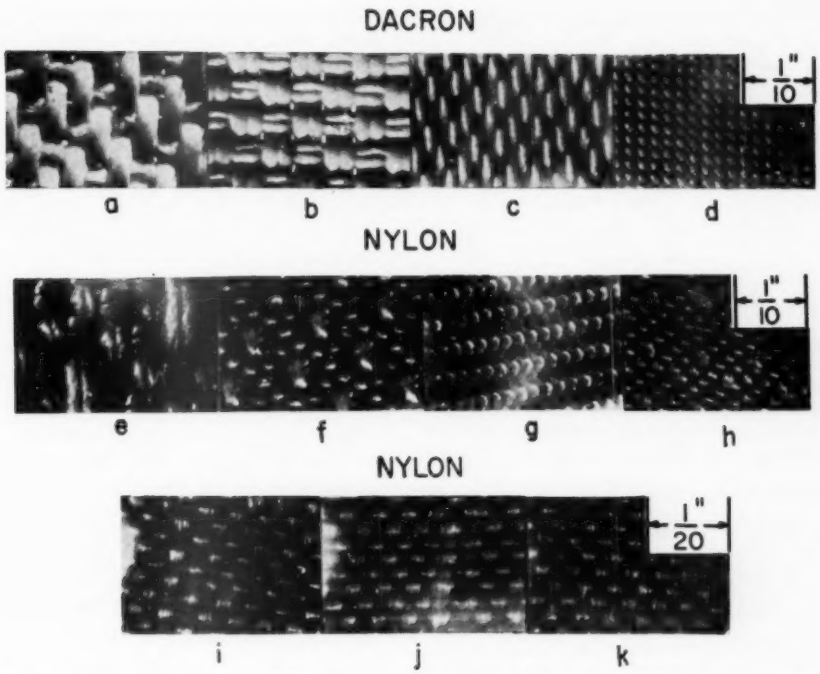

Fig. 4 Parachute fabrics micrographs. Dacron—(a) 800 lb tensile strength, (b) 600 lb tensile strength, (c) 300 lb tensile strength, (d) 100 lb tensile strength. Nylon cloth—(e) 14 oz per sq yd, MIL-C-8021 type III; (f) 7 oz per sq yd, MIL-C-8021 type II; (g) 4.30 oz per sq yd, MIL-C-8021 type I; (h) 2.25 oz per sq yd, MIL-C-7350B type I. Nylon rip stop—(i) (orange) 1.1 oz per sq yd, MIL-C-7020B type I; (j) (white) 1.1 oz per sq yd, MIL-C-7020; (k) (white) 1.6 oz per sq yd, MIL-C-7020B type III.

transmissivity measurements were made. Again the absorptivity was determined from these two values and the results are collected in Table 1.

A black body at a temperature of 350 F was used in this series of tests, and consequently, the impinging radiation was concentrated in the far infrared portion of the spectrum. As contrasted with the solar portion of the spectrum where the absorptivity values are low, the infrared absorptivities are appreciable ranging from 0.72 to 0.90.

If the monochromatic absorptivity is assumed to be invariant with temperature then this measured absorptivity is equal to the emissivity of the parachute material at 350 F.

Acknowledgment

The authors gratefully acknowledge the contributions of Messrs. D. J. Kruskopf and C. Y. Koh for their aid in the design and construction of the experimental apparatus and in obtaining experimental data. The financial support provided by the Aeronautical Accessories Laboratory, Wright Air Development Center, US Air Force, is greatly appreciated.

References

1 E. R. G. Eckert, "Messung der Reflexion von Wärmestrahlen an technischen Oberflüchen," *Forschung auf dem Gebiete des Ingenieurwesens*, vol. 7, 1936, pp. 265–270.

2 E. R. G. Eckert, "Introduction to the Transfer of Heat and Mass," McGraw-Hill Book Company, Inc., New York, N. Y., 1950, pp. 202–203.

3 R. C. Birkebak and J. P. Hartnett, "Measurements of the Total Absorptivity for Solar Radiation of Several Engineering Materials," TRANS. ASME, vol. 80, 1958, pp. 373–378.

4 "Fused Quartz Price Schedule," General Electric Catalogue.

5 F. Benford, G. P. Loyd, and S. Schwartz, "Coefficients of Reflection of Magnesium Oxide and Magnesium Carbonate," *Journal of the Optical Society of America*, vol. 38, 1948, pp. 445.

6 R. V. Dunkle and J. T. Gier, "Thermal Radiation Project," Progress Report, June, 1952 to June, 1953, University of California. Institute of Engineering, Contract No. DA-11-190-Eng. 3.

7 W. E. K. Middleton and C. L. Sanders, "The Absolute Spectral Diffuse Reflectance of Magnesium Oxide," *Journal of the Optical Society of America*, vol. 41, 1951, p. 419.

8 C. L. Sanders and W. E. K. Middleton, "The Absolute Spectral Diffuse Reflectance of Magnesium Oxide in the Near Infrared," *Journal of the Optical Society of America*, vol. 43, 1953, p. 58.

9 P. A. Tellex and J. P. Wadion, "Reflectance of Magnesium Oxide," *Journal of the Optical Society of America*, vol. 45, 1955, pp. 19–22.

10 "Preparation and Colorimetric Properties of a Magnesium Oxide Reflectance Standard," National Bureau of Standards, Letter Circular LC 547, 1939.

11 R. V. Dunkle and J. T. Gier, "Study of the Various Modes of Heat Transfer From and Through Clothing Materials," final report, Contract No. DA 19-129-QM-149.

APPENDIX

Analysis of Data

Reflectivity. The radiant energy G arriving at the thermopile t when the test surface s is in position with incident radiation J_i impinging on the test surface may be written (Fig. 5)

$$G(1s) = J_i\rho_i\rho_m C_s + \epsilon_s\rho_m C_s + \epsilon_t C_s^2 \rho_m^2 \rho_s' \qquad (2)$$

The first term on the right represents the incident solar or infrared energy reflected off the test surface corrected for the reflectivity of the mirrored surface and the loss through the aperture; the second term represents the energy emitted by the test surface and its background with the same corrections, while the third

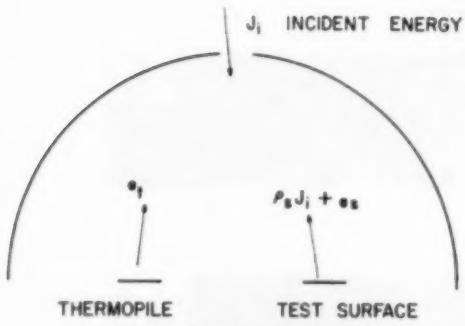

Fig. 5 Thermopile-energy balance

term is the energy originating at the thermopile itself which arrives back on the thermopile after reflection from the test surface.

If the aperture is now closed to external radiation so that J_i is zero, the energy arriving at the thermopile becomes

$$G(2s) = e_s\rho_m C_s + e_t C_s^2 \rho_m^2 \rho_s' \tag{3}$$

Solving Equations (2) and (3) for the reflectivity of the test surface ρ_s,

$$\rho_s = \frac{G(1s) - G(2s)}{J_i \rho_m C_s} \tag{4}$$

The same type of relation obviously holds for the reference surface (r)

$$\rho_r = \frac{G(1r) - G(2r)}{J_i \rho_m C_r} \tag{5}$$

By a combination of equations (4) and (5), the reflectivity ρ_s is obtained

$$\rho_s = \rho_r \left(\frac{C_r}{C_s}\right) \frac{G(1s) - G(2s)}{G(1r) - G(2r)} \tag{6}$$

A heat balance may now be written on the thermopile itself when it is receiving energy in the amount $G(1s)$, since at equilibrium this energy must be balanced by the energy lost by the thermopile surface by radiation, conduction, and convection:

$$G(1s) = \sigma T_{1s}^4 + k_1(T_{1s} - T_c) \tag{7}$$

where the first term on the right represents the radiation loss and the second term the convection and conduction losses. These losses can be assumed proportional to the difference between the temperature of the receiving surface and the temperature of the cold junction of the thermopile embedded in a metal block behind the receiving surface. Similarly we may write

$$G(2s) = \sigma T_{2s}^4 + k_1(T_{2s} - T_c) \tag{8}$$

From equations (7) and (8) it follows:

$$G(1s) - G(2s) = \sigma(T_{1s}^4 - T_{2s}^4) + k_1(T_{1s} - T_{2s}) \tag{9}$$

For small temperature differences, the first right-hand term can be linearized and combined with the second term to give

$$G(1s) - G(2s) = k_2(T_{1s} - T_{2s}) \tag{10}$$

A similar equation holds for the condition that the reference surface is in the test position. Therefore

$$\rho_s = \rho_r \left(\frac{C_r}{C_s}\right) \frac{(T_{1s} - T_{2s})}{(T_{1r} - T_{2r})} \tag{11}$$

The galvanometer reading Δ is, because of the small temperature differences involved, directly proportional to the temperature difference between the hot junction (T_{1s} or T_{2s}) and the cold junction T_c, which is maintained at a constant temperature. Therefore

$$\Delta(1s) = k_3(T_{1s} - T_c) \tag{12}$$

Similar expressions may be written for the other readings. This leads to the final equation

$$\rho_s = \rho_r \frac{C_r}{C_s} \frac{\Delta(1s) - \Delta(2s)}{\Delta(1r) - \Delta(2r)} \tag{13}$$

This equation may be simplified further since the reference material was selected to have similar directional reflection characteristics as the sample. Therefore $C_r = C_s$. The terms $\Delta(2s)$ and $\Delta(2r)$ in equation (13) have been found to be negligible since the test surface and thermopile cold junction were kept at the same temperature by the cooling water. The reflectivity was then calculated from the equations

$$\rho_s = \rho_r \frac{\Delta(1s)}{\Delta(1r)} \tag{14}$$

Surface Transmissivity. The data from the experimental procedure for transmitted energy can be analyzed in a manner similar to that for the reflected energy. Performing heat balances on the thermopile for both the incident i and transmitted τ energies and relating these to the thermopile output Δ result in the following expression for the transmissivity of the test surface:

$$\tau_s = \frac{\Delta(\tau)}{\Delta(i)}$$

where $\Delta(\tau)$ is the galvanometer reading with transmitted energy impinging on the thermopile and $\Delta(i)$ is the galvanometer reading with the total incident energy impinging on the thermopile.

DISCUSSION

M. N. Aref[4]

The authors are to be congratulated for contributing additional information on the radiation properties of porous fabrics. It appears from the comparison technique adopted by the authors that, in order to arrive at the absorptivity and hence the emissivity, direct measurements were obtained first on the reflectivity and transmissivity. The difference of both factors from unity determined the absorptivity. In this method, however, any errors involved in the calculation of the absorptivity will be due to the measurements of both reflectivity and transmissivity. It would be helpful to know the magnitude of such errors, which might be attributed to a possible heat loss through the radiometer aperture and an absorbed heat by the comparatively wide radiometer mirrored surface.

As is well known, however, the emissivity of a surface may not be equal to its absorptivity, unless its monochromatic absorptivity is considered independent of both radiation wave length and temperature. On the other hand, a direct measurement of the emissivity of such surfaces could be determined by either one of the two methods presented in an earlier paper by the writer,[5] with a slight modification of the apparatus for the normal solar radiation measurement. This is basically accomplished by placing a solar radiation or a black-body radiation source at the same temperature as the sample, at a fixed distance from the measuring radiometer, provided that both source and sample bear the same configuration to the radiometer. Both

[4] Research Department, Foster Wheeler Corporation, New York, N. Y. Assoc. Mem. ASME.

[5] M. N. Aref, "Emissivity Measurements of Industrial Surfaces Due to Thermal Radiation," Paper No. 58—HT-18, presented at ASME-AIChE Heat Transfer Conference, Chicago, Ill., August, 1958.

radiations from source and sample could then be directed at the radiometer separately and their ratio would render the emissivity directly, thus eliminating the sources of error in the measurements of the reflectivity and transmissivity.

Authors' Closure

The first two questions asked by Mr. Aref can be answered directly from the Analysis of Data section. The amount of energy lost through the aperture is taken into account by the factor C (amount of energy reaching thermopile from test surface divided by actual amount leaving test surface). Referring to previous work of the authors, Ref. [3] of the paper, the value of energy lost through the aperture for various surfaces varies from 1 to 4 per cent. The amount of energy absorbed by the hemispherical surface is also taken into account in the analysis by the factor $(1 - \rho_m)$.

The authors are well aware of available methods for directly measuring the total emissivity and indeed have made such measurements in the past.[6,7] However, if a radiometer is sighted on a porous surface such as a parachute fabric, the energy reaching the radiometer comes not only from the porous sample but additionally some energy is transmitted through the sample; it is extremely difficult to separate the emitted energy from the transmitted energy and, consequently, the authors chose to determine the absorptivity as outlined in the paper. Mr. Aref appears to have missed the point that the resulting measured absorptivity for infrared radiation coming from a black body at 350 F does indeed yield the emissivity if the monochromatic absorptivity is invariant with temperature (it can still vary with wave length). The proof is straightforward:

Kirchhoff's law states that the spectral emissivity of a surface at a temperature T is equal to the spectral absorptivity at this same temperature

$$\epsilon_{\lambda,T} = \alpha_{\lambda,T} \tag{15}$$

The definition of the total absorptivity α of a surface at a temperature T_s for incoming radiation $J_{i\lambda}$:

$$\alpha = \frac{\int_0^\infty \alpha_{\lambda,T} J_{i\lambda} d\lambda}{\int_0^\infty J_{i\lambda} d\lambda} \tag{16}$$

The definition of the total emissivity of a surface at temperature T is given by

$$\epsilon = \frac{\int_0^\infty \epsilon_{\lambda,T}\, e_{b\lambda,T} d\lambda}{\int_0^\infty e_{b\lambda,T} d\lambda} \tag{17}$$

where

$e_{b\lambda,T}$ = amount of energy emitted by a black body at temperature T at wave length λ, Btu/hr ft^2

Now in the infrared experiments described herein the incoming radiation $J_{i,\lambda}$ corresponded to black body radiation at 350 deg

$$J_{i,\lambda} = e_{b\lambda,\,350\,\mathrm{F}} \tag{18}$$

The surface temperature of the parachute material was approximately 100 F and, if it is assumed that the spectral absorptivity is independent of temperature,

$$\alpha_{\lambda,100\,\mathrm{F}} = \alpha_{\lambda,350\,\mathrm{F}} = \epsilon_{\lambda,350\,\mathrm{F}} \tag{19}$$

Substituting (18) and (19) into equations (16) and comparing with equation (17) it is readily seen that the measured absorptivity directly yields the emissivity.

[6] E. R. G. Eckert, J. P. Hartnett, and T. F. Irvine, Jr., "Measurement of Total Emissivity of Porous Materials in Use for Transpiration Cooling," *Jet Propulsion*, vol. 26, 1956, p. 280.

[7] T. F. Irvine, Jr., J. P. Hartnett, and E. R. G. Eckert, "Solar Collector Surfaces With Wavelength Selective Radiation Characteristics," *Solar Energy Journal*, vol. II, July-Oct., 1958, p. 12.

An Experimental and Analytical Study of Vortex-Flow Temperature Separation by Superposition of Spiral and Axial Flows[1]

Part 1

J. E. LAY

Associate Professor,
Mechanical Engineering Department,
Michigan State University,
East Lansing, Mich.
Assoc. Mem. ASME

This paper reports on an experimental and analytical study of compressible flow in a uniflow vortex tube. Part 1 deals with an experimental study, Part 2 with the analytical study. Its purpose is to provide a better understanding of the separation of a gas stream into regions of high and low stagnation temperatures, there being at present little agreement as to the theory of operation. The problem is first approached from the experimental standpoint. A large, multipurpose vortex tube is so designed and built that pressure, temperature, and velocity traverses can be taken at six different stations throughout the length of the tube. Pressure, temperature, and velocity traverses are taken by means of hypodermic probes. Velocities are checked by means of a miniature hot-wire anemometer. Data are taken for different runs of inlet pressures and plotted against radial distance. Flow visualization is obtained by means of liquid injection. The analytical study consists of using superposition for the solution of the flow equations. It begins with potential vortex flow in the plane. The solution of this flow is characterized by the existence of sonic or limit circles. Superposition of a sink flow to the vortex solution yields a spiral flow in the plane. The general solution in space is obtained by addition of a uniform axial velocity to the spiral flow. When viscosity effects are considered, the potential vortex changes into a forced vortex, and the solution becomes a superposition of a viscous compressible sink to a forced vortex. Performance or stagnation temperature separation is expressed as function of the ratio of vortex strength to sink strength.

Introduction

THE PURPOSE of this work is to provide a better understanding of the separation of a gas stream into regions of high and low stagnation temperatures in a vortex field. Its motivation is the perplexing phenomenon known as the Ranque-Hilsch effect, which occurs when a gas expands in a centrifugal field such as exists in cyclone separators. This effect is a fairly recent discovery, having first been reported in 1931, and rediscovered in 1946. Its history follows the familiar pattern of initial enthusiasm, then apathy, and later, renewed interest. As a phenomenon, relatively little is known concerning it, except for its spectacular effect of producing hot and cold air simultaneously. Despite various hypotheses advanced, there is to date, no general agreement as to its theory of operation [12].[2] Consequently, there is a need for a systematic study of the phenomenon from the ground up. The present paper represents such a study. It is hoped that it will be of help in the understanding of the Ranque-Hilsch effect and of vorticity in general.

The vortex tube is a very simple device which has no moving parts, but merely consists of a straight length of tubing with a tangential entry for the supply air as shown in Fig. 1. The entering stream of compressed air separates into two streams of different temperature; the hot stream leaving through the periphery, and the cold stream leaving through the center. Except for its spectacular effect of producing hot and cold air simultaneously, relatively little is known concerning its operation. So far, analyses have been based on very little systematic experimentation because of the difficulties involved in gathering data. Also, the equations describing the flow are difficult to handle, for they are of the spatial viscous compressible-flow type. Nevertheless, since 1946, when it was brought over from Germany,

[1] Paper is based on some of the experimental work done by the author at the University of Michigan.

Contributed by the Heat Transfer Division and presented at the Semi-Annual Meeting, Detroit, Mich., June 15–19, 1958, of THE AMERICAN SOCIETY OF MECHANICAL ENGINEERS.

NOTE: Statements and opinions advanced in papers are to be understood as individual expressions of their authors and not those of the Society. Manuscript received at ASME Headquarters, May 14, 1958. Paper No. 58—SA-71.

[2] Numbers in brackets designate Bibliography at end of Part 2.

Nomenclature

A = area
K = constant in irrotational flow
M = Mach number
Q = strength of source or sink
R = gas constant
S = entropy
T = absolute temperature
c = speed of sound
m = mass
p = pressure
q = velocity in hodograph plane
r = radial distance
t = time
u, v, w = components of velocity in physical plane
x, y, z = co-ordinate axes
γ = ratio of specific heats
Γ = circulation
θ = velocity angle in hodograph plane
ρ = density
ϕ = velocity potential
ψ = streamline function

Fig. 1 Vortex or Ranque-Hilsch tube

writers of widely different backgrounds have been interested in the phenomenon [5, 6, 8, 17, 22, 30, 31].

The history of the vortex tube dates back to 1931, when it was first reported by G. Ranque in a paper read to the Société Française de Physique. He was a metallurgist at a steel works in Montluçon, Central France, and he had noticed the vortex cooling effect in connection with cyclone separators. He constructed a device to duplicate the effect, and applied for a French patent in December, 1931. A similar patent was applied for in the United States in December, 1932, and was granted in March, 1934. Subsequent developments, however, brought the disappointing realization that the vortex tube was inefficient as a refrigerator, for nothing more was heard of it until 1946, when R. Hilsch, of the Physikalischen Institute, Erlangen, Germany, published a paper relating his experience with the device [16].

In June, 1945, at the end of the war in Europe, C. W. Hansell, investigator for the United States and British Technical Industrial Intelligence Committee, visited Erlangen University and rediscovered the vortex tube. At about the same time, R. M. Milton, of Johns Hopkins University also visited Erlangen, and brought back a model and a thesis by Hilsch. The thesis was translated by I. Estermann, of the Carnegie Institute of Technology, and the translation was circulated through Wright Field. Hilsch's original paper gave some performance data and optimum dimensions for two vortex tubes. Widespread American interest has been given the vortex tube ever since Milton published a short descriptive article in *Refrigerating Engineering*, May, 1946. The extreme simplicity of the device and the spectacular separation of hot and cold streams suggested that it might replace some of the more complicated refrigerator designs. However, subsequent investigations showed that the power required to operate the vortex tube was many times that required by a conventional refrigerator. Nevertheless, other applications have been mentioned for the device, notably as regards jet-aircraft cooling and thermometry [22]. Thus, interest in the phenomenon continues, and in common with other efforts this paper aims to clarify the Ranque-Hilsch effect and to extend the knowledge of vorticity in general.

Experimental Program

Vortex-Tube Design. The main consideration in the test program was the design of a vortex tube of sufficient size and flexibility as to allow velocity, temperature, and pressure traverses to be taken without causing major disturbances in the flow field. The inherent limitations to the experimental study of vortex flow, until recently, have kept the systematic investigation of the vortex tube from progressing very far. Both Ranque's and Hilsch's original models were of very small diameters (4 to 18-mm tubes with 2 to 7-mm orifices) wherein fairly impressive effects could be obtained with relatively low or moderate supply pressures. Such small-size models, however, are not suitable to any basic study of the vortex phenomenon, since they do not lend themselves to any velocity, pressure, or temperature traverses. To perform these operations, considerably larger size models have to be designed, and this in turn requires high flow rates of supply air. In addition, great care must be given to the fact that whatever probes are inserted in the tube, the flow pattern must not be disturbed.

With these considerations in mind, it was decided to design a 2-in-diam vortex tube made of lucite. This is considerably larger than the majority of previously reported designs. The choice of lucite, of course, is to permit flow-visualization studies in addition to the systematic taking of traverses. The installation evolved is flexible for many kinds of measurements at different stations along the length of the tube. It is shown in Figs. 2, 3, and 4.

Compressed air at room temperature is fed tangentially into a center block, Fig. 3, from which it spirals downward along the vortex tube, Fig. 2. The vortex tube is so designed that a number of sections are fitted together to form a tube of any desired length. Stagnation temperature, stagnation pressure, static pressure, and velocity traverses are taken at stations along the tube shown in Fig. 5. The exit end of the tube is fitted with a cone-shaped valve, Fig. 4, which is movable in and out to regulate the flow in the hot tube.

Test Installation. Referring to Figs. 6 and 7, compressed air is supplied by means of valve no. 1 to a New Jersey constant-head flowmeter. It then passes through a DeVilbiss regulator and drier, and is fed by a flexible hose to the center block of the vortex tube. Pressure gage no. 1 and thermocouple no. 1 are installed between the Jersey flowmeter and the DeVilbiss drier, and a mercury U-tube is installed at the outlet of the drier so as to record the pressure of the air at entrance to the vortex tube. A bypass circuit, consisting of valve no. 3, pressure gage no. 3, is included for inlet pressures which exceed the capacity of the DeVilbiss drier.

No further equipment than the foregoing is needed for the study of vortex flow, except that a miniature pitot tube, Fig. 10, is used to measure velocities in the cold tube. The flow in the hot tube is obtained very simply by taking the difference between the supply flow and the flow in the cold tube.

Instrumentation. For the experimental work described in this paper, special velocity, pressure, and temperature probes were designed. The key feature is a probe assembly, Fig. 8, which can be inserted at any station along the length of the vortex tube, and constructed in such a way that a hypodermic needle may be raised, lowered, or even completely revolved within the flow field.

The hypodermic needle is raised or lowered by means of a Brown and Sharpe 605 depth gage and a slider as shown. The probe assembly is so constructed that the hypodermic needle not only may be moved radially into the flow, but also may be revolved completely so as to be sensible to the direction of flow. Fig. 8 shows the probe that is inserted at stations 1, 2, 3, and so forth, whereas Fig. 3 shows the probe that is inserted in the entry block.

The velocity, pressure, and temperature probes are shown in Figs. 9 and 10. Velocities may be obtained by measuring the stagnation and static pressures, respectively, but it is more convenient to use a hot-wire anemometer, the theory, electric circuit, and control panel of which are standard knowledge.

The hot-wire anemometer itself is a miniature version of the more bulky types made by commercial houses. Referring to Fig. 9, it consists of inserting two insulated copper leads through a stainless-steel hypodermic tubing (no. 18 gage), and soldering two sewing needles to these leads. The needles are held apart and in rigid position by binding them with fine thread and coating the whole with layers of electrical insulation which are allowed to dry and harden. The hardened base (shown as a small white mass in Fig. 9) is reduced to proper size by means of a

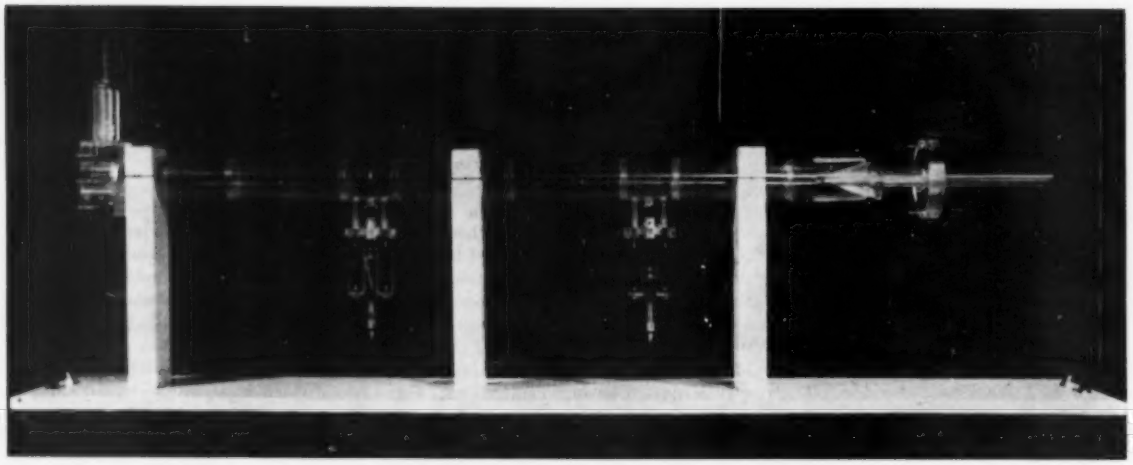

Fig. 2 Vortex-tube design

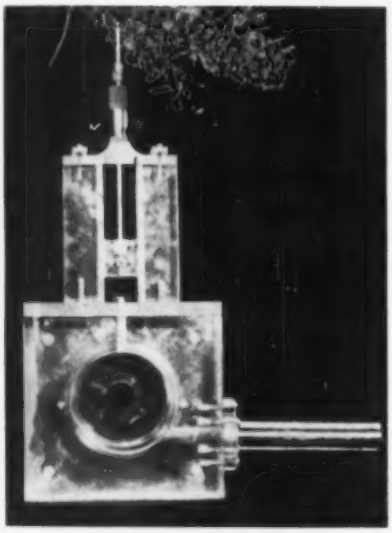

Fig. 3 Entry block and probe

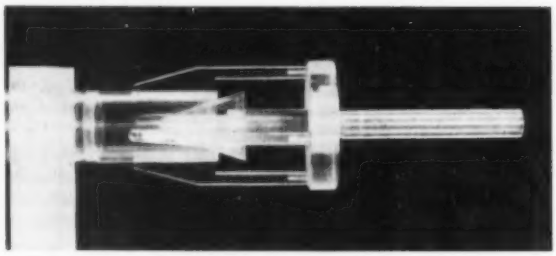

Fig. 4 Tail-cone assembly

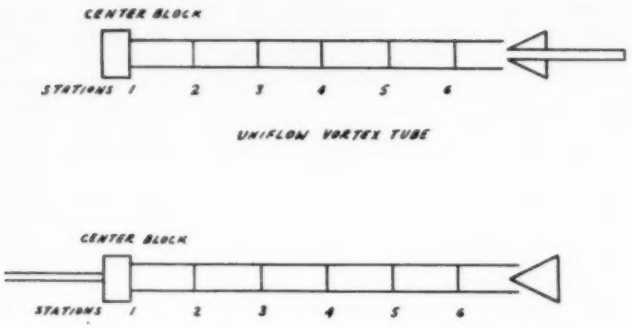

Fig. 5 Traverse stations

grinding wheel, and finally it is given several coverings of aircraft dope to smooth the surface. Across the sewing needles (which can be seen protruding from the base) is soldered a fine Wollaston wire ranging in size from 0.00015 to 0.00030 in. diam. To obtain high sensitivity to velocities, the center portion of the wire is etched in a solution of nitric acid.

The pressure probes, Fig. 10, consist of a static-pressure hypodermic steel tubing (no. 18 gage) polished and left open at the end, and of a stagnation-pressure hypodermic steel tubing (also no. 18 gage), whose end is soldered closed and square cut, but having a small hole which may be directed into the line of flow. By revolving the stagnation tubing on its stand, the impact pressure yields a maximum reading, which indicates the direction of flow.

As for the stagnation-temperature probe, it consists of a stainless-steel hypodermic of the same size (no. 18 gage) as those used for velocity and pressure measurements. Two dissimilar but insulated leads (iron and constantan, no. 36 gage) are inserted through it. The ends of the leads are bared and fused together by acetylene torch of carbon arc, then pulled back close to the end of the tube to make the assembly compact. To keep disturbance of the flow field at a minimum, no further elaboration is included in the design of the probes. All probes, however, are calibrated before use, the velocity probes in a wind tunnel, and the temperature probes by comparison with a probe of unity recovery factor.

Test Configuration. The primary objective of the experimental program was to obtain basic knowledge of the velocity, pressure, and temperature distributions in the vortex field of flow. The emphasis of the study was directed to a vortex which is generated at the entrance block, and which proceeds in one direction down the tube to be discharged through the exit at the far end of the

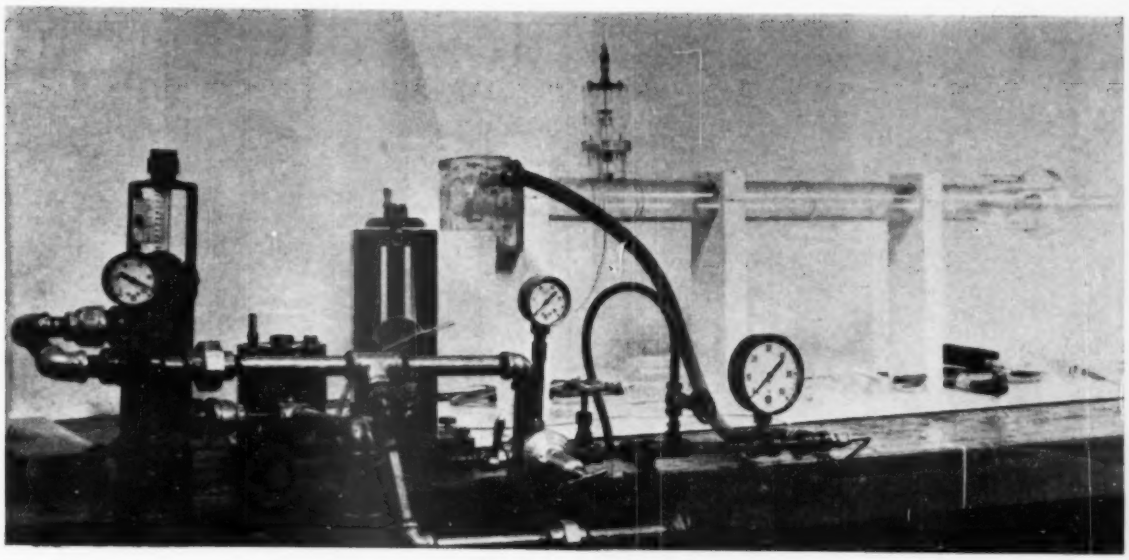

Fig. 6 Test installation

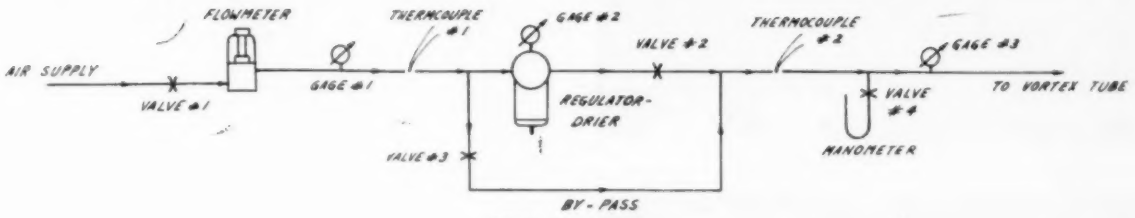

Fig. 7 Flow circuit

tube. This is the so-called uniflow type of vortex tube which heretofore has not been reported upon extensively in the literature. The design of the tube, however, is such that it can be converted easily into a counterflow vortex tube, as demonstrated in Figs. 1 and 2. This is the commonly known Ranque-Hilsch tube.

To cover adequately most of the geometry of flow, the tests were subdivided into flow configurations based on the selected length. Each length is denoted by a letter. The configurations, labelled *A*, *B*, *C*, and so on, are shown in Fig. 11.

Within each geometrical configuration, traverses were obtained for inlet pressures of 10, 20, 30, and so on, psig, maintained by the pressure-regulator valve. Of the measurements gathered, the results for the 10 and 20-psig runs are chosen as representative, and they are reproduced for the greater part in this paper.

Test Procedure. Each run consisted of the following operational procedures: *a*) The valves of the flow circuit, Fig. 7, were cracked open and the inlet valve to the vortex tube adjusted for the desired pressure of the run. *b*) The exit cone was turned all the way in, then backed out fairly slowly until the greatest Ranque-Hilsch effect is obtained and left in that position for the remainder of the run. *c*) After allowing time for steady-state conditions to be reached, the process of traversing the tube was undertaken. Beginning with the probe assembly, Fig. 8, placed in position at station 1, the hypodermic probes for velocity, pressure, and temperature were introduced, one at a time, into the vortex tube and positioned at every tenth of an inch along the radius. The reason for introducing only one probe at a time was to keep the disturbance of the flow field to a minimum. For each radial position of a probe, two readings were taken, one corresponding to the probe on its way from the tube wall to the center of the tube, and the other corresponding to the probe on its way back from the tube center to the tube wall. The two readings were averaged, and this is the value that was recorded as being the probe reading at a given radial position. Since the vortex tube had a radius of 1 in., 20 readings were thus taken per item, and 10 averages were recorded for that item in the table of results. With the existence of the three items of velocity, pressure, and temperature, this meant 60 readings per traverse per station. With 6 stations along the length of the vortex tube, a given run involved no less than 360 readings or a 180 averages to be entered in the tabulation of results. With the additional factors that time had to be allowed for readings to stabilize and ambient conditions to be fairly uniform throughout, it can be seen that it is not easy to make a good run. At that, decent runs, corresponding to inlet pressures of 10, 20, and 30 psig were obtained. The results of the 10-psig run have been plotted in the form of curves in Figs. 12 to 17, and the remainder left in tabular form as Tables 1 and 2 for the sake of economy.

No runs were made above 35 psig because of the large consumption of air and of the noise involved. It should be noted that the readings near the center of the tube and near the wall of the tube were very erratic, and for that reason, neither traverse curves nor traverse data are drawn or given for radial distances less than 0.3 in. or more than 0.9 in.

Axial Velocity. The velocities up to this point represent the magnitude of the velocity vector. The velocity probe, however, can detect direction. It can be rotated 360 deg on its stand, Fig. 8, so that in its position of maximum reading, the direction perpendicular to the hot wire indicates the direction of the

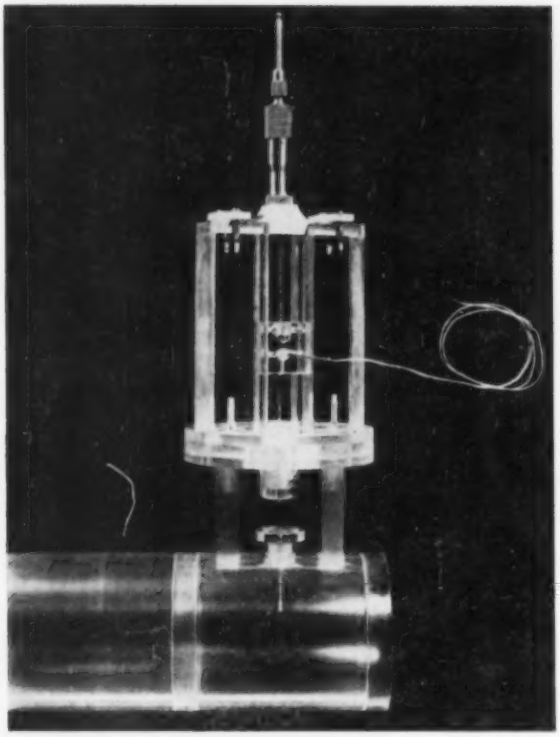

Fig. 8 Probe assembly

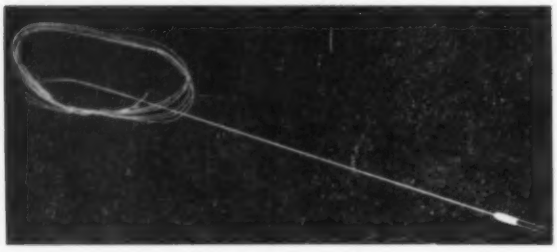

Fig. 9 Velocity probe

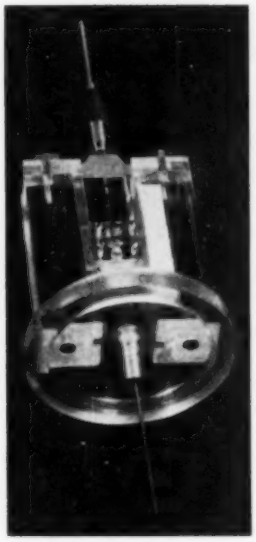

Fig. 10 Temperature and pressure probes

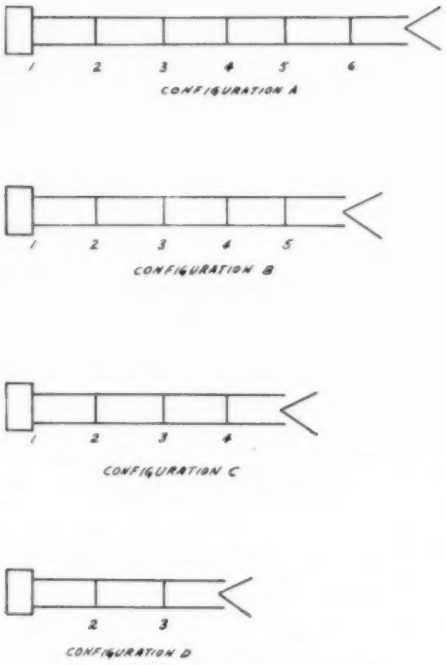

Fig. 11 Test configurations

velocity. With this information, it is possible to resolve velocities into axial and tangential components. Fig. 19 shows the flow angle and the axial-velocity traverses at a typical station; namely, 2.

Traverses at other stations show curves of similar shape, and hence are not drawn. For convenience, the stagger or tangential angle ($90-\alpha$) is plotted, rather than the flow angle itself. Incidentally, it was found that the flow angle is rather independent of changes in inlet pressure over the range of values tested. Fig. 19 also shows that the axial velocities are uniformly small when compared to tangential velocities or to total velocities as cross plotted in Fig. 18. As for distribution, the predominant axial velocities are concentrated in a small annular region near the wall of the vortex tube. The axial velocity falls off sharply toward the center of the tube, and actually indicates a reverse flow near the center. This explains partly how the hot stream travels in one direction, and the cold stream in the other in the case of previous investigations of the vortex tube.

A reasoning concerning the wall friction throws considerable light on the tangential-velocity distribution. Inspection of the data reveals that the tangential or total-velocity peaks do not coincide with the axial-velocity peaks, but are located more toward the center of the tube. This can be explained on the basis that wall friction causes a decrease in both the axial and tangential velocities near the wall as the flow moves along. From continuity considerations, this results in an increase in axial and tangential velocities in regions farther away from the wall. It indicates that some air must move in toward the center as flow progresses down the tube. In so doing, the air tends to conserve its angular momentum, thereby resulting in an increase

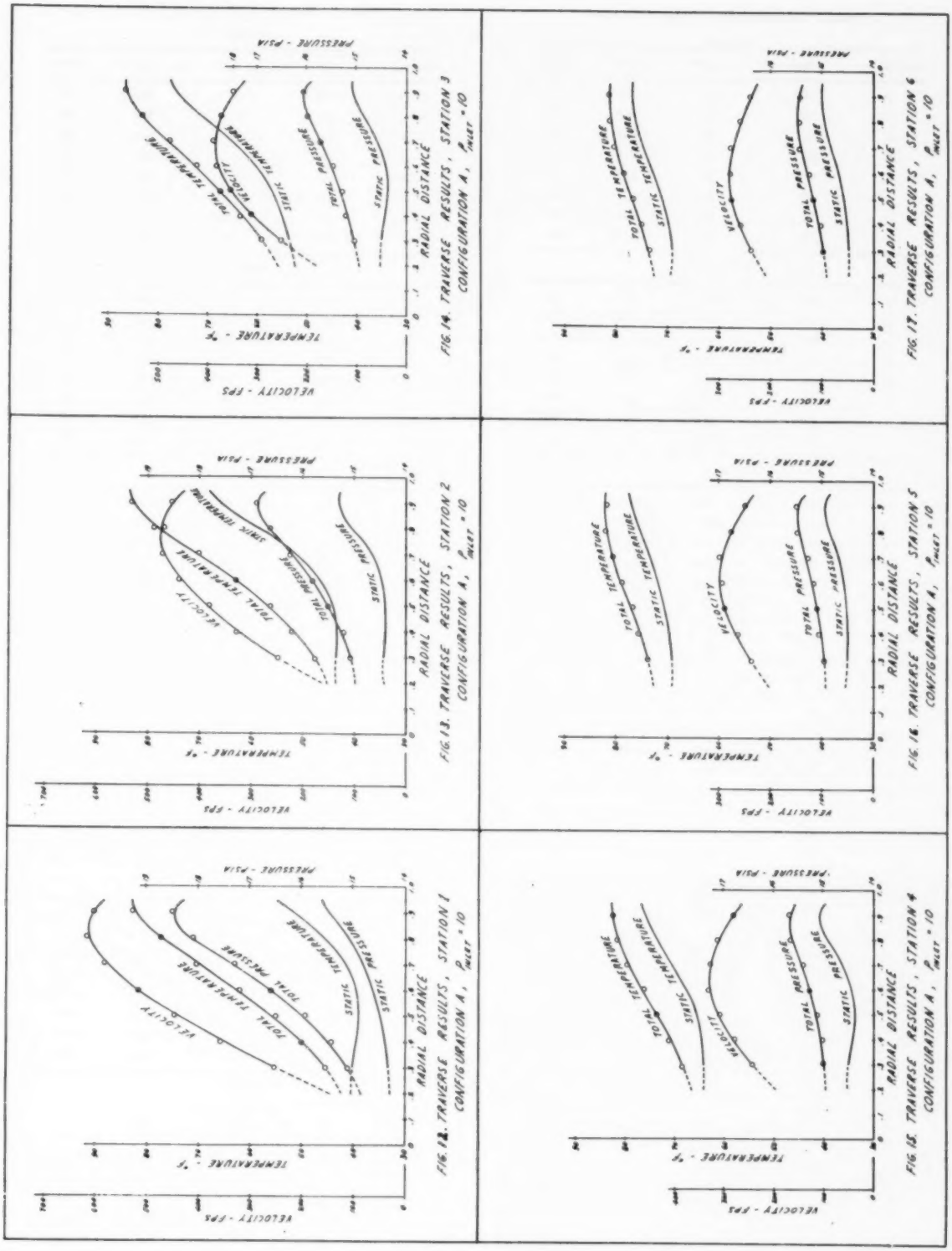

FIG. 12. TRAVERSE RESULTS, STATION 1 CONFIGURATION A, $P_{INLET} = 10$

FIG. 13. TRAVERSE RESULTS, STATION 2 CONFIGURATION A, $P_{INLET} = 10$

FIG. 14. TRAVERSE RESULTS, STATION 3 CONFIGURATION A, $P_{INLET} = 10$

FIG. 15. TRAVERSE RESULTS, STATION 4 CONFIGURATION A, $P_{INLET} = 10$

FIG. 16. TRAVERSE RESULTS, STATION 5 CONFIGURATION A, $P_{INLET} = 10$

FIG. 17. TRAVERSE RESULTS, STATION 6 CONFIGURATION A, $P_{INLET} = 10$

Figs. 12 through 17

Table 1 Traverse data: P_{inlet} = 20 psig

r(inches)	V(fps)	T_T(°F)	p_T(psia)	V_A(fps)
Station 1				
.2	300	8	15.1	45
.3	405	27	14.9	35
.4	505	37	15.3	-8
.5	606	41	18.8	-34
.6	695	55	20.3	10
.7	760	70	21.7	125
.8	795	80	22.4	250
.9	770	84	22.5	293
Station 2				
.2	350	21	15	25
.3	430	29	15.4	-8
.4	510	40	16	-14
.5	580	51	16.9	-10
.6	635	63	17.8	42
.7	660	75	18.8	150
.8	650	82	19.7	254
.9	615	85.5	20	272
Station 3				
.2	375	38.5	15	12
.3	440	43	15.2	-7
.4	495	50.5	15.8	-11
.5	545	58.5	16.4	-8
.6	575	68.5	17	52
.7	590	77	17.7	152
.8	575	82	18.3	233
.9	530	84	18.7	266
Station 4				
.2	410	56	15	3
.3	455	58	15.2	-8
.4	490	63.5	15.7	-9
.5	525	66	16.1	2
.6	540	71.5	16.5	63
.7	540	77.5	17	150
.8	520	88	17.3	208
.9	475	85	17.7	252
Station 5				
.2	405	64.5	15.9	6
.3	445	67	15.1	-2
.4	475	69	15.3	-12
.5	500	72	15.7	-2
.6	520	77	16.1	50
.7	505	80.5	16.5	119
.8	485	83	16.9	206
.9	450	85.5	17.1	212
Station 6				
.2	395	69	14.8	2
.3	430	70	15	-2
.4	465	73.5	15.2	-3
.5	475	73	15.6	2
.6	480	76	15.9	175
.7	480	79	16.3	159
.8	465	82	16.7	200
.9	435	84	16.8	202

Table 2 Traverse data: P_{inlet} = 30 psig

r(inches)	V(fps)	T_T(°F)	p_T(psia)	V_A(fps)
Station 1				
.2	385	-9	16.8	85
.3	435	-3.5	18.4	25
.4	536	7	20.4	-15
.5	675	21	22.6	-32
.6	800	40	25.2	25
.7	877	60	27.8	145
.8	900	78.5	30	275
.9	872	88	30.9	365
Station 2				
.2	430	3	16.5	65
.3	512	10	17.8	10
.4	640	19.5	17.2	-30
.5	750	31	20.8	-15
.6	775	45	22.4	55
.7	790	63	24.2	170
.8	775	79	26.2	285
.9	740	87	27.3	352
Station 3				
.2	450	33	16.4	45
.3	550	37.5	17.5	-4
.4	635	45	18.7	-25
.5	678	53.5	19.9	-10
.6	706	61.5	21.3	65
.7	705	71	22.7	165
.8	681	80.5	24.1	270
.9	638	87	24.6	340
Station 4				
.2	480	52	16.3	35
.3	560	55	17.2	-5
.4	610	60	18.1	-28
.5	660	66	17.1	-8
.6	666	71	20.1	62
.7	655	77	21.4	166
.8	630	83.5	22.5	280
.9	592	86.5	23.1	334
Station 5				
.2	480	60	16.2	25
.3	530	62	16.9	-11
.4	585	66	17.6	-23
.5	615	70	18.4	4
.6	627	74.5	19.3	84
.7	620	80	20.2	175
.8	598	84	21	270
.9	560	86	21.5	330
Station 6				
.2	450	65	16.1	15
.3	535	68	16.6	-18
.4	565	70	17.3	-23
.5	596	73.5	17.9	14
.6	598	76	18.6	80
.7	586	80.5	19.3	160
.8	564	84.5	20	250
.9	530	86	20.3	305

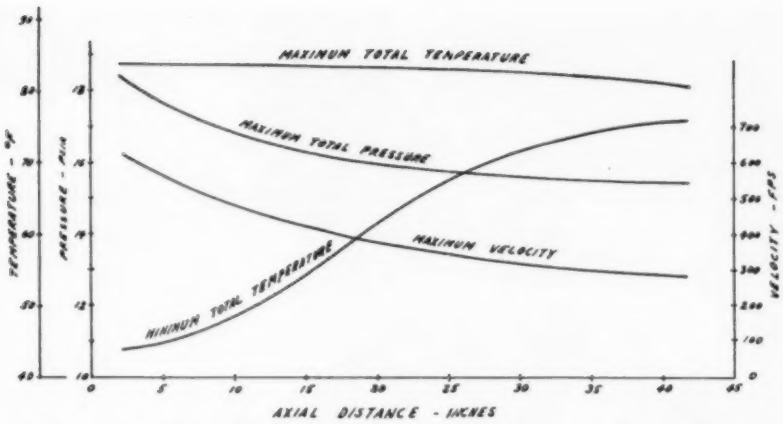

Fig. 18 Axial variation of pressure, temperature, velocity; configuration A, P_{inlet} = 10 psig

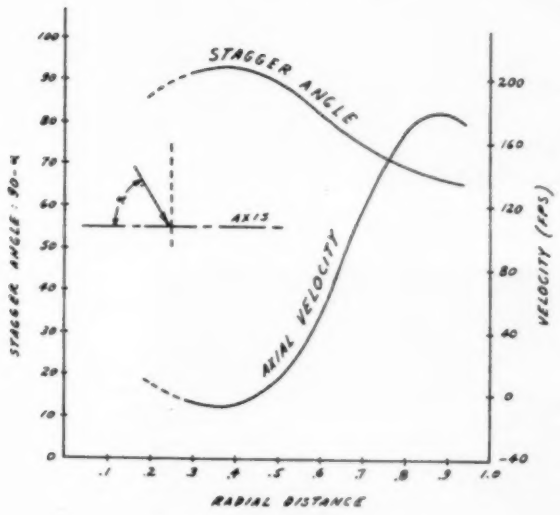

Fig. 19 Flow angle; axial velocity

in angular velocity in those regions farther away from the wall. The tangential velocity, however, drops off at the center of the tube, for as will be shown in Part 2, there is theoretically no flow "in the plane," but only axial flow.

Interrelationship of Internal Data. The experimental study of the vortex tube "from the inside," as is the case in the present investigation, affords some interesting cross checking of data. It was pointed out previously that the plot of axial velocities showed some negative values in the neighborhood of the axis, indicating the existence of a backward flow. This may be verified by considering the pressure relation for circulatory flow:

$$\frac{dp_s}{dr} = \frac{\rho}{r} V_T^2 \qquad (1)$$

Figs. 12 through 18 show an increase in tangential velocities near the center of the tube. Since Equation (1) must be satisfied, it follows that there must be an increase in the pressure differential between the center line and the region immediately away from it as flow progresses down the tube. Now, static-pressure measurements along the center line itself showed fairly constant values along the length of the vortex tube. Therefore, the static pressure in the neighborhood of the center line must increase from station 1 to station 6. Such a pressure gradient explains the tendency for backward flow near the center of the tube, especially in the case of the counterflow vortex tube [16, 25].

Nor is the foregoing the only case of data cross checking. The axial-velocity distribution may be used in conjunction with the local values of the density to determine by integration, the mass rate of flow down the tube. This mass rate can then be compared with the mass rate obtained from the flowmeter. Similarly, an energy balance may be performed by taking the product of the meter flow rate, the specific heat, and the inlet temperature, and comparing with the integrated energy flow at various cross sections along the tube length. This was done on several occasions, and the results agreed well enough within experimental limits. This is one of the many advantages occurring from the "internal" approach to the study of the vortex tube.

Flow Visualization. Construction of a vortex tube of lucite afforded good opportunity for the study of flow patterns by means of visual methods. Accordingly, a smoke chamber was first constructed and connected to the inlet hose. The injected smoke showed up well at low speeds, but at moderate or high speeds it became invisible. Also, there was considerable difficulty in getting the smoke into the vortex-tube center block. The pressure in the smoke chamber being low compared to the

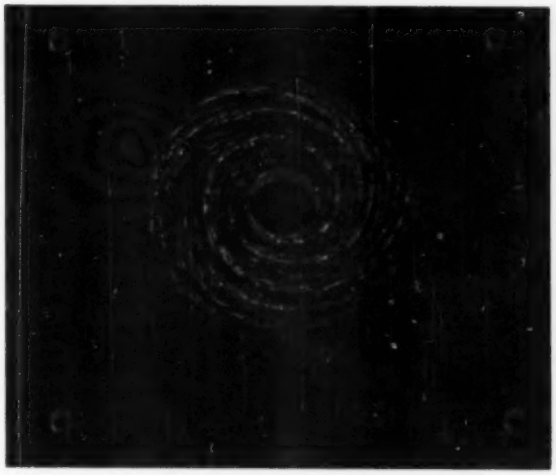

Fig. 20 Flow pattern upon entry

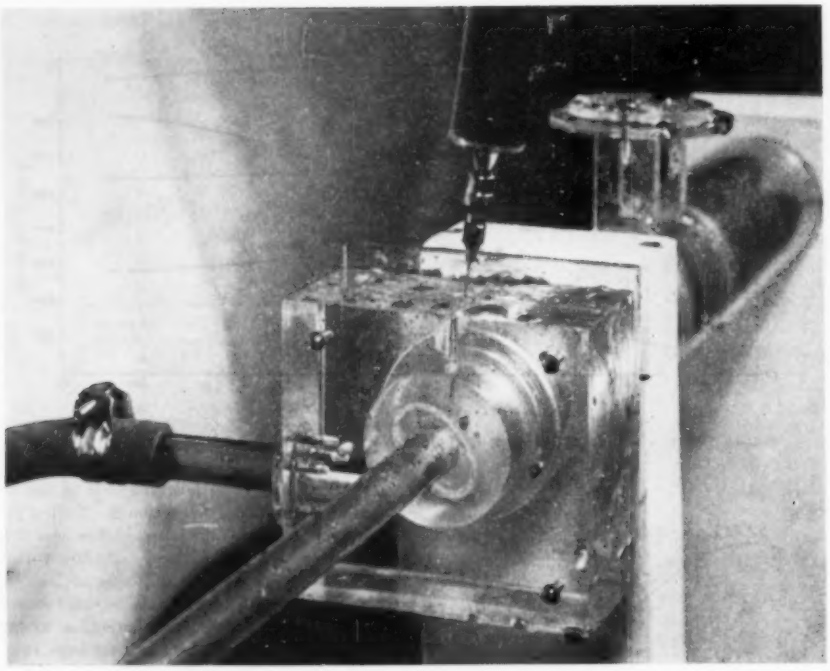

Fig. 21 Limit circle-counterflow vortex tube

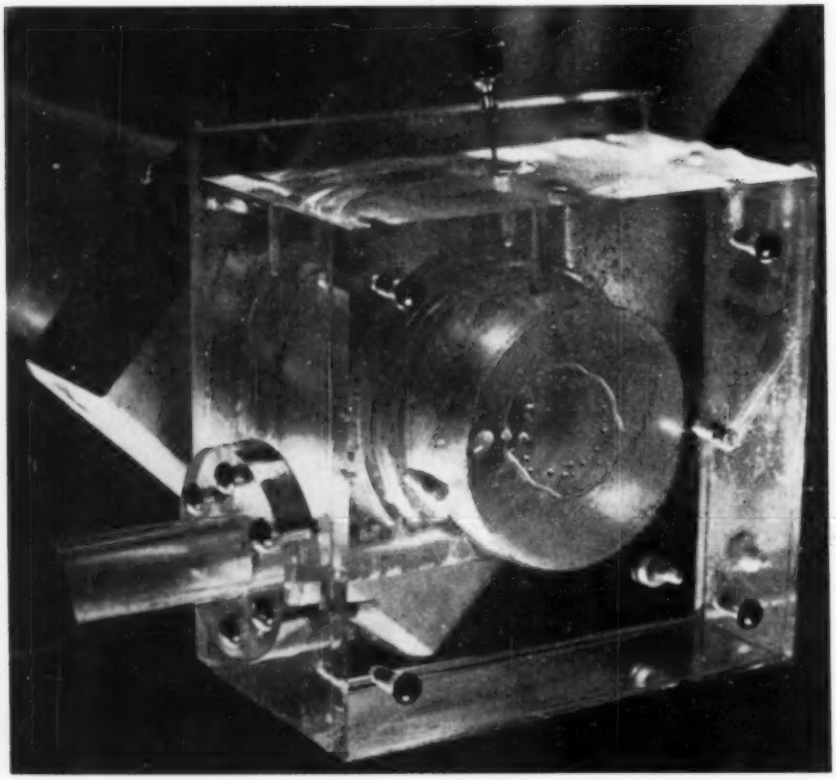

Fig. 22 Limit circle-water injection

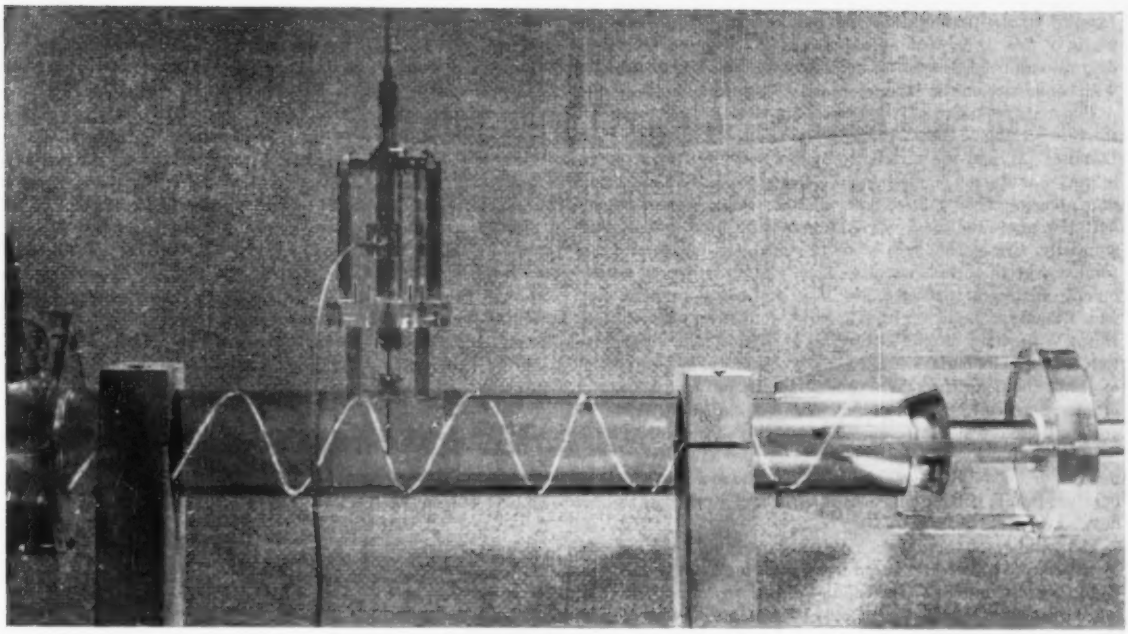

Fig. 23 Envelope streamline

air-supply pressure and to the vortex-tube pressure, the smoke had a tendency to flow out of the tube rather than into the tube.

After smoke, balsa sawdust was tried but it did not show up well at high speeds; also, it covered everything in the vicinity with a coat of dust. Next, fine confetti was tried, with a laundry bag covering the vortex-tube exit cone to prevent the confetti from spreading to the adjacent laboratory space. It worked well for short bursts of speeds, but then the confetti, in rubbing against the lucite, developed static electricity, and it simply clung to the walls of the tube to no avail.

The final and most successful method of flow visualization was the injection of clear or colored water into the vortex tube. The injections were made by means of a horse syringe, and clear water was first used, because it kept the installation clean. Later on, for the sake of taking photographs, colored liquid and milk were used. This entailed washing and cleaning the entire installation after an injection, however, it was not too high a price to pay for the acquisition of good photographs. Fig. 20 shows the flow pattern immediately after entry into the vortex tube. The circle in the field of flow is the limit circle, and represents the inner boundary of the vortex flow. Its existence is a characteristic of compressible flow, and its theory will be developed in Part 2 of this paper. Fig. 21 shows the same condition, but for the case of the counterflow vortex tube. These are interesting pictures, for the existence of limit circles (circles beyond which the flow does not penetrate) has not been discussed in previous investigations. Fig. 22 shows another example of limit line in plane flow. However, it was obtained by injecting a trace of clear water, and it represents one of the few cases where a "clear" trace photographed well.

Fig. 23 shows a streamline in three-dimensional flow. It was obtained by means of clear liquid, but using a short configuration; namely, configuration *D*. A similar streamline in space, but using a longer configuration will be shown in Part 2, where it is included to correlate the theoretical study with some of the experimental results.

Conclusions

While the interpretation of results is deferred to Part 2 of the paper, the conclusions gathered from the experimental study may be stated as follows:

1 Although it is difficult to take measurements inside a vortex tube, traverses are possible if a big enough tube is designed.

2 Hypodermic probes are ideally suited for the purpose of taking measurements inside the tube, but probes must be used separately so as not to disturb the flow. This, however, means numerous changes during a particular run and makes the experimental work tedious.

3 It is hoped that future investigators will design a multipurpose probe, which can be used to measure temperature, pressure, and velocity without interchanges, and yet be small enough not to alter the flow field.

4 Flow visualization is possible by means of liquid injection. An envelope streamline may be obtained by liquid injection, but other streamlines are difficult to obtain either by liquid injection or smoke injection. Liquid injection shows that vortex-sink flow is formed in the entry block rather than farther down the tube.

5 Results of the experimental study are in general agreement with past experimental work that has been done in this field; however, no claim is made that the study is exhaustive. Further work, both experimental and analytical, will add much to the understanding of vorticity temperature separation.

DISCUSSION

Frank Kreith[3]

The experimental phase of this investigation on the separation of a gas stream into regions of high and low stagnation temperatures adds valuable data on the macroscopic characteristics of a uniflow vortex tube. Those interested in phenomena related to energy separation in vortex-type flows are undoubtedly looking

[3] University of Colorado, Boulder, Colo. Mem. ASME.

forward to the presentation and publication of the theoretical phase of this work without which it is difficult to evaluate the over-all significance of the author's contribution, and to comment with confidence on the experimental data presented in this paper.

The macroscopic mechanism of energy transfer has been qualitatively explained by Schultz-Grunow [1],[4] Fulton [2], Van Deemter [3], and most recently by Deissler [4]. Since, except at very low Reynolds numbers, the energy separation in laminar flow appears to be quite small, interest is focused on turbulent flow where the energy separation may be appreciable. Substantially, two mechanisms seem to control the distribution of total energy in turbulent vortex flow. There is first of all turbulent mixing in the presence of a centrifugal pressure field which tends to build up an adiabatic temperature distribution. But near the inlet nozzle, as a result of friction forces acting between faster moving gas in the center and slower moving layers of gas at the periphery, there occurs radially outward a transfer of energy as work. The internal energy in the outer region increases therefore at the expense of the energy stored in the inner core. Simultaneously, however, the inner core is heated by conductive and convective heat transfer. In other words, the temperature profile is determined by the ratio of work flux to heat flux.

The validity of this model can, of course, only be established by comparing predictions based upon it with experimental data. Unfortunately, in order to calculate the temperature distribution it is necessary to make additional assumptions and simplifications. One must, first of all, assume a velocity profile which for turbulent vortex flow can only be based on very scant experimental evidence. These data are indeed a welcome addition here. But in addition to the velocity profile one must also postulate some sort of model of the turbulent heat-transfer mechanism in the presence of a centrifugal force field. As shown in reference [5] there are at least three transferable properties which can be used to evaluate a coefficient of eddy conductivity. The most useful of them appears to be the so-called forced vortex parameter. But even if one accepts the forced vortex parameter and neglects the peculiarities of boundary layers in swirling flow [6], there still remain a number of puzzling effects, such as the qualitative difference in behavior between compressible and incompressible flows in a diabatic vortex flow [7], which can only be partially explained in terms of existing information on the energy transfer in vortex flow. It seems therefore important to supplement the author's macroscopic measurements of time average values of pressure, temperature, and velocity distributions, by measurements of the fluctuations of these quantities. In particular, a knowledge of the effect of swirling on the radial velocity fluctuations would be imperative for a more complete analysis of the energy-transfer mechanism. The approach used by Yeh [6] and Einstein and Li [8] may be applicable and should be explored further.

[4] Numbers in brackets designate References at end of discussion.

References

1 F. Schultz-Grunow, "Turbulenter Wärmedurchgang im Zentrifugalfeld," *Forsch. Ing. Wes.*, vol. 17, no. 3, 1951, pp. 66–76.

2 C. D. Fulton, "Ranque's Tube," *Refrigeration Engineering*, vol. 58, 1950, pp. 473–479.

3 J. J. van Deemter, "On the Theory of the Ranque-Hilsch Cooling Effect," *Applied Scientific Research*, Netherlands, sec. A, vol. 3, 1952, pp. 174–196.

4 R. G. Deissler and M. Perlmutter, "An Analysis of the Energy Separation in Laminar and Turbulent Compressible Vortex Flow," Heat Transfer and Fluid Mechanics Institute, Stanford University Press, 1958.

5 F. Kreith, "The Influence of Curvature on Heat Transfer to Incompressible Fluids," TRANS. ASME, vol. 77, 1955, pp. 1247–1256.

6 H. Yeh, "Boundary Layer Along Annular Walls in a Swirling Flow," TRANS. ASME, vol. 80, 1958, pp. 767–776.

7 F. Kreith and D. Margolis, "Heat Transfer and Friction in Swirling Turbulent Flow," Heat Transfer and Fluid Mechanics Institute, Stanford University Press, 1958.

8 M. A. Einstein and M. Li, "Steady Vortex Flow in a Real Fluid," Heat Transfer and Fluid Mechanics Institute, Stanford University Press, 1951.

An Experimental and Analytical Study of Vortex-Flow Temperature Separation by Superposition of Spiral and Axial Flow Part 2[1]

J. E. LAY

Associate Professor, Mechanical Engineering Department, Michigan State University, East Lansing, Mich. Assoc. Mem. ASME

Part 2 reports on the analytical study. The free vortex motion of the gas upon entrance to the tube is mathematically superposed to a compressible sink to give a spiral flow in the plane. The characteristic existence of limit circles is corroborated by the experimental flow visualization. The solution in space is obtained by addition of a uniform axial velocity to the spiral flow. When viscosity effects are considered, the free vortex is shown to change into a forced vortex. The latter flow is one of minimum kinetic energy and maximum entropy. Energy considerations enable the determination of an optimum cold air radius to give largest stagnation temperature separation. Significantly, this was the radius that gave best performance in the experimental program.

Introduction

PART 1 reported on the experimental study of the vortex effect, and presented the test results. Part 2, which is the present paper, reports on the analytical study, and presents a mathematical solution for the differential equations governing the flow in the vortex tube. For greater understanding, it is recommended that Part 2 be kept in mind when reading the present paper.

Analytical Study

Consider the flow of air upon its entrance into the vortex tube. Its motion is as shown in Fig. 1. The analytical treatment of the problem of solving the flow equations will proceed along the following line of thought: The intrinsic equations of compressible-fluid flow, if tackled head-on in their general form, namely, three-dimensional, with viscosity effects included, involve mathematical difficulties which prevent a direct solution. It is, therefore, only natural that simpler solutions be sought from simpler models of flow, and by superposing the individual solutions, to arrive at the general solution. Using Prandtl's concept of boundary layer, it is possible to initially ignore friction in the flow field outside the boundary layer, and to achieve exact solution based on potential flow.

Free Vortex. Consider a perfect fluid moving in a circular path with no external torque applied:

$$T = m \frac{d}{dt} (rv) = 0 \tag{1}$$

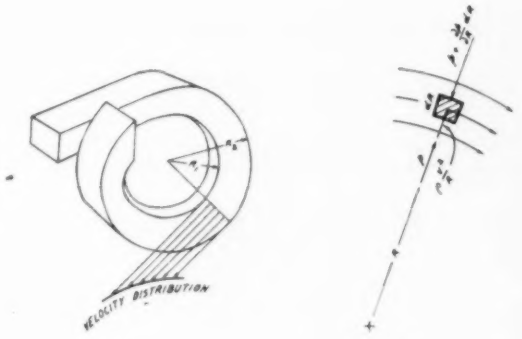

Fig. 1 Flow in circular path

[1] Part 1 was presented at the ASME Semi-Annual Meeting, Detroit, Mich., June 15–19, 1958. It reported on the experimental study as based on work done at the University of Michigan. Part 2 reports on the analytical study.

Contributed by the Heat Transfer Division and presented at the Annual Meeting, New York, N. Y., November 30–December 5, 1958, of THE AMERICAN SOCIETY OF MECHANICAL ENGINEERS.

NOTE: Statements and opinions advanced in papers are to be understood as individual expressions of their authors and not those of the Society. Manuscript received at ASME Headquarters, August 7, 1958. Paper No. 58—A-90.

Nomenclature

A = area
K = constant in irrotational flow
M = Mach number
Q = strength of source or sink
R = gas constant
S = entropy
T = absolute temperature
c = speed of sound
m = mass
p = pressure
q = velocity in hodograph plane
r = radial distance
t = time
u, v, w = components of velocity in physical plane
x, y, z = co-ordinate axes
γ = ratio of specific heats
Γ = circulation
θ = velocity angle in hodograph plane
ρ = density
ϕ = velocity potential
ψ = streamline function

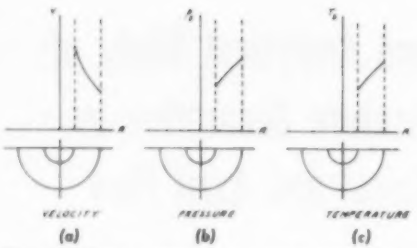

Fig. 2 Velocity, pressure, temperature distribution for free vortex

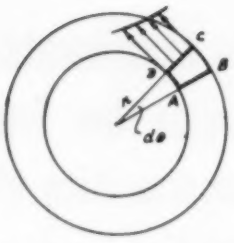

Fig. 3 Circulation for free vortex

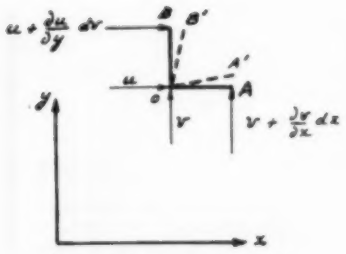

Fig. 4 Fluid rotation at a point

Integration of Equation (1) gives

$$rv = K; \qquad v = \frac{K}{r} \tag{2}$$

Equation (2) is characteristic of a free or potential vortex. The velocity distribution is of the hyperbolic type shown in Fig. 2(*a*). The pressure distribution is determined by considering the force balance in Fig. 1(*b*). The centrifugal force on the fluid element is balanced by the resultant force due to pressure; neglecting infinitesimals of higher order than the first, the force balance in the radial direction is

$$(dp)(dA) = \frac{v^2}{r}(dm) = \frac{v^2}{r}(\rho dr dA)$$

or

$$dp = \frac{v^2}{r^2}\rho dr \tag{3}$$

Substitution of Equation (2) into Equation (3) gives

$$dp = \rho K^2 \frac{dr}{r^3} \tag{4}$$

For a perfect gas, $\rho = \frac{p}{RT}$, and Equation (4) becomes

$$\frac{dp}{p} = \frac{K^2}{RT}\frac{dr}{r^3} \tag{5}$$

To integrate Equation (5), use is made of the fact that the total energy in a stream tube is equal to that in any other stream tube:

$$c_p T + \frac{V^2}{2} = c_p T + \frac{K^2}{2r^2} = c_p T_0 \tag{6}$$

or

$$T = T_0 - \frac{K^2}{2c_p r^2} \tag{7}$$

Replacing T by this value, Equation (5) becomes

$$\frac{dp}{p} = \frac{K^2}{r}\frac{1}{T_0 - \dfrac{K^2}{2c_p r^2}}\frac{dr}{r^3} = \frac{2c_p K^2 dr}{R(2c_p r^2 T_0 - K^2)r}$$

which is integrable by use of partial fractions, and yields a pressure distribution of the form shown in Fig. 2(*b*). As for the temperature distribution, it is obtained very simply from Equation (6), which yields

$$T_2 - T_1 = \frac{K^2}{2c_p}\left[\frac{1}{r_1^2} - \frac{1}{r_2^2}\right] \tag{8}$$

and is shown in Fig. 2(*c*).

Circulation for Free Vortex. The potential, or free vortex just described, is a two-dimensional motion in which the streamlines are concentric circles, with the velocity along any streamline being inversely proportional to the radius. Referring to Fig. 3, the circulation, which is the sum of the products of elements $\overrightarrow{dl}$ of a curve drawn in the plane of flow, and the corresponding component of velocity tangent to the curve, is

$$\Gamma = \oint \vec{v} \cdot \overrightarrow{dl} \tag{9}$$

where $\vec{v}$ is the velocity. For a closed curve such as A-B-C-D, and noting that the line integral is zero along the sides AB and CD, the circulation is

$$\Gamma = (v + dv)(r + dr)d\theta - vrd\theta = d(vr)d\theta = 0 \tag{10}$$

since $vr = K$ from Equation (2). The circulation for an element of area not enclosing the origin is thus zero. This result can be generalized to a finite area, since the line integral around the boundary curve of the finite area is the algebraic sum of all the line integrals around the elements of area comprising the finite area.

The circulation is related to the fluid rotation in the manner shown in Fig. 4. Let the fluid rotation at a point be defined as the mean angular velocity of two mutually perpendicular fluid lines OA and OB drawn through P. During an infinitesimal time dt, OA rotates to OA′, and the vertical displacement is

$$AA' = \frac{\partial v}{\partial x} dx dt$$

The angle AOA′, positive when measured counterclockwise, is then

$$\sphericalangle AOA' = \frac{\partial v}{\partial x} dt$$

and its time rate of change or angular velocity is thus $\frac{\partial v}{\partial x}$. Similarly, the angular velocity of the fluid line OB is $-\frac{\partial u}{\partial y}$, so that the average rotation of the fluid element is

$$\omega = \frac{1}{2}\left(\frac{\partial v}{\partial x} - \frac{\partial u}{\partial y}\right) \tag{11}$$

Now, the circulation, as defined by Equation (9), may be expressed in terms of the velocity components u, v, as

$$\Gamma = \oint (udx + vdy) \tag{12}$$

and this may be transformed by means of Green's Theorem to a surface integral as

$$\Gamma = \oint (udx + vdy) = \oint_A \left(\frac{\partial v}{\partial x} - \frac{\partial u}{\partial y}\right) dx dy \tag{13}$$

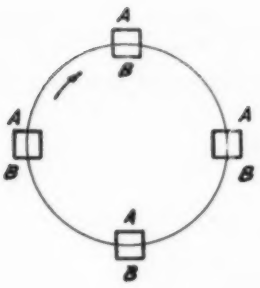

Fig. 5 Motion of fluid particle upon entrance to vortex tube

Since the circulation for the free vortex, as given by Equation (10), is zero, Equation (13) yields

$$\Gamma = 0 = \oint_A \left(\frac{\partial v}{\partial x} - \frac{\partial u}{\partial y} \right) dxdy; \qquad A = \text{arbitrary}$$

or

$$\frac{\partial v}{\partial x} - \frac{\partial u}{\partial y} = 0 \tag{14}$$

Comparing Equations (11) and (14), it is seen that the fluid rotation at any arbitrary point upon entrance into the vortex tube is zero. In other words, the motion of fluid particles upon entrance to the vortex tube is as shown in Fig. 5, and the flow is potential. An exact solution for the flow pattern may therefore be expected.

Potential Equation. The problem of determining the flow pattern for the vortex tube is solved by developing a differential equation of flow in terms of the velocity potential or the stream function which turns out to be linear. With the assumption of irrotational motion, the circulation, as calculated by Equation (10), is zero, and from this it follows that the line integral of the velocity between any two points of the flow field depends solely on the location of the points. Thus, $\vec{v} \cdot \vec{dl}$ is the exact differential of a quantity ϕ such that in Cartesian co-ordinates

$$v \cdot \vec{dl} = d\phi \tag{15}$$

$$\begin{cases} u = \dfrac{\partial \phi}{\partial x} & (16) \\ v = \dfrac{\partial \phi}{\partial x} & (17) \end{cases}$$

where u and v are the x and y components of the velocity. The equation of continuity,

$$\frac{\partial(\rho u)}{\partial x} + \frac{\partial(\rho v)}{\partial y} = 0$$

may then be written with the aid of Equations (16) and (17) as

$$\frac{\partial}{\partial x}(\rho\phi_x) + \frac{\partial}{\partial y}(\rho\phi_y) = \rho(\phi_{xx} + \phi_{yy}) + \phi_x\rho_x + \phi_y\rho_y = 0 \tag{18}$$

Euler's equation,

$$-\frac{1}{\rho}\left[\frac{\partial p}{\partial x}\, dx + \frac{\partial p}{\partial y}\, dy \right] = d\left(\frac{u^2 + v^2}{2} \right) \tag{19}$$

becomes, in terms of the velocity potential,

$$dp = -\rho d\left(\frac{u^2 + v^2}{2} \right) = -\rho d\left(\frac{\phi_x^2 + \phi_y^2}{2} \right) \tag{20}$$

and this, with the expression for the velocity of sound $c^2 = \dfrac{dp}{d\rho}$, may be rewritten as

$$d\rho = -\frac{\rho}{c^2}\, d\left(\frac{\phi_x^2 + \phi_y^2}{2} \right)$$

from which

$$\rho_x = -\frac{\rho}{c^2}(\phi_x\phi_{xx} + \phi_y\phi_{xy}) \tag{21}$$

$$\rho_y = -\frac{\rho}{c^2}(\phi_x\phi_{xy} + \phi_y\phi_{yy}) \tag{22}$$

Substitution of Equations (21) and (22) into Equation (18) gives

$$\rho(\phi_{xx} + \phi_{yy}) - \frac{\rho}{c^2}\phi_x(\phi_x\phi_{xx} + \phi_y\phi_{xy}) - \frac{\rho}{c^2}\phi_y(\phi_x\phi_{xy} + \phi_y\phi_{yy}) = 0$$

or, upon simplification,

$$\left(1 - \frac{\phi_x^2}{c^2}\right)\phi_{xx} + \left(1 - \frac{\phi_y^2}{c^2}\right)\phi_{yy} - \frac{2}{c^2}\phi_x\phi_y\phi_{xy} = 0 \tag{23}$$

Equation (23) is the potential equation in terms of the velocity potential ϕ; however, it is not linear, and will have to be transformed later into an equation which is linear.

Stream Function Equation. Just as the condition of free vortex flow led to the existence of a potential function ϕ, so can the equation of continuity be satisfied by the introduction of a stream function ψ. This is because the equation of continuity

$$\frac{\partial}{\partial x}(\rho u) + \frac{\partial}{\partial y}(\rho v) = 0$$

is satisfied if

$$\rho u = \frac{\partial \psi}{\partial y} \tag{24}$$

$$\rho u = -\frac{\partial \psi}{\partial x} \tag{25}$$

where $\psi(x, y)$ is a point function. For, the order of differentiation being immaterial,

$$\frac{\partial^2 \psi}{\partial x \partial y} - \frac{\partial^2 \psi}{\partial y \partial x} = 0 \tag{26}$$

and it is obvious that Equation (26) satisfies the continuity equation. Equations (24) and (25) define the stream function, but it is more convenient to alter them into

$$u = \frac{\rho_0}{\rho}\frac{\partial \psi}{\partial y} = \frac{\rho_0}{\rho}\psi_y \tag{27}$$

$$v = -\frac{\rho_0}{\rho}\frac{\partial \psi}{\partial x} = -\frac{\rho_0}{\rho}\psi_x \tag{28}$$

where ρ_0 is the stagnation density. The magnitude of the velocity at any point then becomes

$$q^2 = u^2 + v^2 = \left(\frac{\rho_0}{\rho}\right)^2 (\psi_x^2 + \psi_y^2)$$

Just as a differential equation of flow was developed in terms of the velocity potential, so will a differential equation be developed in terms of the stream function. First, the equation of continuity is automatically satisfied with the introduction of the function ψ,

$$\frac{\partial}{\partial x}(\rho u) + \frac{\partial}{\partial y}(\rho v) = \rho_0\left(\frac{\partial^2\psi}{\partial x\partial y} - \frac{\partial^2\psi}{\partial y\partial x}\right) = 0 \qquad (29)$$

Second, the condition of irrotationality

$$\frac{\partial u}{\partial y} - \frac{\partial v}{\partial x} = 0 = \frac{\partial}{\partial y}\left(\frac{\rho_0}{\rho}\frac{\partial\psi}{\partial y}\right) - \frac{\partial}{\partial x}\left(-\frac{\rho_0}{\rho}\frac{\partial\psi}{\partial x}\right)$$

becomes, after differentiation and rearrangement,

$$\rho(\psi_{xx} + \psi_{yy}) - \left(\psi_x\frac{\partial\rho}{\partial x} + \psi_y\frac{\partial\rho}{\partial y}\right) = 0 \qquad (30)$$

Third, Euler's equation,

$$\frac{dp}{\rho} + d\left(\frac{u^2 + v^2}{2}\right) = 0$$

and the expression for the velocity of sound, $c^2 = \frac{dp}{d\rho}$, yield, upon elimination of dp:

$$d\rho = -\frac{\rho}{2c^2}d(u^2 + v^2) = -\frac{\rho}{2c^2}d\left[\left(\frac{\rho_0}{\rho}\right)^2\psi_y^2 + \left(\frac{\rho_0}{\rho}\right)^2\psi_x^2\right]$$

$$= -\frac{\rho}{c^2}\left[\left(\frac{\rho_0}{\rho}\right)^2(\psi_x d\psi_x + \psi_y d\psi_y) - (\psi_x^2 + \psi_y^2)\left(\frac{\rho_0}{\rho}\right)\frac{d\rho}{\rho}\right] \qquad (31)$$

Equation (31) enables the formation of the partial derivatives ρ_x and ρ_y, which upon substitution into Equation (30) results in

$$\left[1 - \frac{1}{c^2}\left(\frac{\rho_0}{\rho}\right)^2\psi_y^2\right]\psi_{xx} + \left[1 - \frac{1}{c^2}\left(\frac{\rho_0}{\rho}\right)^2\psi_x^2\right]\psi_{yy} + \frac{2}{c^2}\left(\frac{\rho_0}{\rho}\right)^2\psi_x\psi_y\psi_{xy} = 0 \qquad (32)$$

Equation (32), along with the relations between local and stagnation quantities

$$c^2 = c_0^2 - \frac{\gamma - 1}{2}\left(\frac{\rho_0}{\rho}\right)^2(\psi_x^2 + \psi_y^2) \qquad (33)$$

$$\frac{\rho_0}{\rho} = \left[1 + \frac{\gamma - 1}{2}\left(\frac{\rho_0}{\rho}\right)^2\frac{\psi_x^2 + \psi_y^2}{c^2}\right]^{(1/\gamma - 1)} \qquad (34)$$

completely determines the flow field. It will be solved by means of a transformation.

Hodograph Transformation. The exact solution applies to that region of flow outside the boundary layer. By excluding the latter from the flow field, the behavior of the fluid becomes irrotational, and it is then possible to use superposition to obtain the general solution. Having obtained Equations (23) and (32), what technique may be employed for their solution? Mathematically speaking, Equations (23) and (32) are nonlinear, and there is consequently no direct solution. The situation, however, is not as hopeless as it seems. The equations are in terms of only two space variables, and for this condition, they are amenable to exact solution by means of the following transformation.

Let x and y be the co-ordinates of the physical or actual flow plane, and q and θ be the polar co-ordinates of a velocity or hodograph plane. Then

$$u = q\cos\theta = \frac{\partial\phi}{\partial x} \qquad (35)$$

$$v = q\sin\theta = \frac{\partial\phi}{\partial y} \qquad (36)$$

and the defining equations for velocity potential and stream function:

$$\begin{cases} u = \dfrac{\rho_0}{\rho}\psi_y \\ v = -\dfrac{\rho_0}{\rho}\psi_x \end{cases} \qquad (37)$$

give, upon differentiation with respect to x and y,

$$d\phi = udx + vdy = q(\cos\theta dn + \sin\theta dy)$$

$$d\psi = -\frac{\rho}{\rho_0}vdx + \frac{\rho}{\rho_0}udy = \frac{\rho}{\rho_0}q(-\sin\theta dx + \cos\theta dy)$$

whereupon

$$dx = \frac{\cos\theta}{q}d\phi - \frac{\rho_0}{\rho}\frac{\sin\phi}{q}d\psi \qquad (38)$$

$$dy = \frac{\sin\theta}{q}d\phi + \frac{\rho_0}{\rho}\frac{\cos\theta}{q}d\psi \qquad (39)$$

Now, considering ϕ and ψ as functions of q and θ, the following may be written

$$d\phi = \frac{\partial\phi}{\partial q}dq + \frac{\partial\phi}{\partial\theta}d\theta \qquad (40)$$

$$d\psi = \frac{\partial\psi}{\partial q}dq + \frac{\partial\psi}{\partial\theta}d\theta \qquad (41)$$

Substitution of Equations (40) and (41) into (38) and (39) gives

$$dx = \frac{\cos\theta}{q}\left(\frac{\partial\phi}{\partial q}dq + \frac{\partial\phi}{\partial\theta}d\theta\right) - \frac{\rho_0}{\rho}\frac{\sin\theta}{q}\left(\frac{\partial\psi}{\partial q}dq + \frac{\partial\psi}{\partial\theta}\right)d\theta$$

which, upon simplification, becomes

$$dx = \left(\frac{\cos\theta}{q}\phi_q - \frac{\rho_0}{\rho}\frac{\sin\theta}{q}\psi_q\right)dq + \left(\frac{\cos\theta}{q}\phi_\theta - \frac{\rho_0}{\rho}\frac{\sin\theta}{q}\psi_\theta\right)d\theta \qquad (42)$$

Similarly, there is obtained

$$dy = \left(\frac{\sin\theta}{q}\phi_q + \frac{\rho_0}{\rho}\frac{\cos\theta}{q}\psi_q\right)dq + \left(\frac{\sin\theta}{q}\phi_\theta + \frac{\rho_0}{\rho}\frac{\cos\theta}{q}\psi_\theta\right)d\theta \qquad (43)$$

Equations (42) and (43) give

$$x_q = \frac{\cos\theta}{q}\phi_q - \frac{\rho_0}{\rho}\frac{\sin\theta}{q}\psi_q; \qquad x_\theta = \frac{\cos\theta}{q}\phi_\theta - \frac{\rho_0}{\rho}\frac{\sin\theta}{q}\psi_\theta$$

$$y_q = \frac{\sin\theta}{q}\phi_q + \frac{\rho_0}{\rho}\frac{\cos\theta}{q}\psi_q; \qquad y_\theta = \frac{\sin\theta}{q}\phi_\theta + \frac{\rho_0}{\rho}\frac{\cos\theta}{q}\psi_\theta$$

The objective is to obtain ϕ and ψ in terms of q and θ. To this end, x and y are eliminated in the foregoing equation by making use of the independence of order in partial differentiation. The result is

$$-\frac{\sin\theta}{q}\phi_q - \frac{\rho_0}{\rho}\frac{\cos\theta}{q}\psi_q = \frac{\cos\theta}{q^2}\phi_\theta + \frac{\rho_0}{\rho}\frac{\sin\theta}{q^2}\psi_\theta - \frac{\sin\theta}{q}\left[\frac{d}{dq}\left(\frac{\rho_0}{\rho}\right)\right]\psi_\theta \quad (44)$$

$$\frac{\cos\theta}{q}\phi_q - \frac{\rho_0}{\rho}\frac{\sin\theta}{q}\psi_q = -\frac{\sin\theta}{q}\phi_\theta - \frac{\rho_0}{\rho}\frac{\cos\theta}{q^2}\psi_\theta + \frac{\cos\theta}{q}\left[\frac{d}{dq}\left(\frac{\rho_0}{\rho}\right)\right]\psi_\theta \quad (45)$$

Multiplying Equation (44) by $\sin\theta$, Equation (45) by $\cos\theta$, and subtracting gives

$$\phi_q = q\left[\frac{d}{dq}\left(\frac{1}{q}\frac{\rho_0}{\rho}\right)\right]\psi_\theta \quad (46)$$

Similarly, multiplying Equation (45) by $\cos\theta$, Equation (46) by $\sin\theta$, and adding gives

$$\phi_\theta = \frac{\rho_0}{\rho}q\psi_q \quad (47)$$

Equations (46) and (47) are the compressible-flow equivalents of the classical Cauchy-Rieman equations of incompressible flow.

Next, using Euler's equation: $\frac{dp}{\rho} + qdq = 0$, and the expression for the speed of sound: $c^2 = \frac{dp}{d\rho}$, there is obtained

$$\frac{d}{dq}\left(\frac{\rho_0}{\rho}\right) = -\frac{\rho_0}{\rho}\frac{d\rho}{dq} = -\frac{\rho_0}{\rho}\frac{d\rho}{dp}\frac{dp}{dq} = -\frac{\rho_0}{\rho}\left(\frac{1}{c^2}\right)(-\rho q) = \frac{\rho_0}{\rho}\frac{q}{c^2} \quad (48)$$

which, substituted into Equation (46) gives

$$\phi_q = -\frac{\rho_0}{\rho}\frac{1}{q}\left(1 - \frac{q^2}{c^2}\right)\psi_\theta = -\frac{\rho_0}{\rho}\frac{1}{q}(1 - \mathbf{M}^2)\psi_\theta \quad (49)$$

Finally, eliminating ϕ from this latter equation and Equation (47) by setting $\phi_{q\theta} = \phi_{\theta q}$, and making use of Equation (48) gives

$$\phi_{\theta q} = -\frac{\rho_0}{\rho}\frac{1}{q}(1 - \mathbf{M}^2)\psi_{\theta\theta} = \phi_{q\theta} = \frac{\rho_0}{\rho}(q\psi_{qq} + \psi_q) + q\psi\left(\frac{\rho_0}{\rho}\frac{q}{c^2}\right)$$

or, upon simplification,

$$q^2\psi_{qq} + q(1 + \mathbf{M}^2)\psi_q + (1 - \mathbf{M}^2)\psi_{\theta\theta} = 0 \quad (50)$$

Equation (50) is the hodograph equation for the flow in the vortex tube. It is a linear equation in the dependent variable ψ.

Superposition. The general procedure for the solution of Equation (50) is as follows: (1) Assuming that a number of simple functions ψ_1, ψ_2 have been found to satisfy Equation (50), more complex solutions are found by linear superposition: $\psi = c_1\psi_1 + c_2\psi_2$. (2) The partial derivatives ψ_q and ψ_θ are obtained by partial differentiation of the solution $\psi = \psi(q, \theta)$. (3) Using the equivalent Cauchy-Rieman equations (46) and (47), ϕ_q and ϕ_θ are found. (4) Knowing ϕ_q and ϕ_θ, the partial derivatives x_q, x_θ, and y_q, y_θ of the physical variables are found from Equations (42) and (43), and integrated to give the streamline.

Solution for Vortex Tube. The solution for the streamline pattern in the vortex tube is obtained by combining a vortex flow with a sink flow. The respective solutions of these individual flows are well known, and are as follows:

Free Vortex. A particular solution of Equation (50) is sought, such that depends only on q. If this is the case, then $\psi_\theta = 0$, and Equation (50) becomes

$$q^2\psi_{qq} + q\left(1 - \frac{q^2}{c^2}\right)\psi_q = 0 \quad (51)$$

which is integrated into

$$\psi = c_1 J + c_2 \quad (52)$$

where $J = \frac{1}{2}\ln\frac{1-j}{1+j} + j + \frac{1}{3}j^3 + \frac{1}{5}j^5$; $j = \left(\frac{\rho}{\rho_0}\right)^{1/2}$. The partial derivative of x and y are

$$x_q = -c_1\frac{\sin\theta}{q^2}; \qquad x_\theta = c_1\frac{\cos\theta}{q}$$

$$y_q = c_1\frac{\cos\theta}{q^2}; \qquad y_\theta = c_1\frac{\sin\theta}{q}$$

Integration of these gives the equations for the streamline in the physical plane:

$$\begin{cases} x = c_1\dfrac{\sin\theta}{q} \\ y = c_2\dfrac{\cos\theta}{q} \end{cases} \quad (53)$$

Equation (53) shows that the streamlines of constant velocity are concentric circles in the physical plane. Choosing the constant to be $c_1 = rq = r^*c^*$ where r^* is the radius corresponding to a Mach number of unity, Equation (53) may be written as

$$\frac{x}{r^*} = \frac{\sin\theta}{\frac{q}{c^*}}; \qquad \frac{y}{r^*} = \frac{\cos\theta}{\frac{q}{c^*}}$$

The velocity distribution, shown in Fig. 6, increases with decreasing radius to a maximum of $q = 2.45\,c^*$. This corresponds to a minimum radius, a zero density, and a zero temperature. In terms of vortex strength, the minimum or limit radius is

$$r_{\min} = \frac{\Gamma}{2\pi c^*}\left(\frac{\gamma - 1}{\gamma + 1}\right)^{1/2} = \frac{\Gamma}{2\pi q_{\max}} \quad (54)$$

The existence of a limit circle has been corroborated in Part 1.

Sink. A solution for Equation (50) is sought, for which ψ depends only on θ. Under these conditions, $\psi_q = 0$, and Equation (50) becomes

$$\psi_{\theta\theta} = 0 \quad (55)$$

the solution of which is

$$\psi = c_1\theta + c_2 \quad (56)$$

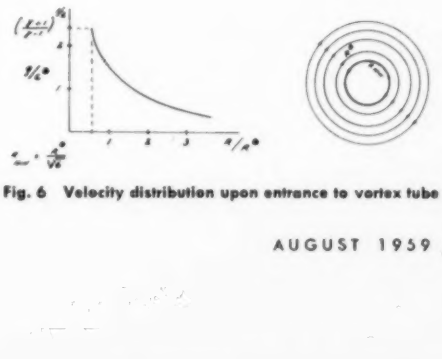

Fig. 6 Velocity distribution upon entrance to vortex tube

The streamlines of constant ψ are straight lines passing through the origin. The partial derivatives are

$$x_q = -c_1 \frac{\rho_0}{\rho} \frac{\cos\theta}{q^2}\left(1 - \frac{q^2}{c^2}\right); \qquad x_\theta = -c_1 \frac{\rho_0}{\rho} \frac{\sin\theta}{q}$$

$$y_q = -c_1 \frac{\rho_0}{\rho} \frac{\sin\theta}{q^2}(1 - \mathbf{M}^2); \qquad y_\theta = c_1 \frac{\rho_0}{\rho} \frac{\cos\theta}{q}$$

They are integrated into

$$x = c_1 \frac{\rho_0}{\rho} \frac{\cos\theta}{q} + c_3$$

$$y = c_1 \frac{\rho_0}{\rho} \frac{\sin\theta}{q} + c_4$$

The constants c_3, c_3, and c_4 merely involve displacements of the entire streamline pattern, and without loss of generality can be set equal to zero. The parametric equations for the streamlines are thus

$$\left.\begin{aligned} x &= c_1 \frac{\rho_0}{\rho} \frac{\cos\theta}{q} \\ y &= c_1 \frac{\rho_0}{\rho} \frac{\sin\theta}{q} \end{aligned}\right\} \tag{57}$$

Equations (57) show, by division of y by x, that the lines of constant θ are radial lines through the origin. The velocity distribution is obtained by choosing c_1 to satisfy the continuity equation, and plotting q/c^* versus r/r^* as shown in Fig. 7. There are two branches to the curve, but only the subsonic branch is of interest, since the vortex tube was run at subsonic velocities. There is no value of q/c^* for $r < r^*$. In other words, the sonic radius is the limiting radius for the flow.

Spiral Flow. The vortex flow and the sink flow are now combined to give a spiral flow in the plane. The result is

$$\psi = \frac{\phi}{2\pi}\theta + \frac{\Gamma}{2\pi} J; \qquad R = \frac{2\pi c_0 r}{\sqrt{\phi^2 + \Gamma^2}} \tag{58}$$

$$\left.\begin{aligned} x &= \frac{\phi}{2\pi c_0} \frac{\cos\theta}{(\rho/\rho_0)(q/c_0)} + \frac{\Gamma}{2\pi c_0} \frac{\sin\theta}{q/c_0} \\ y &= \frac{\phi}{2\pi c_0} \frac{\sin\theta}{(\rho/\rho_0)(q/c_0)} - \frac{\Gamma}{2\pi c_0} \frac{\cos\theta}{q/c_0} \end{aligned}\right\} \tag{59}$$

where Γ and Q are the strengths of the vortex and sink flow, respectively. A plot of the streamlines may be obtained by solving corresponding pairs of values of q/c_0 and 0 for a given ψ, and then determining the values of x and y. The flow pattern in the plane is shown in Fig. 8. A similar picture was obtained in Part 1 by means of oil injection which left a visible trace on a lucite plate.

Solution in Space. In the preceding sections, the equation of continuity, the equation of motion, and the relations for the existence of a velocity potential were combined to yield a differential equation of flow, which being in terms of two space variables, was solved by means of a hodograph transformation. For three-dimensional flow, similar technique does not bring success if the third space variable is brought in indiscriminately. The procedure followed here [23][2] consists in adding to the exact solution just derived an axial velocity such that it does not alter the flow equations in the plane. This velocity is of constant magnitude along the axis of the vortex tube and leaves the pressure, density, and temperature of the fluid unchanged.

That the three-dimensional flow thus obtained obeys the same set of equations heretofore solved may be seen as follows: Let w = constant (in space and time) be the velocity component which is added to the two-dimensional flow. The question may be asked: Does the resultant motion give a flow pattern which is consistent with the flow pattern that has been solved in the plane? The answer lies with the equations governing steady-state compressible flow, namely, the equation of continuity:

$$\frac{\partial(\rho u)}{\partial x} + \frac{\partial(\rho v)}{\partial y} + \frac{\partial(\rho w)}{\partial z} = 0 \tag{60}$$

Euler's equations:

$$u\frac{\partial u}{\partial x} + v\frac{\partial u}{\partial y} + w\frac{\partial u}{\partial z} + \frac{1}{\rho}\frac{\partial p}{\partial x} = 0 \tag{61}$$

$$u\frac{\partial v}{\partial x} + v\frac{\partial v}{\partial y} + w\frac{\partial v}{\partial z} + \frac{1}{\rho}\frac{\partial p}{\partial y} = 0 \tag{62}$$

$$u\frac{\partial w}{\partial x} + v\frac{\partial w}{\partial y} + w\frac{\partial w}{\partial z} + \frac{1}{\rho}\frac{\partial p}{\partial z} = 0 \tag{63}$$

and the equation of property change:

$$p = p_0\left(\frac{\rho}{\rho_0}\right)^\gamma \tag{64}$$

For the case of two-dimensional flow, the last term in Equation (60) does not exist; for the superposed flow, it becomes

$$\frac{\partial(\rho w)}{\partial z} = \rho\frac{\partial w}{\partial z} = 0$$

since ρ is independent of z, and w is constant along z. The continuity equation is thus the same for both the two-dimensional flow and the superposed flow.

For the case of two-dimensional flow, the third relation in Equation (63) does not exist, while the terms $\frac{\partial u}{\partial z}, \frac{\partial v}{\partial z}$ in the first two relations are zero. For the superposed flow, the third relation in Equation (63) vanishes due to the constancy of w with

[2] Numbers in brackets designate Bibliography at end of paper.

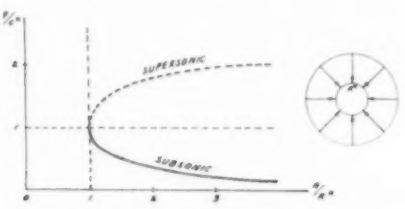

Fig. 7 Velocity distribution for sink

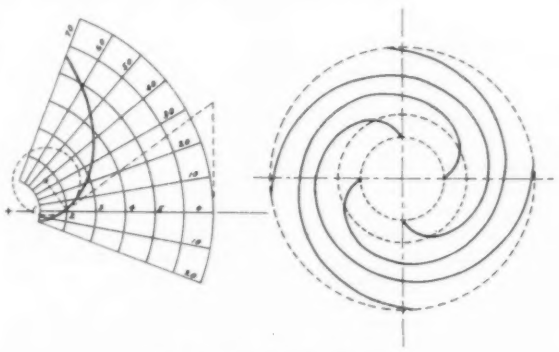

Fig. 8 Spiral flow in the plane

respect to x, y, z, and the independence of p with respect to z. Thus the two-dimensional flow and the superposed flow obey the same dynamical equations.

Lastly, the property-change relation, Equation (64), remains unchanged, since p, ρ, and T are not affected by the addition of a constant axial velocity, and since physical laws are not altered by uniformly translating co-ordinates. Consequently, the same equations describe both flows, and since these equations have been linearized and solved, what remains then is simply to superpose the stream function of the two-dimensional flow with the stream function of the axial flow to obtain the general solution in space. This addition of a constant velocity in the axial direction does not alter the conditions of irrotationality. For, if the two-dimensional flow possesses a velocity potential ϕ, then the addition of a constant velocity w still leads to an irrotational flow field with $\phi + wz$ as the velocity potential. The plot of a streamline for the superposed flow is shown in Fig. 9. It is typical of the flow pattern that prevailed in Part 1 upon entrance into the vortex tube.

Effect of Viscosity. The exact solution just developed is for that region of the tube (relatively near the entrance) where viscosity effects are negligible. The experimental results in Part 1 show that, as flow proceeds down the tube, viscosity effects begin to take over, and the free vortex changes into a forced vortex. Using Kassner's concept of shear stress in circular turbulent flow [18], the following equation is written for the stress:

$$\tau = \epsilon\left(\frac{dq}{dr} - \frac{q}{r}\right) \tag{65}$$

where ϵ is the turbulent exchange rate. Since the velocity distribution upon entrance into the tube is $q = \frac{K}{r}$, differentiation gives

$$rdq + qdr = 0; \quad \frac{dq}{dr} = -\frac{q}{r} = -\frac{K}{r^2} \tag{66}$$

and Equation (65) becomes

$$\tau = \epsilon\left(-\frac{q}{r} - \frac{q}{r}\right) = -2\epsilon\frac{q}{r} \tag{67}$$

The shearing force and the moment of shearing force acting on an annular element of fluid a distance r from the center are, respectively,

$$F_s = 2\pi r\epsilon\left(\frac{dq}{dr} - \frac{q}{r}\right)$$

$$M_s = rF_s = 2\pi r^2\epsilon\left(\frac{dq}{dr} - \frac{q}{r}\right) \tag{68}$$

The latter expression can be rewritten with the aid of Equation (66) as

$$M_s = 2\pi r^2\epsilon\left(-\frac{2K}{r^2}\right) = -4\pi\epsilon K \tag{69}$$

Equation (69) indicates that an elemental moment of shear stress is constant and independent of r.

Since there is no external torque applied to the flow upon entrance to the vortex tube, the summation of internal elemental moments must be zero. Thus,

$$\int_0^r M_s dr = 0 \tag{70}$$

But M_s is constant according to Equation (69); consequently, Equation (70) cannot be satisfied except for $M_s = 0$, since no summation of quantities of like sign can be zero unless all the quantities are zero individually. In other words, the flow, while irrotational immediately after entry into the vortex tube, does not stay irrotational, but changes into something else so as to satisfy Equation (70), which is the (initial) governing relation. That this something else is rotational flow can be seen by applying the equations of rotational flow to Equation (70), and seeing that the latter is satisfied: Since the characteristic equation for rotational flow is $q = \omega r$, it follows that

$$\frac{dq}{dr} = \omega = \frac{q}{r} \tag{71}$$

Substitution of Equation (71) into Equation (68) gives $M_s = 0$; consequently, Equation (70) is satisfied. Thus rotational flow is the stabler form of flow to which the initial flow transforms itself, even though both flows satisfy the conservation of energy principle. It will be shown, however, that the rotational flow has the lesser amount of useful kinetic energy. In other words, its entropy is greater than that of the irrotational flow. The change from one flow to the other is due to viscosity, though it seems surprising that the relatively low viscosity of the air may have such an effect. The experimental results presented in Part 1, however, tend to verify this change, for the velocity traverses show a definite rotational distribution.

Energy Distribution. The kinetic energy of each flow will now be computed. To this end, the velocities before and after conversion from a free vortex to a forced vortex are first obtained by equating the moment of momentum of both flows to each other:

$$M_{\text{irrot}} = \int_{r_1}^{r_2}\left(\frac{K}{r^2}\right)(r^2)(2\pi r\rho dr) = \pi\rho K(r_2^2 - r_1^2) \tag{72}$$

$$M_{\text{rot}} = \int_{r_1}^{r_2}(\omega)(r^2)(2\pi r\rho dr) = \frac{r\rho\omega}{2}(r_2^4 - r_1^4) \tag{73}$$

Setting Equations (72) and (73) equal to each other gives

$$\pi\rho K(r_2^2 - r_1^2) = \frac{\pi\rho\omega}{2}(r_2^4 - r_1^4)$$

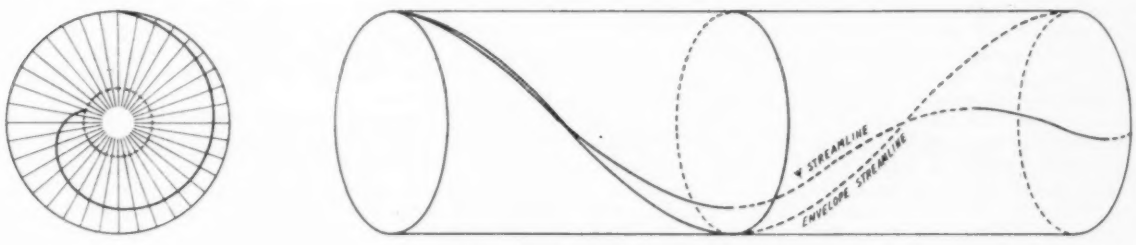

Fig. 9 Flow pattern in space

whence

$$\omega = \frac{2K}{r_2^2 + r_1^2} \tag{74}$$

Equation (74) is the relation between the strength of the forced vortex to that of the free vortex. The kinetic energy for the two modes of flow can now be obtained:

$$E_{irrot} = \int_{r_1}^{r_2} \frac{1}{2} \frac{K^2}{r^3} (2\pi\rho r dr) = \pi\rho K^2 \ln \frac{r_2}{r_1} \tag{75}$$

$$E_{rot} = \int_{r_1}^{r_2} \frac{1}{2} \omega^2 r^2 (2\pi\rho r dr) = \frac{\pi\rho\omega^2}{4} (r_2^4 - r_1^4)$$

The latter may, by means of Equation (74), be rewritten as

$$E_{rot} = \frac{\pi\rho K^2 (r_2^2 - r_1^2)}{r_2^2 + r_1^2} \tag{76}$$

Comparison of Equations (75) and (76) shows that the kinetic energy initially possessed by the free vortex is greater than that possessed by the rotational flow. The total energy of the two modes of flow, however, is the same, since there is no external transfer of heat or work from or to the system in both cases. Upon entry into the vortex tube, the fluid particles, because of the absence of external torque, move in concentric streamlines, with each streamline having the same amount of total energy. As the flow proceeds down the tube, viscosity effects begin to influence the flow (mainly because of the velocity increases to sonic speeds with decreasing radius), and the flow can no longer keep this constancy of energy distribution. The inner layers, having too much kinetic energy, must surrender part of their energy to the outer layers by being slowed down. The process of conversion ends with rotational flow being attained near the tube exit. The difference in kinetic energy between the free vortex and the forced vortex is the energy taken up by friction to make the conversion from irrotational to rotational flow.

The analysis, as given in the foregoing, is primarily mathematical. It has the advantage of being easily derivable, and requiring no elaborate model for comparison. It is also corroborated by some case studies of boundary layers made by Eckert and Hartnett [9], who showed that rotational flow of the forced vortex type, both laminar and turbulent, produced temperature separations that are independent of Prandtl numbers.

Proceeding with the solution of the vortex tube, the problem of determining the flow pattern near the tube exit is obtained by adding an axial velocity to the rotational flow just as it was done for the irrotational flow. The plot of a streamline is similar to that for irrotational flow, except that, strictly speaking, a scalar velocity potential no longer exists, but each streamline is identified instead by a pseudo ψ.

Performance Calculation. The present state of the field does not permit a complete calculation of performance. The dependence on such factors as diameter of tube, length of tube, size of cold air orifice, exit throttling, angle of entry, etc., has not yet been systematically studied. It is therefore too early for the development of a single equation which would predict performance. The optimum size for the cold air orifice, however, can be determined from the present analysis. If Equations (72) and (73), which represent the moment of momentum for the irrotational and rotational flows, are equated, K, the constant of irrotational flow, replaced by rq, and ω, the constant of rotational flow, replaced by q/r, there results

$$\pi\rho r q_{irrot}(r_2^2 - r_1^2) = \frac{\pi\rho}{2} q_{rot}(r_2^4 - r_1^4)$$

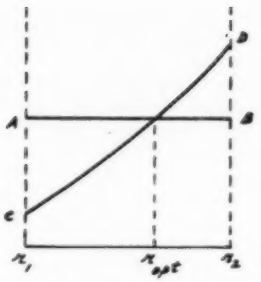

Fig. 10 Optimum size for cold orifice

whence

$$q_{rot} = \left(\frac{2r^2}{r_2^2 + r_1^2}\right) q_{irrot} \tag{77}$$

Equation (77) shows that as $r \to 0$, $q_{rot} \to 0$, and as $r \to r_2$, $q_{rot} \to 2q_{irrot}$. This means that as the flow changes in character from irrotational to rotational, the velocity of the converted flow at the wall tends to twice the velocity of the otherwise irrotational flow at the same location. This, of course, is at the expense of the inner layers, whose velocities decrease from near sonic to close to zero. If T_i is the temperature of the air upon entrance to the vortex tube, then for the irrotational flow, the quantity: $c_pT_i + K^2/2r_2^2$, being the stagnation enthalpy near the wall, has the same value for all streamlines, and is shown by the horizontal line A-B in Fig. 10. For rotational flow, the quantity: $c_pT_i + 2K^2/r_2^2$, while still the stagnation enthalpy near the wall, no longer is constant, but decreases from streamline to streamline as r tends to zero. Now, recall from earlier discussion that the energy of rotational flow is equal to that of the irrotational flow minus the energy taken up by the viscous forces. Let the energy of irrotational flow, which is known from knowledge of the initial stagnation enthalpy, be represented by the area $r_1 - A - B - r_2$. Since the friction energy may be determined by taking the difference between Equation (75) and Equation (76), the energy of rotational flow is known, and may be plotted as the area $r_1 - C - D - r_2$. The intersection of the two energy profiles gives a corresponding radius which is the optimum radius for largest temperature separation. This is the radius that was adopted for the experimental program, and significantly, it gave the best performance with respect to that variable.

Conclusions

The conclusions gathered from the present study on the vortex tube may be summarized by the following statements:

(i) Upon entrance into the tube, the motion of the gas is that of a free vortex, because of the absence of external torque.

(ii) The problem of the vortex tube is, to a great extent, amenable to mathematical solution through the superposition of a vortex and sink, followed by the addition of an axial velocity.

(iii) The presence of viscosity changes the flow from a free to a forced vortex. The latter flow is one of minimum kinetic energy and maximum entropy.

(iv) Though performance calculation for the general case is not possible at this stage, the optimum size for cold orifice may be obtained from energy considerations.

(v) The report is a first study based on relatively detailed and accurate experimental data. In that respect, it has the advantage of being free from conjectures in the analysis of the vortex phenomenon.

Bibliography

1 M. Applegate, "Vortex Tube Applications," Proceedings of the Conference on Cooling of Airborne Electronic Equipment, 1952, Ohio State University, Engineering Bulletin No. 148, July, 1952, pp. 207–209.

2 J. Bertin, "Modified Hilsch Apparatus for Producing Hot and Cold Air Streams" (French Patent No. 521,736, September, 1946), *Journal of Scientific Instruments*, vol. 28, August, 1951, p. 251.

3 W. G. Bickley, "Some Exact Solutions of the Equations of Steady Homentropic Flow of an Inviscid Gas," Modern Developments in Fluid Dynamics, vol. 1, edited by L. Howarth, Clarendon Press, Oxford, England, 1953.

4 A. M. Binnie and S. G. Hooker, "The Radial and Spiral Flow of a Compressible Fluid," *Philosophical Magazine*, vol. 23, January–June, 1937, pp. 597–606.

5 M. P. Blaber, "A Simply Constructed Vortex Tube for Producing Hot and Cold Air Streams," *Journal of Scientific Instruments*, vol. 27, 1950, pp. 168–169.

6 G. Burkhardt, "Theoretical Contribution to the Work of R. Hilsch on the Vortex Tube" (translation by R. C. Murray from *Zeitschrift für Naturforschung*, vol. 3a, no. 1, 1948, pp. 46–51), R. A. E. Library Translation No. 345, June, 1951.

7 S. Comassar, "The Vortex Tube," *Journal of American Society of Naval Engineers*, vol. 63, 1951, pp. 99–108.

8 W. R. Curley, "Report on the Hilsch Vortex Tube," *Journal of Boston College Physics Society*, May, 1950, pp. 3–9.

9 E. R. G. Eckert and J. P. Hartnett, "Experimental Study of the Velocity and Temperature Distribution in a High Velocity Vortex Tube Flow," Heat Transfer and Fluid Mechanics Institute, Stanford University, Calif., June, 1956.

10 K. Elsler and M. Hoch, "The Behavior of Various Gases and the Separation of Mixtures of Gases in a Vortex Tube" (translation by G. Coldewood from *Zeitschrift für Naturforschung*, vol. 6a, no. 1, 1951, pp. 25–31), R. A. E. Library Translation No. 400, February, 1952.

11 C. D. Fulton, "Ranque's Tube," Journal of the ASRE, *Refrigerating Engineering*, vol. 58, 1950, pp. 473–479.

12 C. D. Fulton, "Comments on the Vortex Tube," *Refrigerating Engineering*, vol. 59, 1951, p. 984.

13 I. E. Garrick and C. Kaplan, "On the Flow of a Compressible Fluid by the Hodograph Method: II—Fundamental Set of Particular Flow Solutions of the Chaplygin Differential Equation," NACA Tech. Ref., 790, 1944.

14 C. W. Hansell, "Low Temperature Physics," Miscellaneous Developments in German Science and Industry, C-6, Report No. 68, June, 1945, pp. 29–31, The Joint Intelligence Objective Agency, Washington, D. C.

15 C. W. Hansell, "Miscellaneous Development in German Science and Industry," Report PM-1638, Publications Board, Department of Commerce, Washington, D. C., pp. 36–37.

16 R. Hilsch, "The Use of the Expansion of Gases in a Centrifugal Field in Cooling Process" (unabridged translation from *Zeitschrift für Naturforschung*, vol. 1, no. 4, 1946, pp. 208–214), *Review of Scientific Instruments*, vol. 18, 1947, pp. 108–113.

17 A. V. Johnson, "Quantitative Study of the Hilsch Heat Separator," *Canadian Journal of Research*, vol. 25, 1947, p. 299.

18 R. Kassner and E. Knoernschild, "Friction Laws and Energy Transfer in Circular Flow," Technical Report No. F-TR-2198-ND, GS-USAF Wright-Patterson Air Force Base No. 78, March, 1948.

19 E. Knoernschild and O. Morgenson, "Application of Hilsch Tube to Aircraft and Missiles," A.I.T. 33095, Army Air Force, Air Materiel Command, Engineering Division, Equipment Laboratory, Serial No. MCREXE-664-510A. 45-USAF-Wright Patterson 128, June 10, 1948.

20 R. M. Milton, "Maxwellian Demon at Work," *Industrial and Engineering Chemistry*, Industrial Edition, vol. 38, no. 5, 1946, p. 5.

21 "Modern Developments in Fluid Dynamics—High Speed Flow," vol. 1, edited by L. Howarth, Clarendon Press, Oxford, England, 1953.

22 L. S. Packer and N. C. Box, "Vortex-Tube Free Air Thermometry," ASME Paper No. 55—A-22.

23 H. Poritsky, "Compressible Flows Obtainable From Two-Dimensional Flows Through the Addition of a Constant Normal Velocity," *Journal of Applied Mechanics*, vol. 13, TRANS. ASME, vol. 68, 1946, pp. A-61–65.

24 G. J. Ranque, "Experience sur la Detente Giratoire Avec Productions Simultanées d'un Echappement d'Air Chaud et d'Air Froid," *Journal de Physique et de Radium*, 1933, p. 112 (translation, G. E. Schenectady Works Library, T. F. 3294).

25 G. J. Ranque, "Method and Apparatus for Obtaining From Fluid Under Pressure Two Currents of Fluids at Different Temperatures," United States Patent 1,952,281 (March, 1934).

26 F. Ringleb, "Exakte Lösungen der Differentialgleischungen einer Adiabatischen Gasströmung," *Zeitschrift für Angewandte Mathematik und Mechanik*, vol. 20, 1940, pp. 185–198. Abstract in *Journal of the Royal Aeronautical Society*, vol. 46, 1942, pp. 403–404. Translation, "Ministry of Aircraft Production," Great Britain, R. T. P. Translation 1609, 1942.

27 G. W. Scheper, Jr., "The Vortex Tube—Internal Flow Data and Heat Transfer Theory," *Refrigerating Engineering*, vol. 59, 1951, pp. 985–989.

28 F. Schultz-Grunow, "How the Ranque-Hilsch Vortex Tube Operates," *Refrigerating Engineering*, vol. 59, 1951, pp. 52–53.

29 A. H. Schapiro, "The Dynamics and Thermodynamics of Compressible Fluid Flow," vols. I and II, The Ronald Press Company, New York, N. Y., 1953

30 H. Sprenger, "Observation on the Vortex Tube" (translation by A. O'Donnel from *Zeitschrift für Angewandte Mathematik und Physik*, vol. 2, 1951, pp. 293–300), R. A. E. Library Translation No. 394, December, 1951.

31 D. S. Webster, "An Analysis of the Hilsch Vortex Tube," *Refrigerating Engineering*, vol. 58, 1950, pp. 163–169, discussion, 169–170.

32 R. Westley, "A Bibliography and Survey of the Vortex Tube," The College of Aeronautics, Cranfield, England, 1954.

33 T. Yao-Tsu Wu, "Two-Dimensional Sink Flow of a Viscous, Heat-Conducting, Compressible Fluid," *Quarterly of Applied Mathematics*, vol. XIII, No. 4, January, 1956.

DISCUSSION

W. R. Gambill[3]

This paper and its earlier companion describing an experimental study are valuable contributions to an area of fluid dynamics that has been noted for its complexity and general muddiness. The treatment is broad and generally lucid, and it would appear that most of the effects having an important influence on the sometimes peculiar characteristics of vortex flow have been taken into account.

Two minor errors that do not appear in later equations and that do not affect any conclusions might be noted: v^2/r^2 in Equation (3) should be v^2/r, and K^2/r in the equation following Equation (7) should be K^2/R.

Will the author elaborate on details concerning the axial velocity distribution used? In a recent similar study[4] of vortex-flow energy separation, axial velocity was assumed constant with radius in a core region and, though of different magnitude, also constant with radius in the surrounding annular region. It also was shown that axial velocity varies linearly with length when tangential velocity is independent of length. In this paper, what is the form of the radial and axial variation of axial velocity?

It also might be worth while for the author to outline the presently unavailable knowledge which would be necessary for this theory to be numerically applicable to the design of vortex tubes, the prediction of their performance, and the correlation of vortex-tube data.

F. Kreith[5]

The theoretical part of the author's study of vortex-flow temperature separation deals with a problem which has been the subject of a great deal of research in recent years. His paper presents a welcome addition to the formal solutions available for calculating the potential flow pattern in a frictionless vortex flow. Unfortunately, the assumptions made in the course of the mathematical development are so restrictive that the final results are likely to deviate appreciably from actual conditions in a vortex tube, especially in turbulent flow which appears to be necessary for any substantial separation of hot and cold gas to occur.

In order to ascertain the validity of the model postulated by the

[3] Long Range Planning Group, Oak Ridge National Laboratory, a Division of Union Carbide Corporation, Oak Ridge, Tenn.

[4] R. G. Diessler and M. Perlmutter, "An Analysis of the Energy Separation in Laminar and Turbulent Compressible Vortex Flows," Heat Transfer and Fluid Mechanics Institute Preprints, 1958, pp. 40–53.

[5] University of Colorado, Boulder, Colo. Mem. ASME.

author in his analysis, it would be of interest to know how closely the flow pattern observed visually in the vortex tube used in the experimental work (i.e., Part 1 of this study) agrees with predictions based on Equation (59) in this paper. In particular, since Equation (70) shows that the radial-velocity distribution given by the free-vortex hypothesis in Equations (1) and (2) cannot be maintained in a real fluid, it would be important to know how it varies with axial distance from the entrance. It would also be of interest to know whether or not the experimental results show how to evaluate the strengths of the vortex flow and the sink flow in Equation (59). This information would enhance the practical value of the theoretical results appreciably.

The author's analyses dealing with the effect of viscosity on the flow and the energy distribution also require some amplification. First of all, r_1 and r_2 in Equations (72) through (77) are not defined. Are they the same as R_1 and R_2 in Fig. 1, referring to the inner and outer radii of the injection slots, or are they arbitrary radii? In the section labeled "Effect of Viscosity," no symbol denoting viscosity appears, but in Equation (65) ϵ is defined as the turbulent exchange rate. This terminology is ambiguous, in particular since the equation for the shearing stress in turbulent flow is usually written

$$\tau = (\mu + \rho\epsilon)\left(\frac{dq}{dr} - \frac{q}{r}\right)$$

where μ is the viscosity of the fluid and ϵ is the eddy diffusivity.

If the symbol ϵ in Equation (65) is intended to denote a combined coefficient of viscous and turbulent shear, it is difficult to reconcile this with the statement following Equation (77). "The change from one flow to the other is due to viscosity, though it seems surprising that the relatively low viscosity of the air may have such an effect." The validity of the analysis becomes even more questionable when one attempts to interpret the conclusion "that the energy of the rotational flow is equal to that of the irrotational flow minus the energy taken up by the viscous forces." Since the system used in the analysis, i.e., the vortex tube, is adiabatic, no net transfer of heat into or out of the system can take place. Consequently, viscous or dissipative forces can produce changes in the energy and velocity distribution, but cannot alter the total energy content. If the word energy in the foregoing quotation is intended to denote the sum of the enthalpy and the kinetic energy stored in the fluid, one is at a loss to explain what is meant by "the energy taken up by the viscous forces." The cross-sectional distribution of the energy stored in the fluid can only be evaluated when the static temperature as well as the velocity of the fluid are known. However, the static temperature distribution cannot be obtained from a macroscopic analysis of the flow, but requires a detailed analysis of the interaction between the radially outward transfer of energy as work and the radially inward transfer of heat. In the absence of such an analysis it is difficult to see how the author arrived at Fig. 10.

Clarification of the questions raised in the foregoing discussion will be appreciated by those interested in applying the author's experimental data and his theoretical analysis of the flow pattern to future studies of the problems associated with vortex-flow temperature separation.

Author's Closure

The author thanks Messrs. Gambill and Kreith for their written discussion. He also would like to express his appreciation to those persons who have communicated with him informally.

Concerning Mr. Gambill's discussion, the author acknowledges that v^2/r^2 in Equation (3) should read v^2/r, and the K^2/r in the equation following Equation (7) should read K^2/R. As for the axial velocity distribution, the author assumed a constant axial velocity in Part 2 of his paper. This is somewhat the same assumption that Messrs. Diessler and Perlmutter made in their study of energy separation in vortex flows. There is at present very little detail pertaining to axial velocity distribution because of the difficulty of making accurate measurements inside a vortex tube. Part 1 of the paper reports a little on the distribution, and also gives a graph, but the author was not completely sure of the data, and he did not make use of it in the theoretical analysis in Part 2. The assumption of constant axial velocity is not entirely correct, but in the absence of detailed and reliable experimental data, and also for the sake of obtaining a mathematical solution, it was used in Part 2. There is at present a program being conducted at Michigan State for the Army Ordnance with the objective of getting more internal data. It is expected that in the near future, a more accurate analysis will be possible.

Concerning Professor Kreith's discussion, the author agrees with him that the assumptions made in the course of the mathematical developments are quite restrictive, and that the final results are likely to deviate from actual conditions. It must be remembered, however, that this is a first paper in the sense that it starts back from scratch and does not aim to take in too much territory. It is rather difficult to even get started on any analysis without some simplifying assumption. The model postulated in Part 2 is qualitatively verified by the flow pattern obtained in Part 1 (Figs. 20 and 23), at least upon entrance into the vortex tube. The quantitative verification by means of Equation (59) is a good suggestion. So far, it has not been attempted because it was felt that more data at different stations were desirable. The effect of viscosity was discussed in the last portion of Part 2. The discussion, however, was not intended to be a full treatment of the subject. The author is aware of the shortcomings in the present treatment; he has thought of formulating a more accurate one, but so far, has not had much success. In Equations (72) through (77), r_1 and r_2 designate arbitrary radii in the vortex tube. They do not refer to the radii of the injection slots as Fig. 1 might have implied. Physically, r_2 would approach the radius of the vortex tube, and r_1 would approach zero. As for Equation (65), the author used Kassner's notation for turbulent shear in circular flow, lumping the quantity $1 + \rho\epsilon_M$ into a single factor ϵ. Admittedly, this is courting ambiguity, but it was done with the idea of reducing the number of terms to be carried about in future mathematical developments. It really doesn't make much difference whether a combined coefficient of viscous and turbulent shear is used or not, since the eddy viscosity is so much larger than the molecular viscosity. The statement attributing to viscosity for the change from one flow to another is consistent with the theoretical developments in the paper when it is kept in mind that the viscosity referred to is primarily the eddy viscosity. As for the interpretation of the statement concerning the energy of the rotational flow and that of the irrotational flow, all that it means is a rearrangement in velocity and energy distribution. It does not imply an alteration in the total energy content. It also aimed to point out the fact that irrotational flow (which exists at the start), by virtue of its more orderly arrangement of concentric streamlines, had greater "availability" than rotational flow, which comes about through the mechanism of turbulent momentum exchange.

It is hoped that these remarks will be of help in answering some of the questions pertaining to Parts 1 and 2 of the present paper. A better and more complete paper (based on experimental work now in progress) is being considered. In the meantime, the author thanks his correspondents for their expressions of interest.

Analysis of the Aerodynamic Heating for a Re-Entrant Space Vehicle

M. J. BRUNNER
Specialist, Advanced Studies, Thermodynamic Engineering, General Electric Company, Missiles and Space Vehicle Department, Philadelphia, Pa.
Mem. ASME

An analysis of the aerodynamic heating is presented through the trajectory and over the surface of a re-entrant hypersonic space vehicle. Bodies exhibiting zero and high lift over drag ratios are considered. The turbulent and laminar convective heat inputs are specified as functions of the trajectory and space vehicle parameters. The maximum heating rates and time integrated heat fluxes are given as functions of the local pressure distribution, body geometry, and wall temperature. Examples are presented to illustrate the application of this analysis.

Introduction

One of the prime design considerations for a blunt nosed re-entrant space vehicle is the aerodynamic heating imposed during re-entry. The heating characteristics such as the magnitude of the heat flux, total heating, and heating time will depend on the re-entry trajectory, the geometry of the vehicle, and the nature of the heating (turbulent or laminar). The heating characteristics for a space vehicle will have a considerable influence on the configuration and vehicle design. It is, therefore, necessary to establish an accurate evaluation of the aerodynamic heating so that proper considerations can be given to the heat protection system requirements for the space vehicle.

As the vehicles of interest require hypersonic velocity during re-entry, the environment is one of extremely high temperature. During re-entry, therefore, compressibility and real gas effects must be considered in order to properly evaluate the magnitude of the aerodynamic heating imposed on the vehicle. It has been demonstrated [1, 2][1] that the reference enthalpy method can approximate real gas and compressibility effects. The reference enthalpy method will, therefore, be used throughout the analysis.

The aerodynamic heating analysis will be made for both turbulent and laminar-type boundary layers. The turbulent heating will be extended to all parts of the vehicle while laminar heating will be directed primarily to the stagnation point. The prime purpose of this analysis will be to arrive at a systematic method for analyzing the re-entry heating for specific vehicle geometries in a form that can be applied readily to design. The analysis will be made primarily for three dimensional bodies, however, it can be readily extended to two dimensions.

Since the trajectory has a major influence on the heating, two typical types will be used in the analysis. They will cover the majority of the cases of current interest and will also represent the two extremes in aerodynamic heating that may be encountered. Zero and high lift vehicles will be considered.

From this analysis a convenient and fairly accurate method of estimating the aerodynamic heating for a blunt nosed re-entrant space vehicle will be established which should give an understanding of the heating problems involved in space vehicle design. Previous papers [3, 4] have discussed the problem in a general way but this analysis will essentially present tools for the determination of the aerodynamic heating of any given space vehicle geometry.

[1] Numbers in brackets designate References at end of paper.

Contributed by the Heat Transfer Division and presented at the Aviation Conference, Los Angeles, Calif., March 8–12, 1959, of The American Society of Mechanical Engineers.

Note: Statements and opinions advanced in papers are to be understood as individual expressions of their authors and not those of the Society. Manuscript received at ASME Headquarters, December 2, 1958. Paper No. 59—Av-5.

Ballistic Vehicle

1 Trajectory Considerations. The analysis of the motion of a

Nomenclature

a = drag over lift = D/L
A = reference area, ft²
a = velocity of sound, ft/sec
b = trajectory parameter, $\rho_0/\beta(W/C_D A)\sin\Theta_E$
B = wall temperature parameter, $2gJh_w/U^2_{E,\text{sat}}$
C_D = drag coefficient
C_L = lift coefficient
C_p = specific heat, Btu/lb-deg F
D = drag, lb
g = acceleration of gravity, ft/sec²
h = enthalpy, Btu/lb
J = mechanical equivalent of heat = 778, ft lb/Btu
L = lift, lb
m = mass, lb sec²/ft
M = Mach number
p = pressure, lb/ft²
$\dot{q}$ = heat transfer rate, Btu/ft² sec
Q = time-integrated heat-transfer rate (total heat), Btu/ft²
r_c = distance of vehicle from center of earth, ft
r_0 = radius of earth, ft
R = gas constant, ft/deg R
R_N = nose radius, ft
S = wetted length, ft
t = time, sec
T = temperature, deg R
U = velocity, ft/sec
U_{sat} = satellite velocity (reference), 25,930 ft/sec
V = dimensionless velocity (U/U_{sat})
W = weight, lb
y = altitude, ft
β = constant = 1/22000, ft⁻¹
γ = ratio of specific heats (free stream) = 1.4
$\tilde{\gamma}$ = ratio of specific heats (edge of boundary layer) = 1.2
Θ = local body angle, degree
Θ_E = re-entry angle, degree
μ = viscosity lb/ft sec
θ = partial range, radians
ρ = density, lb/ft³
ϕ = total range, radians

Subscripts

E = re-entry conditions
f = burnout
m = maximum
0 = reference conditions
s = stagnation point
t = turbulent
w = wall conditions
∞ = free stream conditions

hypersonic space vehicle with zero lift re-entering the earth's atmosphere can be simplified by neglecting gravity without substantially affecting the accuracy of the trajectory [3]. This is reasonable since the deceleration of the vehicle is large compared to the acceleration of gravity. The flight path angle will then be constant for this trajectory. The equation of motion for the vertical component may be written as:

$$\frac{d^2y}{dt^2} = -\frac{dU}{dt} = u\frac{dU}{dy} = \frac{C_D\rho U^2 A \sin\Theta_E}{2mg} \tag{1}$$

Based on the assumption of an isothermal atmosphere, the density may be written as:

$$\rho = \rho_0 e^{-\beta y} \tag{2}$$

where

$$\rho_0 = 0.1095 \text{ lb/ft}^3 \quad \beta = 1/22000$$

The velocity can then be obtained from equation (1) if C_D is assumed constant

$$U = U_E e^{-\frac{b}{2}e^{-\beta y}} \tag{3}$$

where

$$b = \rho_0/\beta(W/C_D A)\sin\Theta_E$$

and the time from re-entry can be obtained as a function of altitude from equation (3) as

$$t = \frac{1}{\beta U_E \sin\Theta_E}\left[\ln E + E + \frac{E^2}{2\cdot 2!} + \frac{E^3}{3\cdot 3!}\cdots\right]_{y_2}^{y_1} \tag{4}$$

where

$$E = \frac{b}{2}e^{-\beta y}$$

This trajectory information will be sufficient to make a detailed aerodynamic heating analysis. The variation of the velocity and altitude with re-entry time is shown on Fig. 1. The trajectory time and altitude are based on re-entry at 280,000 feet. The altitude, velocity, and time are shown as dimensionless quantities referred to the re-entry conditions of velocity and flight path angle. The curve shows the effect of the parameter b on the trajectory. The trajectory is shown for values of b of 1 to 50.

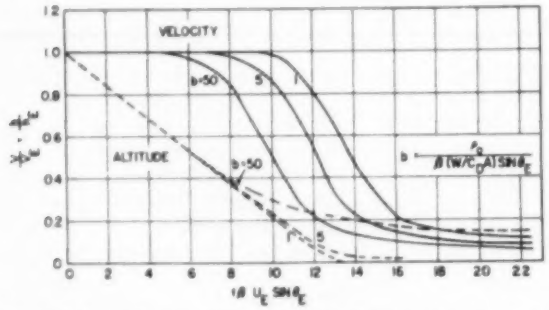

Fig. 1 Trajectory for zero lift vehicle showing dimensionless velocity and altitude versus time

The lower b becomes, the longer is the time required before the velocity is materially changed from the initial re-entry velocity. At a given re-entry time, as b decreases, the altitude decreases and the velocity increases significantly. The trajectory parameter b is inversely proportional to W/C_DA and sin Θ_E as shown in equation (3).

2 Turbulent Heat-Transfer Analysis. It should be noted at the outset that this analysis considers only the convective aerodynamic heating to the re-entry body. This will normally constitute the major portion of the heating, however, at hypersonic velocity the contribution due to radiation from the gas cap may become appreciable for some specific vehicles.

The turbulent heat-transfer rate can be expressed conveniently, considering real gas effects, by a modified flat plate reference enthalpy method [1, 2] as:

$$\dot{q}_t = \frac{0.702\times 10^{-4}(\rho U)^{0.8}S^{-0.2}\Delta h}{j^{0.46}} \tag{5}$$

where

$$j = (0.5h_w + 0.28h + 0.22h_s)/96.8$$

This equation can be written more conveniently by expressing the quantities (p, U, h) behind the bow shock wave of a blunt nosed body in terms of free stream conditions (ρ_∞ and U_∞) by assuming a Prandtl number of unity. For a wall temperature of zero ($h_w/h_s = 0$) the turbulent heat flux can be written as:

$$\dot{q}_t = f(M\gamma P/P_s)S^{-0.2}\rho_\infty^{0.8}U_\infty^{2.48} \tag{6}$$

where

$$f(M\gamma P/P_s) = 2.07\times 10^{-9}\left(\frac{\gamma+1}{2\gamma}\right)^{0.8}(P/P_s)^{0.8}\left[1-(P/P_s)^{\frac{\gamma-1}{\gamma}}\right]^{0.4}\left[1+1.272(P/P_s)^{\frac{\gamma-1}{\gamma}}\right]^{-0.48}$$

For a given point on a body P/P_s is constant at high Mach numbers ($M > 5$), therefore, $f(M\gamma P/P_s)$ is constant.

The turbulent heat-transfer rate of equation (6) can be written in terms of the trajectory equations (2) and (3) as:

$$\dot{q}_t = f(M\gamma P/P_s)S^{-0.2}\rho_0^{0.8}U_E^{2.48}e^{-\left(0.8\beta y + \frac{3.48}{2}be^{-\beta y}\right)} \tag{7}$$

and the maximum heat-transfer rate is then

$$\dot{q}_{t_m} = f(M\gamma P/P_s)S^{-0.2}\rho_0^{0.8}U_E^{2.48}(2.175be)^{-0.8} \tag{8}$$

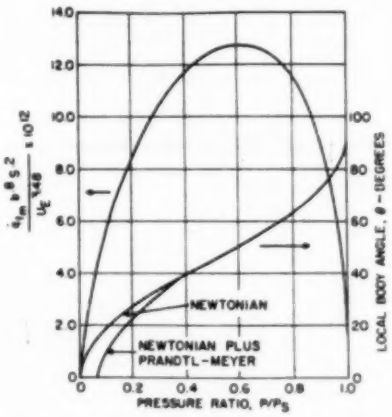

Fig. 2 Maximum turbulent heat flux and local body angle versus local pressure ratio for a zero lift vehicle

The maximum turbulent heat-transfer rate is shown in Fig. 2 as a function of the local pressure ratio. The heating rate function, $F(\dot{q}_{t_m})$, reaches a maximum at a pressure ratio of 0.6. For given re-entry conditions, body location, and local pressure ratio, the maximum turbulent heat flux can be readily evaluated. The pressure ratio is also shown as a function of local body angle for

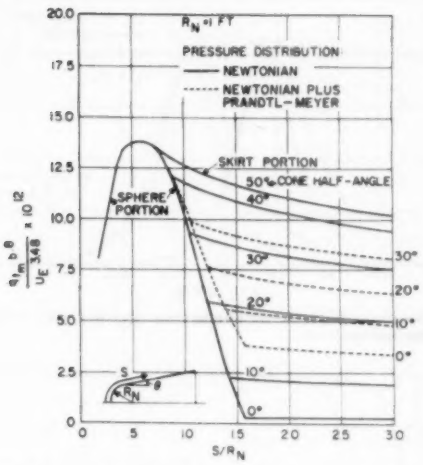

Fig. 3 Maximum turbulent heat flux versus body position for a zero li vehicle

assumptions of Newtonian and Newtonian plus Prandtl-Meyer theories [5]. It is noted that the Newtonian pressure distribution implies free stream pressure for a zero body angle. The zero intercept shown was based on a Mach number of 20.

The heat-transfer rates can now be specified for any given body shape and re-entry condition. The maximum heat-transfer distribution on the surface of a sphere cone has been evaluated for a one-foot nose radius with varied cone angles as shown on Fig. 3. For the purpose of this curve, the pressure on the conical portion of the sphere cone was assumed to be constant. The heating rates are given for both Newtonian and Newtonian plus Prandtl-Meyer pressure distribution assumptions. It is noted that the maximum turbulent heat-transfer rate occurs at a local body angle of approximately 50 degrees. The dimensionless variation of turbulent heat-transfer rate to the maximum rate as a function of altitude can then be obtained from equations (7) and (8) as

$$\dot{q}_t/\dot{q}_{t_m} = (2.175be)^{0.8} e^{-\left(0.8\beta y + \frac{3.48}{2} be^{-\beta y}\right)} \tag{9}$$

The time integrated heat-transfer rate can be conveniently expressed in terms of the maximum heating rate as

$$Q_t/\dot{q}_{t_m} = \int_{t_1}^{t_2} \dot{q}_t/\dot{q}_{t_m} \frac{dt}{dy}\, dy$$

but

$$\frac{dt}{dy} = -\frac{1}{U \sin \theta_E} = \frac{e^{\frac{b}{2} e^{-\beta y}}}{U_E \sin \theta_E} \tag{10}$$

$$Q_t/\dot{q}_{t_m} = -\frac{(2.175be)^{0.8}}{U_E \sin \Theta_E} \int_{\infty}^{0} e^{-(0.8\beta y + 1.24be^{-\beta y})}\, dy$$

The integral in equation (10) can be expressed as an incomplete gamma function [6, 7], therefore:

$$Q_t/\dot{q}_{t_m} = \frac{(1.752e)^{0.8}}{\beta U_E \sin \Theta_E} \Gamma(0.8, 1.24b) \tag{11}$$

The time integrated total heat flux is then

$$Q_t = \frac{f(M\gamma P/P_s)}{1.188} \cdot \frac{\rho_0^{0.8} S^{-0.2} b^{-0.8}}{\beta \sin \Theta_E} U_E^{2.48} \Gamma(0.8, 1.24b) \tag{12}$$

It should be noted that the derived aerodynamic heating relationships were based on assuming $h_w/h_s = 0$. When the wall temperature is greater than zero ($h_w/h_s > 0$), the heat transferred to the body will be reduced as follows:

$$\frac{\dot{q}_{t_{h_w \neq 0}}}{\dot{q}_{t_{h_w = 0}}} = \left[1 - \frac{2gJh_w e^{be^{-\beta y}}}{U^2_E}\right] \left[\frac{1 + 1.272(P/P_s)^{\frac{\gamma-1}{\gamma}}}{1 + 1.272(P/P_s)^{\frac{\gamma-1}{\gamma}} + \frac{4.54gJh_w e^{be^{-\beta y}}}{U^2_E}}\right]^{0.48} \tag{13}$$

A similar correction to the total aerodynamic heating can also be obtained by integrating equation (13) over the trajectory from re-entry to any desired altitude.

3 Laminar Heat-Transfer Analysis. The stagnation point heat-transfer rate can be obtained from Lees' analysis [8] modified to account for real gas and compressibility effects using the reference enthalpy method as follows:

$$\dot{q}_s = \frac{1.526 \times 10^{-8} \sqrt{U_s' P_s}\, \Delta h}{f^{0.18}} \tag{14}$$

The stagnation heating can now be written in terms of the re-entry conditions, trajectory parameters, body shape, and wall temperature as was previously described in the turbulent heating analysis. Equation (14) can be expressed in terms of free stream conditions [9] as:

$$\dot{q}_s = f(M\gamma) \left(\frac{\rho_\infty}{R_N}\right)^{1/2} U_\infty^{3.2} \tag{15}$$

where

$$f(M\gamma) = 6.035 \times 10^{-10} \left(\frac{\gamma - 1}{\gamma + 1}\right)^{1/4} \left(\frac{\gamma + 3}{\gamma + 1}\right)^{1/4} \left(\frac{\gamma + 1}{2\gamma}\right)^{1/2}$$

The stagnation heat-transfer rate can then be written in terms of altitude as

$$\dot{q}_s = f(M\gamma) \left(\frac{\rho_0}{R_N}\right)^{1/2} U_E^{3.2} e^{-\left(\frac{\beta}{2} y + \frac{3.2}{2} be^{-\beta y}\right)} \tag{16}$$

and therefore the maximum heat-transfer rate is

$$\dot{q}_{s_m} = f(M\gamma) \left(\frac{\rho_0}{3.2beR_N}\right)^{1/2} U_E^{3.2} \tag{17}$$

The dimensionless ratio of stagnation heating is then

$$\dot{q}_s/\dot{q}_{s_m} = (3.2be)^{1/2} e^{-\left(\frac{\beta}{2} y + \frac{3.2}{2} be^{-\beta y}\right)} \tag{18}$$

and the time-integrated stagnation-heat flux ratio is

$$Q_s/\dot{q}_{s_m} = \frac{(3.2be)^{1/2}}{U_E \sin \theta_E} \int_{\infty}^{0} e^{-\left(\frac{\beta}{2} y + \frac{2.2}{2} be^{-\beta y}\right)}\, dy \tag{19}$$

The integral in this equation may be expressed as an error function, therefore:

$$Q_s/\dot{q}_{s_m} = \frac{4.98}{\beta U_E \sin \Theta_E} \operatorname{erf} \sqrt{1.1b} \tag{20}$$

The time-integrated heat flux is then

$$Q_s = f(M\gamma) \left(\frac{\pi \rho_0}{1.1bR_N}\right)^{1/2} \frac{U_E^{3.2}}{\beta \sin \Theta_E} \operatorname{erf} \sqrt{1.1b} \tag{21}$$

When the wall temperature is greater than zero, the stagnation point heating rate is reduced as follows:

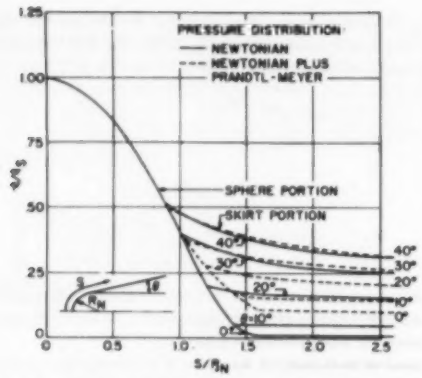

Fig. 4 Laminar heat flux ratio versus body position for a zero lift vehicle

$$\frac{\dot{q}_{s_{h_w \neq 0}}}{\dot{q}_{s_{h_w = 0}}} = \frac{\left[1 - \frac{2gJh_w}{U_E^2} e^{be^{-\beta y}}\right]}{\left[1 + \frac{2gJh_w}{U_E^2} e^{be^{-\beta y}}\right]^{0.15}} \tag{22}$$

The analysis given will establish the stagnation point heat transfer as a function of the trajectory parameters. In order to evaluate the laminar heat transfer at positions on the body, other than at the stagnation point, the following relationship of Lees [8] applies:

$$\frac{\dot{q}}{\dot{q}_s} = \frac{1/2(P/P_s)(U/U_\infty)R\sqrt{R_N}}{\left[\int_0^\infty (P/P_s)(U/U_\infty)R^2\,ds\right]^{1/2}\left[(1/U_\infty)\left(\frac{dU}{d\Theta}\right)_{\Theta=0}\right]^{1/2}} \tag{23}$$

The effect of shape on laminar heating is shown on Fig. 4 for sphere-cone bodies having various conical skirts. The pressure distributions of Newtonian and Newtonian plus Prandtl-Meyer are compared. The maximum laminar heating is always at the stagnation point on the body.

4 Comparison of Turbulent and Laminar Heating. The variation of turbulent and laminar heat flux over the trajectory of typical zero lift vehicles is shown on Fig. 5. The dimensionless heating ratio ($\dot{q}/\dot{q}_m$) is given as a function of dimensionless re-entry time for various trajectory parameters (b). The maximum turbulent heating occurs at longer re-entry times, which implies lower altitudes and lower velocities, than that for maximum laminar heating. This can be readily seen by examining equations (7) and (16) for maximum heating. As the trajectory parameter b decreases, the heat flux curves are displaced to higher re-entry times. The magnitude of the laminar time integrated dimensionless heat flux curves (dashed lines on Fig. 5) appears larger than that for the corresponding turbulent case. This is clearly shown in Fig. 6 where $Q/\dot{q}_m$ is given for both the turbulent and laminar heating as a function b. The dimensionless total heating ratio ($Q/\dot{q}_m$) is about 4.1 for turbulent and 5.0 for laminar heating when the trajectory parameter is greater than 5. The laminar dimensionless total heating ratio is, therefore, over 20 per cent greater than the turbulent ratio.

The maximum heat-transfer rate correction for wall temperature is shown on Fig. 7 as a function of the wall temperature parameter b. The effect of wall temperature on turbulent heating is greater than that for laminar. The correction for total turbulent and laminar heating is shown in Fig. 8 as a function of the trajectory parameter for various wall temperatures. For high values of b the correction is constant for a given wall temperature.

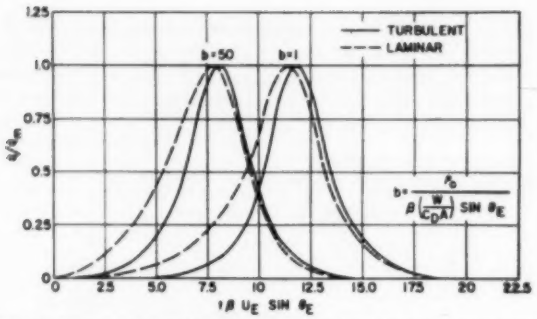

Fig. 5 Dimensionless turbulent and laminar heat flux ratio versus time for zero lift vehicles

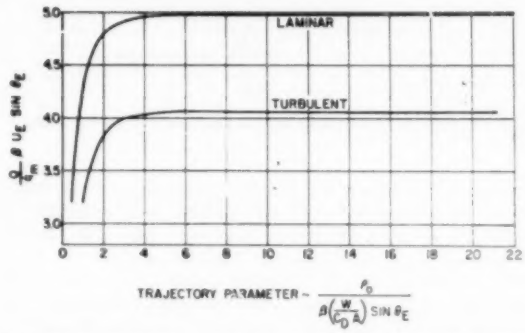

Fig. 6 Total heating ratio versus trajectory parameter for zero lift vehicles

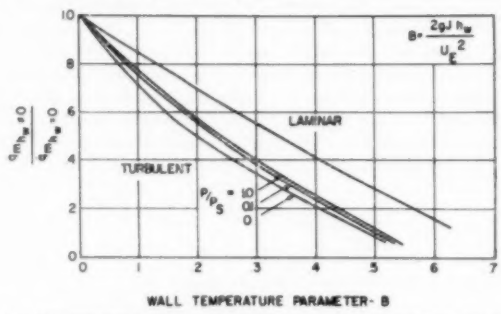

Fig. 7 Temperature correction for maximum turbulent and laminar heating rates versus wall temperature parameter for zero lift vehicles

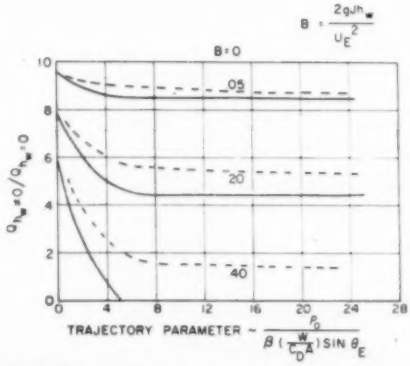

Fig. 8 Temperature correction for total turbulent and laminar heating versus trajectory parameter for zero lift vehicle. (Note: Solid line—turbulent; broken line—laminar.)

Glide Vehicle

1 Trajectory Considerations. The motion of a hypersonic glide vehicle may be expressed as

$$L - mg\cos\Theta = -\frac{mU^2}{r_c}$$

$$-D + mg\sin\Theta = m\dot{U}/dt \tag{24}$$

Based on the assumptions of small path angle, constant gravitational force, constant L/D, and $U^2_{sat} = gr_0$, the equations of motion can be reduced [4] to:

$$\frac{dU^2}{ds} - \frac{2aU^2}{r_0} + 2ag = 0 \tag{25}$$

The free stream velocity then can be obtained as

$$V_\infty = 1 - (1 - V_f^2)e^{2a\phi} \tag{26}$$

where $$a = D/L$$

The maximum range is then [4]

$$\phi = \frac{1}{2a}\ln\left(\frac{1}{1 - V_f^2}\right) \tag{27}$$

and the burnout velocity is

$$V_f^2 = 1 - e^{-2a\phi} \tag{28}$$

The free stream velocity can then be written in terms of the range parameter ($a\phi$) from equations (28) and (30) as

$$V_\infty^2 = 1 - e^{-2a\phi(1-\theta/\phi)} \tag{29}$$

and the time of flight is then

$$t = \frac{U_{sat}}{2ag}\ln\left[\frac{1 + (1 - e^{-2a\phi})^{0.5}}{1 - (1 - e^{-2a\phi})^{0.5}}\right] \tag{30}$$

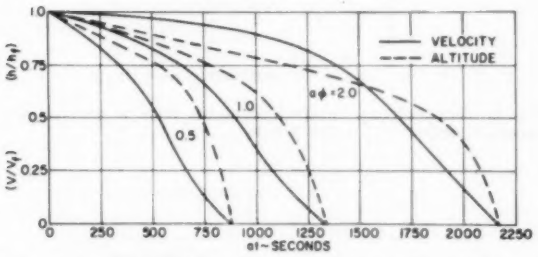

Fig. 9 Trajectory for glide vehicle showing dimensionless velocity and altitude versus time

The variation of velocity and altitude with flight time is shown in Fig. 9. The dimensionless velocity shown applies to any configuration and is a function only of the range parameter $a\phi$. The altitude, however, is a function of W/C_LA and $a\phi$. The altitude corresponding to a W/C_LA of 500 was used as a reference. The burnout velocity (V_f) will vary from 0.84 to 1.0 and the altitude from 175,000 to 250,000 feet for range parameters of 0.5 to 2.0, respectively. The time is a function of the lift to drag ratio (L/D). The altitude required for flight increases with the range parameter but decreases with W/C_LA.

2 Turbulent Heat-Transfer Analysis. The anticipated environment of a hypersonic glide vehicle is such that compressibility and real gas effects must be considered. The turbulent heat-transfer rate which has been derived previously in equation (6) can now be written in terms of the glide vehicle trajectory parameters from equations (24), (28), and (29).

$$\dot{q}_t = f(M\gamma P/P_s)S^{-0.2}\left(\frac{2Wg}{C_LA}\right)^{0.8} U_{sat}^{1.88}\, e^{-1.6a\phi(1-\theta/\phi)}\,[1 - e^{-2a\phi(1-\theta/\phi)}]^{0.84} \tag{31}$$

This then states the turbulent heat-transfer rate at any point of the trajectory for a given point on the body. The heat transfer at burnout is then:

$$\dot{q}_{tf} = f(M\gamma P/P_s)S^{-0.2}\left(\frac{2Wg}{C_LA}\right)^{0.8} U_{sat}^{1.88}\, e^{1.6a\phi}(1 - e^{-2a\phi})^{0.84} \tag{32}$$

The dimensionless heat flux can then be obtained as a function of range from equations (31) and (32) as

$$\dot{q}_t/\dot{q}_{tf} = \frac{e^{1.6a\phi(\theta/\phi)}[1 - e^{-2a\phi(1-\theta/\phi)}]^{0.84}}{(1 - e^{-2a\phi})^{0.84}} \tag{33}$$

The maximum heat flux can be readily determined from equation (31) as

$$\dot{q}_{t_m} = f(M\gamma P/P_s)S^{-0.2}\left(\frac{2Wg}{C_LA}\right)^{0.8} U_{sat}^{1.88}\, e^{-0.8234}(1 - e^{-0.778}) \tag{34}$$

The time-integrated turbulent heat flux can now be obtained from

$$Q_t/\dot{q}_{tf} = \int_0^\phi \dot{q}_t/\dot{q}_{tf}\,\frac{dt}{dU}\,\frac{dU}{d\theta}\,d\theta \tag{35}$$

from equation (25)

$$\frac{dU}{dt} = \frac{1}{2}\frac{dU^2}{ds} = age^{-2a\phi(1-\theta/\phi)} \tag{36}$$

and from equation (26)

$$\frac{dU}{d\theta} = aU_{sat}\frac{e^{-2a\phi(1-\theta/\phi)}}{[1 - e^{-2a\phi(1-\theta/\phi)}]} \tag{37}$$

therefore substituting equations (36) and (37) in (35)

$$Q_t/\dot{q}_{tf} = \frac{U_{sat}}{ag}\,\frac{f_1(a\phi)}{(1 - e^{-2a\phi})^{0.84}} \tag{38}$$

where

$$f_1(a\phi) = \int_0^\phi e^{1.6a\phi}(1 - e^{-2a\phi(1-\theta/\phi)})^{0.44}\,d\theta$$

$$\simeq \left[\frac{1}{1.6}e^{1.6a\phi} - \frac{0.44}{3.6}e^{-2a\phi}(e^{3.6a\phi} - 1) - \frac{0.123}{5.6}e^{-4a\phi}(e^{5.6a\phi} - 1)\ldots\right]$$

The time-integrated heat flux is then

$$Q_t = f(M\gamma P/P_s)(gS)^{-0.2}\left(\frac{2W}{C_LA}\right)^{0.8} U_{sat}^{2.88}\, e^{-1.6a\phi}\,\frac{f_1(a\phi)}{a} \tag{39}$$

Since these relationships were based on assuming the wall temperature zero, the following correction to the heat flux is necessary where $h_w/h_s > 0$

$$\frac{\dot{q}_{t_{h_w\neq 0}}}{\dot{q}_{t_{h_w=0}}} = \left(1 - \frac{h_w}{h_s}\right)\left[\frac{1 + 1.272(P/P_s)^{\frac{\gamma-1}{\gamma}}}{1 + 1.272(P/P_s)^{\frac{\gamma-1}{\gamma}} + 2.27h_w/h_s}\right]^{0.44} \tag{40}$$

similar to the correction for the zero lift trajectory equation (13) except for a high lift trajectory the stagnation enthalpy cannot

conveniently be expressed in terms of altitude without introducing W/C_LA.

3 Laminar Heat-Transfer Analysis. The stagnation point heat flux can be expressed in terms of trajectory parameter from equations (28), (29), and (24) in (15) as

$$\dot{q}_s = f(M\gamma)\left(\frac{2Wg}{C_LAR_N}\right)^{0.5} U_{sat}^{2.2}\, e^{-a\phi(1-\theta/\phi)} [1 - e^{-2a\phi(1-\theta/\phi)}]^{1.1} \quad (41)$$

and at burnout it is

$$\dot{q}_{sf} = f(M\gamma)\left(\frac{2Wg}{C_LAR_N}\right)^{0.5} U_{sat}^{2.2}\, e^{-a\phi}(1 - e^{-2a\phi})^{1.1} \quad (42)$$

The dimensionless heat flux ratio is therefore

$$\dot{q}_s/\dot{q}_{sf} = \frac{e^{a\phi}[1 - e^{-2a\phi(1-\theta/\phi)}]^{1.1}}{(1 - e^{-2a\phi})^{1.1}} \quad (43)$$

The maximum stagnation heating is

$$\dot{q}_{sm} = f(M\gamma)\left(\frac{2Wg}{C_LAR_N}\right)^{0.5} U_{sat}^{2.2}\, e^{-0.8\phi}(1 - e^{-1.6\phi})^{1.1} \quad (44)$$

and the time-integrated heat flux ratio is then obtained from equations (36), (37), and (43) as:

$$Q_s/\dot{q}_{sf} = \frac{U_{sat}}{ag}\,\frac{f_2(a\phi)}{(1 - e^{-2a\phi})^{1.1}} \quad (45)$$

where

$$f_2(a\phi) = \int_0^{\phi} e^{a\phi}(1 - e^{-2a\phi(1-\theta/\phi)})^{0.5}\, d\theta \cong [(e^{a\phi} - 1) - 0.2e^{-2a\phi}(e^{3a\phi} - 1) - 0.024e^{-4a\phi}(e^{5a\phi} - 1)\ldots]$$

and then the total stagnation heating is therefore

$$Q_s = f(M\gamma)\left(\frac{2W}{gC_LAR_N}\right)^{0.5} U_{sat}^{2.2}\, e^{-a\phi}\,\frac{f_2(a\phi)}{a} \quad (46)$$

The wall temperature correction is

$$\frac{\dot{q}_{s_{h_w \neq 0}}}{\dot{q}_{s_{h_w = 0}}} = \frac{1 - h_w/h_s}{(1 + h_w/h_s)^{0.15}} \quad (47)$$

The stagnation point heating can now be readily determined for any point on the trajectory. In order to estimate the laminar heating at other points away from the stagnation point the method of equation (23) applies.

4 Comparison of Turbulent and Laminar Heating. The aerodynamic heat flux comparison for the glide vehicle is shown on Fig. 10. The dimensionless heat flux ratio ($\dot{q}/\dot{q}_f$) is given as a function of referred flight time for various values of the range parameter $a\phi$. The heat flux ratio is appreciably greater for turbulent than for laminar flow. The maximum turbulent ratio ($\dot{q}_m/\dot{q}_f$) reaches 2.5 times the laminar ratio at a range ($a\phi$) of 2.0. The maximum turbulent heat flux occurs at higher flight times than laminar which implies lower altitudes and lower velocities.

The burnout heat flux for both the turbulent and laminar case is shown on Fig. 11. The maximum turbulent heating occurs at a local pressure ratio of 0.6 and also at a range ($a\phi$) of approximately 0.4. The maximum laminar heat flux occurs at a range ($a\phi$) of about 0.6. At satellite re-entry ($Vf = 0.99$, $a\phi = 2.0$), the heating is about $^1/_8$ and $^1/_2$ of the maximum for turbulent and laminar flow, respectively. The dimensionless total heating ratio is shown in Fig. 12 as a function of $a\phi$. The total turbulent

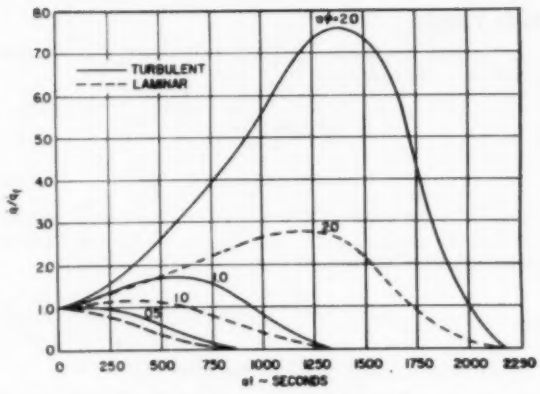

Fig. 10 Dimensionless turbulent and laminar heat flux rates versus time for a glide vehicle

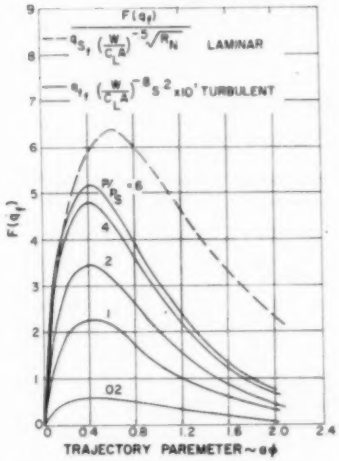

Fig. 11 Turbulent and laminar heat-transfer rates at burnout versus trajectory parameter for a glide vehicle

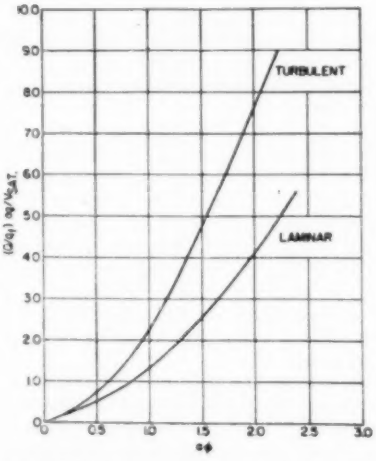

Fig. 12 Total turbulent and laminar heating ratio versus trajectory parameter for a glide vehicle

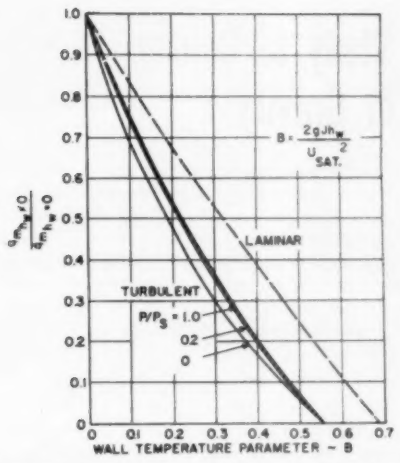

Fig. 13 Temperature correction for turbulent and laminar heating rates versus wall temperature parameter for a glide vehicle

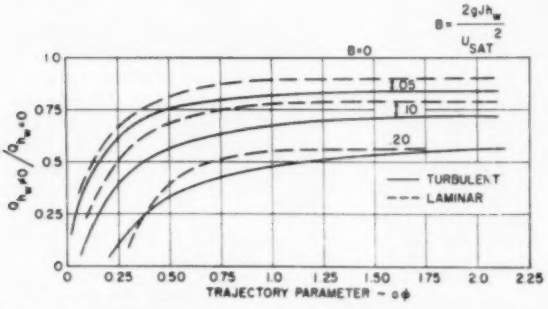

Fig. 14 Temperature correction for total heating versus trajectory parameter for a glide vehicle

heating ratio is greater than the laminar and independent of the local pressure ratio.

The correction for wall temperature is shown on Fig. 13 for the maximum turbulent and laminar heat flux and in Fig. 14 for the total heat. In a manner similar to the zero lift trajectory, the heat flux temperature correction is a function only of the wall temperature while the total heating correction is a function both of wall temperature and range. The temperature correction is greater for the laminar heating. The wall temperature has a large influence on the heat transfer to a space vehicle and must be considered for proper evaluation of a heat protection system design.

Conclusions

The effect of the trajectory on the aerodynamic heating of a blunt nosed re-entrant vehicle is summarized in Table 1. There is a direct similarity between the heating for the zero lift and high lift bodies for all the parameters except the reference velocity. The aerodynamic heating varies as $(W/C_{D,L}A)$ to the 0.8 and 0.5 power and a physical dimension (S, R_N) to the -0.2 and -0.5 power for turbulent and laminar flow, respectively. The heat-transfer rates vary roughly as the cube and the total heating varies as the square of the reference (re-entry) velocity for the zero lift bodies as shown in Table 1. For the glide vehicle the influence of the re-entry (burnout) velocity on the heat flux and

Table 1 Comparison of turbulent and laminar heating

$$\dot{q}_m, Q = k\left(\frac{W}{C_{D,L}A}\right)^m (\sin\Theta_E)^n (U_{E,sat})^o (S, R_N)^p$$

Quantity	Exponent	Turbulent A	Turbulent B	Laminar stagnation point A	Laminar stagnation point B
$\dot{q}_m$	m	0.8	0.8	0.5	0.5
	n	0.8	0	0.5	0
	o	3.48	1.88	3.2	2.2
	p	−0.2	−0.2	−0.5	−0.5
Q	m	0.8	0.8	0.5	0.5
	n	0.8	0	0.5	0
	o	2.48	2.88	2.2	3.2
	p	−0.2	−0.2	−0.5	−0.5

A zero lift vehicle
B high lift (glide) vehicle

total heating cannot be as simply described. The maximum heat flux is practically independent of the burnout velocity [equations (34) and (44)] when the range parameter $(a\phi)$ is greater than 0.39 for turbulent and 0.58 for laminar flow. For lower values of $a\phi$ the maximum heat flux is a function of the burnout velocity since the heat flux at burnout is a maximum. For a given range of flight the total heating is a function of the re-entry velocity and the maximum total heating occurs when the burnout velocity ratio equals 0.75 and 0.89 for turbulent and laminar flow, respectively. It can be stated, however, that the heat-transfer rates are roughly proportional to the square and the total heating as the cube of the glide vehicle reference (satellite) velocity.

In general, the two types of vehicles analyzed showed both extremes in the aerodynamic heating environment. The zero lift vehicle is exposed to very short time, high heat fluxes, and moderate total heating during re-entry. The high lift vehicle on the other hand is exposed to an environment of long time, low heat flux, but very high total heat inputs.

The analysis described in this paper evaluates the turbulent and laminar aerodynamic heating through the trajectory and over the surface of a re-entrant space vehicle for both zero and high lift bodies. It should prove useful for preliminary design purposes in evaluating the effect of various re-entry vehicle shapes on the aerodynamic heating.

References

1 E. R. G. Eckert, "Survey on Heat Transfer at High Speeds," WADC TR 54-70, 1954.

2 M. F. Romig, "Stagnation Point Heat Transfer for Hypersonic Flow," *Jet Propulsion*, December, 1956.

3 J. Allen and A. J. Eggers, "A Study of the Motion and Aerodynamic Heating of Missiles Entering the Earth's Atmosphere at High Supersonic Speed," NACA TN 4047, 1957.

4 A. J. Eggers, H. J. Allen, and S. E. Neice, "A Comparative Analysis of the Performance of Long-Range Hypervelocity Vehicles," NACA TN 4046, October, 1957.

5 G. Grimminger, E. P. Williams, and G. B. W. Young, "Lift on Inclined Bodies of Revolution in Hypersonic Flow," *Journal of Institute of the Aeronautical Sciences*, November, 1950.

6 E. Janke and F. Emde, "Tables of Functions," Dover Publications, New York, N. Y., 1945.

7 K. Pearson, "Tables of the Incomplete Gamma Functions," University Press, Cambridge, England, 1957.

8 L. Lees, "Laminar Heat Transfer Over Blunt Nosed Bodies at Hypersonic Flight Speeds," *Jet Propulsion*, April, 1956, p. 259.

9 M. J. Brunner and P. A. Gallagher, "A Simplified Analysis of the Aerodynamic Heating of a Blunt Body Re-Entering the Earth's Atmosphere at Hypersonic Velocity," G. E. Technical Information Series R58SD227, January, 1958.

R. SIEGEL
NASA Lewis Research Center, Cleveland, Ohio. Assoc. Mem. ASME

C. USISKIN
NASA Lewis Research Center, Cleveland, Ohio

A Photographic Study of Boiling in the Absence of Gravity

A photographic study was made to determine the qualitative effect of zero gravity on the mechanism of boiling heat transfer. The experimental equipment included a container for boiling water and a high-speed motion-picture camera. To eliminate the influence of gravity, these were mounted on a platform which was allowed to fall freely approximately 8 ft. During the free fall, photographs were taken of boiling from various surface configurations such as electrically heated horizontal and vertical ribbons. The heat flux was varied to produce conditions from moderate nucleate boiling to burnout. The results indicate that gravity plays a considerable role in the boiling process, especially in connection with the motion of vapor within the liquid.

Introduction

THE DESIGN OF POWER PLANTS and heat-exchange equipment for satellite and space vehicles has stimulated an interest in heat-transfer phenomena under the conditions of a very small or, in many cases, negligible gravity field. Heat-transfer processes such as free convection and film condensation would be expected to be strongly dependent on the body forces due to the gravity field. The boiling process is especially interesting since the dynamics of bubble motion are quite complex and are probably influenced by a number of factors. These include the buoyancy forces arising from the gravity field, and the forces resulting from surface tension and from the expansion of vapor into the bubble cavity. It is the purpose of this work to gain some insight into the importance of gravity in the boiling mechanism by making a photographic study of the boiling process in the absence of gravity.

The apparatus includes a high-speed motion-picture camera and a heated container for boiling water. These are both mounted on a platform which is allowed to fall freely a distance of about 8 ft, and motion pictures of the boiling phenomena are taken during this time. During the free fall, the inertia forces of the system exactly balance the forces due to the weight of the body, and hence the boiling takes place in a condition of apparent weightlessness. A variety of boiling conditions were observed. These include nucleate pool boiling from the bottom of a container, and boiling from both horizontal and vertical electrically heated ribbons with various heat fluxes including burnout. Only photographic information was obtained, and no attempt was made for this series of tests to determine numerical magnitudes of heat fluxes or heat-transfer coefficients.

Experimental Equipment

A schematic representation of the apparatus is shown in Fig. 1. The main component in the structure is a platform in the form of a cross, which supports a high-speed Fastex motion-picture camera and a container for boiling water. At the ends of three branches of the platform there are large guide holes through which $^1/_8$-in. vertical cables pass. The cables serve as a guide for the falling platform in case of an accident, and during a normal experimental run little or no contact is made between the platform and the cables. A balancing yoke is attached at the top of the platform and can be adjusted so that the solenoid grapple, which holds the platform from above, will be located above the center of gravity of the freely falling equipment.

The features of the apparatus are best described by considering a typical experimental run. A 400-ml beaker is carefully cleaned and partially filled with distilled water. It is then placed on a hot plate which consists of a copper block mounted on a 500-watt electric heater controlled by a Variac. If boiling is to be studied from a horizontal or vertical ribbon the electrical terminals for the ribbon are fastened to the side of the beaker and the ribbon mounted at the desired location in the water. The ribbon power was supplied by a separate 18-amp, 115-volt Variac. The ribbons used, were Nichrome, 0.006 in. thick, 0.125 in. wide, and approximately $^7/_8$ in. long. Power was then supplied to both the ribbon and the hot plate under the beaker, and the water was allowed to boil to remove absorbed gases. During the runs where boiling was observed from the

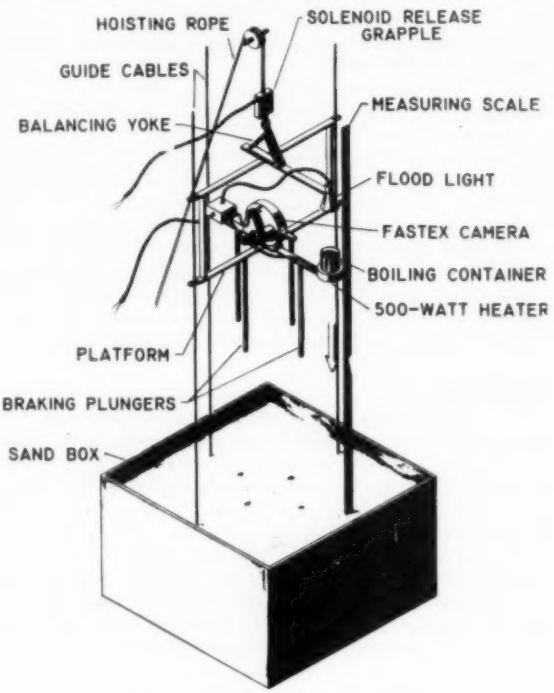

Fig. 1 Schematic diagram of apparatus

Contributed by the Heat Transfer Division and presented at the Aviation Conference, Los Angeles, Calif., March 9–12, 1959, of THE AMERICAN SOCIETY OF MECHANICAL ENGINEERS.

NOTE: Statements and opinions advanced in papers are to be understood as individual expressions of their authors and not those of the Society. Manuscripts received at ASME Headquarters, February 3, 1959. Paper No. 59—Av-37.

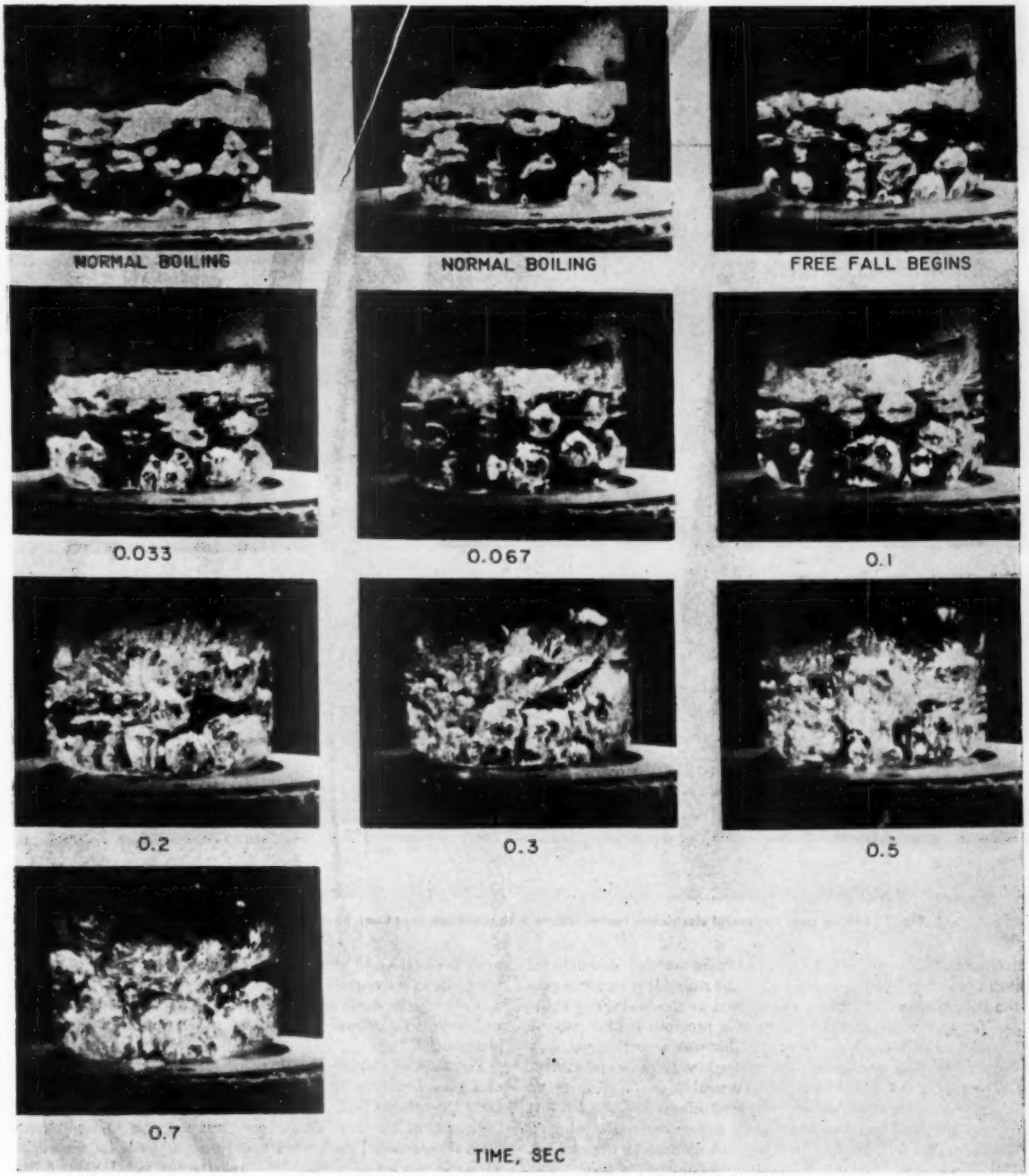

Fig. 2 Pool boiling from the bottom of a glass beaker

ribbon, the heater under the beaker was only used to help maintain the liquid near the saturation temperature and the power was such that very little bubble formation occurred at the bottom of the vessel. The platform was then hoisted eight feet, and final adjustments were made on the heater power to obtain the desired boiling condition.

The drive motor on the camera and the solenoid release grapple which supports the platform are connected to a 6-sec industrial timer. The timer will start the camera and then activate the solenoid release in sequence. Generally, the camera was started 0.3 sec before the platform began to drop, and this gave a record of the initial boiling state before the gravity field was removed. The camera speed was generally 3500 to 4000 frames per sec, which gave a total running time for 100 ft of film of about

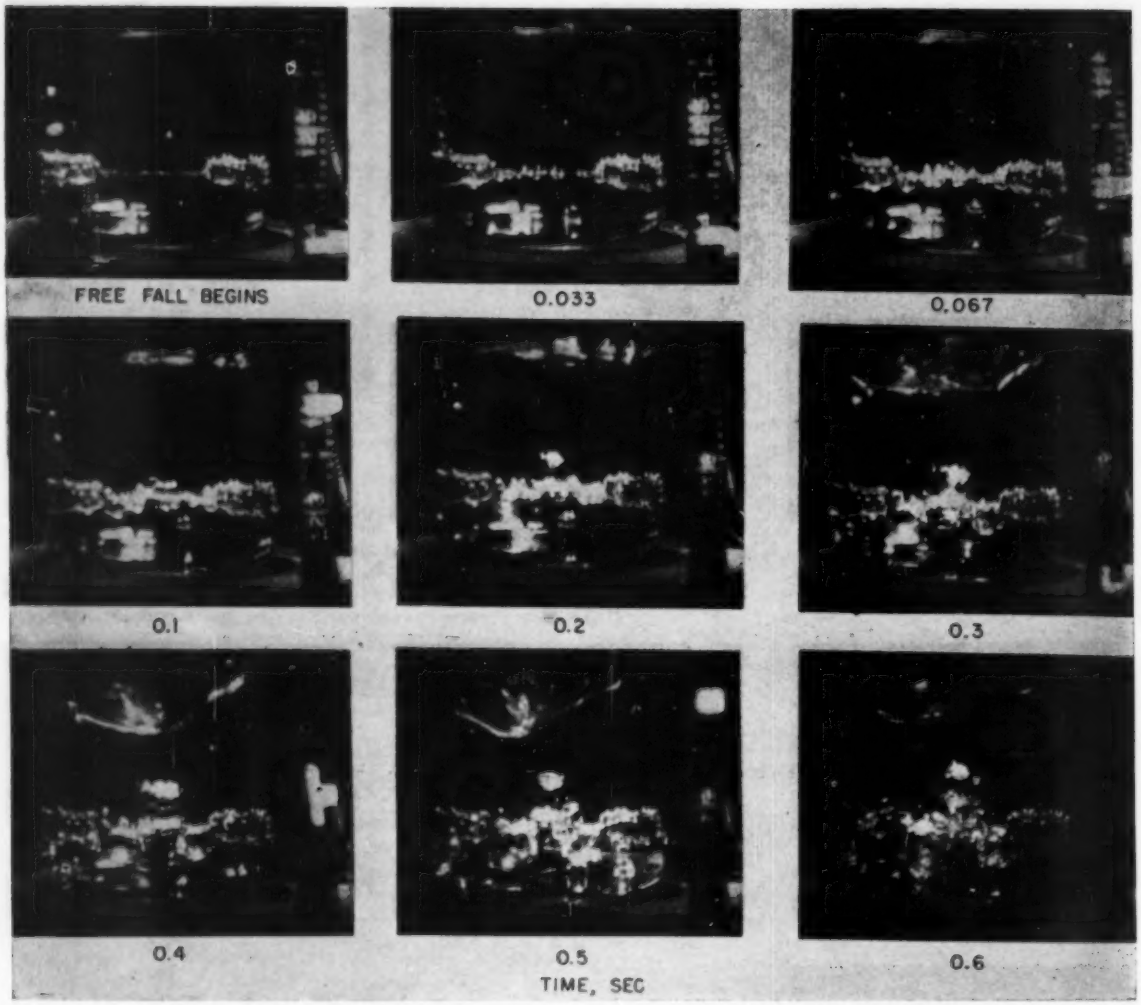

Fig. 3 Boiling from horizontal electrically heated ribbon with moderate heat flux; heat applied at beginning of free fall

1.25 sec; 0.3 sec initially, 0.7 sec during the free fall, and 0.25 sec during the deceleration at the end of the run. During some runs the boiling from the ribbon was started at the beginning of the free fall to eliminate any influence of a previous boiling process under normal gravity conditions. This was accomplished very simply by connecting the ribbon heater into the solenoid circuit.

The platform was decelerated by vertical $^1/_2$-in. pipes, fastened to the bottom of the platform, plunging into a bed of sand 3 ft deep. The sand bed was found to be quite effective in bringing the apparatus to a gradual stop without damage to the camera. The camera was, of course, well supported on the platform.

Adjacent to the boiling container a vertical measuring scale was positioned, so that a continuous record of the vertical location of the platform was recorded on the film. Also the camera recorded timing marks on the film at a rate of 120 per sec so that a record of distance versus time was obtained. This indicated that the friction in the system was negligible and that a true free fall was obtained.

Discussion of Results

The results are obtained as motion pictures and it is naturally more instructive to view these directly. A loan copy of the film is available on request from the authors. For the purposes of this report sequences of pictures were selected from the film and will serve to illustrate fairly well the description of the boiling process.

Fig. 2 shows a series of pictures for pool boiling from the bottom of a glass beaker. The first two pictures in the sequence illustrate the normal boiling process, and the third picture is at the beginning of the free fall. From observing the motion-picture films it was noted that there is only a slight inertia associated with the motion of bubbles through the liquid. Following the beginning of the free fall, the bubbles still continued to move a short distance upward and then remained suspended in the liquid. From the sequence of pictures it is seen that large bubbles are formed and increasing quantities of vapor are contained within the liquid during the zero gravity process. The liquid surface is less stable, and as evidenced by the last few pictures in the sequence, a liquid film has been pushed up the side of the beaker. It was thought that this film might be in part due to surface tension forces at the liquid glass interface which were no longer balanced by the gravity force. To examine this, a few runs were

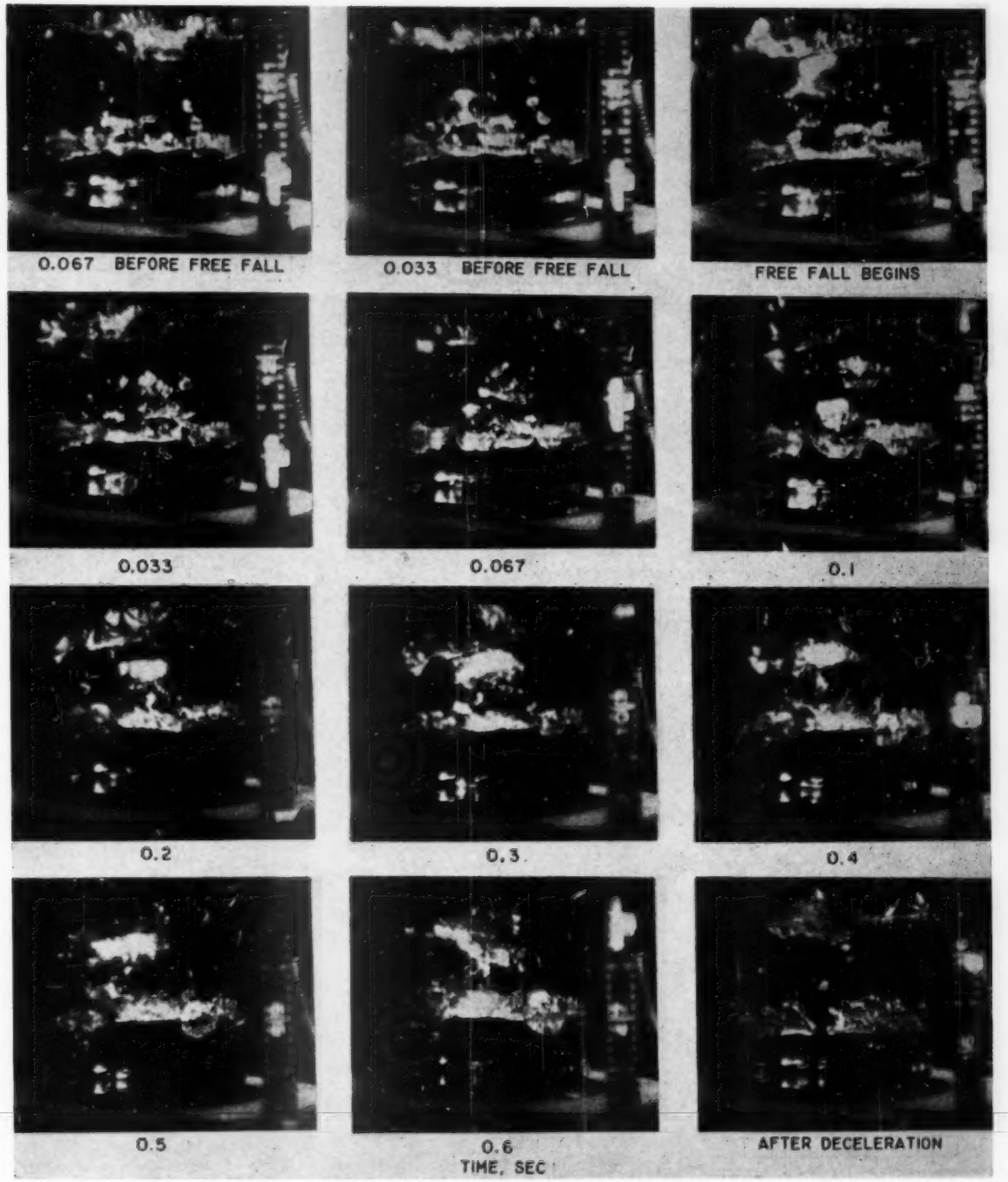

Fig. 4 Boiling from horizontal electrically heated ribbon with high heat flux and burnout

made using an unheated container, and during the 0.7-sec duration of the free fall, the liquid did not move appreciably up the side of the container. However, during boiling the agitation due to the formation and growth of the bubbles pushes liquid up the side and it remains there until the platform is decelerated.

Fig. 3 shows boiling from a horizontal electrically heated ribbon with a moderate heat flux. To eliminate the influence of bubbles formed prior to the free fall, the heating was started at the same moment that the platform was released, so all bubbles were formed under zero-gravity conditions. The hot plate under the beaker was used to maintain the fluid near the saturation temperature and a few bubbles were formed at the bottom of the con-

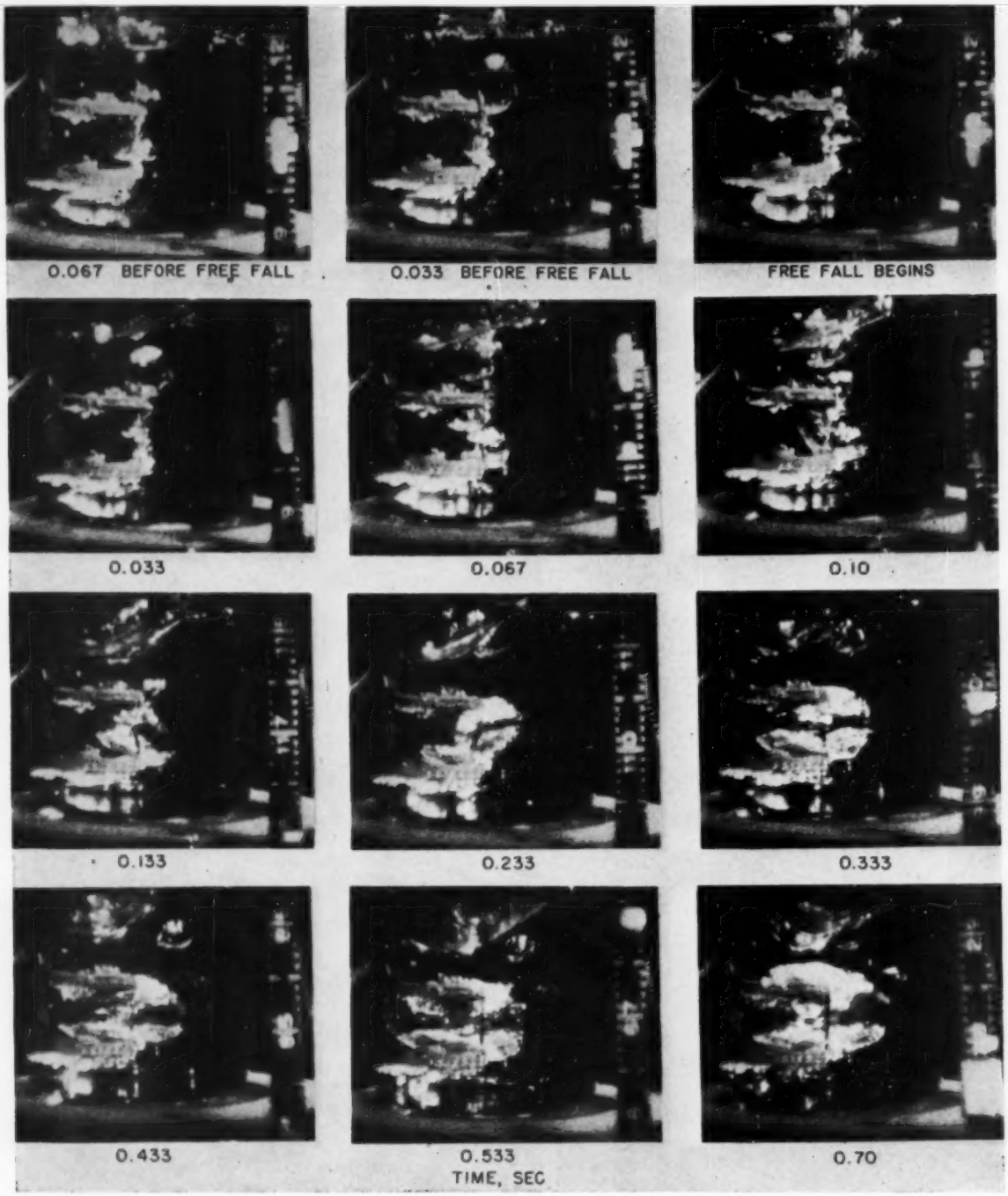

Fig. 5 Boiling from vertical electrically heated ribbon with high heat flux

tainer, but these did not interfere with the vapor formation on the ribbon. The edge of the ribbon is viewed in the pictures, and the flat heating surface extends $^1/_8$ in. into the plane of the paper. Under zero-gravity conditions the bubbles remain attached to the ribbon and grow fairly large so that large areas of the ribbon come into contact with vapor. The size which the bubbles attain during the duration of the fall is of course dependent on the magnitude of the applied heat flux. The bubble formation is equally extensive from the bottom surface of the ribbon as from the top.

In Fig. 4 we again have boiling from a horizontal ribbon, but in this case the heat flux has been raised so that the ribbon burns

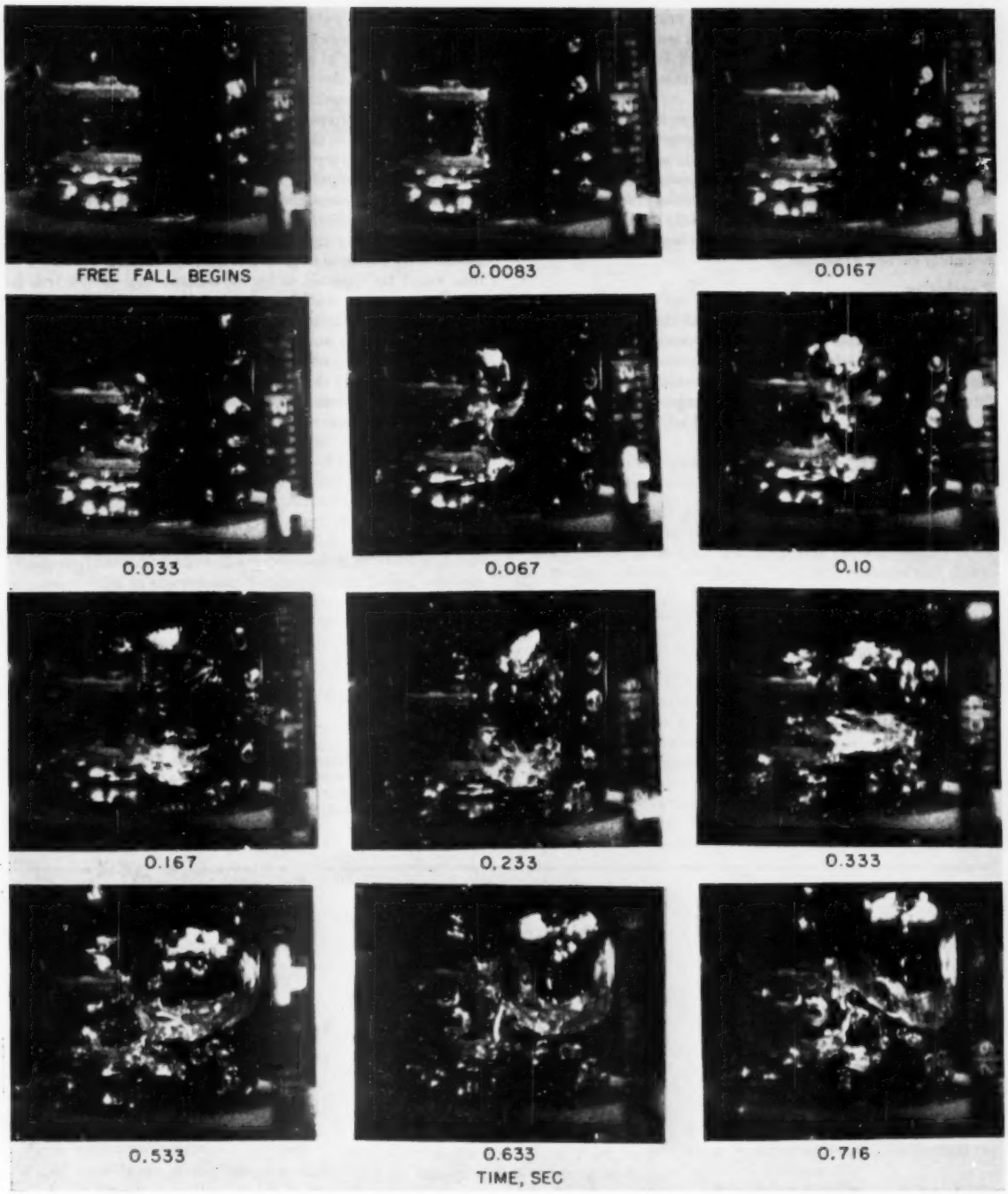

Fig. 6 Boiling from vertical electrically heated ribbon with high heat flux and burnout; heat applied at beginning of free fall

out during the free fall. Also the ribbon is heated prior to the drop, and hence, the first few pictures illustrate the normal boiling process under high heat-flux conditions. During zero gravity a single very large bubble is formed roughly 1.5 in. in diameter (beaker diameter is 3 in.). The bubble in this case is located above the ribbon and this may be due to the initial boiling process which caused the water above the ribbon to be at a higher temperature than the water below it. The last picture in the sequence shows the ribbon after deceleration. The large bubble which obscured the view of the ribbon has moved out of the liquid and the burned out ribbon can be observed.

Figs. 5 and 6 show boiling from a vertical ribbon. The posi-

tion of the ribbon between the terminal posts is seen in the first picture of Fig. 6. In Fig. 5 the heat flux is at a high level, about 10 to 20 per cent less than that required for burnout. The removal of gravity causes a single large bubble to be formed which is about 2 in. in size.

In Fig. 6 the heat flux has been raised so that the ribbon burns out during the free fall. The heating process is initiated at the beginning of the drop. At the right side of the beaker is a column of bubbles originating from a nucleation center at the bottom of the container, and these bubbles remain suspended in the fluid during the run. In the picture at 0.633 sec the lower half of the ribbon can be seen glowing, at the beginning of burnout, as a slightly curved white line.

Conclusion

The photographic study indicates that the gravity field plays a very important role in the removal of vapor from the surface in a normal pool type boiling process. In the situations observed here, the fluid was always near the saturation point and the heat fluxes were sufficiently high to form large quantities of vapor. During the free fall the vapor remained adjacent to the heating surface, and there was no evidence of bubbles being pushed away from the surface to any appreciable extent during their formation. The accumulation of vapor near the surface should make the electrical heater more sensitive to burnout, but the information obtained in this work is insufficient to make any quantitative statement on this hypothesis. In a situation where the liquid is highly subcooled, so that under ordinary conditions the bubbles form and collapse very close to the heated surface, the removal of gravity would be expected to have much less effect.

Under some circumstances the process with zero gravity may actually be a transient one. If the liquid is at the saturation temperature or slightly superheated, the bubbles at the heating surface may continue to grow indefinitely, and hence larger bubbles would be expected in an experiment with longer free fall times. If the liquid is slightly subcooled there is a chance that a steady-state equilibrium can be reached. Under these circumstances the bubbles would increase in size until their surface area is large enough to transfer to the surrounding subcooled liquid the heat being added by the heated surface. Under these conditions the bubbles would remain at a constant size. It appears that a situation like this was reached in Fig. 3.

JOSEPH P. CALLINAN
Instructor, College of Engineering, Loyola University of Los Angeles, Los Angeles, Calif.

WILLARD P. BERGGREN
Dean, College of Engineering, University of Bridgeport, Bridgeport, Conn. Mem. ASME

Some Radiator Design Criteria for Space Vehicles[1]

Nonconvective radiators of single or double-active surface design are analyzed for surface temperature distribution; also for view factors in the case of fin-and-tube geometry. Methods and examples of maximizing heat rejection per unit weight are given.

THE REJECTION OF SURPLUS HEAT during space flight requires possibly for the first time the design of radiators that are strictly radiators.

Radiator configurations for space vehicles may be classified as single-surface or double-surface. The former type would be built into the skin of the vehicle (Fig. 1); the latter would be independent assemblies carried in the plane of the vehicle axis (Fig. 2). In both cases the vehicle should be oriented (at least during periods of heat rejection) to keep the radiator surface in the same plane as the solar vector, unless shielded from solar radiation by the vehicle. Double-surface radiators might be nose-mounted, as indicated in Fig. 2(*a*), position 1, for minimum energy interception by the vehicle.

Single-surface radiators, although economical in terms of structural mass, suffer in effectiveness because of less "active" surface than two-sided designs; also they create insulation problems at the inner surface. On the other hand, double-surface radiators are likely to contain concavities or interior corners occasioned by minimum mass designs. Fin portions, material connecting tubes, Fig. 2(*b*), of these radiators have lower surface temperatures than metal in contact with the heat-transfer fluid; indeed the fin-temperature distributions are significantly influenced by view factors, as illustrated in Appendix 3 (Fig. 12). An analytic evaluation of geometric view factors of tubes and fins, for design of Fig. 2(*b*), is made in Appendixes 1 and 2, respectively.

[1] Study performed at Rocketdyne Division, North American Aviation, Inc., Los Angeles, Calif.

Contributed by the Heat Transfer Division and presented at the Aviation Conference, Los Angeles, Calif., March 9–12, 1959, of THE AMERICAN SOCIETY OF MECHANICAL ENGINEERS.

NOTE: Statements and opinions advanced in papers are to be understood as individual expressions of their authors and not those of the Society. Manuscript received at ASME Headquarters, January 28, 1959. Paper No. 59—Av-29.

Radiator Analysis

From an analytical point of view three general types of radiators have been considered in this study. These are:

1 Radiators whose surfaces have a constant temperature in the direction normal to the direction of the flow of fluid ($\partial T/\partial x = 0$) and whose geometric view factor F is 1.0, Fig. 1(*b*).

2 Radiators which have intermittent fluid passages and, therefore, cyclic variation in the surface temperature in the direction normal to that of fluid flow, and whose geometric view factor is 1.0, Fig. 1(*c*).

3 Radiators which have intermittent fluid passages and whose view factor is a function of position on the surface, Fig. 2(*b*).

1 Flat Parallel-Plane Radiators (Radiation From One or Both Sides). $F = 1.0$ and $\partial T/\partial x = 0$. Consider thermal radiation to an environment of zero degrees Rankine from a radiator consisting of two parallel planes enclosing a flowing fluid, Fig. 3. Incident solar radiation has been assumed zero by orientation. Re-radiation and the interception of radiation by the supporting vehicle have been ignored.

Nomenclature

A = surface area
B = fin width
C = constant of integration
c_p = specific heat at constant pressure of radiator fluid
D = outer diameter of tube
E = dimension of radiator normal to flow
F_f = fin view factor
F_n = view factor in plane normal to tubes
F_t = tube view factor
F_α = view factor at a position α on the tube
h = convective heat-transfer film coefficient
H_{fg} = heat of vaporization of fluid
k = thermal conductivity of radiator material
$K_1 = \sqrt{0.4\,\sigma\epsilon/kt\,T_2^3}$
$K_2 = \sqrt{0.8\,\sigma\epsilon/kt\,T_2^3}$
$K(\phi) = \int_0^{\pi/2} \frac{d\theta}{\sqrt{1 - \sin^2\phi \sin^2\theta}}$
L = dimension parallel to direction of flow
N = normal to tube or fin
p = $2(1 + B/D)$
Q = heat rejection rate
t = fin thickness
T_1, T_2 = tangents to tube surface
T = $T_{xy} = f(x, y)$, surface temperature
T_{1y} = tube surface temperature at a position y
T_{2y} = mid-fin surface temperature at a position y
T_b = fluid bulk temperature
T_{1m} = fourth root-mean-fourth power tube surface temperature, equation (9*d*)
$\Delta T = T_{1y} - T_{2y}$
$T' = dT/dx$
$T'' = d^2T/dx^2$
w = fluid flow rate per tube, lb/sec
W = radiator weight
x = co-ordinate in radiator plane normal to direction of flow
y = co-ordinate parallel to direction of fluid flow
z = co-ordinate normal to plane of radiator
$X = \frac{x - D/2}{B/2}$
α = angular position on tube surface
ϵ = total emissivity of radiator surface
η = fin effectiveness for thermal radiation
θ = angle between plane normal to fluid flow and other planes containing normal line N
σ = Boltzmann constant
$\tau = T/T_{2y}$
ϕ = angle of obstructed view from fin or tube surface
$\psi = \pi/2 - \phi$ = view angle from normal to surface

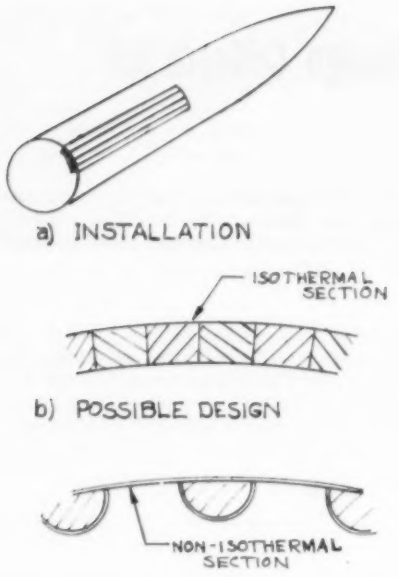

Fig. 1 Single-surface space radiators

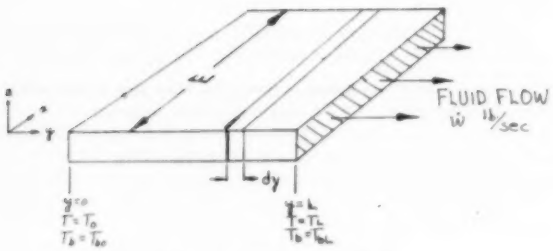

Fig. 3 Flat parallel-plate radiator

From a steady-state heat balance on the elemental volume of width dy, Fig. 3, the heat radiated from the surface equals the heat lost by the fluid.

$$-\sigma\epsilon T^4 E dy = \dot{w} c_p dT_b \tag{1}$$

where

$$T_b = \left(\frac{1}{h_b} + \frac{t}{k}\right)\sigma\epsilon\, T^4 + T \tag{2}$$

If the radiator is constructed of a thin material of high thermal conductivity and if the convective heat-transfer film coefficient on the fluid side is large, i.e., if

$$\frac{1}{h_b} + \frac{t}{k} \ll \frac{1}{\sigma\epsilon T^3}$$

then

$$\frac{dT_b}{dy} \approx \frac{dT}{dy}. \tag{2a}$$

Substituting (2a) into (1) and integrating between $y = 0$ and $y = L$:

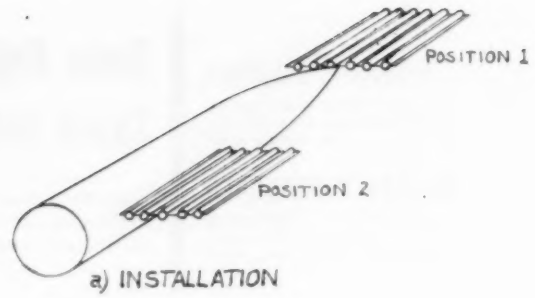

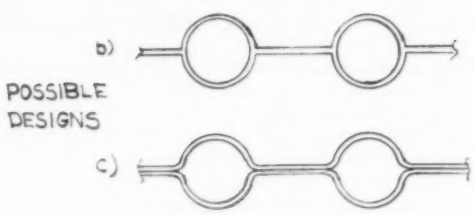

Fig. 2 Double-surface space radiators

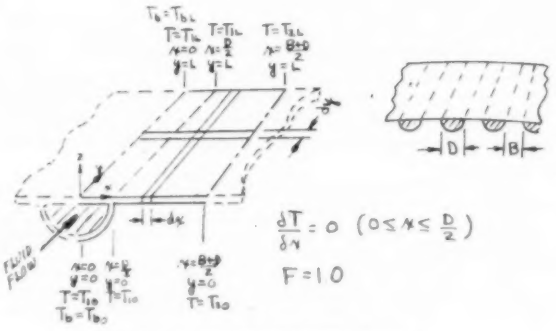

Fig. 4 Intermittent passage radiator

$$EL = A = \frac{\dot{w}\bar{c}_p}{3\sigma\epsilon}\left[\frac{1}{T_L^3} - \frac{1}{T_0^3}\right]. \tag{3}$$

If the fluid is condensing and the surface temperature can be assumed constant then

$$A = \frac{\dot{w}H_{fg}}{\sigma\epsilon T^4} \tag{3a}$$

where H_{fg} is the heat of evaporation.

The total heat rejected is, $Q = \dot{w}\bar{c}_p(T_{b0} - T_{bL})$ (4)

(or $\dot{w}H_{fg}$).

These equations (2), (3), and (4) are sufficient to estimate and minimize sizes and weights of radiators of the first classification.

2 Intermittent Passage, Flat or Convex-Surface Radiators (Radiation From One Side). $F = 1.0$ and $\partial T/\partial x = f(x)$. Consider thermal radiation from the flat (or convex) side of the radiator geometry shown in Fig. 4, assuming no solar or other incident radiation. Assume that heat transferred to or from the opposite side is negligible. Assume also that $\partial T/\partial x = 0$ from $x = 0$ to $x = D/2$ and therefore $T = f(y) = T_{1y}$ for $0 \le x \le D/2$ and $0 \le y \le L$, and that $T = f(x, y) = T_{xy}$ for $D/2 \le x \le \dfrac{B+D}{2}$ and $0 \le y \le L$.

From a steady-state heat balance on the surface area element $\left(\frac{B+D}{2}\right) dy$ the heat radiated equals the heat lost by the fluid flowing in the passage:

$$\frac{\dot{w}}{2} c_p dT_b = -\sigma\epsilon \left[T_{1y}{}^4 \frac{D}{2} + \eta T_{1y}{}^4 \frac{B}{2} \right] dy \tag{5}$$

where

$$\eta \equiv \frac{\int_{D/2}^{\frac{B+D}{2}} T_{xy}{}^4 dx}{T_{1y}{}^4 B/2} \tag{6}$$

and it is assumed that an appropriately determined value of η is a constant, $\bar{\eta}$, over the interval of integration in the y-direction.

Making the substitution of equation (1a) and integrating from $y = 0$, $T = T_{10}$ to $y = L$, $T = T_{1L}$,

$$L = \frac{\dot{w} c_p}{3\sigma\epsilon(D + \bar{\eta}B)} \left(\frac{1}{T_{1L}{}^3} - \frac{1}{T_{10}{}^3} \right); \tag{7}$$

if the fluid is condensing and it can be assumed that

$$\frac{dT_b}{dy} = \frac{dT_1}{dy} = 0,$$

then

$$L = \frac{\dot{w} H_{fg}}{\sigma\epsilon T_1{}^4 (D + \bar{\eta}B)}. \tag{7a}$$

It is now necessary to evaluate $\bar{\eta}$. Consider a steady-state heat balance on the volumetric element $t dx dy$ in Fig. 4. If we assume that conduction in only the x-direction is important, then

$$-kt \frac{dT}{dx} dy = -kt \frac{d}{dx} \left(T + \frac{dT}{dx} dx \right) dy + \sigma\epsilon T^4 dx dy$$

or

$$\frac{d^2T}{dx^2} = \frac{\sigma\epsilon}{kt} T^4 \tag{8}$$

Integrating and applying the boundary conditions $\left(\text{at } x = \frac{B+D}{2}, T = T_{2y}, \text{ and } \frac{dT}{dx} = 0\right)$,

$$\frac{dT}{dx} = \sqrt{0.4 \frac{\sigma\epsilon}{kt} (T^5 - T_{2y}{}^5)}. \tag{8a}$$

By substituting with equation (8a) for dx in equation (6) and integrating equation (6) from $T = T_{1y}$ to $T = T_{2y}$:

$$\eta B = \frac{1}{T_{1y}{}^4} \sqrt{1.6 \frac{kt}{\sigma\epsilon} (T_{1y}{}^5 - T_{2y}{}^5)}. \tag{9}$$

If we let

$$\tau = \frac{T}{T_{2y}} \quad \text{and} \quad K_1 = \sqrt{0.4 \frac{\sigma\epsilon}{kt} T_{2y}{}^3} \tag{9a}$$

then equation (9) becomes

$$\eta B = 2 \frac{kt}{\sigma\epsilon} K_1 \frac{T_{2y} \sqrt{\tau^5 - 1}}{T_{1y}{}^4} \tag{9b}$$

It will be shown later that

$$\bar{\eta}B = \frac{1}{T_{1m}{}^4} \sqrt{1.6 \frac{kt}{\sigma\epsilon} (T_{1m}{}^5 - T_{2m}{}^5)}, \tag{9c}$$

where

$$T_{1m} = \left(\frac{T_{10}{}^4 + T_{1L}{}^4}{2} \right)^{1/4}. \tag{9d}$$

In other words, the fin effectiveness for the radiator is evaluated at the fourth root of the mean fourth power of T_{1y}.

An expression must now be derived relating the fin half-width, $B/2$, to the fin temperature drop, $T_{1y} - T_{2y}$. Making the substitutions of equation (9a) and rearranging, equation (8) becomes

$$K_1 dx = \frac{d\tau}{\sqrt{\tau^5 - 1}} \tag{10}$$

Integrating from $x = \frac{B+D}{2}$, $\tau = 1$ to $x = \frac{D}{2}$, $\tau = \tau_1 = \frac{T_{1y}}{T_{2y}}$:

$$K_1 \frac{B}{2} = \int_1^{\tau_1} \frac{d\tau}{\sqrt{\tau^5 - 1}}. \tag{11}$$

Equation (11) was evaluated graphically and the resulting plot of $K_1 B/2$ versus τ_1 is shown in Figs. 5 and 6. Therefore, given k, t, and ϵ, knowing T_{1y} and T_{2y}, $B/2$ can be found directly. When T_{1y} and $B/2$ are known, T_{2y} can be found by a trial and error method. Using equations (7), (9c), (11), (2), and (4) the size and weights of radiators of the second classification can be estimated and the weights can be minimized.

The recommended procedure for using the previously derived equations for the design of a minimum weight radiator can best be described by working a typical example.

Consider a radiator of the type shown in Fig. 4 which is cooling 0.1 lb of hydrogen per second, per radiator tube from 2000 to 1500 deg R ($\bar{c}_p = 3.4$ Btu/lb deg R). Assume that structural and fabrication requirements necessitate a fin thickness, t, of 0.015 in. and that $D = 0.5$ in., $\epsilon = 0.95$, $k = 30$ Btu/hr ft deg R, density = 0.285 lb/in^3 and the convective heat-transfer film coefficient on the fluid side, h, is 2000 Btu/hr ft^2 deg R. Determine the dimensions, B and L, which will reject this amount of heat with the minimum weight of radiator structure (neglect the fact that part of the weight might ordinarily be considered vehicle structure weight). Note that in this example the material modulus, kt, is specified; however, in general kt should also be allowed to vary within the structurally prescribed limits when determining the minimum radiator weight.

It has been found that by determining a single value of η over the length, L, evaluated at T_{1m}, gives sufficient accuracy and conservative results as compared with an incremental method. From equation (2), $T_{10} = 1986$ and $T_{1L} = 1496$ deg R, and therefore by equation (9d), $T_{1m} = 1789$ deg R.

If the fin width B varies such that $T_{1m} - T_{2m}$ takes on values of 50, 100, 200, and 300 deg R, the corresponding values of $\bar{\eta}B$ can be determined using equation (9). Then from equation (7) and Fig. 5 or 6 we can determine L and B, respectively. Thus the radiator is geometrically specified and for each value of $T_{1m} - T_{2m}$ the radiator weight per tube can be calculated (Table 1). By plotting radiator weight and $B/2$ versus T_{2m} the minimum weight and corresponding fin width which will cool the hydrogen can be determined (Fig. 7).

From Fig. 7 the minimum weight of radiator is 5.035 lb/tube where $B/2$ is 0.31 in. ($B/D = 1.24$) and $T_{2m} = 1656$ deg R. Note that this does not correspond to minimum surface area.

Greater accuracy can be obtained if the radiator is analyzed in longitudinal increments of equal heat rejection. If c_p is assumed

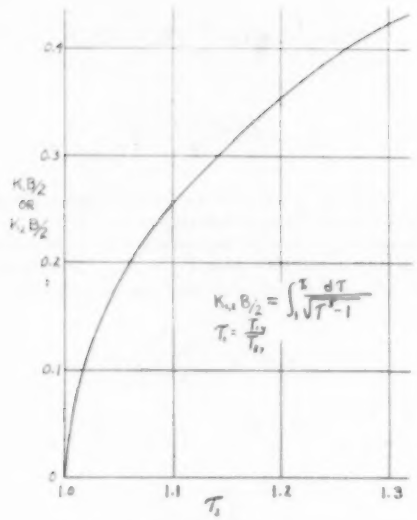

Fig. 5 $K_1B/2$ or $K_2B/2$ versus τ

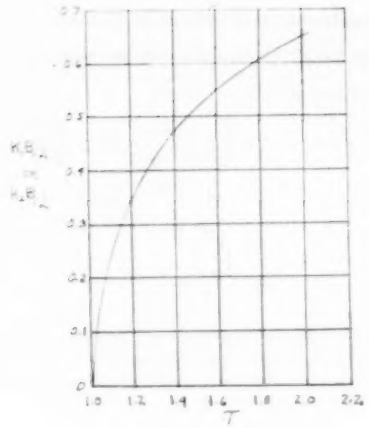

Fig. 6 $K_1B/2$ or $K_2B/2$ versus τ

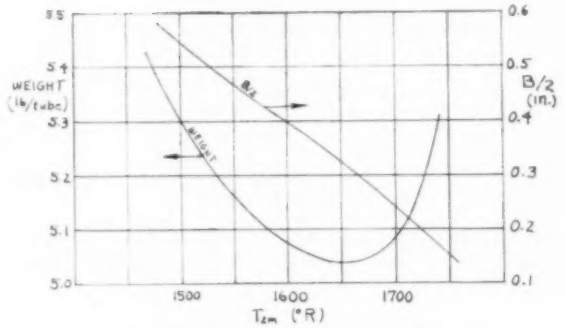

Fig. 7 Example of radiator optimization

constant over the temperature range this then becomes increments of equal fluid bulk temperature drop. This was done for the case of Table 1 where $B/2 = 0.410$ in. Each of these increments was handled in a manner similar to the example given except that T_{2m} was found from Fig. 5 or 6 by a trial and error process for each increment. Knowing T_{1m} and $B/2$, a value of T_{2m} is assumed, thus enabling the computation of $K_1B/2$. From Fig. 5 or 6, knowing τ_1, $K_1B/2$ can be read off the ordinate and checked with the previously computed value. This process is repeated until satisfactory agreement has been reached. The increment of equal fluid bulk temperature chosen was 100 R and the results are shown in Table 2.

In comparing the results of the iterative analysis, $L = 46.26$ ft, with that determined in the example of Table 1 ($B/2 = 0.410$ in.), $L = 47.0$ ft, it can be seen that the latter is slightly larger and therefore represents a conservative estimate. Based upon this comparison it is recommended that in general the former method be used.

3 Double-Surface Radiators: Fin-and-Tube Construction. The fin-and-tube configuration lends itself well to a double-surface, high-pressure, minimum-weight design. View factors, considering three-dimensional effects, have been computed for this design for a wide range of the ratio B/D (Appendixes 1 and 2). A design, Fig. 2(*c*), approximating the fin-and-tube arrangement, which might be easily fabricated and satisfactory for low or medium pressure fluids, would have higher view factors. Hence analyses on the configuration of Fig. 2(*b*) would be conservative for this design.

In this analysis it is assumed that at a given position in the y-direction the temperature on the surface of the tube is constant

Table 1 Radiator design summary

T_{1m}, deg R	T_{2m}, deg R	$\bar{\eta}B$, ft	L, ft	$B/2$, in.	Weight, lb/tube	Surface area, ft²/tube
1789	1739	0.0294	63.3	0.169	5.31	4.41
1789	1689	0.0410	54.4	0.258	5.06	4.60
1789	1589	0.0541	47.0	0.410	5.09	5.17
1789	1489	0.0629	43.1	0.562	5.34	5.85

Heat rejected per tube = 17 Btu/sec = 17.92 kw

Table 2 Results of iterative analysis ($B/2 = 0.410$ in.)

T_b, deg R	T_{1y}, deg R	T_{1m}, deg R	T_{2m}, deg R	$\bar{\eta}B$, ft	ΔL, ft	y, ft
2000	1986	1940	1690	0.0506	5.67	0
1900	1889	1840	1630	0.0518	7.56	5.67
1800	1791	1742	1560	0.0548	8.41	13.23
1700	1693	1645	1495	0.0556	10.80	21.64
1600	1594	1541	1416	0.0588	13.82	32.44
1500	1496					46.26 = L

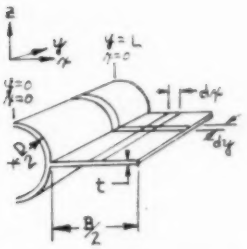

Fig. 8 Fin-and-tube construction

(in the circumferential direction), i.e., on the tube surface $T = f(y) = T_{1y}$ and that the surface temperature on the fin is a function of x and y, $T = T_{xy}$.

From a steady-state heat balance on the volumetric element of width dy (Fig. 8), neglecting solar and other incident radiation,

$$\frac{\dot{w}}{2} c_p dT_b = -\sigma\epsilon \left[F_t T_{1y}^4 \left(\frac{\pi D}{2} - t \right) + \int_{D/2}^{\frac{B+D}{2}} F_f T_{xy}\, dx \right] dy,$$

where F_t is constant and F_f is a function of x $\left(D/2 \leq x \leq \frac{B+D}{2} \right)$ for a given B/D ratio. Integrating as in Section 2,

$$L[(\pi D - 2t)F_t + \tilde{\eta} B] = \frac{\dot{w} c_p}{3\sigma\epsilon} \left[\frac{1}{T_{1L}^3} - \frac{1}{T_{1b}^3} \right] \qquad (12)$$

or

$$= \frac{\dot{w} H_{fg}}{\sigma\epsilon T_1^4}$$

where

$$\tilde{\eta} \equiv \frac{\int_{D/2}^{\frac{B+D}{2}} F_f T_{xm}^4 dx}{T_{1m}^4 B/2}, \qquad (12a)$$

$\tilde{\eta}$ is again evaluated at T_{1m}.

As a result of a heat balance on the volumetric element $t dx dy$ (Fig. 8) with thermal radiation from both sides, it can be shown that

$$\frac{d^2T}{dx^2} = \frac{2\sigma\epsilon}{kt} F_f T_{xy}^4 \qquad (13)$$

with the following boundary conditions:

at $x = \frac{D}{2}$, $T = T_{1m}$ (known)

at $x = \frac{B+D}{2}$, $T = T_{2m}$ (must specify)

and $\frac{dT}{dx} = 0$ (symmetry at mid-fin)

Because of the strong variation of F_f with x, the solution of equation (13) requires a rather tedious trial and error step integration (Appendix 3) and the result is a plot of $F_f T^4$ versus $\frac{x - D/2}{B/2}$ (for a typical example see Fig. 11). From a plot of this type $\tilde{\eta}$ can be determined graphically. From equation (13) and referring to Fig. 11

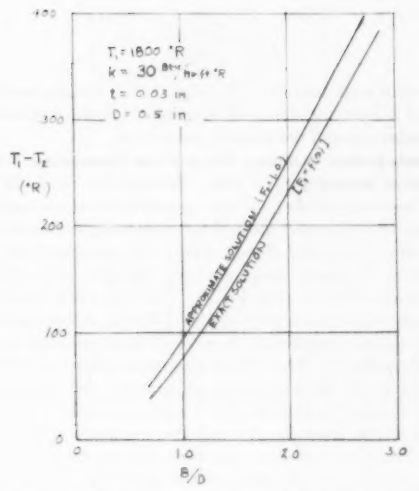

Fig. 9 Fin temperature drop, $T_1 - T_2$ versus B/D (fin-and-tube construction, condensing fluid)

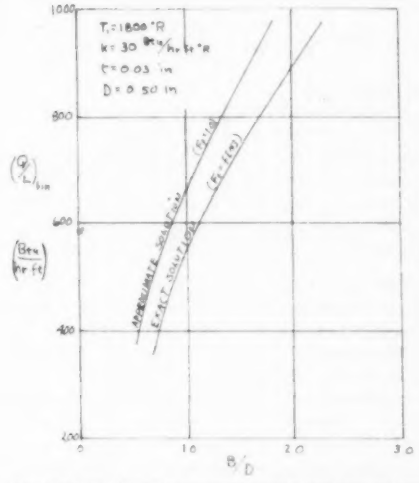

Fig. 10 Heat radiated from fin per unit longitudinal length (fin-and-tube construction, condensing fluid)

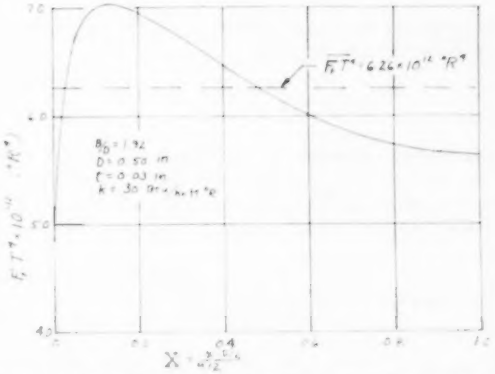

Fig. 11 Fin effectiveness versus position on fin as influenced by fin view factor (T_1 = 1800 deg R, T_2 = 1600 deg R)

$$\bar{\eta} = \frac{\overline{F_f T_{xm}^4}}{T_{1m}^4} \tag{13a}$$

Thus with equations (2), (4), (12*a*), (13*a*), and the methods of Appendix 3, radiator sizes and weights of the third classification can be estimated and the weights minimized.

4 Double-Surface Radiators: Fin-and-Tube Construction. (Approximate Solution Assuming $F_f = 1.0$.) Because the methods of Appendix 3 are so unwieldy and time consuming it was deemed necessary to present a simpler method for estimating sizes and weights of radiators of the third classification. By assuming that the fin view factor F_f equals one, equation (13) reduces to the same easily solvable form as equation (8). In comparing the results of an example worked below using the methods of this section with the exact solution worked in Appendix 3 it is seen that assuming $F_f = 1.0$ results in a 10 to 20 per cent overestimation of heat rejections by the fin portion of the radiator, Fig. 10. It is proposed that, as a result of future analytical work, a generalized correction factor could be generated (possibly a function of B/D) which could readjust the fin heat rejection rate, as calculated by the approximate method, to show closer agreement with the exact solution.

Assuming $F_f = 1.0$ in equations (12*a*) and (13) and integrating equation (13) we find

$$\bar{\eta}B = \frac{1}{T_{1m}^4}\sqrt{3.2\,\frac{kt}{\sigma\epsilon}\,(T_{1m}^5 - T_{2m}^5)} \tag{14}$$

equation (11) becomes

$$K_2 B/2 = \int_1^{\tau_1} \frac{d\tau}{\sqrt{\tau^5 - 1}} \tag{15}$$

where

$$\tau = \frac{T}{T_{2y}} \quad \text{and} \quad K_2 = \sqrt{0.8\,\frac{\sigma\epsilon}{kt}\,T_{2y}^3} \tag{15a}$$

and, therefore, Figs. 5 and 6 are applicable.

The use of equations (12), (14), and (15) for estimating the sizes and weights of radiators of the third classification can again best be demonstrated by means of an example. Consider a fluid (of negligible density) condensing in a fin and tube type of radiator under conditions such that the tube outer surface temperature is constant, T_1. Assume $T_1 = 1800$ R, $k = 30$ Btu/hr ft R, both tube and fin thickness = 0.03 in., $D = 0.5$ in., and $\epsilon = 0.95$. Equation (12) can be rearranged to give the heat rejected per foot of length,

$$Q/L = \frac{\dot{w}H_{fg}}{L} = [(\pi D - 2t)F_f + \bar{\eta}B]\sigma\epsilon T_1^4. \tag{16}$$

Considering a section which includes half a tube (Fig. 8), the heat rejected from the tube section is

$$(Q/L)_t = \left(\frac{\pi D}{2} - t\right)\sigma\epsilon F_f T_1^4 \tag{16a}$$

and the heat rejected from the half fin is

$$(Q/L)_f = \frac{\bar{\eta}B}{2}\,\sigma\epsilon T_1^4 = ktK_2T_2\sqrt{\tau^5 - 1}. \tag{16b}$$

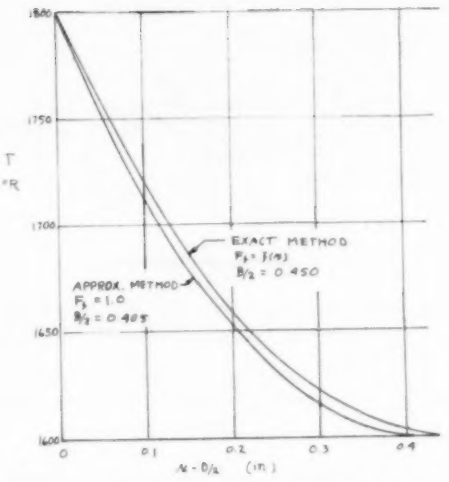

Fig. 12 Temperature distribution on fin ($T_1 = 1800$ deg R, $T_2 = 1600$ deg R)

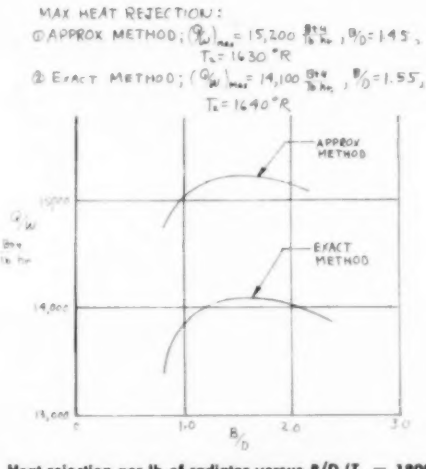

Fig. 13 Heat rejection per lb of radiator versus B/D ($T_1 = 1800$ deg R, $t = 0.03$ in., $D = 0.50$ in., $k = 30$ Btu/hr ft deg R)

If we consider a range of fin temperature drops, $T_1 - T_2$, the corresponding fin widths, $B/2$, can be found using Figs. 5 or 6, the heat rejected per unit length can be computed from equation (16) and the weights can be calculated, knowing the geometry.

The relationship obtained between $(T_1 - T_2)$ and $B/2$ is shown in Fig. 9 and is compared with the exact result from Appendix 3. The heat radiated per unit length from a half fin is shown in Fig. 10, along with the corresponding result from the exact solution. The results are summarized in Table 3 and Fig. 13 where the maximum heat rejection per unit weight is about 15,220 Btu/hr, lb for $B/D = 1.45$ for the approximate solution and 14,100 Btu/hr, lb for $B/D = 1.55$ for the exact solution.

Table 3 Fin-and-tube design summary ($T_1 = 1800$ deg R)

T_2, deg R	τ	$K_2B/2$,	K_2, ft^{-1}	$B/2$, in.	B/D	Q/L, $\left(\frac{\text{Btu}}{\text{hr ft}}\right)$	W/L, lb/ft	Q/W, $\left(\frac{\text{Btu}}{\text{hr lb}}\right)$
1750	1.029	0.135	9.64	0.168	0.672	1320	0.0926	14,250
1700	1.059	0.196	9.25	0.254	1.016	1521	0.1016	15,080
1600	1.125	0.285	8.44	0.405	1.620	1779	0.1170	15,210
1500	1.200	0.354	7.67	0.554	2.216	2003	0.1323	15,140

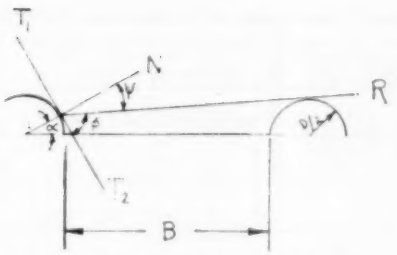

Fig. 14 Determination of view factors on tube

APPENDIX 1

View Factors on the Tube

In Fig. 14, the plane view of space from a point A on the tube surface is bounded by the tangents AT_1 and AR. The following expression gives the complementary angles ψ and ϕ (between AR and the normal, AN; and AR and the tangent AT_2, respectively)

$$\sin \psi = \cos \phi = \frac{p \sin \alpha \sqrt{p^2 - 2p \cos \alpha} - (p \cos - 1)}{p^2 - 2p \cos \alpha + 1} \tag{17}$$

where $p = 2(1 + B/D)$ and α defines point A. To find the three-dimensional view factor we consider an angle θ in the A-N plane (normal to the plane of the sketch) and measured from the plane of the sketch (Fig. 14). The space view factor for any position A is then

$$F_\alpha = \frac{1}{2} + \frac{1}{\pi} K(\phi) \cos \phi. \tag{18}$$

$K(\phi)$ is an elliptic integral

$$K(\phi) = \int_0^{\pi/2} \frac{d\theta}{\sqrt{1 - \sin^2 \phi \sin^2 \theta}} \tag{19}$$

The quadrant, $0 \leq \alpha \leq \pi/2$, was divided into six equal sectors ($\alpha = 7.5$ deg, 22.5 deg, etc.) and the average value of the view factor for the tube was determined and is shown in Fig. 15. It is interesting to note the comparatively narrow limits of tube view factor: at $B/D = 0$, $F_t = 0.648$ and at $B/D = \infty$, $F_t = 0.873$.

APPENDIX 2

View Factors on the Fin

The two-dimensional view of space from point x on the fin is bounded by tangents xT_1 and xT_2. The radiation received at a point S is proportional to $\cos \psi = \sin \phi$. The view factor in the plane of the sketch (Fig. 16) is the ratio of the radiation emitted between the obstruction angles ϕ_1 and ϕ_2 to that emitted by an unobstructed plane

$$F_n = \frac{\int_{\phi_1}^{\pi/2} \sin \phi d\phi + \int_{\phi_2}^{\pi/2} \sin \phi d\phi}{2 \int_0^{\pi/2} \sin \phi d\phi} = \frac{1}{2} [\cos \phi_1 + \cos \phi_2]. \tag{20}$$

To obtain the complete three-dimensional view factor we consider the view limits ϕ_1 and ϕ_2 established by intersections of

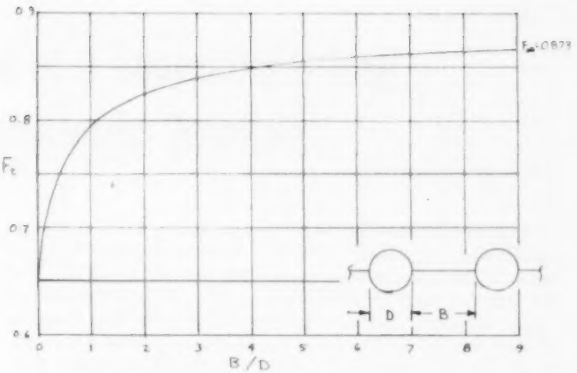

Fig. 15 Tube geometric view factor versus B/D (view of space)

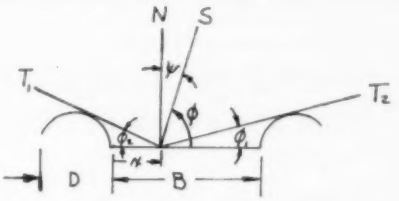

Fig. 16 Determination of view factors on fin

several planes (including the normal xN and making angles θ with the plane of the sketch, Fig. 16) with the tangent planes xT_1 and xT_2. Integration of these view factors F_θ (expressions similar to equation 20) gives the complete fin view factor. The cut-off angles ϕ_1 and ϕ_2 in a plane defined by θ are determined by

$$\tan \phi_{\theta 1} = \tan \phi_1 \cos \theta, \quad \tan \phi_{\theta 2} = \tan \phi_2 \cos \theta; \tag{21}$$

whence

$$\cos \phi_{\theta 1} = \frac{1}{\sqrt{1 + \tan^2 \phi_1 \cos^2 \theta}}, \qquad \cos \phi_{\theta 2} = \frac{1}{\sqrt{1 + \tan^2 \phi_2 \cos^2 \theta}}. \tag{22}$$

Replacing $\cos \phi_1$ and $\cos \phi_2$ in equation (20) by the expressions of (22) and integrating on θ through a quadrant,

$$F_f = \frac{\int_0^{\pi/2} \frac{d\theta}{\sqrt{1 + \tan^2 \phi_1 \cos^2 \theta}} + \int_0^{\pi/2} \frac{d\theta}{\sqrt{1 + \tan^2 \phi_2 \cos^2 \theta}}}{2 \int_0^{\pi/2} d\theta} \tag{23}$$

The denominator of equation (23) "normalizes" the view factor (amounting to evaluation of the numerator for "full view" $\phi_1 = \phi_2 = 0$). Each term in the numerator of equation (23) may again be expressed in terms of a "complete" elliptic integral (cf, equation 19):

$$\int_0^{\pi/2} \frac{\cos \phi_{1,2} \, d\theta}{\sqrt{1 - \sin^2 \phi_{1,2} \sin^2 \theta}} = K(\phi_{1,2}) \cos \phi_{1,2}. \tag{24}$$

These substitutions yield

$$F_f = \frac{1}{\pi} [K(\phi_1) \cos \phi_1 + K(\phi_2) \cos \phi_2], \tag{25}$$

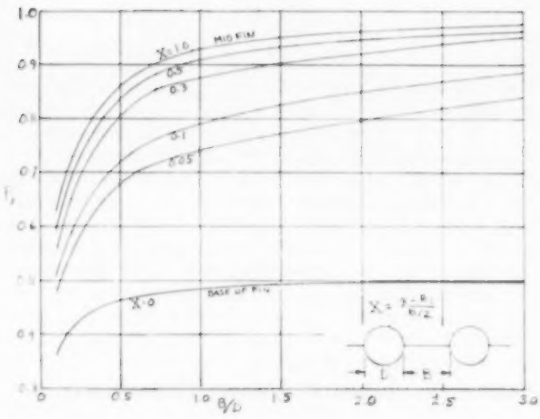

Fig. 17 Fin view factor F_f (at various positions along the fin X) versus B/D

which has the expected extremes $F_f(\phi_1 = \phi_2 = 0) = 1.0$, $F_f(\phi_1 = \phi_2 = \pi/2) = 0$.

The cut-off angles ϕ_1 and ϕ_2 are functions of B/D and $X = \dfrac{x - D/2}{B/2}$:

$$\sin \phi_1 = \frac{1}{1 + X\,B/D}, \qquad \sin \phi_2 = \frac{1}{1 + (2 - X)B/D} \tag{26}$$

The fin view factors are plotted as functions of B/D for various X in Fig. 17. It is interesting to note (Fig. 17) that as $B/D \to \infty$, only the view factor for $X = 0$ (next to the tube) approaches 0.5, while these at all other positions approach 1.0.

APPENDIX 3

Determination of Exact Temperature Distribution on Fin (for Fin-and-Tube Design)

As brought out in Section 3, the temperatures on the fin are influenced by view factors (Appendix 2) which are functions of x. Repeating equation (13) and its boundary conditions,

$$\left.\begin{aligned} & T'' = \frac{d^2T}{dx^2} = 2\,\frac{\sigma\epsilon}{kt}\,F_f T^4; \\ & \text{at} \quad x = D/2, \qquad T = T_{1m} \qquad \text{(known)}, \\ & \text{at} \quad x = \frac{B + D}{2}, \qquad T = T_{2m} \qquad \text{(specify)}, \\ & \text{and} \quad x = \frac{B + D}{2}, \qquad T' = \frac{dT}{dx} = 0 \quad \text{(by symmetry)}. \end{aligned}\right\} \tag{13}$$

One finds the somewhat novel situation here of knowing two boundary conditions at an unknown location, $\dfrac{B + D}{2}$, at which the step solution must nevertheless begin. Since the purpose of these calculations is to provide a fin effectiveness or its equivalent, they should be made at the fourth-root-mean fourth power of the tube surface temperature extremes, T_{1m}.

Starting at $\dfrac{B + D}{2}$, mid-fin, one specifies the temperature, $T = T_{2m}$. It is then necessary to estimate $B/2$, aided by the approximate solution of Section 4 (e.g., assume a value for $B/2$ about 10 per cent greater than that given by the approximate solution for the same T_{2m}). If as a result of the computations the temperature at $x = D/2$ is T_{1m}, then the assumption of $B/2$ is confirmed; if not, then the computations must be repeated using an adjusted estimate of $B/2$. The magnitude of $\left(\dfrac{dT'}{dx}\right)_{x = D/2}$ will result from the computations, and the heat rejected from the fin per unit length, at T_{1m}, is $(Q/L)_f = -kt\left(\dfrac{dT}{dx}\right)_{x = D/2}$.

We will examine the procedure by considering the example of section 4 (a fluid condensing at 1800 deg R). $T_1 = 1800$ R, let $T_1 - T_2 = 200$ R; therefore $T_2 = 1600$ R. Assume $B/2$ is 10 per cent greater than the approximate solution yields (Table 3), i.e., $B/2 = 1.1 \times 0.405 = 0.45$ in. The fin width $B/2$ is broken into five intervals, $\Delta x = 0.90$ in. Starting at mid-fin, $\dfrac{B + D}{2} - x = 0$, $T = 1600$ and F_f can be obtained by replotting the information given in Fig. 17 for $B/D = \dfrac{2 \times 0.45}{0.5} = 1.8$; i.e., a curve of F_f versus x along the fin. T'' is computed from equation (13), and $-\Delta T' = T''\Delta x$ except for the first and last steps, for which $-\Delta T' = {}^1/_2 T''\Delta x$, to establish the slopes at the mid-point of each increment; $-T' = \Sigma(-\Delta T')$. $\Delta T = -T'\Delta x$ and the temperature at the end of the first increment is the temperature at the beginning plus ΔT. The summary for this example appears in Table 4, where T_1 is computed to be 1804.65 deg R, which compares closely with the original value of 1800 deg R. $(Q/L)_f$ (exact) is compared with the approximate value for a range of B/D in Fig. 10. The product $F_f T^4$ is shown in Fig. 11; this represents the effectiveness of fin at any point. Note the adverse effect of poor view factor near the tube-fin junction. Fig. 12 compares the fin temperature distribution for the approximate and exact solution. Fig. 13 compares the maximum heat rejection per unit mass for the exact and the approximate solution. Note that the optimum B/D ratio shifts slightly.

Table 4 Exact solution for fin temperature distribution

$\frac{D+B}{2} - x$ (in.)	0.0000	0.090	0.180	0.270	0.360	0.450
T (°R)	1800	1807.65	1830.89	1870.50	1727.88	1804.65
$T^4 \times 10^{-12}$ (°R)^4	6.55	6.68	7.07	7.79	8.91	10.59
F_f (Fig. 17)	.955	.953	.947	.930	.887	.495
$T'' \times 10^{-5}$ (°R/ft) (Eq. 13)	2.75	2.77	2.92	3.16	3.40	2.28
$-\Delta T' = T''\Delta x$ (°R/ft)	1021*	2077	2184	2368	2585	855*
$-T' = \Sigma(-\Delta T')$ (°R/ft)	1021	3098	5282	7650	10235	11090 = $\left(-\frac{dT}{dx}\right)_{x=\frac{B}{2}}$
$\Delta T = -T'\Delta x$ (°R)	7.65	23.24	39.61	57.68	76.77	

*At each end $-\Delta T' = \frac{1}{2}T''\Delta x$, and $-\Delta T' = T''\Delta x$ elsewhere.

B. W. SWANSON[1]
E. V. SOMERS[2]

Optimization of a Conventional-Fuel-Fired Thermoelectric Generator

Introduction

A THERMOELECTRIC GENERATOR involves the direct production of electrical power by flow of heat into and through a thermocouple system. Thus, as depicted in Fig. 1, if a series circuit of thermocouples of alternate materials "X" and "Y" are placed between a heat source and a heat sink, heat will flow into the hot junctions and part of it will be converted to electric power, as indicated by the + and − signs at the electric terminals, and part of it will be rejected to the sink at the cold junctions.

Shown in Fig. 2 is a schematic diagram of a cross section of a thermoelectric generator duct. The diagram illustrates the extension of the simple scheme of Fig. 1, with the heat source that of the heated gas flow rate in the center of the duct and the heat sink that of the coolant flow rate in the coolant jacket. The coolant is assumed to remain at ambient temperature along the length of the duct. However, the gas drops in temperature as it flows through the duct because of the heat rate transferred by convection to the thermoelectric elements. The convected heat rate at any point along the length of the duct can be computed in terms of the over-all transmission coefficient and the gas-to-ambient temperature drop. The over-all transmission coefficient is a function of the gas and coolant convection coefficients, approximately constant along the length of the duct, and the local thermal conductance of the thermoelectric elements. Since the local thermal conductance is a design variable dependent on the local element thickness, the design of the element thickness along the length of the duct will determine (1) the local gas temperature and the local convected heat rate; and (2) the local thermoelectric power produced. Thus, for a given duct geometry and given gas conditions of inlet temperature and mass flow rate, it is desirable to determine what temperature distribution of the gas along the length of the duct will optimize the total thermoelectric power produced and what distribution of thermoelectric element thickness is necessary to obtain this gas-temperature distribution.

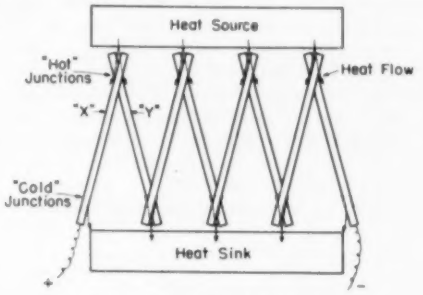

Fig. 1 Thermoelectric generator

[1] Heat Transfer Section, Mechanics Department, Westinghouse Research Laboratories, Pittsburgh, Pa.
[2] Manager, Heat Transfer Section, Mechanics Department, Westinghouse Research Laboratories.
Contributed by the Heat Transfer Division and presented at the Semi-Annual Meeting, St. Louis, Mo., June 14–18, 1959, of THE AMERICAN SOCIETY OF MECHANICAL ENGINEERS.
NOTE: Statements and opinions advanced in papers are to be understood as individual expressions of their authors and not those of the Society. Manuscript received at ASME Headquarters, March 2, 1959. Paper No. 59—SA-14.

Nomenclature

A = cross-sectional area normal to heat flux rate in thermoelectric elements, ft²
A_1, A_2 = equations (15)
c_p = specific heat of heated gas at constant pressure, Btu/lb deg F
D = duct diameter, ft
F = arbitrary function of gas temperature and its derivative with respect to duct length, equation (12)
H = enthalpy rate of heated gas, Btu/hr
h_g = gas heat-transfer coefficient, Btu/hr ft² deg F
h_a = heat-transfer coefficient to sink coolant at an ambient temperature, Btu/hr ft² deg F
K.E. = kinetic energy rate of heated gas, Btu/hr
l = thermoelectric element thickness, ft
l^* = thermoelectric element length optimizing power, ft
L = duct length, ft
M = mass flow rate, lb/hr
P.E. = potential energy rate of heated gas, Btu/hr
P = thermoelectric power, Btu/hr
P^* = optimum thermoelectric power, Btu/hr
Q = heat flow rate, Btu/hr
Q_{in} = heat rate added from fuel to gas flow at duct entrance, Btu/hr
T_g = temperature of heated gas, deg R
T_h = hot-junction temperature of thermoelectric elements, deg R
T_c = cold-junction temperature of thermoelectric elements, deg R
T_a = ambient temperature of surroundings, deg R
T_0 = inlet bulk gas temperature, deg R
T_e = exit bulk gas temperature, deg R
U = over-all transmission coefficient $\left(\frac{1}{h_g} + \frac{l}{\lambda} + \frac{1}{h_a}\right)^{-1}$, Btu/hr ft² deg F
x = distance co-ordinate along length of duct, ft
β = linear gas temperature gradient in the duct, deg F/ft
β^* = linear gas temperature gradient optimizing power, deg F/ft
ϵ_c = Carnot efficiency
$\epsilon_{t.e.}$ = thermocouple efficiency
$\epsilon_{t.e.}^*$ = modified thermocouple efficiency, $\frac{\epsilon_{te}}{T_h}$, deg^{-1} R
λ = thermal conductivity of thermoelectric material, Btu/hr ft deg F
ϵ = thermal efficiency
ϵ^* = optimum thermal efficiency

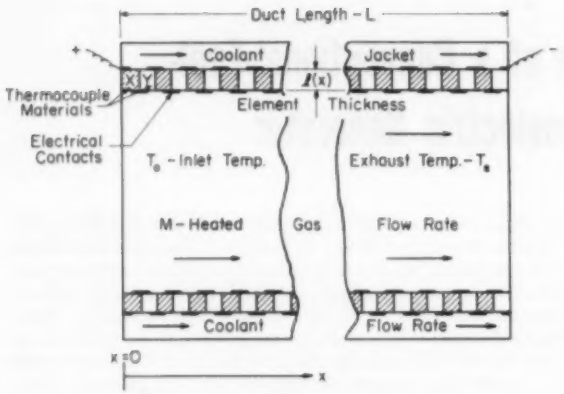

Fig. 2 Cross section of thermoelectric generator duct

Determination of Electric Power in Terms of Design Parameters

The design parameters of the thermoelectric duct are those of geometry, duct diameter D, and duct length L; material, thermoelectric parameter $\epsilon_{t.e.}{}^*$, and specific heat of gas c_p; and operating conditions, inlet gas temperature T_0, gas flow rate M, coolant temperature T_a, and convection coefficients h_g (gas) and h_a (coolant). The local thickness of the thermoelectric elements along the length of the duct determines the local differential heat rate dQ and the local hot and cold junction temperatures T_h and T_c, and these in turn determine the local differential thermoelectric power dP. The integration of dP along the length of the duct yields the total electric power P.

Let P denote thermoelectric power; in differential form [1][2]

$$dP = \epsilon_c \epsilon_{t.e.}\, dQ \tag{1}$$

where ϵ_c is the Carnot efficiency $(T_h - T_c)/T_h$ and $\epsilon_{t.e.}$ is the thermocouple efficiency.

From the first law of thermodynamics, the energy content of the heated gas flowing in the thermoelectric duct is described by

$$\left.\begin{aligned} dQ - dW &= dH + dKE + dPE \\ dW &= dKE = dPE \simeq 0 \\ dQ &= dH = Mc_p dT_g \\ dQ &= Mc_p \frac{\partial T_g}{\partial x}\, dx \end{aligned}\right\} \tag{2}$$

The heat-flow rate described by equation (2) equals that heat rate transferred radially through the thermoelectric elements.

The differential thermoelectric power, dP, may be rewritten from equation (1) as,

$$dP = \epsilon_{t.e.} \frac{T_h - T_c}{T_h}\, dQ \tag{3}$$

By definition[4] let

$$\epsilon_{t.e.} = T_h \epsilon_{t.e.}{}^*$$

$$dP = \epsilon_{t.e.}{}^* (T_h - T_c)\, dQ \tag{4}$$

[2] Numbers in brackets designate References at end of paper.

[4] This definition is approximately correct (very close) for thermal efficiencies around 10 per cent; it results from a binomial expansion of Ioffe's value of M [2] with Ioffe's value of $z/4$ equaling the value of $\epsilon_{t.e.}{}^*$. $\epsilon_{t.e.}{}^*$ is a material parameter.

For any section of thermoelectric elements, the Fourier law for heat conduction states that, as an approximation (for small values of the $\epsilon_c \epsilon_{t.e.}$ product), [3]

$$dQ = \lambda \frac{T_h - T_c}{l}\, dA \tag{5}$$

Therefore, an alternate expression exists for dP

$$dP = \epsilon_{t.e.}{}^* \frac{l}{dA}\, dQ^2 \tag{6}$$

A further representation of dQ is given by

$$dQ = U(T_g - T_a)dA = \frac{(T_g - T_a)dA}{\dfrac{1}{h_g} + \dfrac{l}{\lambda} + \dfrac{1}{h_a}} \tag{7}$$

from which

$$dP = \frac{\epsilon_{t.e.}{}^* l}{\lambda} \left\{ \frac{T_g - T_a}{\dfrac{1}{h_g} + \dfrac{l}{\lambda} + \dfrac{1}{h_a}} \right\}^2 dA \tag{8}$$

An auxiliary condition given by equations (2) and (7), with $dA = \pi D dx$, is

$$Mc_p \frac{dT_g}{dx} = -\frac{\pi D(T_g - T_a)}{\dfrac{1}{h_g} + \dfrac{l}{\lambda} + \dfrac{1}{h_a}} \tag{9}$$

which can be solved for $l(x)$

$$l(x) = -\frac{\lambda \pi D(T_g - T_a)}{Mc_p \dfrac{dT_g}{dx}} - \lambda \left(\frac{1}{h_g} + \frac{1}{h_a} \right) \tag{10}$$

This expression for $l(x)$ can be substituted into equation (8) for dP.

$$P = \int_0^L \epsilon_{t.e.}{}^* \left\{ -Mc_p \frac{dT_g}{dx} (T_g - T_a) - \frac{\left(\dfrac{1}{h_g} + \dfrac{1}{h_a} \right)}{\pi D} \left(Mc_p \frac{dT_g}{dx} \right)^2 \right\} dx \tag{11}$$

Henceforth, $\epsilon_{t.e.}{}^*$ will be assumed to be constant along the length of the duct.[5]

Optimization of Electric Power with the Optimum Temperature Distribution of the Gas

The problem now is to maximize the integrated expression for P.

$$P = \int_0^L F\left(T_g, \frac{dT_g}{dx} \right) dx, \quad \text{with} \quad T_g = T_0 \quad \text{at} \quad x = 0 \tag{12}$$

and T_g unspecified at $x = L$. This requires that $F\left(T_g, \dfrac{dT_g}{dx} \right)$ satisfy the Euler-Lagrange differential equation [1]

[5] The value of $\epsilon_{t.e.}{}^*$ can be assumed constant using temperature-averaged values for the thermal-conductivity-electrical-resistivity product and the mean value of the Seebeck coefficient at the hot and cold junction temperatures [4]. Although the hot and cold junction temperatures vary in this problem, an a priori estimate of $\epsilon_{t.e.}{}^*$ equal to a constant introduces little error.

$$\frac{\partial F}{\partial T_g} - \frac{d}{dx}\left(\frac{\partial F}{\partial T_g'}\right) = 0, \quad T_g' = \frac{dT_g}{dx}, \tag{13}$$

and, in this case, the end point condition that [5]

$$\frac{\partial F}{\partial T_g'} = 0 \quad \text{at} \quad x = L. \tag{14}$$

Let

$$\left.\begin{aligned} A_1 &= -\epsilon_{t.c.}{}^* M c_p \\ A_2 &= -\epsilon_{t.c.}{}^* \left(\frac{1}{h_g} + \frac{1}{h_a}\right)\frac{(Mc_p)^2}{\pi D} \end{aligned}\right\} \tag{15}$$

Then,

$$\left.\begin{aligned} P &= \int_0^L \{A_1 T_g'(T_g - T_a) + A_2(T_g')^2\}\, dx \\ \frac{\partial F}{\partial T_g} &= A_1 T_g' \\ \frac{\partial F}{\partial T_g'} &= A_1(T_g - T_a) + 2A_2 T_g' \end{aligned}\right\} \tag{16}$$

By substituting into equation (13), it can be shown that

$$T_g = T_0 + \beta x \tag{17}$$

The end point condition, equation (14), now determines the optimum values of β, β^*, from equations (15) and (16)

$$\beta^* = -\frac{(T_0 - T_a)}{L + \dfrac{2Mc_p}{\pi D}\left(\dfrac{1}{h_g} + \dfrac{1}{h_a}\right)} \tag{18}$$

with $T_g = T_0 + \beta x$, equation (11) becomes

$$P = \int_0^L -\epsilon_{t.c.}{}^* \left\{ Mc_p\beta[T_0 - T_a + \beta x] - \frac{\left(\dfrac{1}{h_g} + \dfrac{1}{h_a}\right)}{\pi D}(Mc_p\beta)^2 \right\} dx \tag{19}$$

This integrates to

$$P = \left\{ \begin{aligned} &-\epsilon_{t.c.}{}^* Mc_p\beta(T_0 - T_a)L - \epsilon_{t.c.}{}^* Mc_p\beta^2\frac{L^2}{2} \\ &\quad - \epsilon_{t.c.}{}^*\left(\frac{1}{h_g} + \frac{1}{h_a}\right)\frac{(Mc_p\beta)^2}{\pi D}L \\ &-\epsilon_{t.c.}{}^* Mc_p \left\{ {}^1/_2\,[T_0 - T_s][2(T_0 - T_a) \right. \\ &\quad \left. - (T_0 - T_s)] + \frac{Mc_p}{\pi DL}\left[\left(\frac{1}{h_g} + \frac{1}{h_a}\right)\right. \right. \\ &\quad \left. \left. (T_0 - T_s)^2\right]\right\} \end{aligned} \right. \tag{20}$$

Substitution of $\beta = \beta^*$, yields

$$P^* = \frac{\epsilon_{t.c.}{}^* Mc_p(T_0 - T_a)^2}{2 + \left(\dfrac{1}{h_g} + \dfrac{1}{h_a}\right)\dfrac{4Mc_p}{\pi DL}} \tag{21}$$

The expression for P^* can also be written in terms of $T_s{}^*$. In this case L is specified and $T_s{}^*$ is obtained from the equation

$$\left.\begin{aligned} T_s{}^* &= T_0 + \beta^* L \\ \beta^* &= -\frac{T_0 - T_s{}^*}{L} = -\frac{T_0 - T_a}{L + \dfrac{2Mc_p}{\pi D}\left(\dfrac{h}{h_g} + \dfrac{1}{h_a}\right)} \end{aligned}\right\} \tag{22}$$

The solution for $L + \dfrac{2Mc_p}{\pi D}\left(\dfrac{1}{h_g} + \dfrac{1}{h_a}\right)$ substituted into equation (21) gives

$$P^* = \epsilon_{t.c.}{}^* \frac{Mc_p(T_0 - T_a)(T_0 - T_s{}^*)}{2} \tag{23}$$

It is to be noted that satisfaction of the Euler-Lagrange differential equation is a necessary but not sufficient condition for maximizing the power integral. By using exponential and cosine gas temperature distributions for comparison, it can be shown that $T_g = T_0 + \beta x$ does *not* minimize the power.

Determination of Optimum Thermoelectric Element Thickness

In the optimization of the thermoelectric power, the condition used was that

$$Mc_p\frac{dT_g}{dx} = -\frac{\pi D(T_g - T_a)}{\left(\dfrac{1}{h_g} + \dfrac{l}{\lambda} + \dfrac{1}{h_a}\right)} \tag{24}$$

This equation can be solved for $l(x)$

$$l(x) = -\frac{\lambda\pi D(T_g - T_a)}{Mc_p\dfrac{dT_g}{dx}} - \lambda\left(\frac{1}{h_g} + \frac{1}{h_a}\right) \tag{25}$$

For $T_g = T_0 + \beta x$

$$l(x) = -\frac{\lambda\pi D[(T_0 - T_a) + \beta x]}{Mc_p\beta} - \lambda\left(\frac{1}{h_g} + \frac{1}{h_a}\right) \tag{26}$$

Substitution of β^* for β, per equation (22), yields

$$l^*(x) = \frac{\lambda\pi D(L - x)}{Mc_p} + \lambda\left(\frac{1}{h_g} + \frac{1}{h_a}\right) \tag{27}$$

Thermal Efficiency Under Optimum Conditions

The thermal efficiency of interest is defined as the quotient of the optimum thermoelectric power by the heat-addition rate to the system. Thus, for fixed values of M, $\epsilon_{t.c.}{}^*$, $T_0 - T_a$, and L,

$$\epsilon^* = \frac{P^*}{Q_{in}} \tag{28}$$

By equation (23)

$$P^* = \frac{\epsilon_{t.c.}{}^* Mc_p(T_0 - T_a)(T_0 - T_s{}^*)}{2} \tag{29}$$

and since $Q_{in} = Mc_p(T_0 - T_a)$

$$\epsilon^* = {}^1/_2\epsilon_{t.c.}{}^*(T_0 - T_s) \tag{30}$$

As the optimum duct length approaches infinity, the exit temperature approaches ambient. In this case the efficiency approaches its maximum value

$$\epsilon^*(\max) = {}^1/_2\epsilon_{t.c.}{}^*(T_0 - T_a) \tag{31}$$

For the case in which the exit temperature approaches the inlet

temperature the optimum duct length and the efficiency ϵ^* both approach zero.

Summary

The purpose of this report has been to investigate conditions for optimizing the thermal efficiency of the design of a conventional-fuel-fired thermoelectric generator. Equations have been developed for the following:

1 The temperature distribution of the heated gas in a circular duct type of generator, that maximizes the thermoelectric power output, with respect to the temperature distribution within the duct and the exit gas temperature at the end of the duct.

2 The thermoelectric power developed, based upon these optimizing temperature criteria.

3 The required variation of thermoelectric element thickness required to satisfy both optimizing temperature criteria.

4 Thermal efficiency under optimum conditions.

References

1 A. F. Ioffe, "Semiconductor Thermoelements and Thermoelectric Cooling," Infosearch Limited, London, England, 1957, pp. 38–39.
2 Ibid., equations (31) and (32), p. 40.
3 Ibid., equations (50)–(51*a*), pp. 50–51.
4 Ibid., pp. 60–62, 71.
5 R. Weinstock, "Calculus of Variations," McGraw-Hill Book Company, Inc., New York, N. Y., 1952.

Journal of HEAT TRANSFER — Technical Briefs

This section consists of contributions of 750 words or less (about 2½ double-spaced typewritten pages, including figures). Technical Briefs will be reviewed and approved by the specific division's reviewing committee prior to publication. After approval, such contributions will be published as soon as possible, normally in the next issue of the Journal.

Heat Transfer From a Rotating Disk to Fluids of Any Prandtl Number

E. M. SPARROW[1] and J. L. GREGG[1]

Introduction

THE LAMINAR FLOW about a rotating disk situated in a large body of quiescent fluid was first analyzed by von Karman [1].[2] The heat transfer from such a rotating disk has been studied by Millsaps and Pohlhausen [2] for fluids which have Prandtl numbers in the range $0.5 < (c_v/c_p)\mathrm{Pr} < 10$. For gases ($\mathrm{Pr} = 0.72$), the effects of compressibility were examined by Ostrach and Thornton [3]. In the present investigation, the restriction on Prandtl number is lifted, and heat-transfer results are obtained for fluids of all Prandtl numbers.

Analysis

The heat-transfer process in the fluid is governed by the conservation of energy principle, which takes the following form in cylindrical co-ordinates

$$\rho c_p \left(V_r \frac{\partial T}{\partial r} + \frac{V_\phi}{r} \frac{\partial T}{\partial \phi} + V_z \frac{\partial T}{\partial z} \right) = k \nabla^2 T \qquad (1)$$

where T is the static temperature and ∇^2 is the Laplace operator. The velocities may be rephrased in terms of von Karman's similarity variables as follows:

$$\eta = \left(\frac{\omega}{\nu} \right)^{1/2} z, \quad V_r = r\omega F(\eta), \quad V_\phi = r\omega G(\eta),$$

$$V_z = (\omega\nu)^{1/2} H(\eta) \qquad (2a)$$

and in addition, a dimensionless temperature may be defined as

$$\theta(\eta) = (T - T_\infty)/(T_w - T_\infty) \qquad (2b)$$

where T_w and T_∞, respectively, represent the surface temperature (a constant) and the ambient temperature. Introducing these new variables into the energy equation, there is obtained

$$\theta'' = (\mathrm{Pr}) H \theta' \qquad (3)$$

The primes denote differentiation with respect to η and Pr is the Prandtl number of the fluid. From the definition of θ as given by equation (2b), it is clear that the boundary conditions are

$$\theta(0) = 1, \quad \theta \to 0 \quad \text{as} \quad \eta \to \infty \qquad (4)$$

Numerical solutions of equation (3) subject to the boundary conditions (4) have been carried out on an IBM 653 electronic computer for Prandtl numbers of 0.01, 0.1, 1, 10, and 100.[3] The temperature distributions corresponding to these solutions are presented in Figs. 1 and 2, respectively, for the low and high Prandtl number ranges. Also shown on the graphs are the values of the velocity function H used as input data in the solution of equation (3). Inspection of these figures reveals that, for low Prandtl numbers, the thermal boundary layer is much thicker than the velocity boundary layer. The opposite characteristic is displayed for high Prandtl numbers. This suggests a procedure for obtaining asymptotic solutions.

First, as the Prandtl number becomes very small, Fig. 1 indicates that H is essentially constant throughout the thermal boundary layer. Under these circumstances, the solution of equation (3) is

$$\theta = e^{\mathrm{Pr}\, H(\infty)\eta} \qquad (5)$$

where $H(\infty) = -0.88447$. In particular, the temperature derivative at the wall, needed in computing the heat transfer, is

$$(d\theta/d\eta)_{\eta=0} = -0.88447\ \mathrm{Pr} \qquad (5a)$$

From Fig. 2, it is seen that, as the Prandtl number approaches very large values, the thermal boundary layer is confined to a smaller and smaller portion of the velocity boundary layer. This prompts us to write H in terms of a series expansion about $\eta = 0$. So,

$$H = H(0) + H'(0)\eta + \frac{H''(0)}{2}\eta^2 + \ldots$$

Since $H(0) = H'(0) = 0$, we write

$$H = H''(0)\frac{\eta^2}{2}$$

for small values of η. A solution of equation (3) corresponding to this approximation for H is

$$\theta = 1 - \frac{\displaystyle\int_0^{[-\mathrm{Pr}\, H''(0)/6]^{1/3}\eta} \exp(-\xi^3) d\xi}{\displaystyle\int_0^{\infty} \exp(-\xi^3) d\xi} \qquad (6)$$

The dimensionless temperature derivative at the wall associated with this solution is

$$(d\theta/d\eta)_{\eta=0} = [-\mathrm{Pr}\, H''(0)/6]^{1/3}/\Gamma(4/3) = 0.62048\ \mathrm{Pr}^{1/3} \qquad (6a)$$

where the value -1.02046 has been used for $H''(0)$, and Γ represents the gamma function as found in numerous mathematical tables.

Heat-Transfer Results

The local rate of heat transfer from the disk to the fluid may be evaluated using Fourier's law, i.e.,

$$q = -k(\partial T/\partial z)_{z=0} \qquad (7)$$

[1] NASA, Lewis Research Center, Cleveland, Ohio. Assoc. Mem. ASME.

[2] Numbers in brackets designate References at end of paper.

Contributed by the Heat Transfer Division of THE AMERICAN SOCIETY OF MECHANICAL ENGINEERS.

NOTE: Statements and opinions advanced in papers are to be understood as individual expressions of their authors and not those of the Society. Manuscript received at ASME Headquarters, February 16, 1959.

[3] The values of $H(\eta)$ needed to carry out the solutions were obtained by re-solving von Karman's differential equations.

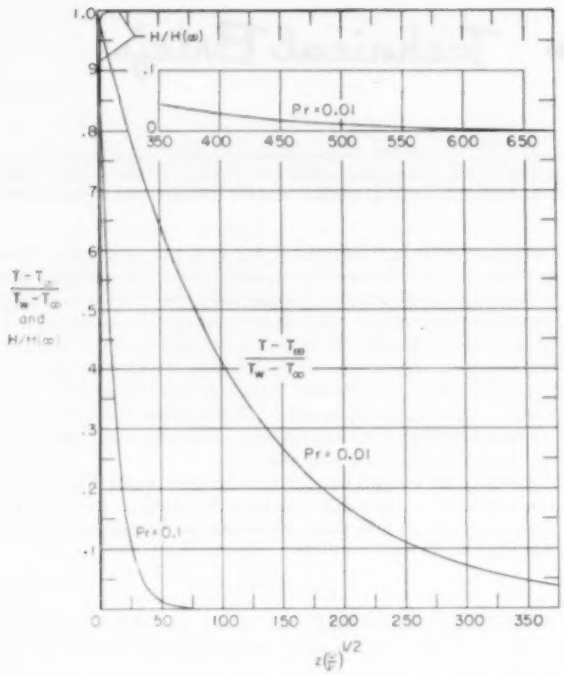

Fig. 1 Temperature distributions for low Prandtl number fluids [$H/H(\infty)$ is input function for temperature solutions]

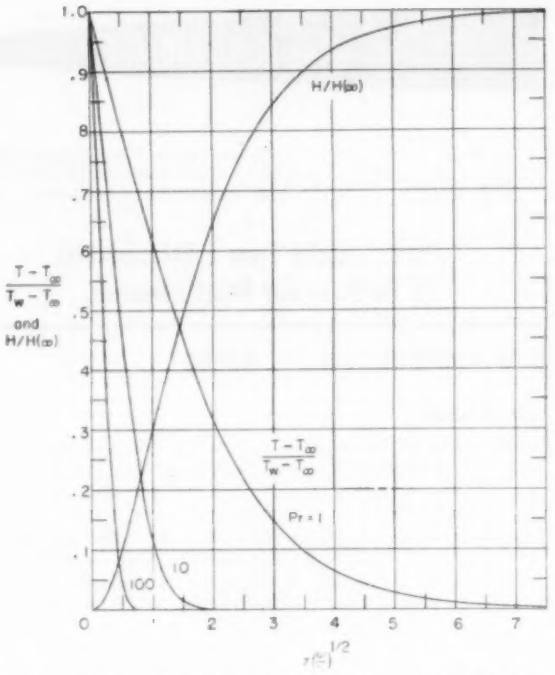

Fig. 2 Temperature distributions for high Prandtl number fluids [$H/H(\infty)$ is input function for temperature solutions]

Introducing a local heat-transfer coefficient h by the definition

$$h = q/(T_w - T_\infty)$$

and evaluating equation (7) in terms of the variables of the analysis, there is obtained

$$\frac{h\left(\frac{\nu}{\omega}\right)^{1/2}}{k} = -\left(\frac{d\theta}{d\eta}\right)_{\eta=0} \tag{7a}$$

Since $(d\theta/d\eta)_{\eta=0}$ depends only on the Prandtl number, it is seen that, for a given fluid, the variation of the heat-transfer coefficient with angular velocity is given by

$$h \sim \omega^{1/2}$$

Further, h is constant over the disk surface.

Using the numerical solutions of equation (3), the dimensionless heat-transfer results are listed in Table 1.

Table 1 Dimensionless heat-transfer results

Pr	$h\left(\frac{\nu}{\omega}\right)^{1/2}\Big/k$
0.01	0.0087051
0.1	0.076581
1	0.39625
10	1.1341
100	2.6871

For the limiting situations of very low and of very high Prandtl numbers, the following asymptotic expressions for the heat transfer may be written utilizing equations (5*a*) and (6*a*)

$$h\left(\frac{\nu}{\omega}\right)^{1/2}\Big/k = 0.88447\ \mathrm{Pr}, \quad \mathrm{Pr} \to 0 \tag{8a}$$

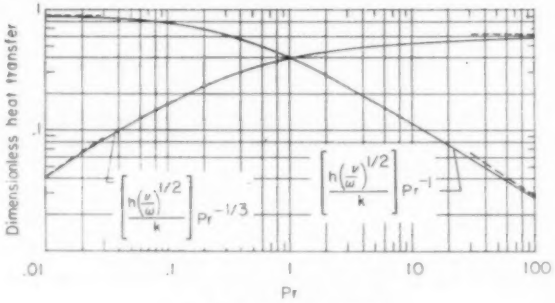

Fig. 3 Heat-transfer results

$$h\left(\frac{\nu}{\omega}\right)^{1/2}\Big/k = 0.62048\ \mathrm{Pr}^{1/3}, \quad \mathrm{Pr} \to \infty \tag{8b}$$

A graphical presentation of the heat-transfer results is given in Fig. 3. The results have been plotted in two different ways, one appropriate to low Prandtl number fluids and the other appropriate to high Prandtl number fluids. The asymptotic lines are also shown (dashed). It is seen that the low Prandtl number asymptote already closely coincides with the computed curve at Pr = 0.01, the deviation being only 1.5 per cent. The high Prandtl number heat-transfer results approach their asymptote somewhat less rapidly, the difference between the computed and asymptotic curves being about 7 per cent at Pr = 100; this deviation is not large from the practical point of view. The significant fact is that the asymptotic curves provide sufficiently accurate heat-transfer results *outside* the Prandtl number range for which the numerical solutions have been obtained.

By utilizing either the numerically computed results or the asymptotic expressions, heat-transfer calculations can be carried out for fluids of any Prandtl number.

References

1 Th. von Karman, "Über Laminare und Turbulent Reibung," *Zeitschrift für Angewandte Mathematik und Mechanik*, vol. 1, 1921, pp. 233–252.

2 Knox Millsaps and Karl Pohlhausen, "Heat Transfer by Laminar Flow From a Rotating Plate," *Journal of Aeronautical Sciences*, vol. 19, 1952, pp. 120–126.

3 Simon Ostrach and Phillip R. Thornton, "Compressible Laminar Flow and Heat Transfer About a Rotating Isothermal Disk," NACA TN 4320, 1958.

An Approximate Treatment of Unsteady Heat Conduction in Semi-Infinite Solids With Variable Thermal Properties

KWANG-TZU YANG[1] and ALBIN SZEWCZYK[2]

THE PROBLEM of property variations in unsteady one-dimensional conduction analysis has become increasingly important in practice, especially in view of extreme temperature changes encountered in many applications. As the boundary temperature conditions are usually arbitrary, it is therefore desirable to have a relatively simple, yet accurate, calculation procedure for such a general problem so that the variation of properties may readily be taken into account. The primary purpose of this note is to present such a calculation procedure. The integral method is well known in boundary-layer theory; its extension to conduction analysis, however, has only attracted attention recently. Goodman [1],[3] utilizing temperature profiles approximated by polynomials, solved integral equations involving a phase change. Very recently, Reynolds and Dolton [2] presented a more general analysis applicable to a variety of conduction problems, also using temperature polynomials. The present procedure may be considered as a significant improvement over that of Reynolds and Dolton [2] for treating conduction in semi-infinite solids with arbitrarily varying surface temperatures, since their method fails to yield physically sensible results for large dependence of thermal properties on temperature.

By introducing the following dimensionless quantities: $x^* = x/L$, $t^* = at/L^2$, $T^* = T/T_i$, $k^* = k/k_0$, $C^* = C/C_0$, $a = k_0/C_0$, and $\theta = (T - T_i)/(T_s - T_i)$, where x is the depth into the solid, T the time variable, L a characteristic length, k the conductivity, C the volumetric specific heat, and subscripts i, s, 0, indicate initial, surface, and reference conditions, respectively, the usual one-dimensional unsteady conduction equation with variable properties may now be written as

$$C^*\left[\theta\frac{dT_s^*}{dt^*} + (T_s^* - 1)\frac{\partial\theta}{\partial t^*}\right] = (T_s^* - 1)\frac{\partial}{\partial x^*}\left(k^*\frac{\partial\theta}{\partial x^*}\right) \quad (1)$$

which is to be solved with the conditions $\theta(x^*, 0) = 0$ for $0 \leqslant x^* \leqslant \infty$, $\theta(0, t^*) = 1$ for $t^* \geqslant 0$, and $\theta(\infty, t^*) = 0$ for $t^* \geqslant 0$. Now integrating Equation (1) with respect to x^* from 0 to ∞ and imposing the condition $C^* = 1 + \beta T^* = 1 + \beta[(T_s^* - 1)\theta + 1]$, where β is a constant, we obtain:

$$\left(\frac{1}{T_s^* - 1}\frac{dT_s^*}{dt^*}\right)[(1 + \beta)\delta_1^* + \beta(T_s^* - 1)\delta_2^*] + \left[(1 + \beta)\frac{d\delta_1^*}{dt^*} + \frac{\beta}{2}(T_s^* - 1)\frac{d\delta_2^*}{dt^*}\right] = -k_s^*\left(\frac{\partial\theta}{\partial x^*}\right)_s \quad (2)$$

where $\delta_1^* = \int_0^\infty \theta dx^*$ and $\delta_2^* = \int_0^\infty \theta^2 dx^*$. In order to solve Equation (2), it is necessary to introduce an assumed unsteady temperature profile. Because of the limitation on using polynominals as indicated earlier, the present analysis utilizes an exponential form of the type

$$\theta(x^*, t^*) = e^{-\frac{x^*}{\delta^*(t^*)}}\left[1 - J(t^*)\frac{x^*}{\delta^*(t^*)}\right] \quad (3)$$

where $\delta^*(t^*)$ and $J(t^*)$ are two unknown functions. Physical consideration requires J to assume negative values, and in fact it ranges only from -1 to 0, the former being corresponding to no heat flux at surface. It is also seen that usual asymptotic conditions as $x^* \to \infty$ are automatically satisfied in the assumed profile. With Equation (3) substituted in Equation (1) for $x^* = 0$ and in Equation (2), and $\delta^*(t^*)$ eliminated, there results the final integral equation:

$$\frac{dJ}{dt^*} = \frac{P(J, t^*) - M(J, t^*)}{N(J, t^*)} \quad (4)$$

where

$$P(J, t^*) = k_s^* F_2$$

$$M(J, t^*) = \left(\frac{1}{T_s^* - 1}\frac{dT_s^*}{dt^*}\right)(E^* F_1 + G^* F_2)\{\beta[1 + F_4(T_s^* - 1)] + 1\} + \frac{1}{4}(E^{*\prime} F_1 + G^{*\prime} F_2)\{\beta[2 + F_4(T_s^* - 1)] + 2\}$$

$$N(J, t^*) = \frac{1}{4}(E^* F_1' + G^* F_2')\{\beta[2 + F_4(T_s^* - 1)] + 2\} + \frac{\beta}{2}(T_s^* - 1)F_4'(E^* F_1 + G^* F_2)$$

$$E^*(t^*) = \frac{k_s^*(T_s^* - 1)}{C_s^*\left(\frac{dT_s^*}{dt^*}\right)} \qquad G^*(t^*) = \frac{\left(\frac{dk^*}{dT^*}\right)_s (T_s^* - 1)^2}{C_s^*\left(\frac{dT_s^*}{dt^*}\right)}$$

$$F_1(J) = (2J + 1)(1 - J)^2 \qquad F_2(J) = (1 - J^2)^2$$

$$F_3(J) = 1 - J^2 \qquad F_4(J) = \frac{J^2 - 2J + 2}{1 - J}$$

and the prime indicates derivatives. A limiting process of Equation (4) as $t^* \to 0$ yields the initial condition $J(0)$, which is determined from

$$F_3[J(0)] = \left[1 + \frac{1 + \beta}{2}\left(\frac{E^{*\prime}}{k_s^*}\right)_{t^*=0}\right]F_1[J(0)] \quad (5)$$

Equation (4) may now be solved by any convenient numerical procedure, yielding $J(t^*)$. Finally, unsteady temperature profiles are given by Equation (3) with $\delta^*(t^*) = (E^* F_1 + G^* F_2)^{1/3}/(1 - J)$ and surface heat flux q_s by $(q_s L/k_0 T_i) = (T_s^* - 1)k_s^*(1 + J)/\delta^*$.

[1] Department of Mechanical Engineering, University of Notre Dame, Notre Dame, Ind. Assoc. Mem. ASME.

[2] Now at Institute for Fluid Dynamics and Applied Mathematics, University of Maryland, College Park, Md. Assoc. Mem. ASME.

[3] Numbers in brackets designate References at end of paper.

Contributed by the Heat Transfer Division of THE AMERICAN SOCIETY OF MECHANICAL ENGINEERS.

NOTE: Statements and opinions advanced in papers are to be understood as individual expressions of their authors and not those of the Society. Manuscript received at ASME Headquarters, March 2, 1959.

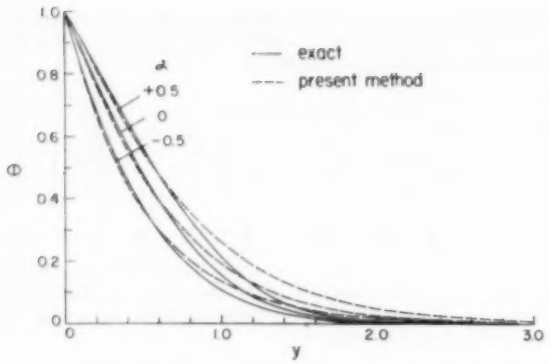

Fig. 1 Transient temperature distribution with stepwise surface temperature change and variable thermal conductivity

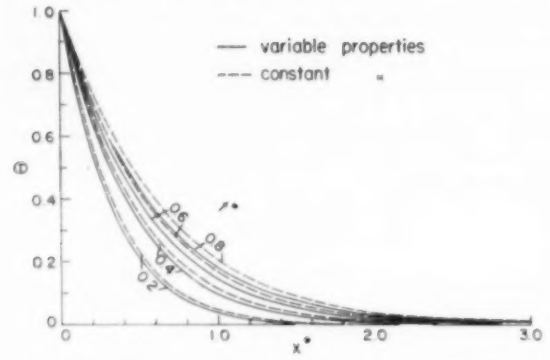

Fig. 2 Transient temperature distribution for the numerical example

For a demonstration of the accuracy, the present procedure is compared with an exact solution given by Yang [3] for the problem of a semi-infinite solid undergoing a stepwise surface temperature change with $\beta = 0$ and $k^* = 1 + \alpha\theta$. Such a comparison is shown in Fig. 1 for $\alpha = +0.5$, 0, and -0.5, where $y = x^*/2t^{*1/2}$. It is seen that the present procedure is entirely satisfactory, especially in the region where large temperature variations occur. Incidentally, during the course of this study, a fourth-degree polynomial was also tried, and it was found that no physically sensible results were obtainable for this problem with $\alpha = \pm 0.5$. Finally, to show an application of the present procedure to a general problem, an example with $T_s^* = e^{t^*}$, $\beta = 0.034$, and $k^* = 1 - 0.0577T^*$ is chosen. The results are shown in Figs. 2 and 3. Also shown are the corresponding curves for constant properties. It is interesting to note that in this particular problem, the unsteady temperature distribution is affected by the property variation more than the surface heat flux is. It is believed that the present procedure may also be extended to more general conduction problems.

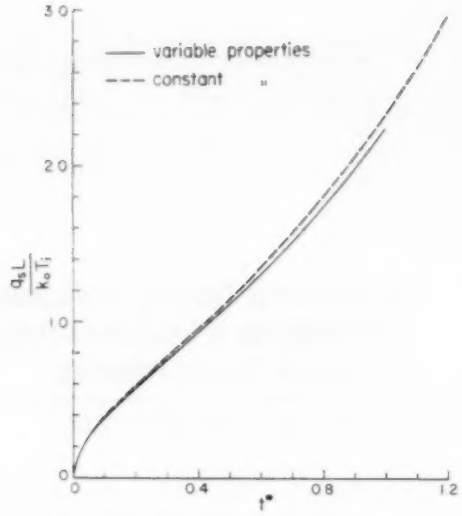

Fig. 3 Surface heat-flux characteristics for the numerical example

References

1 T. R. Goodman, "The Heat-Balance Integral and Its Applications to Problems Involving a Change of Phase," TRANS. ASME, vol. 80, 1958, pp. 335–342.

2 W. C. Reynolds and T. A. Dolton, "Use of Integral Methods in Transient Heat-Transfer Analysis," ASME Paper No. 58—A-248.

3 K. T. Yang, "Transient Conduction in a Semi-Infinite Solid With Variable Thermal Conductivity," *Journal of Applied Mechanics*, vol. 25, TRANS. ASME, vol. 80, 1958, pp. 146–147

Journal of HEAT TRANSFER

Information for Authors

• Manuscripts should be submitted in final form to the Editor. Each manuscript must be accompanied by a statement that it has not been published elsewhere nor has it been submitted for publication elsewhere. A paper which would occupy more than 8 pages of the Journal may be returned to the author for abridgment.

• The author should state his business connection, the title of his position, and his mailing address. A short abstract (50 to 100 words) should be included on the first page immediately preceding the introductory paragraph of the paper.

Three copies of the manuscript are required. One of these must be a carefully prepared printer's copy, typed in double spacing, on one side of the page only, with wide margins, on $8^1/_2$ by 11-in. opaque white paper. Mimeographed manuscripts, if prepared with exceptional care, can be accepted provided they are completely edited.

• As far as possible, all mathematical expressions should be typewritten. Greek letters and other symbols not available on the typewriter should be carefully inserted in ink. Care should be taken to distinguish between capital and lowercase letter, between zero (0) and the letter (*O*), between the numeral (1) and the letter (*l*), etc. A letter representing a vector cannot be printed with an arrow above or below it. The letter should be underscored with a single wavy line, wherever it appears in the text, to designate boldface type.

• A list of symbols carefully marked for the use of the editor (thus: κ, Greek l.c. kappa), if it has not been included in the body of the paper, should accompany the manuscript on a separate page.

• Before preparing a manuscript the author should study printed articles in the Journal, with special attention to the form and style of mathematical expressions, tables, footnotes, references, and abstract. Numbers that identify mathematical expressions should be enclosed in parentheses. Numbers that identify references at the end of the paper should be enclosed in brackets. Care should be taken to arrange all tables and mathematical expressions in such a way that they will fit into a single column when set in type. Equations that might extend beyond the width of one column (fractions that should not be broken or long expressions enclosed in parentheses) should be rephrased to go on two or more lines within column width. Fractional powers are preferred to root signs and should always be used in more elaborate formulas. The solidus should be used instead of the horizontal line for fractions wherever possible.

• A normal paper should not exceed 8 pages in the Journal. It is about 8000 words or 20 double-spaced typewritten pages exclusive of drawings. A Technical Brief should not exceed 750 words or about one page in the Journal inclusive of drawings.

• Originals and two copies of figures must accompany the manuscript. Line drawings should not be larger than $8^1/_2 \times 11$ in. and should be planned for reduction to column width. Lettering should be large enough to be clearly legible when the illustration is reduced. The originals of line drawings must be in India ink on white or pale blue tracing paper or tracing cloth. Photographs of equipment or test specimens must be glossy prints and should be used sparingly. Captions for figures should be typed double-spaced and included as the last page of the manuscript. The figure number and author's name should be written in the margin or on the back of each illustration.

• Titles of papers should be brief.

• Authors can obtain copies of the ASME Manual MS-4, "An ASME Paper," from the Editor and are urged to do so before drafting their papers in final form.

• Papers published in Journals of the Transactions of the ASME must be presented at a Meeting, either in person or by title.

• An author is entitled to 25 preprints free of charge (in the case of two authors, 15 each; three or more authors, 10 each). Larger quantities of preprints or reprints can be ordered from Editorial Department, The American Society of Mechanical Engineers, 29 West 39th Street, New York 18, N. Y. Quotations will be sent on request.

Please address all communications to:

Editor, ASME,

29 West 39th Street,

New York 18, N. Y.

ASME Publications Committee

For information that can be profitably applied to the solution of problems in various areas demanding a knowledge of thermal properties of materials look to . . . .

Thermodynamic and Transport Properties of Gases, Liquids and Solids

This volume covers the present theoretical and experimental state of the science and reports a large number of data on current experimental and theoretical techniques. These data cover thermodynamic and transport properties, PVT data and equation of state, some experimental transport properties, and high-temperature thermodynamic properties of gases. A great deal of heretofore unpublished material appears in the form of tables, charts, and graphs.

CONTENTS

I. THEORETICAL ESTIMATION OF TRANSPORT PROPERTIES

Relations Between Molecular Absorptivities and Emissivities
Theories of Gas Transport Phenomena
Review of Modern Theory of the Thermal Conductivity of Metals

II. REVIEW OF RECENT WORK ON TRANSPORT PROPERTIES

Survey of Recent Work on the Viscosity, Thermal Conductivity, and Diffusion of Gases and Gas Mixtures
Review of Available Experimental Data on the Viscosity of Steam
Systems and Procedures Developed for the Search, Coding, and Mechanized Processing of Bibliographic Information on Thermophysical Properties
Transport Properties of Multicomponent Gas Mixtures at High Temperatures

III. THERMODYNAMIC PROPERTIES: GASES AND LIQUIDS

Thermodynamic Properties of Methane-Nitrogen Mixtures
Correlations and Equations Used in Calculating the Thermodynamic Properties of Freon Refrigerants
The Unmixing of Metal Solutions by a Temperature Gradient
Thermodynamic and Electrical Properties of Nitrogen at High Temperatures
Isentropic Checking of Vapor Tables at Saturation Boundary Lines and Ways of Improving Them

IV. PVT DATA AND EQUATION OF STATE

The Liquid Pressure-Volume-Temperature Relationships, Dew and Bubble Point Pressures, and Densities of a Binary Mixture Containing 75 Wt. % Freon-12 and 25 Wt. % Freon-22
Vapor-Liquid Phase Equilibria in the Binary Systems of Methane, Ethane, and Nitrogen
Application of the B-W-R Equation to Hydrocarbon-Carbon Dioxide Mixtures
An Equation for the Critical Isotherm of Gases
The Virial Equation Applied to Steam

V. THERMODYNAMIC PROPERTIES OF BORON COMPOUNDS

Characterization of Unusual Gaseous Oxide and Hydroxide Molecules in M-O-H Systems at High Temperatures
Thermochemistry and Thermodynamic Functions of Some Boron Compounds
The Combustion of Boron Hydrides
A Generalized Data-Fitting Routine for the LGP-30 Computer; Application to Real-Gas Properties of Diborane
The Low Temperature Thermal and Chemical Thermodynamic Properties of Boron Compounds

VI. TRANSPORT PROPERTIES: EXPERIMENTAL

Thermal Conductivity of Some Epoxy Plastics
Measurements of the Thermal Conductivity of Milk
Thermal Conductivity of Helium-Air Mixtures
Thermal Conductivity of Liquid Ozone
Thermal Diffusivity of Nitrogen as Determined by the Cyclic Heat-Transfer Method

VII. TRANSPORT PROPERTIES: EXPERIMENTAL

Experiments in the Molecular Diffusion of Gases at High Temperatures
The Effect of Moderate Pressures on the Viscosity of Five Gases
The Viscosity of Steam
The Viscosity of Steam-Nitrogen Mixtures at Atmospheric Pressure and Elevated Temperatures
Fluid Thermal Conductivity by a Transient Method
Thermodynamic and Transport Properties of Gaseous Carbon Dioxide

VIII. HIGH TEMPERATURE TRANSPORT PROPERTIES OF METALS AND CERAMICS

Thermal Expansion Coefficients of Binary Substitutional Solid Solution Alloys
Thermal Diffusivity of Metals at Elevated Temperatures
Thermal Conductivity of Aircraft Structural and Reactor Materials
The Total Emissivity of Aircraft Construction Materials
Specific Heat of Materials

IX. HIGH TEMPERATURE THERMODYNAMIC PROPERTIES OF GASES

Mechanized Computation of Thermodynamic Tables at the National Bureau of Standards: The Calculation of the Equilibrium Composition and Thermodynamic Properties of Dissociated and Ionized Gaseous Systems
Equilibria in C + H_2 and C + $2H_2$ Systems at Temperatures Between 1000 K and 6000 K
Equilibria in a Thermal Plasma Composed of C + H_2 and C + $2H_2$ in a Temperature Range From 5000 K to 50,000 K at a Total Pressure of 1 Bar
Mollier Enthalpy-Entropy Charts for High-Temperature Plasmas

The forty-two papers in this volume were originally presented at a symposium sponsored by the Standing Committee on Thermophysical Properties of the ASME Heat Transfer Division.

472 pages **274 illustrations** **$12.50 — 20% discount to ASME members**

THE AMERICAN SOCIETY OF MECHANICAL ENGINEERS, 29 West 39th Street, New York 18, N. Y.